INFORMATION TO USERS

This manuscript has been reproduced from the microfilm master. UMI films the text directly from the original or copy submitted. Thus, some thesis and dissertation copies are in typewriter face, while others may be from any type of computer printer.

The quality of this reproduction is dependent upon the quality of the copy submitted. Broken or indistinct print, colored or poor quality illustrations and photographs, print bleedthrough, substandard margins, and improper alignment can adversely affect reproduction.

In the unlikely event that the author did not send UMI a complete manuscript and there are missing pages, these will be noted. Also, if unauthorized copyright material had to be removed, a note will indicate the deletion.

Oversize materials (e.g., maps, drawings, charts) are reproduced by sectioning the original, beginning at the upper left-hand corner and continuing from left to right in equal sections with small overlaps. Each original is also photographed in one exposure and is included in reduced form at the back of the book.

Photographs included in the original manuscript have been reproduced xerographically in this copy. Higher quality 6" x 9" black and white photographic prints are available for any photographs or illustrations appearing in this copy for an additional charge. Contact UMI directly to order.

UMI

A Bell & Howell Information Company
300 North Zeeb Road, Ann Arbor, MI 48106-1346 USA
313/761-4700 800/521-0600

ANALYSIS OF FLUID FLOW AND HEAT TRANSFER AROUND AND INSIDE A LIQUID SPHERE

BY

MOHAMED ABDELKARIM MOHAMED ANTAR

A Dissertation Presented to the

FACULTY OF THE COLLEGE OF GRADUATE STUDIES

KING FAHD UNIVERSITY OF PETROLEUM & MINERALS

DHAHRAN, SAUDI ARABIA

In Partial Fulfillment of the
Requirements for the Degree of

DOCTOR OF PHILOSOPHY

In

MECHANICAL ENGINEERING

JANUARY, 1996

UMI Number: 9619328

UMI Microform 9619328
Copyright 1996, by UMI Company. All rights reserved.

This microform edition is protected against unauthorized
copying under Title 17, United States Code.

UMI
300 North Zeeb Road
Ann Arbor, MI 48103

KING FAHD UNIVERSITY OF PETROLEUM AND MINERALS

DHAHRAN 31261, SAUDI ARABIA

COLLEGE OF GRADUATE STUDIES

This dissertation, written by **Mohamed Abdelkarim Mohamed Antar** under the direction of his Dissertation advisors and approved by his Dissertation committee, has been presented to and accepted by the Dean of the College of Graduate Studies, in partial fulfillment of the requirements for the degree of

DOCTOR OF PHILOSOPHY

IN MECHANICAL ENGINEERING

Dissertation Committee

Dissertation Advisor (Dr. Abdulghani. A. Al-Farayedhi)

3/1/96

Dissertation Co-Advisor (Dr. Maged A. El-Shaarawi)

Saad Ahmed

Member (Dr. Saad A. Ahmed)

Member (Dr. Dulaihan Al-Harbi)

Dr. Muhammad O. Budair
Department Chairman

Dr. Ala Al-Rabeh
Dean, College of Graduate Studies

16·1·96

Date

This work is dedicated to

My Parents

May ALLAH reward them in the best way

for all what they have done to me

ACKNOWLEDGMENT

In the name of Allah, Most Gracious, Most Merciful " Of knowledge it is only a little that is communicated to you , (O men!)" S. 17 A.85, The Holy Quran

My deepest appreciation goes to my thesis advisor, Dr. Abdulghani Al-Farayedhi for his continuous help, encouragement, suggestions and constructive criticism throughout this work . I am also greatly indebted to my Dissertation co-advisor, Dr. Maged El-Shaarawi for his continuous and endless help, valuable guidance, patience and advice .

Thanks are also due to my thesis committee members, Dr. Saad Ahmed and Dr. Dulaihan Al-Harbi for their interest, encouragement, cooperation, advice and constructive criticism . Indeed working in this dissertation has been so much beneficial, interesting and effective in enrichment of my background .

Appreciation also goes to King Fahd University of Petroleum and Minerals for supporting this work and providing all literature and computer facilities .

I would also like to acknowledge my family for their patience, encouragement and understanding while carrying out this work .

CONTENTS

	Page
ACKNOWLEDGMENT	i
LIST OF FIGURES	viii
ABSTRACT (English)	xix
ABSTRACT (Arabic)	xx
NOMENCLATURE	xxi
CHAPTER I : INTRODUCTION	1
1.1 General	1
1.2 Scope of the present work	2
CHAPTER II : LITERATURE SURVEY	4
2.1 Introduction	4
2.2 Flow Over a Solid Sphere	4
1.2.1.1 Forced Flow	4
1.2.1.2 Induced Flow	8
2.3 Motion of a Gas Bubble in Liquid	8
2.4 Flow Over a Liquid Sphere	9
2.4.1 The Case Without Heat or Mass Transfer	9
2.4.2 The Case With Heat and Mass Transfer to a Single Liquid Droplet	13

2.4.2.1 Spherically Symmetric Models 14

2.4.2.2 Axially Symmetric Models 18

2.4.2.2.a. Non-Boundary-Layer Models 18

2.4.2.2.b. Boundary-Layer Models 27

CHAPTER III : GOVERNING EQUATIONS 34

3.1 Introduction 34

3.2 Gas Phase Governing Equations 35

3.2.1 Governing Equations in Dimensionless Form 37

3.2.2 Governing Boundary Layer Equations 38

3.2.3 Boundary Conditions 39

3.3 Liquid Phase Governing Equations 44

3.3.1 Governing Equations in Dimensionless Form 44

3.3.2 Governing Boundary-Layer Equations 45

3.3.3 Boundary Conditions 46

CHAPTER IV : NUMERICAL REPRESENTATION OF THE GOVERNING EQUATIONS 49

4.1 Introduction 49

4.2 Gas Phase Equations 50

4.2.1 Numerical Grid 50

4.2.2 Linearizing Technique 51

4.2.3 Finite Difference Representation of the derivatives 54

4.2.4 Finite Difference Representation of the Meridional Momentum Equation 56

4.2.5 Finite Difference Representation of the Continuity Equation 59

4.2.6 Finite Difference Representation of the Energy Equation 60

4.3 Liquid Phase Equations 63

4.3.1 Numerical Grid and Linearizing Technique 63

4.3.2 Finite Difference Representation of the meridional Momentum Equation 66

4.3.3 Finite Difference Representation of the Continuity Equation 68

4.3.4 Finite Difference Representation of the Energy Equation 69

CHAPTER V : SOLUTION METHODOLOGY 73

5.1 Introduction 73

5.2 Numerical Grid 74

5.3 Criteria For Convergence 75

5.4 Flow Separation 76

5.5 Matching Conditions at The Surface 77

5.6 Calculating Engineering Parameters 79

5.6.1 Calculating the Shear Stress at the Surface 79

5.6.2 Calculating the Vorticity at the Surface 79

5.6.3 Calculating the Coefficient of Drag 80

5.6.4 Calculating Nusselt Number 80

5.6.5 Calculating the Coefficient of Friction 80

5.7 Solution Procedure 80

5.7.1 Gas Phase Solution 81

5.7.2 Liquid Phase Solution 82

CHAPTER VI : HYDRODYNAMIC RESULTS AND DISCUSSION 84

6.1 Introduction 84

6.2 Results of Velocity Profiles Around the Sphere 85

6.2.1 Meridional Velocity Profiles 85

6.2.2 Radial Velocity Profiles 99

6.2.3 Results of Engineering Parameters 101

6.3 Results of Velocity Profiles Inside the Sphere 112

6.3.1 Meridional Velocity Profiles 112

6-3-2 Radial Velocity Profiles 118

CHAPTER VII : HEAT TRANSFER RESULTS AND DISCUSSION 124

7.1 Introduction 124

7.2 Results of Temperature Profiles Around the Sphere 125

7.2.1 Case 1 : Steady State Temperature Distribution Around the Sphere 126

7.2.1.1 Temperature Profiles 126

7.2.1.2 Nusselt Number 132

7.2.2 Case 2 : Transient Temperature Distribution Around the Sphere 135

7.2.2.1 Case (2-a) : Step Change in Temperature at the Sphere's Surface 135

7.2.2.1 Case (2-a) : Step Change in Temperature at the Sphere's Surface 135

7.2.2.1.1 Temperature Profiles 136

7.2.2.1.2 Nusselt Number 155

7.2.2.2 Case (2-b) : Linear Initial Temperature Profiles 160

7.2.2.2.1 Temperature Profiles 160

7.2.2.2.2 Nusselt Number 172

7.2.2.3 Case (2-c) A Step Change in Temperature at the Boundary Layer Edge 172

7.2.2.3.1 Temperature Profiles 174

7.2.2.3.2 Nusselt Number 204

7.3 Temperature Profiles Inside the Sphere 218

7-4 Computer Run Time 224

CHAPTER VIII : CONCLUSIONS AND RECOMMENDATIONS 226

8.1 Conclusions 226

8.2 Recommendations 228

REFERENCES 229

APPENDIX A : GAS PHASE GOVERNING EQUATIONS 240

A.1 Introduction 240

A.2 Continuity and Momentum Equations 240

A.2.1 Equations in the Spherical Polar Coordinates 241

A.2.2 Orthogonal Curvilinear Axisymmetric Coordinate System 242

A.2.3 Dimensionless Form of the Equations 243

A.3 Order of Magnitude Analysis of the Governing Equations 244

A.3.1 Order of Magnitude Analysis for the Continuity Equation 244

A.3.2 Order of Magnitude Analysis for the Meridional Momentum Equation 245

A.3.3 Order of Magnitude Analysis for the Radial Momentum Equation 246

A.4 Formulation of the Energy Equation Around the Liquid Sphere 247

APPENDIX B : LIQUID PHASE GOVERNING EQUATIONS 251

B.1 Equations in Spherical Coordinates 251

B.2 Order of Magnitude Analysis for the Governing Equations 253

B.2.1 Order of Magnitude Analysis for the Continuity Equation 253

B.2.2 Order of Magnitude Analysis for the Meridional Momentum Equation 254

B.3 Formulation of the Energy Equation Inside the Liquid Sphere 255

APPENDIX C : FLOW CHARTS OF THE COMPUTER PROGRAMS 259

C.1 Flow Chart of the Gas-Phase Program 259

C.2 Flow Chart of the Liquid-Phase Program 261

C.3 List of Gas-phase Program 263

C.4 List of Liquid-Phase Program 268

LIST OF FIGURES

Page

Fig. 3-1 : Schematic of the flow patterns inside and outside the droplet 36

Fig. 3-2 :Coordinate system 36

Fig. 4-1 : Numerical grid 52

Fig. 4-2 : Gas phase finite-difference domain 54

Fig. 4-3 : Liquid phase finite-difference domain 65

Fig. 6-1 : Meridional velocity profiles versus radial distance at different viscosity ratios for different meridional locations 86

Fig. 6-2 : Effect of changing Reynolds number on meridional velocity profiles 88

Fig. 6-3a : Meridional velocity distribution for different viscosity ratios , Re = 1000 90

Fig. 6-3b : Meridional velocity distribution for different viscosity ratios compared to solid sphere case of reference [10] 90

Fig. 6-4a: Effect of Reynolds number on the surface velocity versus the angle , $\mu^* = 2$ 92

Fig. 6-4b: Effect of Reynolds number on the surface velocity versus the angle , $\mu^* = 5$ 92

Fig. 6-5a : Effect of viscosity ratio on surface velocity versus angle, ($\mu^* = 1.05, 1.1$) 93

Fig. 6-5b : Effect of viscosity ratio on surface velocity versus angle, ($\mu^* = 1.5, 2, 5, 100$) 93

Fig. 6-6a : Effect of viscosity ratio on surface velocity versus angle for Re = 1000, $\mu^* = 1.05$ and 1.1 94

Fig. 6-6b : Effect of viscosity ratio on surface velocity versus angle for Re = 1000, $\mu^* = 1.5, 2, 5$ and 100 94

Fig. 6-7 : Maximum surface velocity versus Reynolds number for different values of viscosity ratio 96

Fig. 6-8 : Variation of maximum surface velocity with viscosity ratio at different values of Reynolds number 97

Fig. 6-9 : Effect of viscosity ratio on the variation of the angle of separation with Reynolds number 98

Fig. 6-10 : Radial velocity distribution at different meridional locations 100

Fig. 6-11a : Effect of Reynolds number on radial velocity profiles, $\theta = 90^o$ 102

Fig. 6-11b : Effect of Reynolds number on radial velocity profiles, $\theta = 60^o$ 102

Fig. 6-12a : Effect of Reynolds number on the interface shear stress 103

Fig. 6-12b : Effect of Reynolds number on the interface shear stress at a given viscosity ratio 103

Fig. 6-13 : Effect of viscosity ratio on the wall shear stress at a fixed Reynolds number 105

Fig. 6-14 : Surface vorticity distribution versus angle for different values of Reynolds number 106

Fig. 6-15 : Surface vorticity compared with boundary layer solution of [1] 108

Fig. 6-16 : Effect of Reynolds number on the coefficient of friction 110

Fig. 6-17 : Effect of viscosity ratio on the coefficient of friction 111

Fig. 6-18 : Effect of viscosity ratio on the meridional velocity inside the sphere 113

Fig. 6-19a: Effect of Reynolds number on the meridional velocity distribution inside the sphere, (Re = 200,300 and 500) 114

Fig. 6-19b: Effect of Reynolds number on the meridional velocity distribution inside the sphere, (Re = 1000,5000 and 10000) 114

Fig. 6-20 : Effect of kinematic viscosity ratio on the meridional velocity inside the sphere 116

Fig. 6-21 : Meridional velocity distribution inside the sphere at different angles 119

Fig. 6-22 : Meridional velocity distribution inside the sphere at different angles 120

Fig. 6-23 : Effect of viscosity ratio on the radial velocity inside the sphere 121

Fig. 6-24 : Effect of kinematic viscosity ratio on the radial velocity inside the sphere 123

Fig. 7-1 : Effect of Reynolds number on the temperature profiles for $\theta = 60^{o}$, case (1) 127

Fig. 7-2 : Effect of viscosity ratio on the temperature profile profiles for $\theta = 60^{o}$, case (1) 128

Fig. 7-3 : Temperature profiles at different angles, case (1) 130

Fig. 7-4 : Temperature and meridional velocity profiles at various values of Prandtl number, case (1) 131

Fig. 7-5 : Effect of Reynolds number on the local Nusselt number distribution, case (1) 133

Fig. 7-6 : Effect of viscosity ratio on the local Nusselt number distribution, case (1) 134

Fig. 7-7a : Transient temperature distribution at different radial distances for $\theta = 30^{\circ}$ and Re = 500, case (2-a) 136

Fig. 7-7b : Transient temperature distribution at different radial distances for $\theta = 45^{\circ}$ and Re = 500, case (2-a) 136

Fig. 7-7c : Transient temperature distribution at different radial distances for $\theta = 60^{\circ}$ and Re = 500, case (2-a) 137

Fig. 7-7d : Transient temperature distribution at different radial distancesfor $\theta = 75^{\circ}$ and Re = 500, case (2-a) 137

Fig. 7-7e : Transient temperature distribution at different radial distances for $\theta = 90^{\circ}$ and Re = 500, case (2-a) 138

Fig. 7-7f : Transient temperature distribution at different radial distances for $\theta = 105^{\circ}$ and Re = 500, case (2-a) 138

Fig. 7-8a : Transient temperature distribution at different radial distances for $\theta = 30^{\circ}$ and Re = 1000, case (2-a) 139

Fig. 7-8b : Transient temperature distribution at different radial distances for $\theta = 45^{\circ}$ and Re = 1000, case (2-a) 139

Fig. 7-8c : Transient temperature distribution at different radial distances for $\theta = 60^{\circ}$ and Re = 1000, case (2-a) 140

Fig. 7-8d : Transient temperature distribution at different radial distances for $\theta = 75^{\circ}$ and Re = 1000, case (2-a) 140

Fig. 7-8e : Transient temperature distribution at different radial distances for $\theta = 90^{\circ}$ and Re = 1000, case (2-a) 141

Fig. 7-8f : Transient temperature distribution at different radial distances for $\theta = 105^{\circ}$ and Re = 1000, case (2-a) 141

Fig. 7-9a : Transient temperature profiles at $\theta = 60^{\circ}$, Re = 500, case(2-a) 143

Fig. 7-9b : Transient temperature profiles at $\theta = 60^{\circ}$, Re = 1000, case(2-a) 143

Fig. 7-10 : Temperature distribution at different angles at t = 0.0005, case (2-a) 145

Fig. 7-11 : Effect of Reynolds number on the transient temperature profiles at a selected radial location (Z = 0.02), case (2-a) 146

Fig 7-12 : Effect of Reynolds number on the time required to reach uniform surface temperature, (case 2-a) 147

Fig. 7-13 : Effect of viscosity ratio on the temperature profiles, t = 0.0005, case (2-a) 149

Fig. 7-14 : Effect of viscosity ratio on the transient temperature distribution at Z = 0.02, case (2-a) 150

Fig. 7-15a: Transient surface temperature distribution around the sphere, Re = 500, case (2-a) 152

Fig. 7-15b: Transient surface temperature distribution around the sphere, Re = 1000, case (2-a) 152

Fig. 7-16 : Effect of Reynolds number on the transient surface temperature ditribution, case (2-a) 153

Fig. 7-17 : Effect of viscosity ratio on the transient surface temperature , case (2-a) 154

Fig. 7-18 : Effect of Prandtl number on the transient surface temperature distribution, case (2-a) 156

Fig. 7-19 : Rate of change of surface temperature versus time at different central angles, case (2-a) 158

Fig. 7-20 : Transient local Nusselt number profiles along the surface of the sphere, case (2-a) 159

Fig. 7-21 : Transient temperature profiles around the sphere, case (2-b) 161

Fig. 7-22 : Temperature distribution at different angles, t = 0.005, case (2-b) 162

Fig. 7-23 : Effect of Reynolds number on the transient temperature profiles at a fixed radial distance (Z = 0.02), case (2-b) 164

Fig. 7-24 : Effect of Reynolds number on the time required to reach uniform surface temperature, case (2-b) 165

Fig. 7-25a: Transient surface temperature profiles at different times for Re = 500, case (2-b) 166

Fig. 7-25b: Transient surface temperature profiles at different times for Re = 1000, case (2-b) 166

Fig. 7-26 : Effect of Reynolds number on the transient surface temperature profiles, case (2-b) 168

Fig. 7-27 : Effect of viscosity ratio on the transient surface temperature profiles, case (2-b) 169

Fig. 7-28 : Effect of Prandtl number on the transient surface temperature profiles, case (2-b) 170

Fig. 7-29 : Rate of change of surface temperature versus time at different central angles, case (2-b) 171

Fig. 7-30 : Transient profile of local Nusselt number along the surface of the sphere, case (2-b) 173

Fig. 7-31a: Transient temperature distribution at different radial distances for $\theta = 30^{\circ}$ and Re = 200, case (2-c) 175

Fig. 7-31b: Transient temperature distribution at different radial distances for $\theta = 45^{\circ}$ and Re = 200, case (2-c) 175

Fig. 7-31c: Transient temperature distribution at different radial distances for $\theta = 60^{\circ}$ and Re = 200, case (2-c) 176

Fig. 7-31d: Transient temperature distribution at different radial distances for $\theta = 75^{\circ}$ and Re = 200, case (2-c) 176

Fig. 7-31e: Transient temperature distribution at different radial distances for $\theta = 90^{\circ}$ and Re = 200, case (2-c) 177

Fig. 7-31f : Transient temperature distribution at different radial distancesfor

$\theta = 105^{o}$ and Re = 200, case (2-c) 177

Fig. 7-32a : Transient temperature distribution at different radial distances for

$\theta = 30^{o}$ and Re = 1000, case (2-c) 178

Fig. 7-32b : Transient temperature distribution at different radial distances for

$\theta = 45^{o}$ and Re = 1000, case (2-c) 178

Fig. 7-32c : Transient temperature distribution at different radial distances for

$\theta = 60^{o}$ and Re = 1000, case (2-c) 179

Fig. 7-32d : Transient temperature distribution at different radial distances for

$\theta = 75^{o}$ and Re = 1000, case (2-c) 179

Fig. 7-32e : Transient temperature distribution at different radial distances for

$\theta = 90^{o}$ and Re = 1000, case (2-c) 180

Fig. 7-32f : Transient temperature distribution at different radial distances for

$\theta = 105^{o}$ and Re = 1000, case (2-c) 180

Fig. 7-33a : Transient temperature distribution at different radial distances for

$\theta = 30^{o}$ and Re = 10000, case (2-c) 181

Fig. 7-33b : Transient temperature distribution at different radial distances for

$\theta = 45^{o}$ and Re = 10000, case (2-c) 181

Fig. 7-33c : Transient temperature distribution at different radial distances and

$\theta = 60^{o}$ and Re = 10000, case (2-c) 182

Fig. 7-33d : Transient temperature distribution at different radial distances for

$\theta = 75^{o}$ and Re = 10000, case (2-c) 182

Fig. 7-33e : Transient temperature distribution at different radial distances for $\theta = 90^{o}$ and Re = 10000, case (2-c) 183

Fig. 7-33f : Transient temperature distribution at different radial distances for $\theta = 105^{o}$ and Re = 10000, case (2-c) 18

Fig. 7-34 : Transient temperature profiles for $\theta = 60^{o}$, case (2-c) 183

Fig. 7-35 : Temperature distribution at different angles, (t = 0.005), case (2-c) 186

Fig. 7-36 : Effect of Reynolds number on the temperature distribution at a fixed radial distance (Z = 0.02) , case (2-c) 187

Fig. 7-37 : Effect of Reynolds number on the time required to reach uniform surface temperature , case (2-c) 189

Fig. 7-38 : Effect of Prandtl number on the transient temperature profile for $\theta = 60^{o}$ and t = 0.005, case (2-c) 190

Fig. 7-39 : Effect of viscosity ratio on the transient temperature profile for $\theta = 60^{o}$ and t = 0.005, case (2-c) 191

Fig. 7-40a: Temperature profiles around the sphere at different angles, Re = 500, t = 0.002, case (2-c) 193

Fig. 7-40b: Temperature profiles around the sphere at different angles, Re = 500, t = 0.01, case (2-c) 193

Fig. 7-41a: Temperature profiles around the sphere at different angles, Re = 1000, t = 0.001, case (2-c) 194

Fig. 7-41b: Temperature profiles around the sphere at different angles, Re = 1000, t = 0.005, case (2-c) 194

Fig. 7-42 : Temperature distribution at different angles at a fixed radial distance ($Z = 0.02$), case (2-c) 195

Fig. 7-43 : Transient temperature distribution at different radial distances, case (2-c) 196

Fig. 7-44a : Surface temperature profiles around the sphere at different times, Re = 500, case (2-c) 198

Fig. 7-44b : Surface temperature profiles around the sphere at different times, Re = 1000, case (2-c) 198

Fig. 7-45 : Surface temperature profiles at different central angles, case (2-c) 200

Fig. 7-46 : Effect of viscosity ratio on the surface temperature distribution, case (2-c) 201

Fig. 7-47 : Effect of Reynolds number on the surface temperature distribution, case (2-c) 202

Fig. 7-48 : Effect of Prandtl number on the surface temperature distribution, case (2-c) 203

Fig. 7-49 : Rate of change of surface temperature versus time at a different central angles, case (2-c) 205

Fig. 7-50 : Effect of Reynolds number on the local Nusselt number along the surface of the sphere, case (2-c) 206

Fig. 7-51 : Effect of viscosity ratio on the local Nusselt number profile, case (2-c) 208

Fig-7-52 : Nusselt number profiles at different times around the sphere, case (2-c) 209

Fig. 7-53 : Comparison of the local Nusselt number distribution of case (2-c) with the analysis of Renksizbulut and Yuen [48] 211

Fig. 7-54 : Comparison of the local Nusselt number distribution of case (2-c) with the analysis of Chiang et. al. [58] 212

Fig. 7-55 : Effect of Reynolds number on the time average Nusselt number 216

Fig. 7-56 : Effect of Reynolds number on the time required to reach uniform surface temperature for the three cases 217

Fig. 7-57 : Transient temperature profiles inside the liquid sphere 219

Fig. 7-58 : Effect of Reynolds number on the temperature distribution inside the liquid sphere, (t = 0.009) 221

Fig. 7-59 : Temperature profiles inside the liquid sphere at different angles, (t = 0.009) 222

Fig. 7-60 : Effect of viscosity ratio on the temperature distribution inside the sphere, (t = 0.009) 223

Fig. 7-61 : Transient temperature distribution both outside and inside the liquid sphere 225

DISSERTATION ABSTRACT

Name : Mohamed Abdelkarim Mohamed Antar

Title : ANALYSIS OF FLUID FLOW AND HEAT TRANSFER AROUND AND INSIDE A LIQUID SPHERE

Major Field : Mechanical Engineering

Date of Degree : January, 1996

The problem of fluid flow and transient heat transfer around and inside a liquid sphere is investigated using an implicit finite difference scheme .

The investigation is based on the boundary layer theory . The governing equations are uncoupled at the interface between the gas-phase and the liquid-phase by specifying the boundary conditions . Hence, two computer codes were developed to solve the flow-field as well as temperature profiles in both phases . Results obtained from the gas-phase solution such as the surface velocity and the transient surface temperature are used as input data to the second program to solve the flow-field and temperature distribution inside the sphere .

Results are presented for the velocity components and transient temperature profiles in the gas-phase boundary-layer outside the liquid sphere and in the liquid-phase up to the center of the sphere . Engineering parameters such as the wall shear stress, vorticity, drag coefficient, friction coefficient and Nusselt number are calculated and presented . Comparisons with results found in the literature are carried out to validate of the present analysis.

خلاصة الرسـالة

الأسـم : محمد عبد الكريم محمد عنتـر

عنـوان الرسـالة : تحليل سريان المائع و انتقال الحرارة حول و داخل كـرة من المائع

التخصـص : الهندسـة الميكانيكية

تاريخ الشـهادة : ينـاير ١٩٩٦م

فى هذه الأطروحة ، تمت دراسة سريان المائع وانتقال الحرارة المتغير مـع الزمـن حـول و داخـل كـرة من المائع باستخدام طريقة الفروق العددية .

تعتمد هذه الدراسة على نظرية الطبقة المتاخمة و تـم فصـل معـادلات سـريان المـائع عـن معـادلات انتقال الحرارة بتحديد قيم المتغيرات السرعة و درجة الحرارة عند سطح الكرة . و قـد تـم تصميـم برنـامجين يقوم أحدهما بتحليل سريان المائع وانتقال الحرارة حول الكرة والآخـر بذلـك التحليـل داخـل الكـرة . و قـد تـم استخدام نتائج البرنامج الأول مثل السرعة وتغـير درجـات الحـرارة حـول سـطح الكـرة مـع الزمـن كمعطيـات للبرنامج الآخر .

و قد تم عرض النتائج الخاصة بسرعات المـائع ودرجـات الحـرارة المتغيـرة مـع الزمـن فـى الطبقـة المتاخمة حول الكرة وكذلك داخل الكرة حتى نقطة المركز ، كذلك تم عرض بعض المتغيرات الهندسـية مثـل إجهاد القص ، معامل الدوران عند السطح ، معامل الجر و معامل الإحتكاك كدوال متغيرة مع زاوية الـدوران و رقم رينولدز . وتمت مقارنة بعض نتائج الدراسة مع نتائج مناظرة من أبحاث سابقة للتأكد من دقـة الـبرامج المستخدمة .

درجة الدكتوراه فى الفلسفة

جامعة الملك فهد للبترول والمعادن

الظهران – المملكة العربية السعودية

يناير ١٩٩٦م

NOMENCLATURE

a	sphere radius
A	vortex strength inside the droplet, $3U_\infty/(2a^2)$ for inviscid fluids, or $3\ C\ U_\infty/(2a^2)$ for viscous fluids
C	a factor less than unity which equals the ratio between the vortex strength inside the droplet for viscous and inviscid fluids
C_D	dimensionless drag coefficient , $D/\frac{1}{2}\pi\rho U_\infty{}^2a^2$
C_f	local coefficient of friction, $\frac{\tau_o}{\frac{1}{2}\rho U_\infty^2}$
C_P	specific heat at constant pressure
D	frictional drag, $\int_0^{\bar{x}_s} 2\pi r\tau' d\bar{x}$
K	thermal conductivity
K^*	interior-to-exterior thermal conductivity ratio
m	number of steps of the numerical mesh network in the x-direction
n	number of steps of the numerical mesh network in the z-direction
Nu	Nusselt number, $\frac{2ah}{K}=-2\frac{\partial T}{\partial Z}\Big\vert_o$
Pr	Prandtl number, ν/α
r	radial coordinate measured from the sphere's center
Re	Reynolds number, $2U_\infty a/\nu$

t' time

t dimensionless time, $t'\alpha/a^2$

t_s time required to reach a uniform surface temperature

t_x shear stress in meridional direction at the sphere's surface, $\mu\ \partial u / \partial z)_0$

T' temperature

T dimensionless temperature, $\frac{T' - T'_o}{T'_\infty - T'_o}$ for steady case

$$\frac{T' - T'_i}{T'_\infty - T'_i} \text{ for transient case}$$

T_x dimensionless shear stress in the meridional direction at the sphere's surface, $t_x(Re/2)^{0.5}/\rho U^2_\infty$

u^* meridional (x-direction) component of velocity

U dimensionless meridional component of velocity, u/U_∞

u_H velocity component in x-direction for potential flow inside the sphere's (Hill's spherical vortex), $-(\partial\psi_H/\partial r)/(r \sin\theta) = - A \sin\theta\ [a^2 - 2(1-z)^2]$

u velocity component in x-direction for the potential flow outside the external boundary layer, $-(\partial\psi/\partial r)/(r \sin\theta) = U_\infty \sin\theta\ [1 + a^3/(2r^3)]$

U_H dimensionless potential velocity component in the x-direction for the internal flow (Hill's spherical vortex), $u_H/U_\infty = -\frac{3}{2}C\sin\theta\ [1-2(1-Z)^2]$

U^* dimensionless potential velocity component in the x-direction for external flow, u^*/U_∞

U_∞ free stream velocity in the exterior flow

w radial (z-direction) velocity component

w_H radial (z-direction) velocity component for potential flow inside the internal boundary layer (Hill's spherical vortex), $(\partial\psi_H/\partial\theta)/(r^2 \sin\theta)$

w^* radial (z-direction) velocity component for potential flow outside the external boundary layer, $(\partial\psi/\partial\theta)/(r^2 \sin\theta) = -U_\infty \cos\theta\,[\,1 - a^3/r^3]$

W dimensionless radial velocity component, w/U_∞

W^* dimensionless radial velocity component for the external potential flow, w^*/U_∞

W_H dimensionless radial velocity component for the internal potential flow, w_H/U_∞

x meridional distance (along the circular generator of the sphere's surface) measured from the stagnation point

$\bar{x}$ the projection of the meridional coordinate x on the axis of symmetry (sphere diameter coincident with the stagnation line)

X dimensionless meridional distance along the surface measured from the stagnation point, $2x/\mathrm{Re}\,a$

z distance from the sphere's surface measured along the normal to the surface in the radial direction, being positive for the external flow and negative inside the sphere

Z dimensionless distance perpendicular to the surface in the radial direction, z/a

Greek symbols

δ boundary layer thickness

θ center angle measured from the frontal stagnation line .

μ dynamic fluid viscosity

μ^* interior-to-exterior (liquid-to-gas) dynamic viscosity ratio

ν kinematic fluid viscosity

ν^* interior-to-exterior (liquid-to-gas) kinematic viscosity ratio

α thermal diffusivity, $\dfrac{K}{\rho C_p}$

τ' meridional shear stress at the droplet's surface, $\mu \left.\dfrac{\partial U}{\partial Z}\right|_o$

τ dimensionless shear stress, $\dfrac{\tau' \sqrt{Re/2}}{(\rho U_\infty^2)}$

ζ' vorticity at the droplet's surface , $\zeta = \dfrac{u}{r} + \dfrac{\partial u}{\partial r} - \dfrac{1}{r}\dfrac{\partial w}{\partial \theta}$

ζ dimensionless vorticity , $\zeta'/(U_\infty/a)$

ρ fluid density

ρ^* interior-to-exterior (liquid-to-gas) density ratio

ϕ third spherical polar coordinate

ψ stream function of external potential flow far away from the droplet, given by

$$\psi = 0.5 u_\infty r^2 \sin^2\theta \left(1 - \frac{a^3}{r^3}\right)$$

ψ_H stream function of Hill's spherical vortex inside the droplet, given by

$$\psi_H = 0.5 A r^2 \sin^2\theta \, (a^2 - r^2)$$

Subscripts

H	Hill's spherical vortex flow inside the sphere
g	gas phase
i	initial (at time, t = 0)
ℓ	inside the liquid sphere (droplet)
o	on the sphere surface
s	at separation point for fluid flow and at time to reach the state of uniform surface temperature for heat transfer

CHAPTER I

INTRODUCTION

1.1 General

The process of evaporation and burning of a fuel droplet has gained enormous attention in recent years . Studies on this subject are of primary importance for predicting and improving fuel spray injection systems . Practical applications of such studies exist in gas turbines, rocket combustors, diesel engines, fire suppression, spray drying, etc., where the processes of gasification, oxidation, and dynamics of the fuel droplet are essential . Moreover, they might also be useful in the fields of air pollution, and cloud and precipitation physics .

In spray combustion computations, it is usually assumed that the overall spray behavior can be obtained by summing behavior of individual isolated droplets surrounded by a gas phase . Even when the assumption that droplets behave as if they were isolated from each other is not satisfactory to represent the real situation , the behavior of a single droplet in an oxidizing environment will provide a fundamental input to the overall spray analysis .

In the present study, laminar axisymmetric flow around a fluid sphere at moderate to high Reynolds numbers (Re) is numerically investigated by a finite difference technique . Flow field as well as heat transfer around and inside the sphere

are analyzed for a wide range of Re and Prandtl numbers (Pr) . The governing boundary layer equations for both gas and liquid phases are developed, non-dimensionalized and solved . These equations are coupled at the sphere surface where the shear stress exerted on the sphere surface by the external flow induces an internal circulation represented by Hills spherical vortex in the sphere's core . Conditions at the interface are obtained by equalizing both the tangential velocity and shear stress for both gas-phase and liquid-phase . Then, heat transfer to the cold sphere injected in a hot surrounding air is analyzed .

1.2 Scope of the Present Work

In the present work, a finite-difference method has been used to analyze the flow field and heat transfer around and inside a cold liquid sphere present in a hot surrounding flow . The method needs less computer time and storage in comparison with numerical methods discussed in the literature and it handles much wider range of Reynolds number as well as Prandtl number . The model is based on boundary layer theory and the following assumptions :

1. Laminar, axisymmetric, steady flow, and unsteady heat transfer .
2. Viscous dissipation, thermal radiation, buoyancy effects are neglected .
3. Both fluids are Newtonian .
4. Reynolds number is large enough to allow the use of boundary-layer theory .
5. Fluid sphere remains spherical in shape (small Weber number) .

6. The shear stress on the fluid-sphere surface induces internal motion inside the sphere

.

The flow field is classified into four main regions :

1. Outer flow represented by an inviscid flow over a sphere .
2. Gaseous boundary layer near the outer surface of the sphere .
3. Liquid phase boundary layer adjacent to the surface .
4. Potential flow inside the sphere core represented by the known Hill's spherical vortex.

This chapter included an introduction and the scope of the present study . Chapter II presents the literature survey . Chapter III will be devoted to the problem formulation, nondimensional form of the governing equations as well as the boundary-layer simplification . In Chapter IV, the grid system and finite-difference forms of the governing equations are presented . The overall solution methodology and the method employed for calculating the engineering parameters are discussed in Chapter V . The results are presented and discussed in Chapters VI for the hydrodynamic results and in Chapter VII for the heat transfer results . Finally the conclusions and recommendations are included in Chapter VIII followed by the references and the appendices . Appendix A presents the detailed derivation of the governing equations for the gas phase while the detailed derivation for liquid-phase equations is presented in Appendix B . Appendix C contains the flow charts and the program codes .

CHAPTER II

LITERATURE SURVEY

2.1 Introduction

The literature survey for the flow around spheres can be classified into three main categories . **First,** flow over a solid sphere which can be subdivided into forced flow around a sphere and induced flow due to the rotation of a solid sphere in a stagnant medium. **Second**, the motion of a gas bubble in a liquid . Then the **third** category represents the flow of a gas over a liquid sphere . This latter category can be subdivided into the case without heat or mass transfer and the case with heat and/or mass transfer . The present survey refers to the aforesaid three categories with a special attention to the third category .

2.2 Flow Over a Solid Sphere

2.2.1 Forced Flow

The laminar incompressible axisymmetric flow over a solid sphere with or without mass efflux was investigated by **Hamielec et al.** [1] for Reynolds numbers up to 500 . Finite-difference method was used and their results presented the drag coefficient (C_d), frontal stagnation pressure, and wake geometry . They found that nonuniform mass efflux

can significantly reduce the drag on a submerged surface , and that the most successful approximate solution can be obtained by boundary-layer assumptions .

Pruppacher [2] investigated numerically the steady incompressible flow around a sphere . He solved Navier-Stokes equations for $20 \leq Re \leq 40$ in terms of the standing eddy length behind the sphere and the separation angle . He found that the drag coefficient agrees well with experiments and that both eddy length and separation angle increase with increasing Reynolds number .

Transient axisymmetric flow was studied numerically by **Rimon and Cheng** [3] for the uniform incompressible, homogeneous fluid flow around a sphere . Complete Navier Stokes equations were solved for $1 \leq Re \leq 1000$ where a recirculatory wake appears . Time dependent stream function-vorticity equation in a finite difference representation on an expanding polar grid system by Dufort-Frankel approximation for time and space was applied . They presented the detailed vorticity distribution on the sphere and values of drag coefficient which agree with standard drag curve over the investigated range of Reynolds number . They recommended curvilinear co-ordinates with variable mesh size as being highly desirable to obtain quantitative results and that downstream outflow boundary condition is of great importance .

Experimental investigation of the forced laminar flow around a solid sphere was a point of interest to many investigators. **Achenbach** [4] found that laminar flow around a

sphere can still be obtained with Reynolds number values up to 1 x 10^5 . **Seeley et al.** [5] conducted a series of experiments for the flow over a fixed hollow pyrex sphere and obtained the normal and tangential velocities in the boundary layer using a non-disturbing flow visualization technique . Their results show that increasing Reynolds number resulted in decreasing the separation angle . **Esmail et al.** [6] measured radial and tangential velocities using electronic scanning devices for a Reynolds number range of 300 to 3000 . Comparing their results with numerical solutions they suggested that using maximum tangential velocity as an outer boundary condition for boundary-layer models is a definite improvement over the use of potential flow values . **El-Shaarawi et al.** [7] investigated the forced flow around a rotating solid sphere for a Reynolds number of 10000 and for values of the spinning parameter of 0,1 and 5 . **Karyagin et al.** [8] experimentally investigated steady flow over a solid sphere for Reynolds number ranging from $3x10^4$ to $3x10^7$ and Mach numbers from 0.3 to 3 and presented pressure distribution and separation angle . Their results show that increasing the free stream velocity leads to the displacement of separation angle upstream while increasing the Mach number displaces it downstream .

Axisymmetric laminar boundary-layer flow around a rotating solid sphere was investigated numerically by **El-Bedeawi** [9] and **El-Shaarawi et al.** [10] for a value of Reynolds number of 10000 and for various values of the spinning parameter . In their numerical solution, a non-iterative, low computer storage program utilizing finite-difference scheme was used to solve the governing boundary-layer equations and results

were presented for the velocity profiles, shear stress components and the angle of separation.

Forced convection mass transfer around solid and fluid spheres for Reynolds number up to 100 was investigated by **Baird and Hamielec** [11] . They studied this case where the diffusion equation was solved analytically for a thin concentration boundary layer and approximate local and overall Sherwood numbers had been predicted theoretically .

In 1987, **LePalec and Daguenet** [12] applied a power series of several variables to study the laminar mixed convection about an isothermal rotating sphere in a stream of arbitrary direction with respect to the axis of rotation, so that the velocity profile is essentially three-dimensional . Boundary layer equations were numerically solved and the results for different values of rotation parameter and buoyancy parameter were obtained and well agreement with previously published work were observed .

Mixed convection over rotating bodies with blowing and suction was investigated by **Wang and Kleinstreuer** [13] . **LePalec and Daguenet** [14] developed solutions for heat and mass transfer from a rotating sphere placed coaxially in an upward flowing stream. The theoretical results developed by boundary layer analysis were verified by experiments utilizing an electrochemical reaction at the surface of an electrically charged

sphere . The governing equations were , by means of series, transferred into ordinary differential equations that were solved by Runge Kutta-Gill method [15] .

2.2.2 Induced Flow

The induced flow due to a rotating solid sphere in a quiescent fluid was studied theoretically by **Dennis et al.** [16] . **Yefimova et al.** [17] investigated the same case using expansion coefficients as vector spherical functions and his results are valid for a Reynolds number up to a value of 10 . The low Reynolds number range was explored by **Iosilevskii** [18] who used an analytical solution for the creeping flow engendered by steady axisymmetric rotation of a sphere in an isotropic Newtonian fluid .

Raman [19] solved this case numerically by integrating the boundary-layer equations over a control volume and solving iteratively . **El-Shaarawi et al.** [20] used a simple, low computer storage, less computer time, non-iterative finite-difference scheme to solve boundary layer equations governing this case and their results detected no separation point .

2.3 Motion of a Gas Bubble in Liquid

The case of a gas bubble rising steadily in a quiescent liquid has been studied by **Moore** [21] for an irrotational flow past a bubble at a Reynolds number of 100 and he

obtained the drag coefficient $C_d = 32/Re$. However, he did not consider the tangential stresses in his calculations of the coefficient of drag . **Chao** [22] investigated the same case. He used boundary layer equations and calculated the drag for the case with negligible separation assuming complete internal circulation . He found that increasing Re has the effect of thinning the boundary layer. However, he reported that his solution is not applicable near the front stagnation point .

2.4 Flow Over a Liquid Sphere

2.4.1 The Case Without Heat or Mass Transfer

Hadamard [23] was the first to analyze fluid flow around fluid spheres , he extended Stokes calculation of the resistance opposing the motion of a solid sphere through a viscous medium of infinite extent to the case when the sphere is composed of fluid immiscible with the medium . He considered that tangential velocity component , normal and tangential shear stresses at both sides of the interface are equal and that motion can occur within the sphere due to the action of the forces of viscous origin across its surface .

The circulatory motion inside the droplet was first analyzed in 1894 by **Hills** [24] for the case of an inviscid fluid inside a sphere due to external irrotational flow and he gave an expression for the stream function .

In the experimental work done by **Spells** [25] , the technique used to reveal the circulation patterns depended on the striae which appear in glycerin and glycerin-water mixtures when sheared . Instantaneous flash photographs were taken of circulation patterns in drops of glycerin falling slowly (1 cm/sec) in caster oil where the drops were spherical and the circulation pattern agreed with the theoretical prediction of Hadamard [23]; and in drops of various glycerin-water mixtures falling at 10 cm/sec in heavy white oil (viscosity 0.37 poise at 15 C) where the drops were no longer spherical and the center of circulation was displaced below the equatorial plane .

Hamielec and Johnson [26] investigated fluid spheres moving in viscous media under the influence of gravity using a numerical method of solution . They reported that a good agreement with experiments up to Re = 90 was achieved . Circulatory motion inside the droplets was observed by suspending fine aluminum particles in the sphere interior. Drag coefficient lies on or above the experimental value for a solid sphere as long as Re<45 . Navier Stokes equations in stream function form for steady, viscous, axisymmetric flow in polar co-ordinates were solved taking continuity of tangential velocity and shear stress at the interface as boundary conditions (no droplet distortion) . However, they reported that the solution was not accurate at low Re . Also, they reported that separation starts to occur at Re = 39 . They found that lowering viscosity ratio decreases the asymmetry of the flow while as Reynolds number increases, the vortex ring (interior flow) moves toward the front stagnation point . When exterior flow separates, surface velocity changes direction and a second vortex is formed in the rear portion of the

sphere . The second (rear) vortex has never been observed because velocities in the neighborhood of rear stagnation point are relatively small since surface active materials tend to accumulate near point of separation preventing the transmission of the tangential stress to the interior fluid .

In 1967, **Hamielec et al.** [27] investigated viscous flow around circulating fluid spheres of low viscosity at intermediate Reynolds numbers . Steady Navier-Stokes equations in stream function and vorticity form were solved for Re = 0.1, 1, 50, 100, and 200 by a finite difference method . Computed values of C_d compared favorably with experiments and no separation was found for $Re \leq 200$. The accuracy of boundary layer theory was confirmed .

Rivikind and Ryskin [28] studied uniform and rectilinear motion of a drop under the action of a uniform steady mass-force field in viscous liquid at rest at infinity . They investigated the Reynolds number range of $1 \leq Re \leq 200$ where integration of full Navier-Stokes equations was applied for Re = 200 and for arbitrary values of viscosity ratio . Both fluids are incompressible with constant properties, droplet also remains spherical (very small Weber number) . They concluded that if the viscosity of the dispersed phase does not exceed that of the continuous phase, the flow around the sphere does not separate and there is no return flow region behind the drop (results were confirmed by experiments). At Re = 100, there is separation in the immediate vicinity of the rear critical point and a return flow appears . However, increasing Re expands this region and the

return flow region. This return flow is induced if a fair amount of vorticity accumulates behind the droplet as a result of convective large Re . They also reported that the internal flow resembles Hill's vortex . For high viscosity, the picture is close to the flow around a solid sphere (small internal flow velocity) . For high Re (both outside and inside sphere), circulatory flow inside the drop breaks up into two vortices . C_d was found to be decreasing with increasing Re up to 100 (its value for a gas bubble was greater than that for a liquid drop and the lowest value was for a solid sphere) . They indicated that when the liquid phase density is much larger than gas phase density, the assumption of a single vortex is reasonable .

In 1985, **Oliver and Chung** [29] studied flow over a fluid sphere by hybrid series truncation and finite-difference technique for steady , axisymmetric, laminar flow. They found that density ratio has no effect on C_d at low Re, while shear stress and C_d increase with increasing viscosity ratio and decrease with increasing Re . For intermediate Re, flow pattern is insensitive to interior Reynolds number . They reported that internal circulation strength increases with Re . Then, in 1987 **Oliver and Chung** [30] studied the case of steady motion of a fluid sphere translating in a quiescent medium using semi-analytical series truncation method in conjunction with a cubic finite element scheme . The range for Reynolds number is 0.5 to 50 and for viscosity ratio is from 0 (representing a gas bubble) to 1×10^7 (representing the flow around a solid sphere) .

In a study by **Mechailidis** [31], he gave analytical solutions to the particle equation of motion for several expressions of the drag coefficient and he pointed out the differences between them .

Harper and Moore [32] studied the steady motion of a liquid drop in another fluid of comparable density and viscosity with the assumption that the drop remains spherical and that Reynolds number is sufficiently high to apply boundary layer analysis . Internal circulations (represented by Hill's vortex) are obtained and they reported that the obtained C_d values agreed quite well with experiments .

Slow flow of rarefied gas about a spherical liquid drop was studied by **Tomoeda** [33] . He neglected inertial effect but internal circulation was included and kinetic theory analysis was considered for the external flow field . It was found that the significant internal circulation would occur when the viscosity of the external gas and that of the internal liquid are comparable to each other in magnitude . This results in a reduction of the sphere drag from the conventional Stokes drag .

2.4.2 The Case of Heat and Mass Transfer to a Single Liquid Droplet

The existing literature on a single droplet vaporization can still be classified into two major categories, spherically symmetric model and axisymmetric model where the former was first introduced in 1954 by **Godsave** [34] and **Spalding** [35] for the

vaporization and combustion of a fuel droplet in stagnant surroundings leading to the known d^2 -law . The axisymmetric model accounts for convection terms in the flow field as well .

2.4.2.1 Spherically Symmetric Models

In the spherically symmetric models, the surrounding air is assumed to be stagnant simplifying the governing energy equation to be one-dimensional . In the models of **Godsave** [34] and that of **Spalding** [35], the temperature was assumed to be spatially uniform and temporally constant and that gas phase heat and mass transfer rates were much faster than droplet regression rate ignoring initial transient heating of the droplet where regression rate increases till it reaches a quasi-steady value . Models also neglected liquid phase heat and mass transfer, considered the droplet to be motionless with constant properties for both the pure liquid and gas phases as well as assuming Lewis number to equal unity . Another inadequacy of the model was that the temperature predicted was too high to neglect dissociation .

Kotake and Okazaki [36] solved numerically the unsteady gas and liquid heat and mass transfer conservation equations. They showed significant unsteadiness through entire droplet life time with temporary decreasing surface regression rate . Quasi-steadiness can never be reached , so, d^2-law is largely unrealistic . Their accuracy was suspected by **Hubbard et al.** [37] who repeated this work and obtained different results indicating that regression rate is monotonically increasing with time and gas phase is quasisteady .

Moreover, **Hubbard et al.** [37] investigated the problem by numerical integration for the governing equations with variable properties assuming stagnant gas surrounding the droplet (spherically symmetric model), quasi-steady evaporation process and that a reference property scheme for temperature is $T_r = T_s + (T_e - T_s)/3$ and a similar one for mass transfer (referred to as 1/3 rule where T_r is the reference temperature, T_e is the external flow temperature and T_s is the surface temperature of the droplet) . Effects of temporal storage of mass species, energy and radial pressure variations in gas phase were negligible and the early transient behavior is solely due to sensible heating within the droplet . Proportionality constant in R^2 expression (where R is the droplet radius) was decreasing with time rather than constant which is considered as a modification of the d^2-law and flame temperature predicted was much lower than measured values . They proved that transient evaporation into stagnant gas is independent of initial size for a quasi-steady evaporative process, that the effect of blowing in reducing the normalized temperature and species gradient in the vapor at droplet surface is enhanced, and that the 1/3 rule is the most appropriate for calculating reference temperature and species mass fraction .

Justification for the 1/3 rule is originated from the film theory by **Faeth** [38] who assumed that the resistance to heat and mass exchange between surface and gas flow is concentrated within some frictional gas film of constant thickness . The temperature and species composition along the surface as well as the external boundary of the film , are uniform. The thickness of the film is determined from the requirement that the rates of a purely molecular transport by thermal conduction or diffusion through the film must equal

the actual intensity of convective heat and mass transfer between surface and external flow.

Yuen and Chen [39] obtained the drag data of evaporating droplets of water, methanol, heptane and benzene . This data covered Reynolds number range from 1 to 2000 and mass transfer numbers B_m from 0 to 3 ($B_m = C_m(T_s-T_d)/L$, where C_m is the specific heat of surroundings calculated at the arithmetic mean of droplet vapor at droplet temperature T_d and air at free stream temperature T_s, and L is the latent heat of vaporization of droplet at T_d) . This study showed that the drag coefficient correlates well with the standard drag curve provided that the characteristic density is the free stream density and the characteristic viscosity coefficient is a function of temperature . The presented correlation was insensitive to mass transfer numbers leading to the result that mass efflux has little effect on drag of evaporating droplets .

Kadota and Hiroyasu [40] conducted theoretical studies on ignition delay of a single droplet in high pressure gaseous environments. Calculations were made for the unsteady case of droplet evaporation considering the effect of natural convection . The effects of non-ideal mixtures, fuel vapor concentration at the surface and the non-ideality of the enthalpy of evaporation were considered where all of these effects were important . Non-linear simultaneous ordinary differential equations were utilized for n-heptane droplet in nitrogen using Runge-Kutta-Gill method . Their results presented the size and temperature history of a droplet and its lifetime .

A spherically symmetric model in stagnant surroundings with constant properties and unity Lewis number was used by **Law** [41] who reported that droplet heating is the source of unsteady combustion . He assumed quasi-steady gas phase processes and that droplet temperature is spatially uniform but temporally varying considering conduction and internal circulation . Ignoring internal circulation leads to gross underestimation of heat transfer rate within the droplet . Vigorous internal circulation was observed in the experiments . It was reported that if droplet heating is a significant source of the observed unsteady combustion, then the rapid approach of the rate of change of droplet surface area to a constant value implies that internal heat transfer mode is much faster then can be provided by conduction alone . However, **Law and Sirignano** [42] used the same assumptions to consider quasi steady gas phase, spherically symmetric, thin flame combustion of a pure component, where conduction is the only heat transfer mechanism within the droplet and it was found that droplet heating was dominant for the initial 10-20% of droplet lifetime (rapid changes in combustion characteristics occur) then droplet surface decreased almost linearly .

The importance of liquid phase heating was pointed out by **Law** [41] who stated that droplet heating should be included in any attempt to analyze the flame behavior for unsteady droplet burning with an initially cold droplet .

Law and Law [43] accounted for the temperature dependency of specific heat at constant pressure (C_p), thermal conductivity (K), the binary diffusion coefficient (D) and

concentration dependency of C_p and K and recommended a simplified model to obtain estimates of the various vaporization characteristics .

2.4.2.2 Axially Symmetric Models

Axially Symmetric models take into account the convective term in the energy equation . Therefore, continuity and momentum equations are to be considered in describing the flow field around the droplet . This leads to a two-dimensional representation of the governing equations which is more representative of the real case than the spherically symmetric model that simply ignores the flow around and inside the liquid sphere .

2.4.2.2.a. Non-Boundary Layer Models

Sayegh and Gauvin [44] carried out a theoretical study to investigate the effects of large temperature differences on the rate of pure heat transfer from a very hot gas to stationary spheres . They solved numerically the simultaneous momentum and energy equations for variable property flow past a sphere, using finite difference techniques . Results were obtained for Reynolds numbers up to 50 . The flow behavior, C_d, and Nusselt number were presented . Effect of variable properties was to drastically increase flow vorticity and temperature and vorticity gradients at the surface . A generalized heat transfer correlation was derived that included large variations in physical properties of the fluid as a result of temperature difference .

The analysis carried out by **Law** [45] in 1982 concluded that conductive and convective heat transfer within the droplet are efficient to maintain temperature spatially uniform but temporally varying and that liquid phase heat conduction rate is of the order of droplet surface regression rate, thus, spatially uniform temperature can not be achieved without internal circulation . He reported that the difficulties in the experimental work include the influence of gravity, that has an undesirable varying buoyancy effect as droplet size diminishes, and the forced convective effects due to droplet motion .

In the study carried out by **Dwyers et al.** [46] for an evaporating droplet, they found that C_d decreases significantly as droplet vaporizes and gas/droplet relative velocity decreases . In his review paper, **Sirignano** [47] in 1983 reported that because transient heating of droplet surface continues throughout the droplet lifetime without the surface reaching the boiling point temperature, quasi-steady assumption has no justification .

Renksizbulut and Yuen [48, 49] considered quasi steady evaporation, but liquid motion and heating were ignored, variable thermophysical properties were considered resulting in correlations for droplet drag coefficient and Nusselt number which are less than that for the case of solid sphere due to the blowing effect of evaporation . All thermophysical properties were evaluated at arithmetic mean (film condition) except the density in Reynolds number which was evaluated at free stream values .

Aggarwal et al. [50] , **Aggarwal** [51], and **Aggarwal and Sirignano** [52] examined different liquid phase heat transfer models (Infinite conductivity, Conduction limit, Vortex model) for a stagnant or slightly convective environment on ignition characteristics of a pure fuel droplet . They reported that ignition delay times predicted by different models are significantly different over a wide range of pressure, droplet size, and fuel volatility . In the regions where droplets are formed, slow vaporization without any active chemical reactions is expected to prevail initially . As the droplets move into the hotter regions, vaporization becomes significant, and eventually a flame may get established around (or in the wake of) an individual or a group of droplets . In regions where an envelope flame gets established , the burning process is diffusional .

Patnaik et al. [53] analyzed the dynamics of an evaporating droplet including the effect of transient convection, Stefan flow (surface blowing due to vaporization) , internal circulation, and liquid heating for the incompressible liquid phase . Continuity and momentum equations were expressed in streamline and vorticity representation . Numerical solution was carried on iteratively by ADI method and special cells composed partly of liquid and gas were used to represent the conditions at the interface . Clausius-Clapeyron equation was used for mass fraction at the interface while the equation of state was used for calculating the density .

In 1988, **Renksizbulut and Haywood** [54] analyzed an n-heptane droplet evaporating in its vapor at a temperature of 800 K and at two values of the pressure (1 and

10 bar) . Transient droplet evaporation, variable properties, internal circulation, Reynolds number range between 100 and 250, a finite volume numerical scheme for laminar, axisymmetric flow condition and using effective thermal conductivity expression for liquid phase heating were used . They found that liquid phase heating plays an important role in overall droplet behavior . They reported that quasisteady gas phase can be made since gas phase heat and momentum diffusion rates at atmospheric pressure are 2 to 3 order of magnitude larger than droplet surface regression rate and that transient effect of liquid heating can still be handled in a quasisteady manner using effective latent heat . They noticed that at higher pressures, droplet lifetime is much shorter since density increases about 10 times . Also at high pressures, increasing gas density and reduced viscosity (due to high temperature) both intensify liquid phase motion . The secondary recirculating zone dies out very quickly and has negligible effect on heat transfer, Nusselt number decreases with time while C_d increases and heating time increases at high pressure . They introduced a simplified semi-analytical model which proved to be valid for low pressure cases . But **Abramzon and Sirignano** [55, 56] reported that it is unclear whether their results are applicable to the practical case of a non-vapor environment where diffusion may be one of the controlling factor in vaporization process . They calculated the transient droplet temperature using both the rapid mixing model (infinite conductivity model) and the Conduction limit model (both represented the two extremes bounding the possible range of real conditions) . The standard assumption that (Prandtl number = Lewis number = Schmidt number = 1) which is widely used is invalid for heavy fuels such as n-decane (Le = 1-4) and incorrect evaluation of physical properties leads to considerable

errors in the prediction of vaporization rate . Thermophysical properties were evaluated at a reference temperature using 1/3 rule and an implicit iterative method of second order accuracy with time was used . Internal droplet temperature for the conduction limit model was calculated using Crank-Nicolson scheme with uniform finite difference grid .

In 1989, **Haywood et al.** [57] developed a model to analyze evaporation of an n-heptane droplet in air at atmospheric pressure considering variable thermophysical properties, liquid phase motion and heating, and transient variation in droplet size and velocity . Quasi-steady correlations were shown to predict the transient histories of C_d, Nu and Sherwood number (Sh) . They reported that the nature liquid phase heating (Nu) remained constant through droplet lifetime and they observed that C_d increases in the course of droplet motion and vaporization and that the standard drag curve for a solid sphere may be used here provided that thermophysical properties in gas film are evaluated at an average temperature and the appropriate correction is made to account for the blowing effect.

Numerical work of **Renksizbulut and Haywood** [54] showed that instantaneous C_d, Nu for n-heptane droplet in their own vapor at 1 and 10 atm could be predicted using the correlation of Renksizbulut and Yuen (1983) with a suitable correction for the effects of liquid phase heating. Complete droplet life histories could be predicted by a simple analytical model using correlations in a quasi-steady manner together with effective thermal conductivity model for liquid heating and proved to be good for low ambient

pressures . They proved that unsteady gas phase effects resulting from perturbations to velocity and temperature fields due to higher surface regression rates at higher pressure were responsible for the departure from quasi-steady behavior . Physical reality does not approve rapid mixing (infinite conductivity) nor conduction limit models for droplet heating . **Renksizbulut and Haywood** showed that rapid mixing occurring initially followed be gradual heating and that transient drag coefficient, Nusselt and Sherwood numbers computed by a complete numerical method could be predicted by the quasi steady correlations previously obtained . Therefore, gas phase transient effects , recession of gas-liquid interface, and second order drag effects are unimportant at pressures < 10 atm. The justification for liquid unsteady behavior comes from the decrease in Re that results in a slow transient decline in liquid phase motion despite it adjusts quickly with shear stress . Also, liquid phase heating was shown to be unsteady and transient heating persists most of the droplet lifetime . They explained that vaporization acts to reduce drag by thickening boundary layer and reducing shear at the surface, and reducing mixture viscosity in gas phase boundary layer by increasing concentration of cold fuel vapor drag correlation .

Chiang et al [58] reported that although net effects of variable properties and surface blowing decrease drag, the increase in pressure drag is remarkable and wondered whether that correlation developed by Renksizbulut and Haywood is applicable for high transfer numbers with noticeable mass transfer at the interface . In 1992, they investigated the case of a cold droplet injected in a hot gas stream taking into consideration the variable thermophysical properties (since they reported that constant property calculations

overestimate the drag coefficient), transient heating, liquid internal circulation, flow deceleration due to drag of the droplet, boundary layer blowing, moving interface. The parameters changed in their model were initial droplet temperature, ambient temperature, initial Reynolds number, fuel type, and droplet heating model . The purpose of their investigation was to solve numerically the equations governing the exchange of momentum, mass and energy between a vaporizing droplet and the convective gas stream with high transfer numbers, to analyze local as well as overall behavior of the droplet, to study the important effects due to variable properties and to Reynolds number, transfer numbers, and finally to find appropriate correlations for the transfer coefficients.

They considered laminar axisymmetric flow, initially uniform ambient conditions, a thin boundary layer near the interface, recirculating zone after separation point, that shear stress at interface causes internal circulation (represented by Hill's spherical vortex), that drag retards the droplet (although small thrust drag due to nonsymmetrical blowing accelerates it) decreasing Reynolds number and surface shear . They also considered that liquid temperature is initially uniform, part of heat transferred from the gas goes to droplet evaporation while the rest is for heating the droplet interior , mass transfer is characterized by flow convection and rate of vaporization (fuel vapor diffuses away to gas stream). Molecular weight of mixture surrounding the droplet is altered due to the presence of fuel vapor . Density, as well as pressure distributions are totally different from the case of liquid sphere without vaporization . They found that for higher transfer numbers, there are larger vaporization rate, reduced drag coefficient and for lower transfer rate, weak

effect of boundary layer blowing, C_d is dominated by Reynolds number . Vaporization results in decreased droplet radius and an expansion of wake region

Lately in 1993, **Chiang and Kleinstreueur** [59] investigated the case of laminar axisymmetric thermal flow of a spherical vaporizing droplet neglecting thermal radiation, buoyancy, thermo-diffusion effects . Reference fluid properties are evaluated at free stream conditions while gas phase properties are evaluates at a reference state (arithmetic mean point). All gradients at stagnation line are set equal to zero because of symmetry . The solution of governing equations was by using cylindrical coordinates for gas phase and spherical coordinates in liquid phase and finite-element technique . Droplet investigated was an n-hexane or n-octane droplet of initial Reynolds number = 100, droplet temperature = 399 K, ambient temperature = 800 K and pressure = 10 atm .

In the numerical study of **Chen et al** [60], the problem was simplified by neglecting internal liquid circulation and transient heating . They showed that heat and mass transfer rates are enhanced by the narrow thermal boundary layer in the leading region and wake flow which is excited at high Reynolds numbers . They also showed that the steepest temperature gradient occur at the front center point . They reported that their results are in good agreement with empirical results with the following assumptions; quasi-steady, incompressible flow, constant properties, Lewis number equals unity, constant droplet temperature, no heat transfer to heat the droplet, no chemical reactions, and that

droplet internal circulation is ignored (zero tangential velocity at the droplet surface) . However, these assumptions seem to be oversimplifying the real situation .

Megaridis [61] used the data produced in an experimental investigation for vaporization rates and internal temperature distribution of large, hydrocarbon, suspended droplets vaporizing at atmospheric pressure, and which involves Reynolds number up to 100 to validate the methods employed in a detailed numerical model that simulated liquid-fuel droplet vaporization in a high-temperature , laminar, convective environment . A series of comparisons was performed between model predictions and experimentally measured relevant quantities . He reported that the agreement in the droplet interior was favorable . The model predicted higher vaporization rates, as indicated by lower values of droplet diameter at corresponding instances in droplet lifetime . The predicted temperature distribution in the interior were in good agreement with measured values . Both experiments and modeling agree on the establishment of internal circulation in liquid droplet exposed to laminar high temperature gaseous flows and relative insensitivity of the droplet temperature distribution when a considerable increase of free stream momentum occur . Although the model predictions showed that substantially increased liquid viscosity slows down the establishment of the liquid phase motion, the experimental observations conclude that substantially higher liquid viscosity eliminates liquid phase motion entirely .

Also in 1993, **Takie et al** [62] examined experimentally the ignition time of suspended fuel drop with high ambient temperature . A stationary fuel droplet suspended by a fine silica fiber was taken into a furnace moving on rail and is quickly exposed to high ambient temperature . The effect of fuel mixture ratio , initial diameter and ambient temperature were observed . An interesting result was drawn from this experimental work that is; for pure hexadecane, ignition time increases with increasing initial diameter, but decreases for pure heptane especially at lower temperatures . For mixtures, results show that an initial droplet diameter exists at which ignition time has a maximum value and that this diameter increases with a decrease of heptane concentration or ambient temp.

2.4.2.2.b. Boundary Layer Models

In the analysis of **Prakash and Sirignano** [63], axisymmetric quasi steady liquid motion with a spherical core vortex surrounded by a viscous boundary layer and internal wake was assumed with the vortex strength being a function of shear stress along droplet surface . Moreover, they assumed droplet heating to be unsteady during its lifetime . Internal circulation was shown to one-dimensionalize heat conduction in the liquid core . Quasi-steady thermal boundary layer near the surface was analyzed and droplet temperature field was determined thus providing a gas liquid interface constraint . The results of their work showed that droplet fuel vapor concentration at the interface depends exponentially on the surface temperature .

Prakash and Sirignano [64] conducted a gas-phase , viscous, thermal and species boundary-layer analysis by an integral approach . They modified their previous analysis of the liquid droplet to account for changing droplet size due to vaporization and hence the droplet vaporization was found to be unsteady . However, the temperature distribution within the droplet is nonuniform for a significant part of droplet lifetime . The range of Reynolds number investigated was about 100 where it is assumed that shear stress at liquid-gas interface is large enough to induce internal liquid circulation thus modifying the vaporization rate . Although the coupling between gas phase and liquid phase equations occurred at interface, liquid phase problem was uncoupled from gas phase problem by specifying the interface conditions . Unsteady gas phase flow is expected, however, since the characteristic time for changes is much less than the droplet lifetime, quasi-steady gas-phase assumption can be employed even at high pressure .

It should be pointed out here that an error is expected due to applying boundary layer equations for values of Reynolds number as low as 100 . However, **Prakash and Sirignano** reported that this error in boundary layer thickness is of the order of square root of Reynolds number . Moreover, for the case of flow over a liquid droplet, liquid motion will shift the point of zero shear stress toward the rear stagnation point reducing both the size of the wake and its contribution . Although the conditions in their combustor are turbulent; however, having droplet size much less than larger eddy size, a locally laminar boundary layer exists over spherical droplet surface . In their analysis, they considered Prandtl and Lewis numbers equal to unity . They used a fourth order polynomial for the

integral equations used for predicting the vaporization rate since boundary layer details are assumed to be of minor importance . Droplet core heating was assumed to be unsteady and normal to closed streamlines

Tong and Sirignano [65] examined the case of a non vaporizing droplet with Hill's vortex in the droplet core, viscous and thermal boundary-layers near droplet surface, inviscid wake near axis of symmetry . They assumed that the droplet core heating is unsteady, normal to streamlines because of a very short residence and circulating time along the streamline compared to droplet life time .

A discussion on the validity of the quasi-steady model can also be found in the work of **Tong and Sirignano** [66, 67] . They reported that unless the thermal boundary layer is very thin, thermal inertia term is important and hence quasi-steady assumption is invalid . Elimination of thermal boundary layer and assuming that the core is valid up to the droplet surface may give accepted accuracy . Boundary layer in the liquid is a region of adjustment between one-dimensional core behavior and two-dimensional gas phase behavior . They added that although Peclet number (defined as the product of Reynolds number and Prandtl number) is high , energy equation for the thermal layer does not take the limiting form with primary balance of a convective term with diffusion term and that time derivative term is an important as other terms . Finally, neglecting convective term is not a bad approximation and it allows for reducing the problem from two to one dimensional . They also analyzed the problem of convective diffusion in a liquid droplet

with internal circulation considering both vaporizing and non vaporizing droplets . An approach which simplifies the governing equations was taken and series solutions for both temperature and temperature gradient boundary condition cases were obtained .

Fernandez-Pello [68] in 1982 carried out a theoretical study for combustion of a spherical fuel particle in a forced convective oxidizing gas flow . He used boundary layer equations and flame sheet approximation to describe the reacting flow . The boundary layer equations were solved by expanding the velocity , temperature, and species distributions into a series of the azimuthal angle . Profiles for variables at several angular positions along particle surface and local mass burning rates were presented and an explicit expression for particle regression rate was developed in terms of Reynolds number and mass transfer numbers.

Again in 1982 **Fernandez-Pello and Law** [69] extended the previous model to account for highly buoyant combustion on a condensed spherical particle where self similar solutions with the same Grashof scaling law (solutions are scaled by 1/4 power of Grashof number) were obtained for the bottom stagnation and the lateral regions . These solutions were used to generate the leading two terms of a series expansion solution for the flow . They provided an explicit expression of the mass burning rate along droplet periphery up to separation point . They reported that burning rates were found to be larger than those predicted by spherical symmetry models . The upper spherical segment of the particle where wake flame combustion occurs was only treated qualitatively by

comparison with pool burning liquids . The streamlines in boundary layer and induced inviscid flow are obtained and superimposed to provide an overall description of the gas flow field . In the same year **Wu et al.** [70] established an extinction criterion for buoyancy generated stagnation point boundary layer flow of a burning particle using large activation energy asymptotics .

Then **Fernandez-Pello** [71] in 1983 developed an analysis for the mixed convective combustion of a spherical fuel particle . A mixed convection parameter was introduced in the non-dimensionalization of the governing boundary layer equation which provides solutions as a function of Froude number and it is valid from one convective limit to the other . Explicit expressions for local mass burning rate and overall regression rate were obtained . He reported that the predicted dependencies on Reynolds number, Grashof number, and mass transfer numbers agreed qualitatively with existing experimental data .

Rangel and Fernandez-Pello [72] studied the single component fuel droplet evaporation and combustion (when transient heating was completed) leading to steady state case of simpler solution . The flow field was classified into four main regions, first is the inviscid flow surrounding the droplet that can be treated as a potential flow around a sphere, followed by a gaseous boundary layer (second region) , the third region is a liquid phase boundary layer in the liquid side of the droplet interface followed by a fourth region of an inviscid spherical vortex . So, liquid and gaseous boundary layers near droplet surface were bounded by a liquid and gaseous inviscid flow . Analysis was applied to

most of droplet lifetime . Their analysis is applicable for low boiling point fuel and low ambient pressure . Liquid heating flux was neglected because of its low value compared to the heat required for evaporation . The boundary layer equations (Reynolds number was assumed to be high enough for boundary layer analysis to be applied) for both gas and liquid phases were expressed in terms of power series that transformed them to ordinary differential equations . The parameters investigated were mixed convection parameter, ratio of (viscosity × density) in gas and liquid phases (representing internal circulation) . They assumed that in the boundary layer lies a diffusion flame that establishes a uniform and approximately constant elevated droplet temperature obtained by balancing the heat transfer from the flame and the endothermic evaporation of the droplet where the fuel vapor is transported by convection and diffusion . Heat generated by chemical reaction is transferred both outward to the ambient and inward to droplet . The real addition to their previous effort was to consider the internal circulation of the droplet induced by the shear stress exerted by the outer flow on the droplet surface and which can be represented by Hill's vortex . However, the strength of this vortex is predicted to be less than that for inviscid case as a result of the boundary layer in the liquid phase, so it is represented by a fraction that is obtained from the solution by " equating the vorticities of the liquid boundary-layer as the radial coordinate in the liquid region (Z_l) goes to infinity and of the Hill's vortex at sphere surface (r = a)" . The assumptions used include that boundary layer thicknesses in both phases are small compared to droplet radius, high surface tension to keep droplet in spherical shape, and axisymmetric flow . The analysis is not applicable upon separation because of applying boundary layer equations . However, they reported

that this does not affect Hill's vortex and the chemical reaction is represented be a quasi-steady one-step chemical reaction neglecting radiation .

Further details of early models can be found in the review papers of **Williams** [72] in 1973, **Faeth** [38] in 1977, **Law** [64] in 1982, and **Sirignano** [47] in 1983 . Despite many years of research, further understanding of isolated droplet flow characteristics, heat transfer and evaporation in the intermediate Reynolds number regime is still required . In particular, the literature demonstrates a lack of consensus as to the transport processes that may be considered quasi-steady and still are there conflicts whether to consider the gas-phase as a quasi-steady process or a transient one . Also, the exact nature of liquid phase momentum and heat transfer processes for a realistic droplet are not well characterized . Moreover, there is a partially conflicting conclusions in the results regarding $C_d = C_d(Re)$ between the results of **Dwyers et al.** and those of **Haywood and Renksizbulut** [74] . Therefore, this seems to be a point that requires further effort to examine the factors upon which the coefficient of drag is dependent .

A careful review of the literature reveals the need of detailed information of the flow field and heat transfer around and inside a liquid sphere at moderately high values of Reynolds number and at a wide range of interior-to-exterior viscosity ratio on the flow characteristics and transient heat transferred to the sphere . The present study is aimed at covering this gap by introducing the effect of the former parameters on the flow field as well as the heat transfer profiles both around and inside the sphere .

CHAPTER III

GOVERNING EQUATIONS

3.1 Introduction

In this chapter, the governing equations that describe both fluid flow and transient heat transfer development around and inside the liquid sphere are presented . The detailed derivation of these equations starting from the Navier-Stokes equations as well as the Energy equation for spherical polar coordinates , transformation of the governing equations to the orthogonal curvilinear coordinates, nondimensionalizing, and order of magnitude analysis that is carried on to simplify the equations are presented in Appendix A for the gas phase governing equations and in Appendix B for the liquid phase governing equations .

The major assumptions employed in the derivation of the governing equations in both gas and liquid phases are :

1. Steady incompressible flow around and inside the liquid sphere .
2. Fluid is Newtonian with constant properties .
3. The liquid sphere is initially cold and suddenly introduced to a hot gas stream .
4. Body forces are negligible .
5. Flow is axisymmteric .

6. Non-evaporating liquid sphere and no chemical reactions .
7. No viscous dissipation .
8. Surface active impurities and turbulence are absent .
9. Reynolds number is large enough to apply boundary-layer theory but not to induce turbulence .
10. Small Weber number so that the sphere remains spherical in shape .
11. The flow outside the external boundary layer is the potential flow around a sphere .
12. The flow outside the internal boundary layer can be represented by the classical Hill's vortex, although its strength is smaller than that for the case of potential flow and it is to be determined from the solution .

A schematic of the flow patterns outside and inside the sphere is shown in Figure 3-1 where the sphere is experiencing an internal motion engendered by the external flow.

3.2 Gas Phase Governing Equations

In this work, the orthogonal curvilinear coordinates shown in Figure 3-2 are used where the x-axis is measured along the surface of the sphere starting from the front stagnation point and extends in the meridional direction till the rear stagnation point . The z-axis passes through the origin of the sphere where its zero value is at the sphere surface . The reader can refer to Appendix A for the detailed transformation of the gas phase governing equations to its orthogonal curvilinear coordinates .

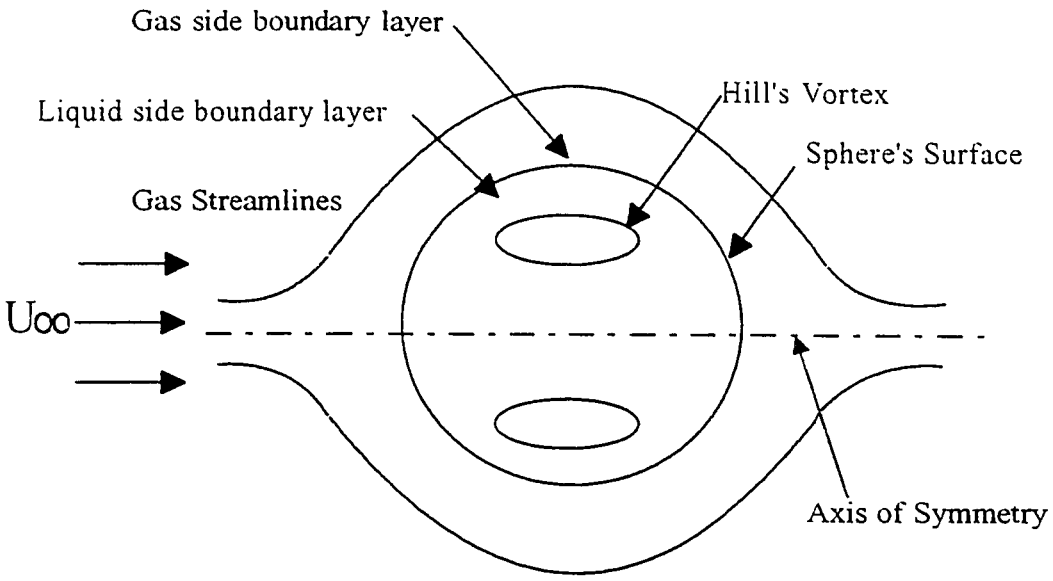

Fig. 3-1 A schematic of the flow patterns inside and outside the droplet

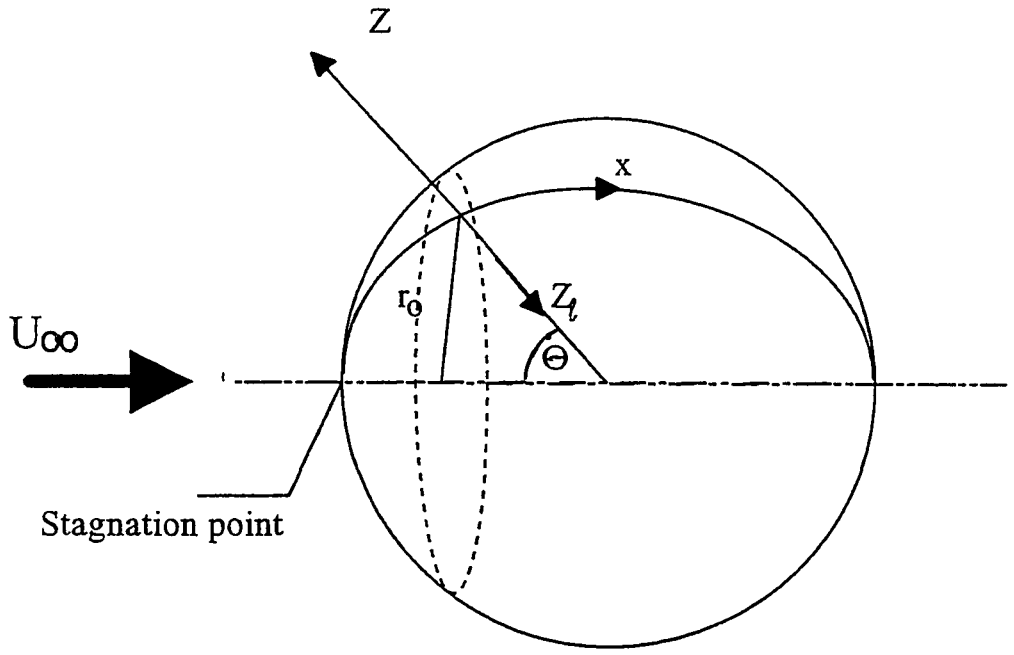

Fig. 3-2 : Coordinate System

3.2.1 Governing Equations in Dimensionless Form

The following non-dimensionalizing parameters are used for obtaining the dimensionless form of the governing equations :

$$U \equiv \frac{u}{U_\infty} \;,\; W \equiv \frac{w}{U_\infty} \;,\; Z \equiv \frac{z}{a} \;,\; X \equiv \frac{2x}{a\,\mathrm{Re}} \;,\; \mathrm{Re} \equiv \frac{2U_\infty a}{\nu_g}$$
$$U^* \equiv \frac{u^*}{U_\infty} \;,\; R \equiv \frac{2r_o}{a\,\mathrm{Re}} \;,\; P \equiv \frac{p}{\rho_g U^2_\infty} \;,\; T = \frac{T^* - T_i}{T_\infty - T_i} \;,\; \mathrm{Pr} = \frac{\nu}{\alpha} \qquad \textbf{(3. 1)}$$

Using the above dimensionless parameters (refer to the detailed procedure in Appendix A), the transformed form of the governing equations can be written as follows:

Continuity equation

$$\frac{\partial W}{\partial Z} + \frac{2}{\mathrm{Re}}\frac{\partial U}{\partial X} + \frac{2W}{(1+Z)} + \frac{U\cot\theta}{(1+Z)} = 0 \qquad \textbf{(3. 2)}$$

Meridional momentum equation

$$W\frac{\partial U}{\partial Z} + U\frac{2}{\mathrm{Re}}\frac{\partial U}{\partial X} + \frac{UW}{1+Z} = -\frac{dP}{dX}\frac{1}{\mathrm{Re}} + \left[\begin{array}{l} \dfrac{2}{\mathrm{Re}(1+Z)}\dfrac{\partial^2 (1+Z)U}{\partial Z^2} + \dfrac{8}{\mathrm{Re}^3}\dfrac{\partial^2 U}{\partial X^2} \\ + \dfrac{4\cot\theta}{(1+Z)\,\mathrm{Re}^2}\dfrac{\partial U}{\partial X} + \dfrac{8}{(1-Z)\,\mathrm{Re}^2}\dfrac{\partial W}{\partial X} - \dfrac{2U}{(1+Z)\,\mathrm{Re}\sin^2\theta} \end{array}\right] \qquad \textbf{(3. 3)}$$

Radial momentum equation

$$W\frac{\partial W}{\partial Z} + U\frac{2}{\mathrm{Re}}\frac{\partial W}{\partial X} - \frac{U^2}{1+Z} = \frac{-1}{2}\frac{dP}{dZ} + \left[\begin{array}{l} \dfrac{2}{\mathrm{Re}(1+Z)}\dfrac{\partial^2 (1+Z)W}{\partial Z^2} - + \dfrac{8}{\mathrm{Re}^3}\dfrac{\partial^2 W}{\partial X^2} \\ + \dfrac{4\cot\theta}{(1+Z)\,\mathrm{Re}^2}\dfrac{\partial U}{\partial X} - \dfrac{8}{(1+Z)\,\mathrm{Re}^2}\dfrac{\partial U}{\partial X} - \dfrac{4W}{(1+Z)^2\,\mathrm{Re}^2} - \dfrac{4UCot\theta}{\mathrm{Re}(1+Z)^2} \end{array}\right] \qquad \textbf{(3. 4)}$$

Energy Equation

$$\frac{1}{\Pr}\frac{\partial T}{\partial t}+U\frac{\partial T}{\partial X}+\frac{\mathrm{Re}}{2}W\frac{\partial T}{\partial Z}=\frac{1}{\Pr}\left[\begin{array}{l}\dfrac{1}{(1+Z)^2}\dfrac{\partial}{\partial Z}\left((1+Z)^2\dfrac{\partial T}{\partial Z}\right)+\\ \dfrac{4}{(1+Z)\sin\theta}\dfrac{1}{\mathrm{Re}^2}\dfrac{\partial}{\partial X}\left((1+Z)\sin\theta\dfrac{\partial T}{\partial X}\right)\end{array}\right]+S \qquad (3.5)$$

where S is the the dimensionless source term defined as , $S=\dfrac{aq'''\mathrm{Re}}{2U_\infty \rho C_p(T_\infty^* - T_o^*)}$ (3. 6)

3.2.2 Governing Boundary Layer Equations

An order of magnitude analysis is applied for the above equations taking into account that the value of Reynolds number is very large compared to unity and that the dimensionless boundary-layer thickness is very small compared to unity . Thus, a simplification to the above governing equations can be done by dropping the terms of order δ and higher orders of δ (as shown in Appendix A) . The simplified governing equations are the following boundary-layer equations :

Continuity equation

$$\frac{\partial U}{\partial X}+\frac{\mathrm{Re}}{2}\frac{\partial W}{\partial Z}+\mathrm{Re}\frac{W}{1+Z}+\frac{U}{R}\frac{dR}{dX}=0 \qquad (3.7)$$

Meridional momentum equation

$$U\frac{\partial U}{\partial X}+\frac{\mathrm{Re}}{2}W\frac{\partial U}{\partial Z}=U^*\frac{\partial U^*}{\partial X}+\frac{\partial^2 U}{\partial Z^2} \qquad (3.8)$$

Energy equation

$$\frac{1}{Pr}\frac{\partial T}{\partial t}+U\frac{\partial T}{\partial X}+\frac{Re}{2}W\frac{\partial T}{\partial Z}=\frac{1}{Pr}\frac{\partial^2 T}{\partial Z^2}+S \qquad (3.9)$$

It is clear from the previous order of magnitude analysis of the governing equations that the radial momentum equation could be dropped out completely because all its terms were of a low order of magnitude . It should be noted; however, that although the third term in the continuity equation has a lower order of magnitude than the other three terms, it was retained in the simplified equations to take curvature effects into consideration (El-Shaarawi [78]) .

3.2.3 Boundary Conditions

Examining the boundary-layer equations presented in the last section leads to the determination of the required number of boundary and initial conditions needed to make the problem investigated well-posed and amenable to numerical solution . The second derivative with respect to X is absent from the momentum equation and only the first derivative of U is present . Therefore, only the boundary condition at one end is required in the meridional direction , namely, at the front stagnation point . The derivatives with respect to Z are of second order; i.e., two boundary conditions should be used along the radial coordinate . These two boundary conditions can be determined at two locations : at the surface of the sphere where the condition comes from the continuity of the shear stress and meridional velocity of the surface of the liquid sphere and the second location is at the edge of the gas phase boundary layer ($X > 0$, $Z = \delta^*$)

where only U is specified and may be taken equal the value for the potential flow around a sphere.

Only the first derivative of W is present with respect to Z and therefore only a boundary condition at one location is enough and can be determined from the assumption of a non-evaporating sphere . This leads to the fact that no radial velocity component crosses the surface of the sphere (interface between both gas and liquid phases) and hence the value of W at the surface of the sphere (Z = 0) is essentially zero. Similarly, by investigating the energy equation (3.9), it is clear that the first derivative of temperature with respect to X is present and hence only one boundary condition in the meridional direction is required . This boundary condition can be estimated at the front stagnation point where the boundary-layer thickness is essentially zero and hence the temperature is assumed to equal the free stream temperature . The derivative of the temperature in the Z direction is of the second order revealing that two boundary conditions are required along the radial direction . The first is at the surface of the sphere and is determined from the continuity of temperature and heat flux between both gas and liquid phases and is treated in a similar manner to the continuity of shear stress . The second boundary condition is estimated at the edge of the boundary layer where the temperature would equal to its free stream value . Three case were considered for the initial condition of temperature T'. In the first case, a step change in the temperature from zero to unity is assumed at the surface of the sphere . In the second case, a linear temperature profile is assumed and the initial dimensionless temperature equals zero at

the surface and increases linearly till the edge of the boundary-layer where its value is unity . In the third case, a step change from zero to unity occurs at the edge of the boundary-layer and hence the initial temperature throughout the boundary-layer is set equal to zero while it is equal to unity at the boundary-layer edge . Therefore, all boundary conditions required for the governing equations can be summarized in the following dimensional forms :

at $z = 0$ (surface of the sphere) $u = u_\ell$ **(3.10-a)**

$T' = T'_\ell$ **(3.10-b)**

$\tau_{gas} = \tau_{liq}$ *or* $\mu \frac{\partial u}{\partial z} = -\mu_\ell \frac{\partial u_\ell}{\partial z_\ell}$ **(3.10-c)**

$w = 0$, **(3.10-d)**

and $K_g \frac{\partial T'}{\partial z} = -K_\ell \frac{\partial T'_\ell}{\partial z_\ell}$ **(3. 10-e)**

at $z = \infty$ (boundary layer edge) $u = u^*$ **(3.10-f)**

$T' = T'_\infty$ **(3.10-g)**

at $x = 0$ (front stagnation point) $T' = T'_\infty$, **(3.10-h)**

$u = 0$ **(3.10-i)**

and $w = w^*$ **(3.10-j)**

at $t' = 0$ (initial condition)

case a : at $Z = 0$, $X > 0$ $T' = T'_i$ **(3.10-k)**

at $Z > 0$, $X > 0$ $T' = T_\infty$ **(3.10-l)**

case b: at $Z = 0$, $X > 0$ $\quad T' = T'_i$ **(3.10-m)**

at $Z = \delta$, $X > 0$ $\quad T' = T'_\infty$ **(3.10-n)**

case c : at $Z \geq 0$, $X > 0$ $\quad T' = T'_i$ **(3.10-o)**

where T'_i is the initial temperature of the liquid sphere .

Meridional as well as radial potential velocity components which are applied at the edge of the boundary layer can be obtained from the theoretical potential flow around a stationary sphere [75] . Considering the sphere radius as "a", stream function as "ψ" and the potential function as "φ" we have

$$\psi = \frac{1}{2} u_\infty r^2 \sin^2\theta \left(1 - \frac{a^3}{r^3}\right) \qquad \textbf{(3. 11)}$$

and

$$\varphi = u_\infty r \cos\theta \left(1 + \frac{a^3}{2r^3}\right) \qquad \textbf{(3. 12)}$$

meridional and radial velocity components (u and w respectively) are related to the previous two equations by the following relations :

$$u = -\frac{1}{r}\frac{\partial \psi}{\partial \theta} = u_\infty \left(1 + \frac{a^3}{2(a+z)^3}\right) \sin\theta \qquad \textbf{(3. 13)}$$

and

$$w = -\frac{\partial \varphi}{\partial r} = -u_\infty \left(1 - \frac{a^3}{2(a+z)^3}\right) \cos\theta \qquad \textbf{(3. 14)}$$

Using the nondimensional parameters defined previously in equation (3.1) we get the following dimensionless form of the potential flow velocity components :

$$U^* = \left(1 + \frac{1}{2(1+Z)^3}\right) \sin\theta \qquad \textbf{(3. 15)}$$

$$W^* = -\left(1-\frac{1}{(1+Z)^3}\right)\cos\theta \qquad (3.16)$$

Similarly, the final form of the non-dimensional boundary conditions can be written as :

at $Z = 0$, $X > 0$ $\qquad U = U_t \quad , \quad T = T_t$ **(3.17-a)**

$$\frac{\partial U}{\partial Z} = -\mu^* \cdot \frac{\partial U_t}{\partial Z_t} \qquad \textbf{(3.17-b)}$$

$$\frac{\partial T}{\partial Z} = -K^* \cdot \frac{\partial T_t}{\partial Z_t} \qquad \textbf{(3.17-c)}$$

Where μ^*, K^* are the internal-to-external fluids viscosity ratio and thermal conductivity ratio, respectively .

at $Z = \infty$, $X > 0$ $\qquad U = U^* = \left(1+\frac{1}{2(1+Z)^3}\right)\sin\theta$ **(3.18-a)**

$$W = W^* = -\left[1-\frac{1}{(1+Z)^3}\right]\cos\theta \qquad \textbf{(3.18-b)}$$

$$T = 1 \qquad \textbf{(3.18-c)}$$

at $X = 0$, $Z \geq 0$ $\qquad T = 1$ **(3.18-d)**

$$U = W = 0 \qquad \textbf{(3.18-e)}$$

$$W^* = -\left(1-\frac{1}{(1+Z)^3}\right)\cos\theta \qquad \textbf{(3.18-f)}$$

at $t = 0$ (initial condition) $\qquad T = T_i = 0$ **(3.18-g)**

Now, having the governing equations in the final dimensionless forms as well as the dimensionless boundary conditions make the problem well posed and amenable to numerical solution .

3.3 Liquid Phase Governing Equations

In this section , the orthogonal curvilinear coordinates shown in Fig. 3-2 are also used with the same notation of both meridional and radial directions . However, a slight change in the definition of the transformed radial direction will be noticed as will be explained later in the following subsections . The reader can refer to Appendix B for the detailed transformation of the liquid phase governing equations to their orthogonal curvilinear coordinates .

3.3.1 Governing Equations in Dimensionless Form

The following non-dimensional parameters are used for obtaining the dimensionless forms of the governing equations :

$$U_\ell = \frac{u_\ell}{U_\infty} \quad , \quad W_\ell = \frac{w_\ell}{U_\infty} \quad , \quad Z_\ell = \frac{z}{a} \quad , \quad X_\ell = \frac{2x_\ell}{a\,\mathrm{Re}} \quad , \quad \mathrm{Re} = \frac{2U_\infty a}{\nu_g}$$
$$U_H = \frac{u_H}{U_\infty} \quad , \quad R = \frac{2r_o}{a\,\mathrm{Re}} \quad , \quad P = \frac{p}{\rho_g U^2_\infty} \quad , \quad T = \frac{T' - T_i}{T_\infty - T_i} \quad , \quad \mathrm{Pr} = \frac{\nu_\ell}{\alpha_\ell} \qquad \textbf{(3. 19)}$$

Using the above definitions (refer to the detailed procedure in Appendix B), the governing equations can be written in the following non-dimensional forms :

Continuity equation

$$-\frac{\partial W_\ell}{\partial Z_\ell}+\frac{2}{\mathrm{Re}}\frac{\partial U_\ell}{\partial X_\ell}+\frac{2W_\ell}{(1-Z_\ell)}+\frac{U_\ell \cot\theta}{(1-Z_\ell)}=0 \qquad \textbf{(3. 20)}$$

Meridional momentum equation

$$-W\frac{\partial U_\ell}{\partial Z_\ell}+U\frac{2}{\mathrm{Re}}\frac{\partial U_\ell}{\partial X_\ell}+\frac{U_\ell W_\ell}{1-Z_\ell}=\frac{-4}{\mathrm{Re}}\frac{dP}{dX_\ell}\rho^{\bullet}+$$
$$+\nu^{\bullet}\left[\begin{array}{l}-\frac{2}{\mathrm{Re}}\frac{\partial^2 U_\ell}{\partial Z_\ell^2}-\frac{4}{\mathrm{Re}(1-Z_\ell)}\frac{\partial U_\ell}{\partial Z_\ell}+\frac{8}{\mathrm{Re}^3}\frac{\partial^2 U_\ell}{\partial X_\ell^2}\\ +\frac{4\cot\theta\,\nu_g}{(1-Z_\ell)\mathrm{Re}^2}\frac{\partial U_\ell}{\partial X_\ell}+\frac{8}{(1-Z_\ell)\mathrm{Re}^2}\frac{\partial W_\ell}{\partial X_\ell}-\frac{2U_\ell}{\mathrm{Re}(1-Z_\ell)^2\sin^2\theta}\end{array}\right] \qquad \textbf{(3. 21)}$$

Energy Equation

$$\frac{1}{\mathrm{Pr}}\frac{\partial T_\ell}{\partial t}-W_\ell\frac{\mathrm{Re}}{2}\frac{\partial T_\ell}{\partial z_\ell}+U\frac{\partial T_\ell}{\partial x_\ell}=$$
$$\frac{1}{\mathrm{Pr}}\left[\begin{array}{l}\frac{1}{(1-Z_\ell)^2}\frac{\partial}{\partial Z_\ell}\left((1-Z_\ell)^2\frac{\partial T_\ell}{\partial Z_\ell}\right)+\\ \frac{4}{\mathrm{Re}^2(1-Z_\ell)\sin\theta}\frac{\partial}{\partial X_\ell}\left(\sin\theta\frac{\partial T_\ell}{\partial X_\ell}\right)\end{array}\right]+\frac{\mathrm{Re}\,q'''}{2\rho C_p(T^{*}_{\infty}-T^{*}_{,})U_\infty} \qquad \textbf{(3. 22)}$$

3.3.2 Governing Boundary-Layer Equations

Similarly as has been done for the gas-phase equations, by applying an order of magnitude analysis for the above equations, a further simplification to these governing equations can be done . By dropping the terms of order δ and higher orders of δ (as explained in Appendix B) , the governing equations can be simplified to the following forms :

Continuity equation

$$\frac{\partial U_\ell}{\partial X_\ell}-\frac{\mathrm{Re}}{2}\frac{\partial W_\ell}{\partial Z_\ell}+\mathrm{Re}\frac{W_\ell}{1-Z_\ell}+\frac{\mathrm{Re}\,U_\ell}{2}\frac{Cot\,\theta}{1-Z_\ell}=0 \qquad \textbf{(3. 23)}$$

Meridional Momentum equation

$$U_\ell \frac{\partial U_\ell}{\partial X_\ell} - \frac{\mathrm{Re}}{2} W_\ell \frac{\partial U_\ell}{\partial Z_\ell} = U_H \frac{\partial U_H}{\partial X_\ell} + \nu^* \frac{\partial^2 U_\ell}{\partial Z_\ell^2}$$

$$\textit{where;} \quad \nu^* = \frac{\nu_\ell}{\nu} = \mu^* \frac{\rho_g}{\rho_\ell} \qquad \textbf{(3. 24)}$$

The simplification of the energy equation will not follow exactly the order of magnitude analysis as has been done for the continuity and the momentum equations since the solution of the energy equation extends from the surface of the liquid sphere to its center . Inspecting the dimensionless form of this equation shows that the second term on the right hand side is divided by Re^2 and this is the only term that will be dropped because of the high Reynolds-number range in this study . Hence, the energy equation for the sphere can be written as :

$$\frac{\nu^*}{\mathrm{Pr}} \frac{\partial T_\ell}{\partial t} - \left(W_\ell \frac{\mathrm{Re}}{2} - \frac{2\nu^*}{\mathrm{Pr}(1 - Z_\ell)} \right) \frac{\partial T_\ell}{\partial z_\ell} + U_\ell \frac{\partial T_\ell}{\partial x_\ell} = \frac{\nu^*}{\mathrm{Pr}} \frac{\partial^2 T_\ell}{\partial Z_\ell^2} \qquad \textbf{(3. 25)}$$

3.3.3 Boundary Conditions

Examining the final form of the governing equations developed in Appendix B and presented in the last section leads to the determination of the required number of boundary conditions as well as the initial condition in a similar manner to what was done for the gas phase equations. From the momentum equation , equation (3.19), it can be noted that two boundary conditions are required for the meridional velocity component (U_ℓ) , one at the surface of the sphere which is assumed to be known from the gas phase solution and which represents the surface velocity of the liquid sphere and the second is assumed to be at the edge of the liquid phase boundary layer and which can be

obtained by matching the meridional velocity at the boundary layer edge with that of the Hill's vortex . However, it should be noted that the Hill's vortex strength is expected to be lower than its value for the potential flow because of the presence of the two boundary layers adjacent to the surface of the sphere [72] and it is calculated during the solution as will be explained later . Only one boundary condition for the radial velocity component (W_ℓ) will be sufficient and it is determined, as has been done previously in the gas phase solution, from the assumption of the non-evaporating liquid sphere and therefore the value of W_ℓ at the surface of the sphere ($Z_\ell = 0$) is zero . Inspecting the derivatives in the meridional (X) direction will reveal the need of only one boundary condition for the meridional velocity component; it can be assumed equal zero at the front stagnation point (X = 0) . Similarly, the boundary conditions for the energy equation can be determined at any time by considering the continuity of heat flux at the surface and the condition in the radial direction that at the center of the sphere the temperature gradient is set to zero due to the axisymmetric nature of the problem . The initial condition is easily determined from the assumption of an initially cold sphere subjected to a hot stream . This means that the initial temperature of the sphere is homogenous and set to a determined value (T'_i) . Summing up the boundary conditions for the liquid phase can be written in the following forms :

at $z_\ell = 0$ $\quad u = u_\ell \quad , \; w = 0$ **(3.26-a)**

$T' = T'_o$ **(3.26-b)**

$\tau_{gas} = \tau_{liq}$ **(3.26-c)**

at $z_\ell = \delta$ $\quad u_\ell = u_H$ **(3. 26-d)**

at $z_\ell = a$ (i.e., center of the sphere) $\quad \frac{\partial T^*}{\partial z_\ell} = 0$ **(3.26-e)**

at $t^* = 0$ $\quad T' = T'_i$ **(3.26-f)**

Therefore, the non-dimensional boundary conditions can be written as :

at $Z_\ell = 0$ $\quad U_\ell = U_o$ (dimensionless surface velocity) **(3.27-a)**

$W = 0$ **(3.27-b)**

$T = T_o$ **(3.27-c)**

at $Z_\ell = \delta$ $\quad U_\ell = U_H$ **(3.27-d)**

at $Z_\ell = 1$ $\quad \frac{\partial T}{\partial Z_\ell} = 0$ **(3.27-e)**

at $t = 0$ $\quad T = T_i = 0$ **(3.27-f)**

It is worth mentioning that the ratio of the actual strength of the internal vortex compared to that for potential flow (Hill's vortex) [75] is calculated in the liquid-phase solution by dividing the actual surface velocity obtained from the gas phase solution by the meridional component of the potential vortex calculated at the surface of the sphere . This ratio could be obtained along the meridional direction up to the point of the external flow separation . Now, the liquid phase governing equations along with their boundary conditions are complete and the liquid phase problem can be considered well posed . However, uncoupling the gas and liquid phase solutions will be explained in details in chapter V while explaining the method of solution and overall numerical algorithm .

CHAPTER IV

NUMERICAL REPRESENTATION OF THE GOVERNING EQUATIONS

4.1 Introduction

The governing equations developed in the previous chapter are nonlinear second order equations . No analytical solution is possible for this type of equations, therefore, approximate methods of solution are used to solve them . The method used in this work is the finite difference approximation where the governing equations are first transformed to difference equations by dividing the domain of solution to a grid of points in the form of a mesh and the derivatives are expressed along each mesh point referred to as a node . Therefore, the differential governing equations can be written for a set of nodes of the grid in the shape of algebraic equations that are linearized to a system of linear algebraic equations and then solved by an appropriate technique for matrix inversion . In this chapter, the finite difference representation of the governing equations and their accompanied boundary as well as initial conditions are presented for both the gas phase in Section 4.2 and for the liquid phase in Section 4.3 .

The numerical grid is shown for each phase where in the gas phase the grid starts at the surface of the sphere (Z = 0) and then progresses outward to match with the inviscid flow around the sphere determining the edge of the gas phase boundary layer. For the liquid phase the grid starts at the surface of the sphere (Z_i = 0) and progresses inward toward the center of the sphere to meet the internal vortex (Hill's vortex) thus defining the internal boundary layer thickness .

4.2 Gas Phase Equations

4.2.1 Numerical Grid

The grid shown in Figure 4.1 is consisting of two sets of perpendicular lines representing the meridional direction (circles) and the radial direction (straight lines) where the intersection of these lines constitute the mesh points (the nodes) where the solutions of the governing equations are obtained . The circles are concentric starting from the surface of the sphere with constant Z values and extended until the edge of the boundary layer while the straight lines pass through the center of the sphere and each of them is a constant X-line (at a constant angle) . The grid consists of n+1 points in the radial direction where the first being the surface of the sphere (Z = 0) and the last is located outside the boundary layer edge . On the other hand, the number of meridional stations is m+1starting from X = 0 (at the front stagnation line) and extending until the angle of flow separation . The index i represents the radial mesh points (Z-direction) starting with i=1 at the surface of the sphere (Z = 0) till i = n+1 in the free stream while

the index j represents the X-mesh points starting from j = 1 at the front stagnation line (X = 0) till the point of separation where j = m + 1 . Therefore, the finite difference representation of these mesh points will be as follows ;

$Z_i = (i-1)\,\Delta Z$ where i = 1, 2, 3, ..., n+1

$X_j = (j-1)\,\Delta X$ where j = 1, 2, 3, ..., m+1

Here, ΔX and ΔZ represent the step sizes for the meridional and the radial directions, respectively, and the subscripts denote the location of the variable under consideration, e.g. $U_{i,j}$ means the meridional velocity at the i'th radial location and j'th meridional location .

4.2.2 Linearizing Technique

The finite difference formulation of the governing equations should retain the same characteristics of the parent equations developed in the previous chapter . The governing boundary-layer equations are parabolic in nature with the terms in the marching (X) direction are the convective terms while those in the transverse direction (Z) are diffusive . Therefore, backward differences are employed for the convective terms and central differences are employed for the diffusive terms . For each meridional location, the variables with subscript (j) will be assumed to be known and those of subscripts (j+1) are assumed unknowns for all values of i and the solution of all (i) variables will be organized in a matrix form solved along the constant (j) line then it marches forward for the next meridional step till the separation occurs and the solution

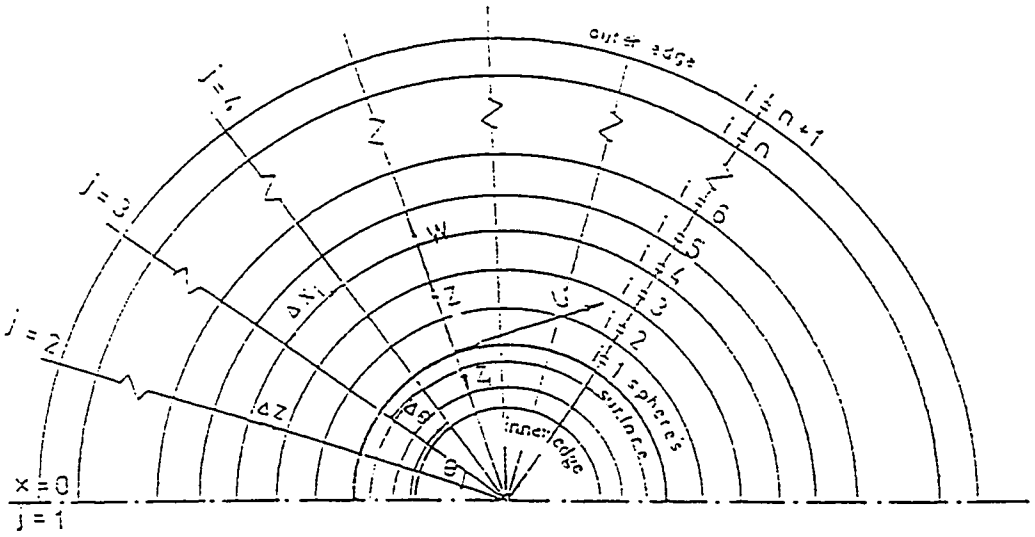

Fig. 4.1 : Numerical grid

stops for the current time step and restarts from the beginning for the next time step . The entire solution will terminate if the surface temperature reaches the free stream temperature .

The governing equations are approximated by finite differences in separate domains [9] where the location of each derivative was chosen to ensure stability and consistency of the solution , following the technique used in [9] a ringed point will represent the location where derivatives are calculated while the cross points represent the grid points involved in the difference approximation, for the ringed points that do not coincide on grid points, derivatives are approximated and an average value is taken . The grid is shown in Figure (4.2) .

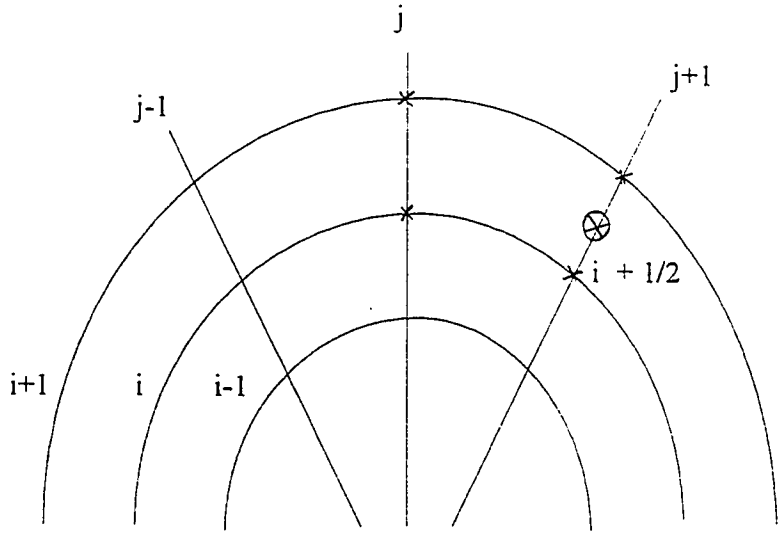

Continuity equation

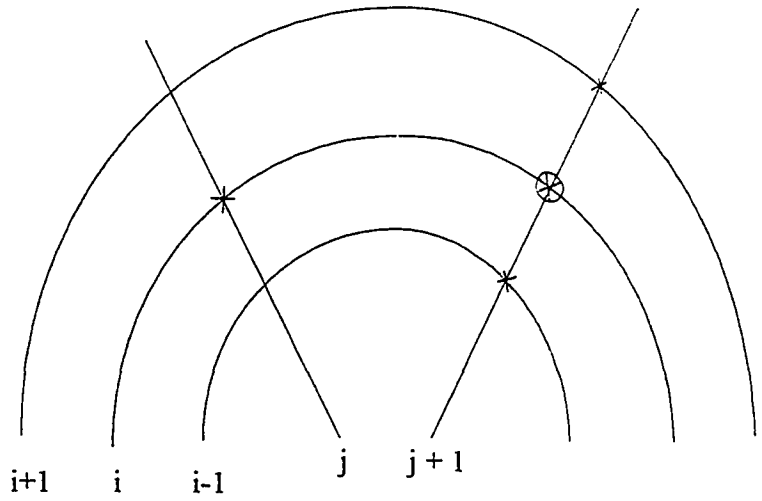

Meridional momentum and energy equation

Fig. 4-2 : Gas phase finite difference domain

The order by which the numerical solution is devised for starts by solving the meridional momentum equation for $U_{i,j+1}$, then the continuity equation has to be solved for $W_{i,j+1}$. Therefore, the term W found in the meridional momentum equation will be represented by $W_{i,j}$ (i.e. from the previous meridional step), while in the continuity equation U will be expressed as $U_{i,j+1}$ since it would have been already obtained from the solution of the preceding momentum equation . Both U and W in the energy equation will be represented at the (i,j+1) points since the flow field is assumed to be steady, and the energy equation is the last to solve (after solving the momentum and continuity equation and hence the flow field components are all known) . Therefore there are no changes in U and W as time elapses, and the transient term is solved as if we had a series of spheres where U and W are constants and the only variable is the temperature which will be solved for at each meridional location for all Z values starting from the surface of the sphere until the free stream and then these values are used to repeatedly march the solution to the next meridional station till the external flow separation point is reached . Then the whole procedure is repeated for the next time step until the state of uniform surface temperature is reached when the surface temperature reaches the free stream temperature .

4.2.3 Finite-Difference Representation of the Derivatives

Following the notation described in the previous section and shown in Figure (4.2) the finite difference representation of the various derivatives present in the governing equations can be written as follows :

$$\frac{\partial U}{\partial X}=\frac{U_{i,J+1}-U_{i,j}}{\Delta X_i} \tag{4. 1}$$

$$\frac{\partial U}{\partial Z}=\frac{U_{i+1,J+1}-U_{i-1,j+1}}{2\Delta Z} \tag{4. 2}$$

$$\frac{\partial^2 U}{\partial Z^2}=\frac{U_{i+1,J+1}-2U_{i,j+1}+U_{i-1,j+1}}{\Delta Z^2} \tag{4. 3}$$

$$\frac{\partial W}{\partial Z}=\frac{W_{i+1,J+1}-W_{i,j+1}}{\Delta Z} \tag{4. 4}$$

$$\frac{\partial T}{\partial X}=\frac{T_{i,J+1,k+1}-T_{i,j,k+1}}{\Delta X_i} \tag{4. 5}$$

$$\frac{\partial T}{\partial Z}=\frac{T_{i+1,J+1,k+1}-T_{i-1,j+1,k+1}}{2\Delta Z} \tag{4. 6}$$

$$\frac{\partial^2 T}{\partial Z^2}=\frac{T_{i+1,J+1,k+1}-2T_{i,j+1,k+1}+T_{i-1,j+1,k+1}}{\Delta Z^2} \tag{4. 7}$$

$$\frac{\partial T}{\partial t}=\frac{T_{i,j+1,k+1}-T_{i,j+1,k}}{\Delta t} \tag{4. 8}$$

4.2.4 Finite-Difference Representation of the Meridional Momentum Equation

$$U\frac{\partial U}{\partial X}+\frac{\mathrm{Re}}{2}W\frac{\partial U}{\partial Z}=U^*\frac{\partial U^*}{\partial X}+\frac{\partial^2 U}{\partial Z^2} \tag{3. 8}$$

$$U_{i,j}\frac{U_{i,j+1}-U_{i,j}}{\Delta X_i}+\frac{\mathrm{Re}}{2}W_{i,j}\frac{U_{i+1,j+1}-U_{i-1,j+1}}{2\Delta Z}= \frac{3}{2}\sin(j\Delta\theta)\frac{3}{4}\mathrm{Re}\cos(j\Delta\theta)+\frac{U_{i+1,j+1}-2U_{i,j+1}+U_{i-1,j+1}}{\Delta Z^2} \tag{4. 9}$$

Boundary conditions :

$$U_{i,1}=0 \qquad \text{(stagnation line)} \tag{4.10-a}$$

$$W_{i,1} = \frac{-1}{(1+(i-1)\Delta Z)^3} - 1 \qquad \textbf{(4. 10-b)}$$

$$U_{1,j} = U_{\ell 1,j} \qquad \& \quad W_{1,j} = 0 \qquad \textbf{(4.10-c)}$$

$$U_{n+1,j} = \left(1 + \frac{1}{2((1+n)\Delta Z)^3}\right) \sin((j-1)\Delta\theta) \qquad \textbf{(4.10-d)}$$

Matching of the shear stress at the surface :

$$\frac{1}{\mu^*}\left(\frac{U_{2,j} - U_{1,j}}{\Delta Z}\right) = -\left(\frac{U_{\ell_2,} - U_{1,j}}{\Delta Z_\ell}\right) \qquad \textbf{(4. 11a)}$$

It is worth mentioning that in the present studty, all runs were carried out considering equal magnitudes of the radial step . i.e. $\Delta Z = -\Delta Z_\ell$

therefore, $$\frac{U_{2,j}}{\mu^*} - \frac{U_{1,j}}{\mu^*} = U_{\ell_2,} - U_{1,j}$$

or $$U_{\ell_2,} = \frac{U_{2,j}}{\mu^*} - U_{1,j}\left(\frac{1}{\mu^*} - 1\right) \qquad \textbf{(4. 11b)}$$

Rearranging :

$$U_{i-1,j+1}\left(\frac{-W_{i,j}\,Re}{4\Delta Z} - \frac{1}{(\Delta Z)^2}\right) + U_{i,j+1}\left(\frac{U_{i,j}}{\Delta X_i} + \frac{2}{(\Delta Z)^2}\right) +$$

$$+ U_{i+1,j+1}\left(\frac{W_{i,j}\,Re}{4\Delta Z} - \frac{1}{(\Delta Z)^2}\right) = \frac{(U_{i,j})^2}{\Delta X_i} + \frac{9}{8} Re\ Sin\ j\Delta\theta\ Cos\ j\Delta\theta \qquad \textbf{(4. 12)}$$

Note that $$\frac{9}{8} Re\ Sin\ j\Delta\theta\ Cos\ j\Delta\theta = \frac{9}{16} Re\ Sin\ (2j\Delta\theta)$$

Let $$C(i) = \left(\frac{-W_{i,j}\,\mathrm{Re}}{4\Delta Z} - \frac{1}{(\Delta Z)^2}\right) \tag{4.13}$$

$$A(i) = \left(\frac{U_{i,j}}{\Delta X_i} + \frac{2}{(\Delta Z)^2}\right) \tag{4.14}$$

$$B(i) = \left(\frac{W_{i,j}\,\mathrm{Re}}{4\Delta Z} - \frac{1}{(\Delta Z)^2}\right) \tag{4.15}$$

$$D(i) = \frac{(U_{i,j})^2}{\Delta X_i} + \frac{9}{16}\mathrm{Re}\ Sin(2j\Delta\theta) \tag{4.16}$$

note that $$U_{o,j} = U_{\ell 2,j} = \frac{U_{2,j}}{\mu^*} - U_{1,j}\left(\frac{1-\mu^*}{\mu^*}\right)$$

Therefore, the momentum equation can be written as :

For i = 1 : $C_1 U_o + A_1 U_1 + B_1 U_2 = D_1$

taking into consideration that $U_{0,j} = U_{\ell 2,j}$ and using (4-13), the above equation can be rewritten, for a given j, as

for i = 1 : $$(A_1 - C_1\frac{1-\mu^*}{\mu^*})U_1 + (\frac{C_1}{\mu^*} + B_1)U_2 = D_1$$

similarly ,

For i = 2 : $C_2 U_1 + A_2 U_2 + B_2 U_3 = D_2$

For i = 3 : $C_3 U_2 + A_3 U_3 + B_3 U_4 = D_3$ **(4.17)**

For i = n : $C_n U_{n-1} + A_n U_n + B_n U_{n+1} = D_n$

Or $C_n U_{n-1} + A_n U_n = D_n - B_n U_{n+1}$

These equations can be represented in a matrix form as follows;

$$\begin{bmatrix} A_1' & B_1' & & & & & & \\ C_2 & A_2 & B_2 & & & & 0 & \\ & C_3 & A_3 & B_3 & & & & \\ & & \cdot & \cdot & \cdot & & & \\ & & & \cdot & \cdot & \cdot & & \\ & & & & \cdot & \cdot & \cdot & \\ & & & & & \cdot & \cdot & \cdot \\ & 0 & & & & \cdot & \cdot & \cdot \\ & & & & & C_{n-1} & A_{n-1} & B_{n-1} \\ & & & & & & C_n & A_n \end{bmatrix} \begin{bmatrix} U_1 \\ U_2 \\ U_3 \\ \cdot \\ \cdot \\ \cdot \\ \cdot \\ \cdot \\ U_{n-1} \\ U_n \end{bmatrix} = \begin{bmatrix} D_1 \\ D_2 \\ D_3 \\ \cdot \\ \cdot \\ \cdot \\ \cdot \\ \cdot \\ D_{n-1} \\ D_n' \end{bmatrix} \quad \textbf{(4. 18)}$$

Where;

$$D_n' = D_n - B_n\ U_{n+1} \quad \textbf{(4.19a)}$$

$$A_1' = A_1 - C_1\left(\frac{1-\mu^*}{\mu^*}\right) \quad \textbf{(4. 19b)}$$

$$B_1' = B_1 + \frac{C_1}{\mu^*} \quad \textbf{(4.19c)}$$

4.2.5 Finite Difference Representation of the Continuity Equation

$$\frac{\partial U}{\partial X} + \frac{\mathrm{Re}}{2}\frac{\partial W}{\partial Z} + \mathrm{Re}\frac{W}{1+Z} + \frac{\mathrm{Re}}{2}\frac{U\,Cot\theta}{1+Z} = 0 \quad \textbf{(3. 7)}$$

Finite Difference Representation :

$$\frac{U_{i+1,j+1} + U_{i,j+1} - U_{i+1,j} - U_{i,j}}{2\Delta X_{i+1/2}} + \frac{\mathrm{Re}}{2}\frac{W_{i+1,j+1} - W_{i,j+1}}{\Delta Z} + \frac{(U_{i+1,j+1} + U_{i,j+1})\,\mathrm{Re}\,Cot(j\Delta\theta)}{4(1+Z_{i+1/2})} + \frac{\mathrm{Re}(W_{i+1,j+1} + W_{i,j+1})}{2(1+Z_{i+1/2})} = 0 \quad \textbf{(4. 20)}$$

Rearranging :

$$W_{i,j+1}\frac{Re}{2}\left(\frac{1}{1+Z_{i+1/2}}-\frac{1}{\Delta Z}\right)+W_{i+1,j+1}\frac{Re}{2}\left(\frac{1}{(1+Z_{i+1/2})}+\frac{1}{\Delta Z}\right)= \\ =-\frac{U_{i+1,j+1}+U_{i,j+1}-U_{i+1,j}-U_{i,j}}{2\Delta X_{i+1/2}}-\frac{(U_{i+1,j+1}+U_{i,j+1})\,ReCot(j\Delta\theta)}{4(1+Z_{i+1/2})} \quad \textbf{(4. 21)}$$

Let ;

$$A(i)=\frac{Re}{2}\left(\frac{1}{1+Z_{i+1/2}}-\frac{1}{\Delta Z}\right) \quad \textbf{(4. 22)}$$

$$B(i)=\frac{Re}{2}\left(\frac{1}{1+Z_{i+1/2}}+\frac{1}{\Delta Z}\right) \quad \textbf{(4. 23)}$$

$$D(i)=-\frac{U_{i+1,j+1}+U_{i,j+1}-U_{i+1,j}-U_{i,j}}{2\Delta X_{i+1/2}}- \\ -\frac{(U_{i+1,j+1}+U_{i,j+1})\,ReCot(j\Delta\theta)}{4(1+Z_{i+1/2})} \quad \textbf{(4. 24)}$$

Equations can be represented, for a given j, as;

$$\text{for } i=1 \qquad A_1 W_1+B_1 W_2 = D_1 \quad (W_1=0 \text{ "Sphere Surface"}) \quad \textbf{(4. 25)}$$

$$\text{for } i=2 \qquad A_2 W_2+B_2 W_3 = D_2$$

$$\text{for } i=n\text{-}1 \qquad A_{n-1} W_{n-1}+B_{n-1} W_n = D_{n-1}$$

$$\text{for } i=n \qquad A_n W_n + B_n W_{n+1} = D_n$$

4.2.6 Finite-Difference Representation of the Energy Equation :

$$\frac{1}{Pr}\frac{\partial T}{\partial t}+U\frac{\partial T}{\partial X}+\frac{Re}{2}W\frac{\partial T}{\partial Z}=\frac{1}{Pr}\frac{\partial^2 T}{\partial Z^2}+S \quad \textbf{(3. 9)}$$

$$\frac{T_{i,j+1,k+1}-T_{i,j+1,k}}{\Delta t}+Re.Pr\frac{W_{i,j+1}}{2}\frac{T_{i+1,j+1,k+1}-T_{i-1,j+1,k+1}}{2\Delta Z}+ \\ +Pr\,U_{i,j+1}\frac{T_{i,j+1,k+1}-T_{i,j,k+1}}{\Delta X_i}=\frac{T_{i+1,j+1,k+1}-2T_{i,j+1,k+1}+T_{i-1,j+1,k+1}}{\Delta Z^2}+S.Pr \quad \textbf{(4. 26)}$$

Rearranging ;

$$T_{i-1,j+1,k+1}\left(\frac{-\mathrm{Re\,Pr}\,W_{i,j+1}}{4\Delta Z}-\frac{1}{\Delta Z^2}\right)+T_{i,j+1,k+1}\left(\frac{1}{\Delta t}+\frac{2}{\Delta Z^2}+\frac{U_{i,j+1}\,\mathrm{Pr}}{\Delta X_i}\right)+$$
$$T_{i+1,j+1,k+1}\left(\frac{\mathrm{Re\,Pr}\,W_{i,j+1}}{4\Delta Z}-\frac{1}{\Delta Z^2}\right)=\frac{T_{i,j+1,k}}{\Delta t}+\frac{U_{i,j+1}\,\mathrm{Pr}\,T_{i,j,k+1}}{\Delta X_i}+S.\,\mathrm{Pr} \qquad \textbf{(4. 27)}$$

For a given j, let ;

$$C(i)=\left(\frac{-W_{i,j+1}\,\mathrm{Re\,Pr}}{4\Delta Z}-\frac{1}{(\Delta Z)^2}\right) \qquad \textbf{(4. 28)}$$

$$A(i)=\left(\frac{1}{\Delta t}+\frac{2}{(\Delta Z)^2}\right)+\frac{U_{i,j+1}\,\mathrm{Pr}}{\Delta X_i} \qquad \textbf{(4. 29)}$$

$$B(i)=\left(\frac{W_{i,j+1}\,\mathrm{Re.Pr}}{4\Delta Z}-\frac{1}{(\Delta Z)^2}\right) \qquad \textbf{(4. 30)}$$

$$D(i)=\frac{T_{i,j+1,k}}{\Delta t}+\frac{U_{i\,j+1}\,T_{i,j,k+1}\,\mathrm{Pr}}{\Delta X_i}+S\,\mathrm{Pr} \qquad \textbf{(4. 31)}$$

Hence, equation (4.27) can be rewritten as

$$B(i)\,T_{i+1,j+1,k+1}+A(i)\,T_{i,j+1,k+1}+C(i)\,T_{i-1,j+1,k+1}=D(i) \qquad \textbf{(4. 32)}$$

subject to the boundary conditions :

$$T_{1,i,k}=1 \qquad \textbf{(4.33-a)}$$

$$T_{n+1,j,k}=1 \qquad \textbf{(4.33-b)}$$

$$T_{0,j}=T_{2,j}/K^{*}\;-\;T_{1,j}(1-K^{*})/K^{*} \qquad \textbf{(4.33-c)}$$

case a : $T_{1,j,1}=0$ **(4. 33-d)**

$$T_{i,j,1}=1 \qquad \textbf{(4.33-e)}$$

case b: $T_{1,j,1}=0$ **(4.33-f)**

$$T_{i,j,1} = \frac{(i-1)}{n-1} \qquad \textbf{(4.33-g)}$$

case c : $T_{i,j,1} = 0$ **(4.33-h)**

for the three cases (a,b and c) $T_{n,j,1} = 1$ **(4.33-i)**

substituting and rewriting (4.32) for given j and k one gets

For i = 1 : $B_1 T_2 + A_1 T_1 + C_1 T_0 = D_1$

For i = 2 : $B_2 T_3 + A_2 T_2 + C_2 T_1 = D_2$ **(4. 34)**

For i = n : $B_n T_{n+1} + A_n T_n + C_n U_{n-1} = D_n$

Or $C_n T_{n-1} + A_n T_n = D_n - B_n T_{n+1}$

Taking into consideration (4.33d), the first equation becomes :

$$\left[A_1 - C_1\left(\frac{1-K^*}{K^*}\right)\right] T_1 + \left(\frac{C_1}{K^*} + B_1\right) T_2 = D_1$$

$$A_1' = A_1 - C_1\left(\frac{1-K^*}{K^*}\right) \qquad \textbf{(4.35)}$$

$$B_1' = \left(\frac{C_1}{K^*} + B_1\right)$$

Equations (4.34) can be represented in a matrix form as follows;

$$\begin{bmatrix} A_1' & B_1' & & & & & & \\ C_2 & A_2 & B_2 & & & & 0 & \\ & C_3 & A_3 & B_3 & & & & \\ & & \cdot & \cdot & \cdot & & & \\ & & & \cdot & \cdot & \cdot & & \\ & & & & \cdot & \cdot & \cdot & \\ & & & & & \cdot & \cdot & \cdot \\ & 0 & & & & \cdot & \cdot & \cdot \\ & & & & & C_{n-1} & A_{n-1} & B_{n-1} \\ & & & & & & C_n & A_n \end{bmatrix} \begin{bmatrix} T_1 \\ T_2 \\ T_3 \\ \cdot \\ \cdot \\ \cdot \\ \cdot \\ \cdot \\ T_{n-1} \\ T_n \end{bmatrix} = \begin{bmatrix} D_1 \\ D_2 \\ D_3 \\ \cdot \\ \cdot \\ \cdot \\ \cdot \\ \cdot \\ D_{n-1} \\ D_n \end{bmatrix} \quad \textbf{(4.36)}$$

Where;

$$D_n' = D_n - B_n \; T_{n+1}$$

Note that in the computer program, the initial time step (t = 0) is a case in which the sphere surface temperature is known (T=0) . Therefore the matrix starts in this case from i = 2 while for any other time step (t > 0) the temperature at the surface is to be calculated and this will be taken care of in the program code .

4.3 Liquid Phase Equations

4.3.1 Numerical Grid and Linearizing Technique

The numerical grid used to solve the governing equations in the liquid phase (inside the sphere) is shown in Figure 4.1 while the numerical domain in which the finite difference equations are written is shown in Figure 4.3 for the continuity, momentum and energy equations . The main differences between this solution and the gas-phase

solution is mainly in the marching direction with respect to Z; it starts at the surface of the sphere and moves towards its center (increasing Z_t) . In addition, the X-grid spacings (ΔX) decrease in the direction for Z_t . The details of uncoupling the gas and liquid phases may be noticed in the boundary conditions at the interface ($Z = Z_t = 0$) and will be explained in the next chapter .

It should be pointed out that for solving the liquid phase equations, the boundary conditions at the surface of the sphere (where the solution begins) are supposed to be known from the solution of the gas-phase equations leading to simple Direchlet boundary conditions (i.e., values of the velocity are known at the surface of the sphere, $Z_t = 0$) rather than employing the viscosity ratio or the thermal conductivity ratio as done in the case of external flow (gas phase solution) .

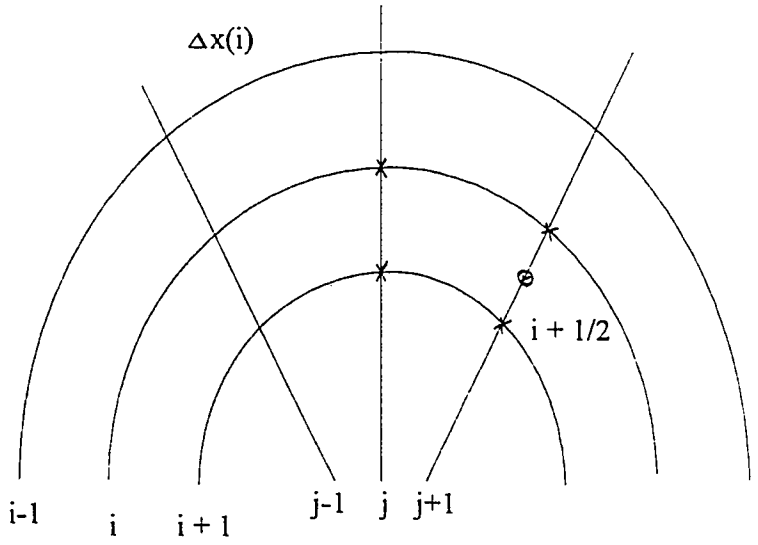

Continuity equation

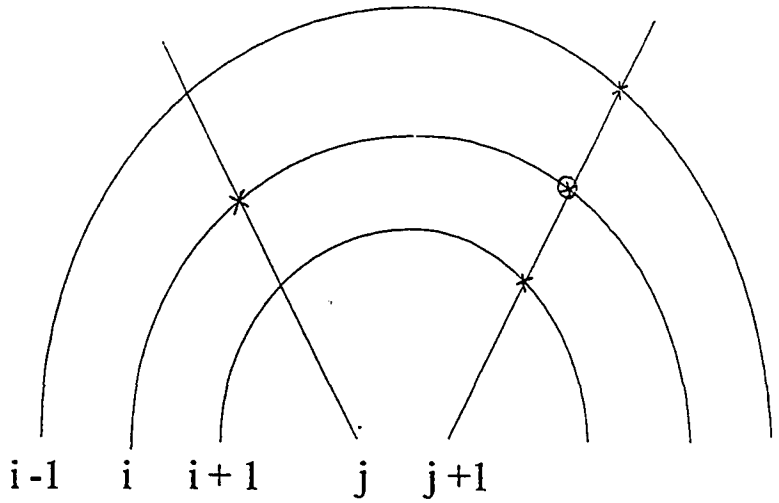

Meridional momentum and energy equation

Fig. 4-3 : Liquid phase finite difference domain

4.3.2 Finite-Difference Representation of the Meridional Momentum Equation

$$U_t \frac{\partial U_t}{\partial X_t} - \frac{\mathrm{Re}}{2} W_t \frac{\partial U_t}{\partial Z_t} = U_H \frac{\partial U_H}{\partial X} + \nu^* \frac{\partial^2 U_t}{\partial Z_t^2} \tag{3.24}$$

$$U_{ti,j} \frac{U_{ti,j+1} - U_{ti,j}}{\Delta X_t} - \frac{\mathrm{Re}}{2} W_{ti,j} \frac{U_{ti+1,j+1} - U_{ti-1,j+1}}{2\Delta Z_t} = \frac{9}{4} C(j) \left[1 - 2\,(1 - Z_t)^2\right]^2 \times \left(\sin^2\theta \frac{C_{j+1} - C_j}{\Delta X_t(i)} + \frac{\mathrm{Re}\, C_j}{4(1 - Z_t)} \sin 2\theta\right) + \nu^* \frac{U_{ti+1,j+1} - 2U_{ti,j+1} + U_{ti-1,j+1}}{\Delta Z_t^2} \tag{4.37}$$

where C(j) is the ratio between the actual meridional surface velocity and the meridioanl component of the potential Hill's vortex at the sphere's surface and it represents the ratio between actual and inviscid Hill's vortex strength .

Rearranging;

$$U_{ti-1,j+1}\left(\frac{\mathrm{Re}}{2} \frac{W_{ti,j}}{2\Delta Z_t} - \frac{\nu^*}{\Delta Z_t^2}\right) + U_{ti,j+1}\left(\frac{U_{ti,j}}{\Delta X_{ti}} + \frac{2\nu^*}{\Delta Z_t^2}\right) + U_{ti+1,j+1}\left(-\frac{W_{ti,j}\,\mathrm{Re}}{4\,\Delta Z_t} - \frac{\nu^*}{\Delta Z_t^2}\right) = \frac{9}{4} C_j \left[1 - 2\,(1 - Z_t)^2\right]^2 \left(\sin^2\theta \frac{C_{j+1} - C_j}{\Delta X_t(i)} + \frac{\mathrm{Re}\, C_j}{4(1 - Z_t)} \sin 2\theta\right) + \frac{(U_o)^2}{\Delta X_{ti}} \tag{4.38}$$

Now, for given j, let ;

$$C(i) = \left(-\frac{W_{ti,j}\,\mathrm{Re}}{4\Delta Z_t} + \frac{\nu^*}{(\Delta Z_t)^2}\right) \tag{4.39}$$

$$A(i) = \left(\frac{U_{ti,j}}{\Delta X_{ti}} - \frac{2\nu^*}{(\Delta Z_t)^2}\right) \tag{4.40}$$

$$B(i) = \left(\frac{W_{ti,j}\,\mathrm{Re}}{4\Delta Z_t} + \frac{\nu^*}{(\Delta Z_t)^2}\right) \tag{4.41}$$

$$D(i)=\frac{9}{4}C_j\left[1-2\,(1-Z_\ell)^2\right]^2(\sin^2\theta\,\frac{C_{j+1}-C_j}{\Delta X_{\ell i}}+ \\ +\frac{\mathrm{Re}\,C_j}{4(1-Z_\ell)}\sin 2\theta)+\frac{(U_o)^2}{\Delta X_{\ell i}} \qquad \textbf{(4. 42)}$$

Equation (4.38) now becomes;

$$C_i\,U_{\ell i-1}+A_i\,U_{\ell i}+B_i\,U_{\ell i+1}=D_i \qquad \textbf{(4. 43)}$$

For i = 2 : $C_2\,U_{\ell 1}+A_2\,U_{\ell 2}+B_2\,U_{\ell 3}=D_2$

For i = 3 : $C_3\,U_{\ell 2}+A_3\,U_{\ell 3}+B_3\,U_{\ell 4}=D_3$

For i = n-1 : $C_{n-1}\,U_{\ell n-2}+A_{n-1}\,U_{\ell n-1}+B_{n-1}\,U_{\ell n}=D_{n-1}$

For i = n : $C_n\,U_{\ell n-1}+A_n\,U_{\ell n}+B_n\,U_{\ell n+1}=D_n$

Or $C_n\,U_{\ell n-1}+A_n\,U_{\ell n}=D_n-B_n\,U_{\ell n+1}$

It should be noted that $U_{\ell n+1}=U_H$

$$U_{\ell 1}=U_o$$

and these are the two boundary conditions in this case . These equations can be represented in a matrix form as follows;

$$\begin{bmatrix} A_2 & B_2 & & & & & & \\ C_3 & A_3 & B_3 & & & & 0 & \\ & C_4 & A_4 & B_4 & & & & \\ & & \cdot & \cdot & \cdot & & & \\ & & & \cdot & \cdot & \cdot & & \\ & & & & \cdot & \cdot & \cdot & \\ & & & & & \cdot & \cdot & \cdot \\ & 0 & & & & C_{n-1} & A_{n-1} & B_{n-1} \\ & & & & & & C_n & A_n \end{bmatrix}\begin{bmatrix} U_{\ell 2} \\ U_{\ell 3} \\ U_{\ell 4} \\ \cdot \\ \cdot \\ \cdot \\ \cdot \\ U_{\ell n-1} \\ U_{\ell n} \end{bmatrix}=\begin{bmatrix} D_2 \\ D_3 \\ D_4 \\ \cdot \\ \cdot \\ \cdot \\ \cdot \\ D_{n-1} \\ D_n \end{bmatrix} \qquad \textbf{(4. 44)}$$

Where;

$$D_2 = D_2 - C_2\ U_{\ell 1}$$

$$D_n = D_n - B_n\ U_{\ell n+1}$$

It is worth mentioning here that the surface velocity distribution is obtained from gas side solution . For the selection of n_ℓ at each meridional station (j) an iterative type method is used . In this method the values of n_ℓ should be large enough so that the computed meridional velocity distribution U_ℓ is close in tangent at the innermost points ($i = n_\ell+1$), within an arbitrarily chosen accuracy, to the corresponding modified potential spherical vortex distribution U_H . For given j and a value of n_ℓ, once the computations have been carried out for U_ℓ and the aforesaid matching was not attained, the values of n_ℓ could be increassed, the computations again performed and the computed values of U_ℓ accepted if the aforesaid matching criterion is satisfied and hence the boundary layer thickness is determined .

4.3.3 Finite Difference Representation of the Continuity Equation

$$\frac{\partial U_\ell}{\partial X_\ell} - \frac{\mathrm{Re}}{2}\frac{\partial W_\ell}{\partial Z_\ell} + \mathrm{Re}\frac{W_\ell}{1-Z_\ell} + \frac{\mathrm{Re}}{2}\frac{U_\ell\, Cot\theta}{1-Z_\ell} = 0 \qquad \textbf{(3. 23)}$$

The finite difference representation of eqn (3.23) is :

$$\frac{U_{\ell i+1,j+1} + U_{\ell i,j+1} - U_{\ell i+1,j} - U_{\ell i,j}}{2\,\Delta X_{\ell i+1/2}} - \frac{\mathrm{Re}}{2}\frac{W_{\ell i+1,j+1} - W_{\ell i,j+1}}{\Delta Z_\ell} +$$

$$+ \frac{\mathrm{Re}(W_{\ell i+1,j+1} + W_{\ell i,j+1})}{2(1-Z_{\ell i+1/2})} + \frac{(U_{\ell i+1,j+1} + U_{\ell i,j+1})\,\mathrm{Re}\,Cot(j\Delta\theta)}{4(1-Z_{\ell i+1/2})} = 0 \qquad \textbf{(4. 45)}$$

Rearranging :

$$W_{\ell i,j+1}\frac{\mathrm{Re}}{2}\left(\frac{1}{1-Z_{\ell i+1/2}}-\frac{1}{\Delta Z_\ell}\right)+W_{\ell i+1,j+1}\frac{\mathrm{Re}}{2}\left(\frac{1}{(1-Z_{\ell i+1/2})}+\frac{1}{\Delta Z_\ell}\right)= \\ =-\frac{U_{\ell i+1,j+1}+U_{\ell i,j+1}-U_{\ell i+1,j}-U_{\ell i,j}}{2\Delta X_{\ell i+1/2}}-\frac{(U_{\ell i+1,j+1}+U_{\ell i,j+1})\,\mathrm{Re}\,Cot(j\Delta\theta)}{4(1-Z_{\ell i+1/2})} \qquad \textbf{(4. 46)}$$

Now, Let ;

$$A(i)=\frac{\mathrm{Re}}{2}\left(\frac{1}{1-Z_{\ell i+1/2}}-\frac{1}{\Delta Z_\ell}\right) \qquad \textbf{(4. 47)}$$

$$B(i)=\frac{\mathrm{Re}}{2}\left(\frac{1}{1-Z_{\ell i+1/2}}+\frac{1}{\Delta Z_\ell}\right) \qquad \textbf{(4. 48)}$$

$$D(i)=-\frac{U_{\ell i+1,j+1}+U_{\ell i,j+1}-U_{\ell i+1,j}-U_{\ell i,j}}{2\Delta X_{\ell i+1/2}} \\ -\frac{(U_{\ell i+1,j+1}+U_{\ell i,j+1})\,\mathrm{Re}\,Cot(j\Delta\theta)}{4(1+Z_{\ell i+1/2})} \qquad \textbf{(4. 49)}$$

For a given j, equation (4.46) can be represented as;

for i = 1 $\quad A_1 W_{\ell 1} + B_1 W_{\ell 2} = D_1 \quad (W_1 = 0,$ "Sphere Surface") **(4. 50)**

for i = 2 $\quad A_2 W_{\ell 2} + B_2 W_{\ell 3} = D_2$

for i = n-1 $\quad A_{n-1} W_{\ell n-1} + B_{n-1} W_{\ell n} = D_{n-1}$

for i = n $\quad A_n W_{\ell n} + B_n W_{\ell n+1} = D_n$

4.3.4 Finite-Difference Representation of the Energy Equation

$$\frac{\nu^*}{\mathrm{Pr}_\ell}\frac{\partial T_\ell}{\partial t}-\left(W_\ell\frac{\mathrm{Re}}{2}-\frac{2}{\mathrm{Pr}_\ell(1-Z_\ell)}\right)\frac{\partial T_\ell}{\partial Z_\ell}+U_\ell\frac{\partial T_\ell}{\partial X_\ell}=\frac{\nu^*}{\mathrm{Pr}}\frac{\partial^2 T_\ell}{\partial Z_\ell^2} \qquad \textbf{(3. 25)}$$

let ,
$$\frac{\partial T_t}{\partial Z_t} = \frac{T_{ti+1,j+1,k+1} - T_{ti-1,j+1,k+1}}{2\Delta Z_t} \tag{4. 51}$$

$$\frac{\partial^2 T_t}{\partial Z_t^2} = \frac{T_{ti+1,j+1,k+1} - 2T_{ti,j+1,k+1} + T_{ti-1,j+1,k+1}}{\Delta Z_t^2} \tag{4. 52}$$

$$\frac{\partial T_t}{\partial t} = \frac{T_{ti,j+1,k+1} - T_{ti,j+1,k}}{\Delta t} \tag{4. 53}$$

$$\frac{\partial T_t}{\partial X_t} = \frac{T_{ti,j+1,k+1} - T_{ti,j,k+1}}{\Delta X_{ti}} \tag{4. 54}$$

Substitute eqns. (4.51) - (4-54) in energy equation (3.25) to get ;

$$\frac{T_{ti,j+1,k+1} - T_{ti,j+1,k}}{\Delta t} + \left(\frac{2}{1-(i-1)\Delta Z_t} - \frac{\mathrm{Re}\,\mathrm{Pr}_t\, W_{ti,j+1}}{2\nu^*}\right)\left(\frac{T_{ti+1,j+1,k+1} - T_{ti-1,j+1,k+1}}{2\Delta Z_t}\right) + \frac{U_{ti,j+1}\,\mathrm{Pr}_t}{\nu^*\Delta X_{ti}}\left(T_{ti,j+1,k+1} - T_{ti,j,k+1}\right) = \frac{T_{ti-1,j+1,k+1} - 2T_{ti,j+1,k+1} + T_{ti+1,j+1,k+1}}{\Delta Z_t^2} \tag{4.55}$$

Rearranging;

$$T_{ti+1,j+1,k+1}\left[\left(\frac{2}{1-(i-1)\Delta Z_t} - \frac{\mathrm{Re}\,\mathrm{Pr}\, W_{ti,j+1}}{2\nu^*}\right)\frac{1}{2\Delta Z_t} - \frac{1}{\Delta Z_t^2}\right] + T_{ti-1,j+1,k+1}\left[-\left(\frac{2}{1-(i-1)\Delta Z_t} - \frac{\mathrm{Re}\,\mathrm{Pr}\, W_{ti,j+1}}{2\nu^*}\right)\frac{1}{2\Delta Z_t} - \frac{1}{\Delta Z_t^2}\right] + T_{ti,j+1,k+1}\left(\frac{1}{\Delta t} + \frac{2}{\Delta Z_t^2} + \frac{U_{ti,j+1}\,\mathrm{Pr}}{\nu^*\Delta X_{ti}}\right) = \frac{T_{ti,j+1,k}}{\Delta t} + \frac{U_{ti,j+1}\,\mathrm{Pr}_t}{\Delta X_{ti}} T_{ti,j,k+1} \tag{4. 56}$$

Now define ;

$$\mathrm{C(i)} = \left[-\left(\frac{2}{1-(i-1)\Delta Z_1} - \frac{\mathrm{Re}\,\mathrm{Pr}_t\, W_{ti,j+1}}{2\nu^*}\right)\frac{1}{2\Delta Z_t} - \frac{1}{\Delta Z_t^2}\right] \tag{4. 57}$$

$$A(i)=\left(\frac{1}{\Delta t}+\frac{2}{\Delta Z_{\ell}^{2}}+\frac{U_{\ell i,j+1}\,\mathrm{Pr}_{\ell}}{\nu^{*}\Delta X_{\ell i}}\right) \qquad \textbf{(4. 58)}$$

$$\mathrm{B(i)}=\left[\left(\frac{2}{1-(i-1)\Delta Z_{\ell}}-\frac{\mathrm{Re}\,\mathrm{Pr}_{\ell}\,W_{\ell i,j+1}}{2\nu^{*}}\right)\frac{1}{2\Delta Z_{\ell}}-\frac{1}{\Delta Z_{\ell}^{2}}\right] \qquad \textbf{(4. 59)}$$

$$D(i)=\frac{T_{\ell i,j+1,k}}{\Delta t}+\frac{U_{\ell i,j+1}\,\mathrm{Pr_l}}{\Delta X_{\ell i}}T_{\ell i,j,k} \qquad \textbf{(4. 60)}$$

Finally, the energy equation (eqn. 4.55) becomes

$$\mathrm{C(i)T_{\ell\,i\text{-}1,j+1,k+1}}+\mathrm{A(i)\,T_{\ell\,i,j+1,k+1}}+\mathrm{B(i)\,T_{\ell\,i+1,j+1,k+1}}=\mathrm{D(i)} \qquad \textbf{(4. 61)}$$

for k = 1

for i = 2 $\quad \mathrm{C(2)\,T_{\ell\,1,2,2}}+\mathrm{A(2)\,T_{\ell 2,2,2}}+\mathrm{B(2)\,T_{\ell 3,2,2}}=\mathrm{D(2)}$

$$\mathrm{A(2)\,T_{\ell 2,2,2}}+\mathrm{B(2)\,T_{\ell 3,2,2}}=\mathrm{D(2)-C(2)\,T_{\ell\,1,2,2}}=\mathrm{D'(2)}$$

for i = 3 $\quad \mathrm{C(3)\,T_{\ell 2,2,2}}+\mathrm{A(3)\,T_{\ell 3,2,2}}+\mathrm{B(3)\,T_{\ell 4,2,2}}=\mathrm{D(3)}$

for i = nn-1 $\quad \mathrm{C(nn\text{-}1)\,T_{\ell\,nn\text{-}2,,2,2}}+\mathrm{A(nn\text{-}1)\,T_{\ell nn\text{-}1,2,2}}+\mathrm{B(nn\text{-}1)\,T_{\ell nn,2,2}}=\mathrm{D(nn\text{-}1)}$

Note that ; at i = nn

$$\text{at } Z_{t}=1 \qquad \frac{\partial \mathrm{T}_{\ell}}{\partial Z_{\ell}}=0 \;\Rightarrow\; \frac{\mathrm{T}_{\ell nn,2}-\mathrm{T}_{\ell nn-1,2}}{\Delta Z_{\ell}}=0 \;\Rightarrow\; \mathrm{T}_{\ell nn,2}=\mathrm{T}_{\ell nn-1,2} \qquad \textbf{(4. 62)}$$

Therefore,

for i = nn-1, $\quad \mathrm{C(nn\text{-}1)\,T_{\ell\ nn\text{-}2,2,2}}+\mathrm{[A(nn\text{-}1)+B(nn\text{-}1)]\,T_{\ell\ n,2,2}}=\mathrm{D(nn\text{-}1)}$

$$\mathrm{C(nn\text{-}1)\,T_{\ell\ nn\text{-}2,2,2}}+\mathrm{A'(nn\text{-}1)\,T_{\ell\ nn,2,2}}=\mathrm{D(nn\text{-}1)}$$

Now we can express these equations in a matrix form as follows ;

$$\begin{bmatrix} A_2 & B_2 & & & & & & & \\ C_3 & A_3 & B_3 & & & & 0 & & \\ & C_4 & A_4 & B_4 & & & & & \\ & & \cdot & \cdot & \cdot & & & & \\ & & & \cdot & \cdot & \cdot & & & \\ & & & & \cdot & \cdot & \cdot & & \\ & & & & & \cdot & \cdot & \cdot & \\ & 0 & & & & \cdot & \cdot & \cdot & \\ & & & & & C_{nn-2} & A_{nn-2} & B_{nn-2} & \\ & & & & & & C_{nn-1} & A'_{nn-1} & \end{bmatrix} \begin{bmatrix} T_{\ell 2} \\ T_{\ell 3} \\ T_{\ell 4} \\ \cdot \\ \cdot \\ \cdot \\ \cdot \\ \cdot \\ T_{\ell nn-2} \\ T_{\ell nn-1} \end{bmatrix} = \begin{bmatrix} D'_2 \\ D_3 \\ D_4 \\ \cdot \\ \cdot \\ \cdot \\ \cdot \\ \cdot \\ D_{nn-2} \\ D_{nn-1} \end{bmatrix} \qquad \textbf{(4. 63)}$$

Thomas method can by used to solve these sets of algebraic equations corresponding to the meridional and energy equations for both phases while the continuity equation can be solved by direct back substitution. However, it should be pointed out that for the energy equation in the liquid side, the final point in the radial direction to be solved was expressed as nn instead of n as was used previously since this equation is solved along the entire domain of the sphere till it reaches the center of the sphere and the velocity components used in the equation will be the boundary layer velocity component inside the liquid boundary layer and then the Hill's vortex velocity components from the edge of the internal boundary layer up to the cent er of the sphere .

CHAPTER V

SOLUTION METHODOLOGY

5.1 Introduction

This chapter is aimed at introducing the detailed method of solution for the problem under investigation where the finite difference form of the derived governing equations is used in the programs repetitively at each node in the numerical grid to generate the solution for the specified boundary and initial conditions .

Engineering parameters such as the shear stress at the surface of the sphere, the vorticity at the surface , the angle of flow separation and the coefficient of drag were calculated during the solution and their values were reported for a wide range of independent variables such as Reynolds number and viscosity ratio . Shear stress is responsible for generating the internal motion of the liquid sphere and its values is of extreme importance for determining the internal circulation flow patterns .

The numerical scheme in the whole domain is obtained by marching in the meridional (X) direction starting from the front stagnation line where the velocity and temperature profiles are assumed to be known and the solution proceeds in this direction step by step till the point of flow separation is reached . At each meridional station,

systems of equations were solved to obtain the values of the dependent variables (velocities and/or temperature) along this line starting from the surface of the sphere up to the edge of the boundary layer which is obtained by iterating the solution until a matching condition is satisfied as will be explained later in this chapter . Upon obtaining the required profiles for the gas phase, the program that handles the liquid phase can be run using the quantities at the surface of the sphere that were obtained from the gas phase solution as boundary conditions . The solution proceeds in a similar manner until the edge of the internal boundary layer (that is also obtained iteratively) or until the core of the sphere for the temperature distribution . The solution of the liquid phase continues in the marching X-direction until the point of external flow separation is reached .

5.2 Numerical Grid

The numerical grid parameters are selected to be variable and have small values in the meridional direction especially at the points where high gradients are expected as in the case of the flow near the separation point . Along each meridional station, the grid size is assumed constant ($\Delta Z = 0.001$) where a minimum number of mesh points was given and the convergence criterion was tested at the outer point, if the convergence criterion was met, the solution proceeds to the next meridional step, otherwise the number of steps is increased by 2 and the solution is repeated along this meridional step. This process is repeated till the criterion which is presented in the next section is met .

The solution proceeds in the marching X-direction with an equal grid size (1^{o}) until the point of separation is reached then the program adjusts itself and returns one meridional step back to reduce the X-direction grid size to (0.1^{o}) in order to accurately determine the point of flow separation .

5.3 Criteria For Convergence

Two criteria are supposed to be met during the solution, the first is at each meridional step where a minimum number of grids is assumed and the velocity gradient is tested at the uppermost point against the corresponding gradient of the potential flow around a sphere. The details of this procedure are given in the following paragraph .

For the flow around the liquid sphere, a minimum number of mesh points in the Z-direction for a certain meridional step was chosen to be 20 (n = 20) . Upon calculating the meridional velocity component along this line, the tangent of the velocity at the upper most point was calculated and the slope of the velocity ($\partial U/\delta Z$) is calculated at the uppermost point (n+1) . Then the slope of the potential flow around a sphere is calculated at the same point and the two values are compared . If both slopes are matched within a certain arbitrarily specified tolerance (a value of 0.005 was chosen in the present work) the solution is supposed to be convergent and this would determine the edge of the boundary layer . Otherwise, the number of radial steps (n) is increased by two and the procedure is repeated until the matching criterion is met .

The matching criterion for the liquid phase solution is done in a similar way . However the potential flow used for comparison this time is the meridional component of Hill's vortex of reduced strength (strength is reduced because of the presence of the boundary layers and it is calculated by dividing the surface velocity obtained from the gas phase solution by that calculated for potential Hill's vortex at the surface of the sphere; this ratio represents the reduction in the Hill's vortex strength) . It is worth mentioning that the minimum number of mesh points in the Z_ℓ-direction for a certain meridional step was chosen to be 20 (similar to the gas phase solution) after which the equations for the reduced Hill's vortex velocity components are applied up to the center of the sphere and hence the fluid flow pattern will be available for the whole domain inside the sphere .

5.4 Flow Separation

External fluid particles accelerate in the region $0 \leq \theta \leq 90$ and decelerate in the region where $\theta > 90$, hence the pressure decreases in the accelerated region and then increases in the decelerated region [75] . Since the external pressure is imposed at the boundary layer, the transformation of pressure into kinetic energy takes place in the accelerated region and a great deal of the kinetic energy of the particles adjacent to the wall is consumed to move against the friction forces . In the decelerated region, the remainder of the kinetic energy is too small to keep those fluid particles moving in the

region of the high pressure, so, they would be eventually arrested and the external pressure would force them to move in the opposite direction separating from the surface of the sphere and the point of flow separation can be detected by the condition that the velocity gradient at the wall vanishes or ($\partial U/\partial Z = 0$) . Therefore the flow separation would be accompanied by a vanishing velocity gradient, a larger boundary layer thickness due to the increase of the number of radial steps required to satisfy the matching criterion at the edge of the boundary layer and a larger value of the radial velocity component because of the increasing outward direction of the flow .

The program is developed such that a constant meridional step is followed in the marching X-direction until flow separation occurs where zero or negative values unexpected values of U can be obtained . Then a finer mesh is used in X-directions (i.e for ΔX) and the point of separation is obtained .

5.5 Matching Conditions at the Surface

The boundary conditions at the surface of the sphere are applied by matching the meridional velocity of both gas and liquid phases , matching the shear stresses and matching the heat flux at the surface as well . These matching conditions were the factors utilized in uncoupling the gas and liquid phase solutions so that the gas phase solution may be solved first and thus computing the quantities at the surface of the sphere . These quantities (namely velocity and transient temperature distribution) are then used as boundary conditions for the liquid-phase solution . This uncoupling of the

solution leads to savings in computer storage and time . For example, for a given interior-to-exterior viscosity ratio, μ^*, gas phase solution would be needed only once if the internal fluid flow or heat transfer patterns are obtained for different internal to external density ratios, while the liquid phase needs not to be run at all for testing parameters for the external flow around the sphere .

Conditions used at the interface are

1. Equality of the meridional velocity component , i.e. $U = U_l$

2. Continuity of the shear stress leading to equation (3.13)

$$U_{2l} = \frac{U_2}{\mu^*} - U_1\left(\frac{1}{\mu^*} - 1\right) \qquad \textbf{(3. 13)}$$

Hence, the whole matrix solved for the gas phase is expressed in terms of the gas phase meridional velocity components and the internal-to-external viscosity ratio μ^*.

3. Continuity of the heat flux leads to a similar equation for the temperatures around the sphere ,namely, equation (3.39)

$$T_{2l} = T_2/K^* \quad - \quad T_1(1-K^*)/K^* \qquad \textbf{(3. 39)}$$

where K* is the internal to external thermal conductivity ratio . However, it should be noted that studying the effect of viscosity ratio or thermal conductivity ratio on the internal profiles encounters the solution of the gas phase first before running the liquid phase program .

5.6 Calculating Engineering Parameters

Upon computing the velocity and temperature fields (for the whole domain of numerical solution) , the engineering parameters can be calculated . The parameters of interest are, the shear stress at the surface, the vorticity at the surface, the coefficient of drag and the Nusselt number .

5.6.1 Calculating the Shear Stress at the Surface

Shear stress can be calculated as $$\tau = -\mu \left.\frac{\partial u}{\partial z}\right|_{z=0} \qquad (5.1)$$

or, in dimensionless form $$T_x = \frac{\tau \sqrt{Re/2}}{\rho U_\infty^2} \qquad (5.2)$$

Eqn. 5-2 can be written as $$T_x = \sqrt{\frac{2}{Re}} \left.\frac{\partial U}{\partial Z}\right|_{Z=0} \qquad (5.3)$$

5.6.2 Calculating the Vorticity at the Surface

Since the vorticity is equal to twice the average rate of rotation ; then for our case and in the spherical polar coordinates it can be defined as;

$$\begin{aligned} \zeta &= \frac{v_\theta}{r} + \frac{\partial v_\theta}{\partial r} - \frac{1}{r}\frac{\partial v_r}{\partial \theta} \\ &= \frac{u}{r} + \frac{\partial u}{\partial r} - \frac{1}{r}\frac{\partial w}{\partial \theta} \end{aligned} \qquad (5.4)$$

Using the non-dimensionalizing parameters introduced in Chapter II, we get

$$\zeta' = \frac{\zeta}{(U_\infty / a)} = \frac{U}{1+Z} + \frac{\partial U}{\partial Z} - \frac{2}{Re}\frac{\partial W}{\partial X} \qquad (5.5)$$

Now, using finite-differences for the derivatives, we get :

$$\zeta' = \frac{U_{i,j+1}}{1+(i-1)Z} + \frac{-U_{3,j+1}+4U_{2,j+1}-3U_{1,j+1}}{2\Delta Z} - \frac{2}{Re}\frac{W_{i,j+1}-W_{i,j}}{\Delta X_i} \qquad (5.6)$$

5.6.3 Calculating the Coefficient of Drag

$$C_D = 4\int_0^{\theta_s} \left.\frac{\partial U}{\partial Z}\right|_0 R\,\mathrm{Sin}\theta\; d\theta \qquad (5.7)$$

5.6.4 Calculating Nusselt Number

$$Nu = \frac{2ah}{K} \qquad (5.8)$$

or,
$$Nu = -2\left.\frac{\partial T}{\partial Z}\right|_0 \qquad (5.9)$$

5.6.5 Calculating the Coefficient of Friction

$$C_f = \frac{\tau_o}{\frac{1}{2}\rho U_\infty^2} \qquad (5\text{-}10)$$

or,
$$C_f = \frac{T_x}{\sqrt{Re/8}} \qquad (5\text{-}11)$$

5.7 Solution Procedure

The governing finite-difference equations obtained in Chapter IV to solve the problem under investigation are governed by some controlling parameters, namely, Reynolds number, viscosity ratio, density ratio and Prandtl number . These controlling parameters should be fixed each time the programs are run . The solution starts by selecting appropriate values for these parameters and then proceeds as follows ;

5.7.1 Gas Phase Solution

1. The program starts in the marching X-direction; the variables at the first meridional station (j=1, i.e. at the front stagnation line) are known where boundary-layer thickness is assumed zero . Hence U,W, and T are known and specified at this first station (U = 0, T= 1, and W is obtained from the potential flow distribution) . So the program starts to obtain solutions at the line j=2 assuming a number of radial grid points of 20 .
2. Finite-difference equations arranged in a form of a matrix for U values are solved first, then followed by solving the continuity equation to get W values .
3. The matching criterion at the uppermost point is checked . If the criterion is not met, the number n is increased by 2 and the solution is repeated again .
4. Steps 2 and 3 are repeated till the convergence criterion is met . Then the energy equation matrix is solved and the temperature distribution along this line (X = constant) is obtained.
5. The obtained values are reported and prepared to be the initial values for the next meridional step .
6. The solution then proceeds in the marching X-direction repeating the same previous steps (2 through 5) until the separation point is reached where finer mesh is used (smaller increments in the X-direction), and the angle of separation is estimated as explained previously .

7. Engineering parameters like drag coefficient and local Nusselt number are calculated .
8. The whole process is repeated for the next time step until the state of uniform surface temperature is reached which is characterized by the condition that the average surface temperature approaches the free stream temperature within a specified tolerance .
9. The liquid phase solution then continues until the temperature of the sphere's center reaches the free stream temperature and this will be the final steady state condition .

5.7.2 Liquid Phase Solution

First, it should be pointed out that the surface velocity distribution as well as the surface temperature along the time period till the uniform surface temperature is reached are reported and written from the gas-phase solution in data files that can be logged into the liquid-phase program as boundary conditions . The liquid-phase program works in a similar manner as the gas-phase program . However, the solution of the flow field starts at (n_t=20) until the boundary-layer edge where the matching criterion between boundary layer flow and reduced Hill's vortex flow is met . Then the domain of flow solution is extended by calculating Hill's vortex velocity components up to the center of the sphere to provide the required values of the velocity to be used in solving the energy equation . Solution of the energy equation is extended till the center of the sphere where the temperature gradient is essentially zero (because of the axisymmetric nature of the

problem) . The solution marches in the meridional (X-) direction until the point of external flow separation is reached and in time until the required criterion pertinent to sphere core heating is encountered . This means that although the surface temperature approaches the free stream temperature, the liquid phase heating continues until the core is heated .

CHAPTER VI

HYDRODYNAMIC RESULTS AND DISCUSSION

6.1 Introduction

In this chapter, the results of solving the governing momentum and continuity equations are presented for both around and inside the liquid sphere . First, the velocity profiles , shear stress and vorticity around the sphere are presented . These clarify the effect of the controlling parameters such as Reynolds number and viscosity ratio on the flow field and the angle of flow separation . Then velocity profiles inside the sphere are presented considering the effect of the aforesaid controlling parameters plus the ratio of the densities between the liquid and gas phases . Results of solving the energy equation are reported afterwards in Chapter VII highlighting the effect of the former parameters (Reynolds number and the interior-to-exterior viscosity ratio) and Prandtl number on the temperature distribution around the sphere as well as the local Nusselt number . Comparisons between the present study with some data reported in the literature are carried out for the sake of validation of the present results .

6.2 Results of Velocity Profiles Around the Sphere

6.2.1 Meridional Velocity Profiles :

External flow about a liquid sphere is mainly controlled by the free stream Reynolds number and the viscosity ratio between the gas and liquid phases . The main purpose of this work is to investigate the effect of each of them on the flow characteristics including velocity profiles (meridional as well as radial velocity components), surface velocity distribution, separation angle and on some engineering parameters such as the shear stress at the surface of the sphere (which motivates the internal motion inside the sphere) and the vorticity at the surface .

A wide range of Reynolds number is considered in this work ranging from values that may be as small as a few hundreds to as high as 10000 in magnitude . The range investigated for the viscosity ratio is between unity and 100 . This range proved to be enough to approach the case of a flow over a solid sphere .

Figure 6.1 shows the meridional velocity profiles along the radial distance (Z) starting with a certain value at the surface of the sphere (Z=0) till it matches the free stream velocity components thus representing the edge of the boundary layer surrounding the sphere . These profiles are plotted at four meridional stations (angles) measured from the front stagnation point namely at 30,60,90 and 105 degrees where the last one was very close to the point where the separation occurs . The figure also shows the increase in the boundary layer thickness as we move further on the sphere surface in

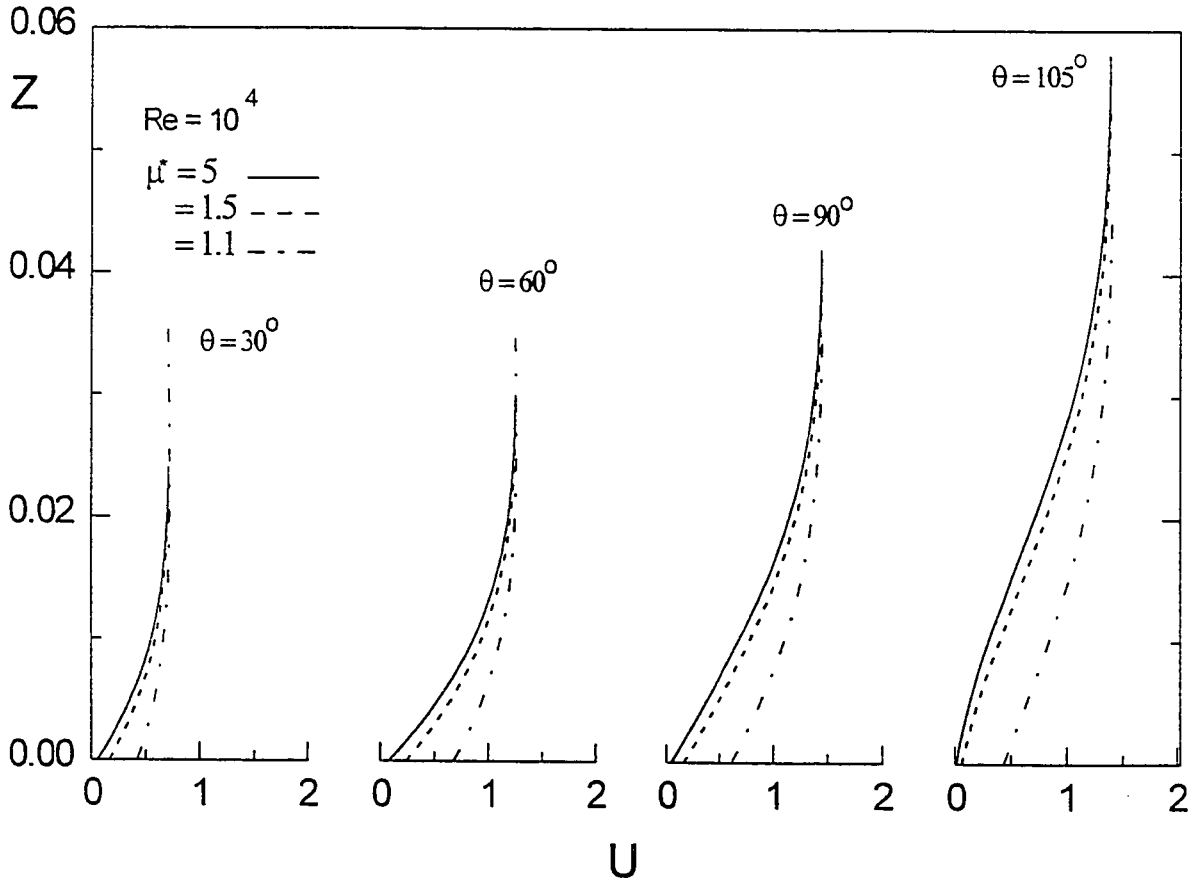

Fig. 6-1 : Meridional velocity profiles versus radial distance at different viscosity ratios for different meridional locations

the meridional direction illustrating the boundary layer development near to the point of separation where maximum boundary layer thickness is encountered .

As can be seen from this figure, these profiles are greatly influenced by the viscosity ratio . For a given θ, each of these profiles has its own value of the surface velocity U_o but all profiles asymptotically approach the potential flow at large Z (far away from the surface) . It is also clear that higher surface velocities correspond to lower viscosity ratios and the extreme case of zero surface velocity is corresponding to infinite viscosity ratio (the case of flow about a solid sphere) . However, it should be pointed out that in the case of a flow about a solid sphere, the surface velocity is imposed on the solution as a boundary condition (U_o=0), while for the case considered in the current work it is treated as a variable and calculated from the solution .

For a given value of the viscosity ratio ($\mu^* = 5$), Fig. 6-2 shows the meridional velocity profiles at a fixed angle ($\theta = 60^o$) for different values of Reynolds number ranging from 200 to 10000 . This figure clarifies effect of Reynolds number on the boundary-layer thickness; the higher the value of Reynolds number, the thinner the boundary layer . This is attributed to the high velocity gradient at higher Reynolds numbers requiring less boundary layer (less distance) for the velocity to drop from its free stream value at the edge of the boundary layer to its value at the surface of the sphere . It is also worth mentioning that as Reynolds number increases, the rate of

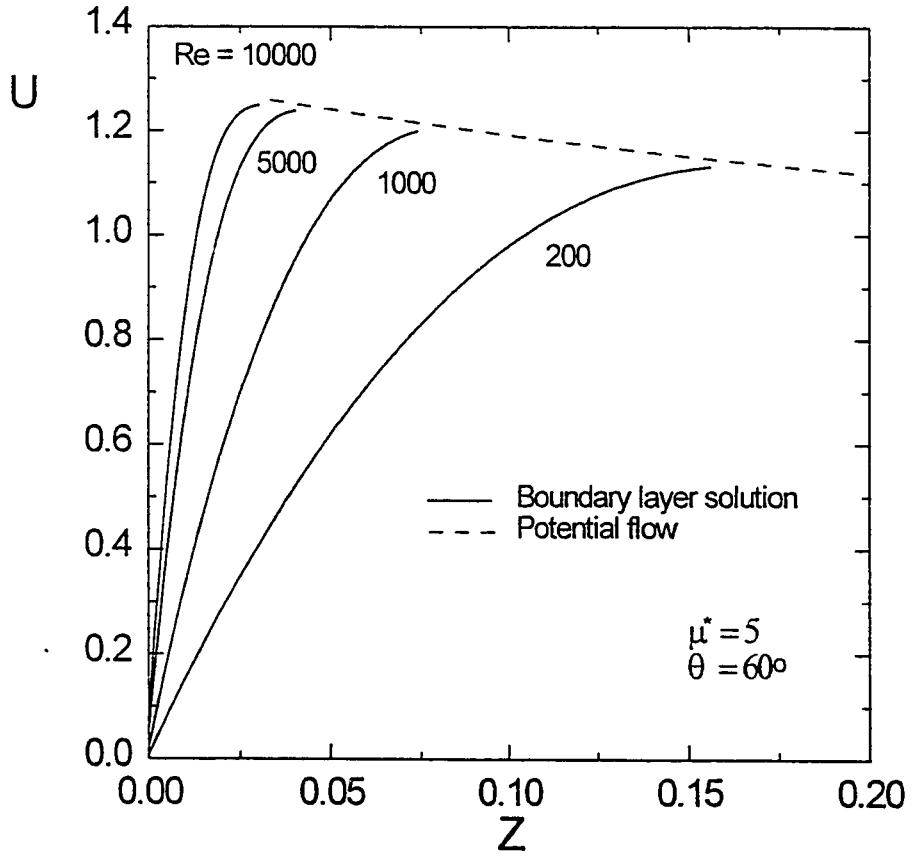

Fig. 6-2 : Effect of changing Reynolds number on meridional velocity profiles

transfer of momentum increases too leading to higher velocity gradients and hence less boundary layer thickness.

Figures 6-3a and 6-3b illustrate the effect of viscosity ratio on the meridional velocity profiles in the boundary layer at a fixed meridional station ($\theta = 60^{o}$) and at two given values of Reynolds number (Re=1000 and 10000 respectively) . The range of viscosity ratio shown in each figure is from 1.01 to 2 and the effect on the surface velocity (at Z = 0) is clear; the higher the viscosity ratio (i.e. more viscous liquid sphere) , the lower the surface velocity . The case of flow about a solid sphere (previously investigated by El-Shaarawi et al. [10]) at the same value of Reynolds number ($Re = 10^{4}$) is plotted in Fig. 6-3b for the sake of comparison and validation of the present analysis . It is clear that increasing the viscosity ratio leads finally to that case of a flow about a solid sphere . Thus, this latter case can be a special case of the present study by using a very high value of the viscosity ratio. It was found that increasing the viscosity ratio more than a certain value ($\mu^{*} >100$) leads to insignificant changes in meridional velocity profiles which almost coincide with the corresponding profiles of [10] , this provided a check on the adequacy of the present model and the computer code .

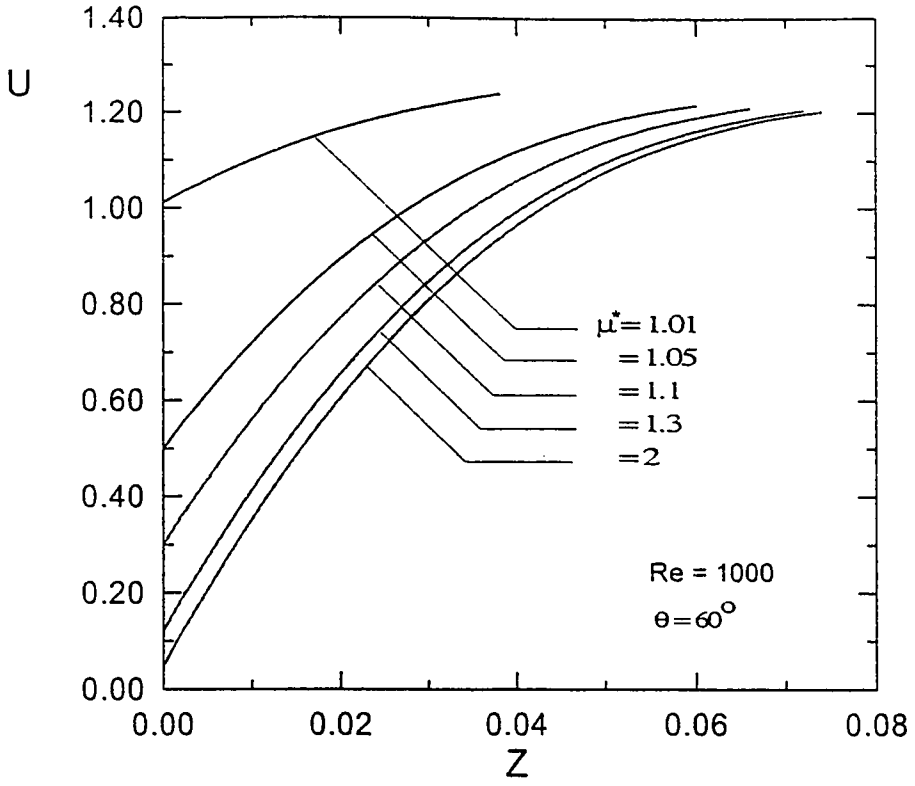

Fig. 6-3a : Meridional velocity distribution for different viscosity ratios, Re = 1000

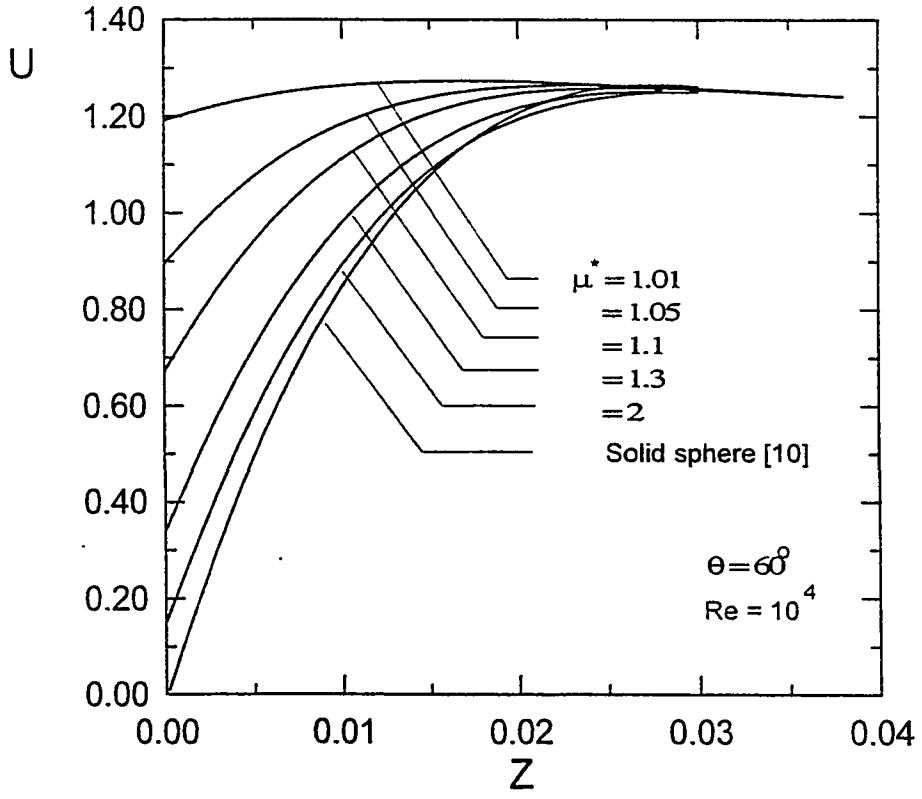

Fig. 6-3b : Meridional velocity distribution for different viscosity ratios compared to solid sphere case of reference [10]

The velocity distribution on the sphere surface up to the point of separation is shown in Figs. 6-4a and 6-4b which are plotted at two different viscosity ratios ($\mu^* = 2$ and 5, respectively) and for various values of Reynolds number . It is clear from the figure that the values of the surface velocity are increasing from their initial zero value at the front stagnation point reaching a maximum at about ($\theta = 60^o$) and then decreasing till they reach the minimum (almost zero) value at the point where the flow separates and the boundary-layer solution is not valid anymore . It can also be shown from the figure that increasing Reynolds number increases the surface velocity due to increasing the free stream velocity ($Re = 2\ U_\infty\ a\ /\nu$).

The effect of viscosity ratio on the surface velocity distribution along the meridional direction at a fixed value of Reynolds number (Re = 10000) is illustrated in Figs. 6-5a and 6-5b . Figure 6-5b shows such a variation for values of viscosity ratio representing its high range (namely $\mu^* = 1.5,2$ and 5) while Fig. 6-5a is limited to low values of μ^* (1.05 and 1.1) . It is clear that increasing the viscosity ratio (i.e. using more viscous liquid spheres) leads to the decrease in the surface velocity and in the extreme case of very large value of viscosity ratio zero values of the surface velocity are expected . Figures 6-6a and 6-6b also present the same trend at another value of Reybolds number (Re = 1000) and it would be pointed out that these latter figures show less values of the surface velocity for each viscosity ratio when compared to the former case of $Re = 10^4$.

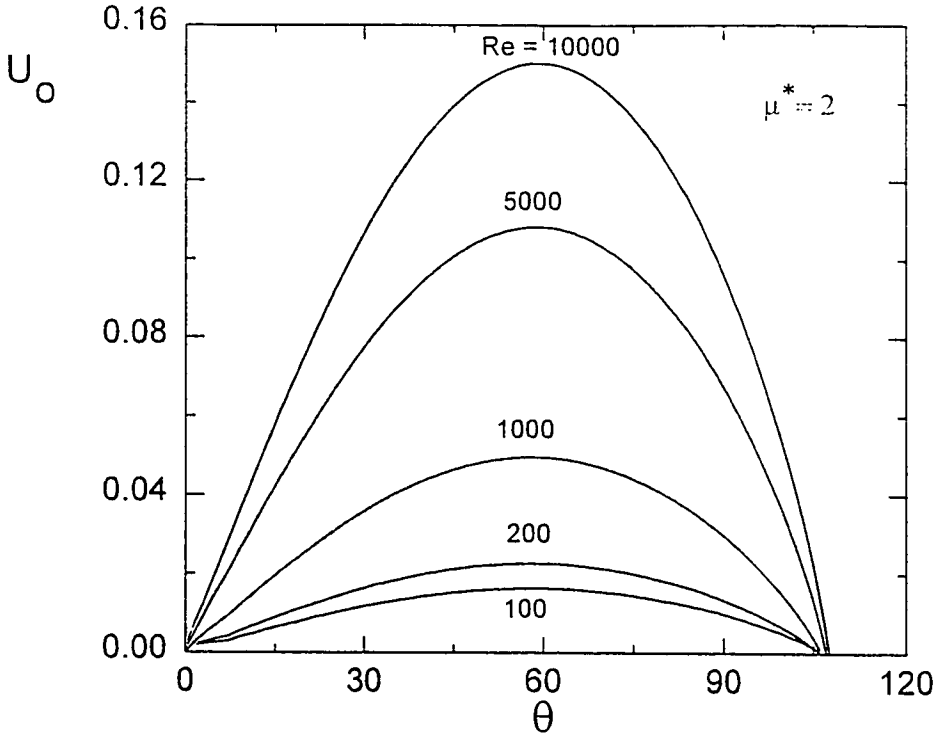

Fig. 6-4a : Effect of Reynolds number on the surface velocity versus the angle , $\mu^* = 2$

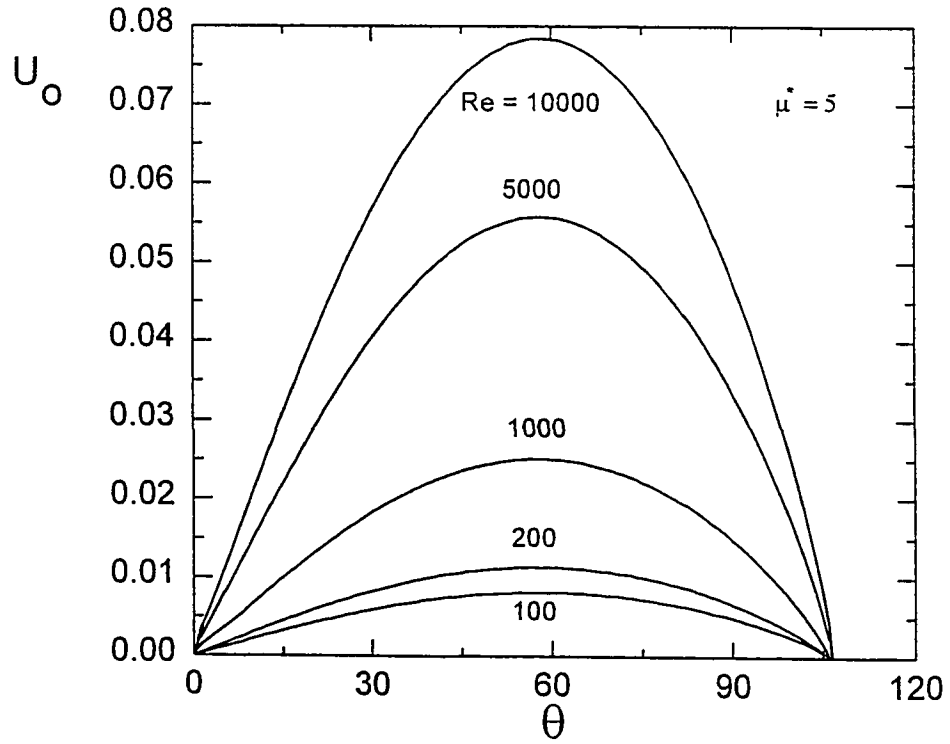

Fig. 6-4b : Effect of Reynolds number on the surface velocity versus the angle , $\mu^* = 5$

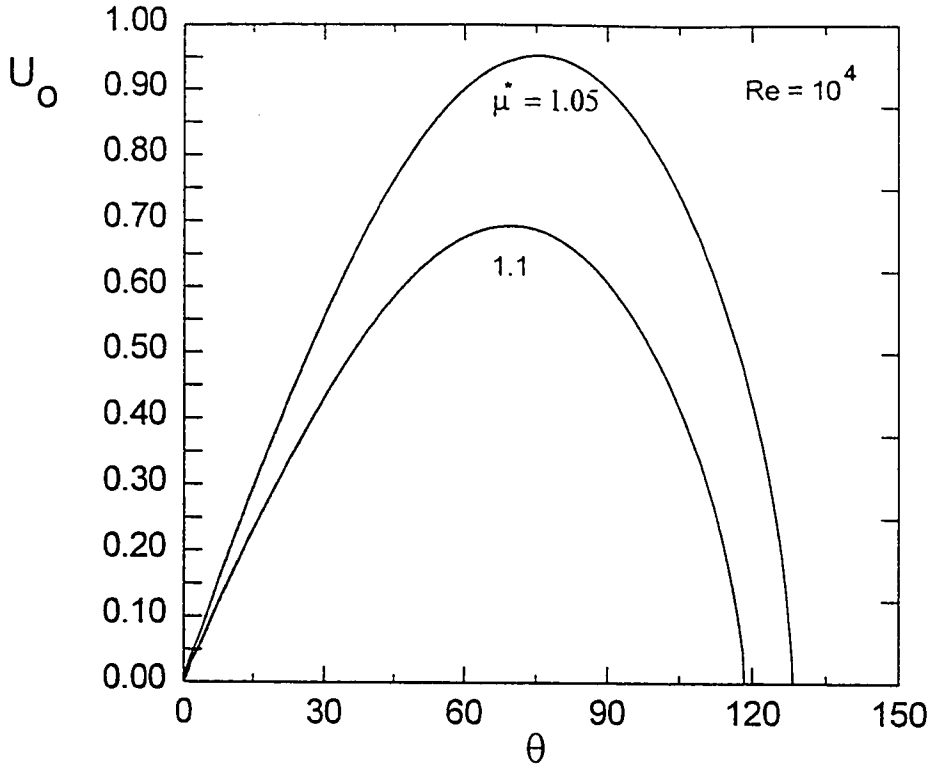

Fig. 6-5a : Effect of velocity ratio on surface velocity versus angle, ($\mu^* = 1.05$ and 1.1)

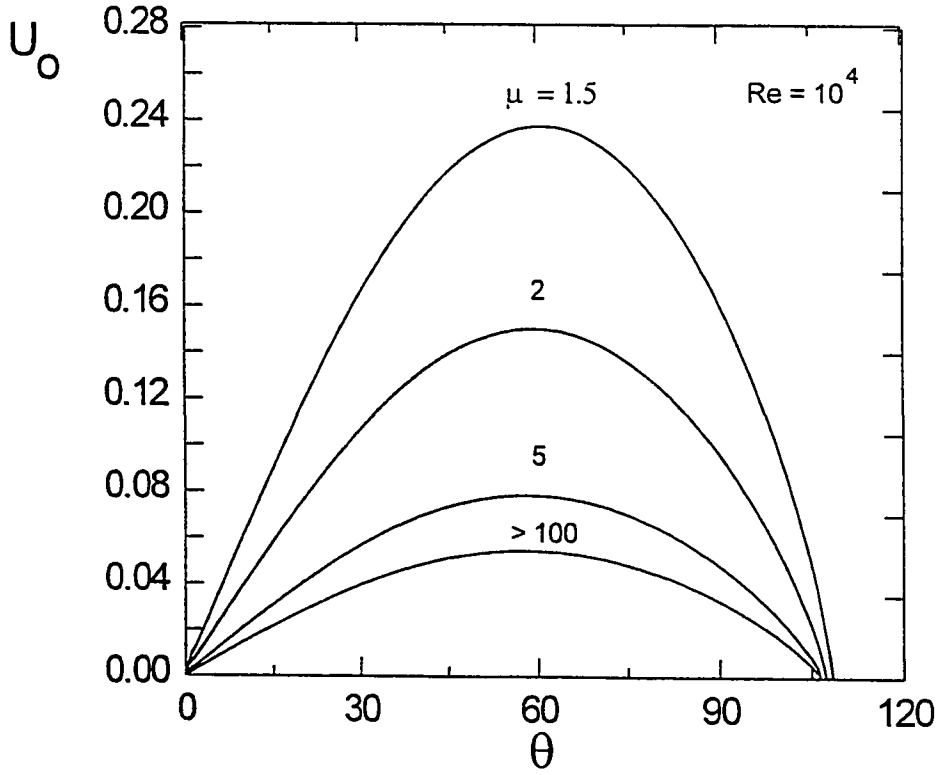

Fig. 6-5b : Effect of velocity ratio on surface velocity versus angle, $\mu^* = 1.5,2,5$ and 100

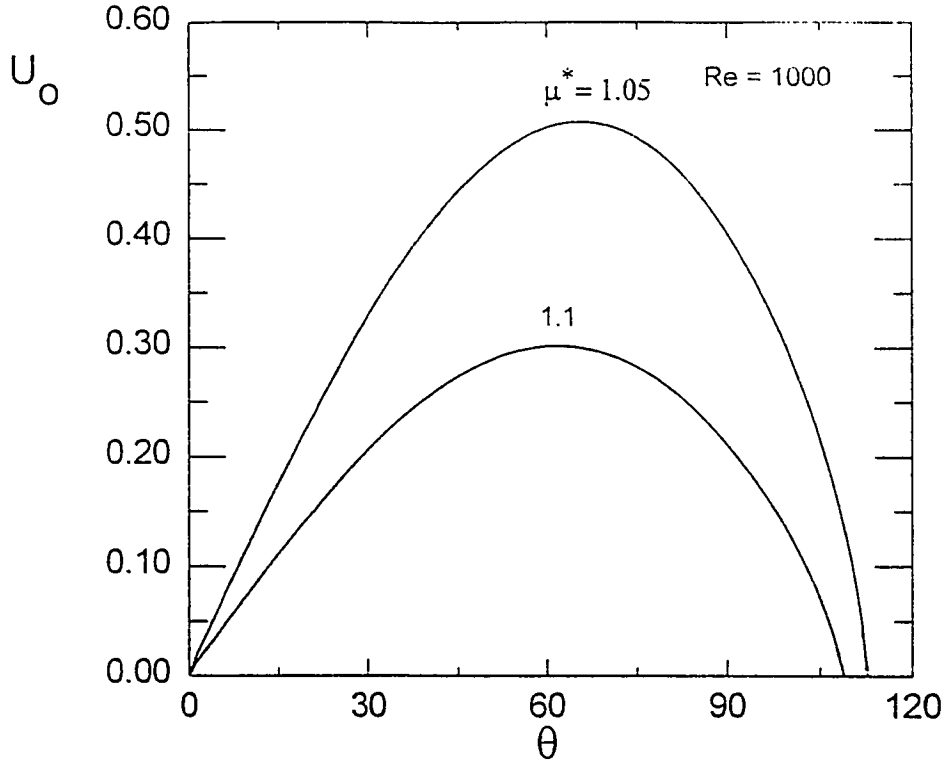

Fig. 6-6a : Effect of viscosity ratio on surface velocity versus angle for Re = 1000, μ^* = 1.05 and 1.5

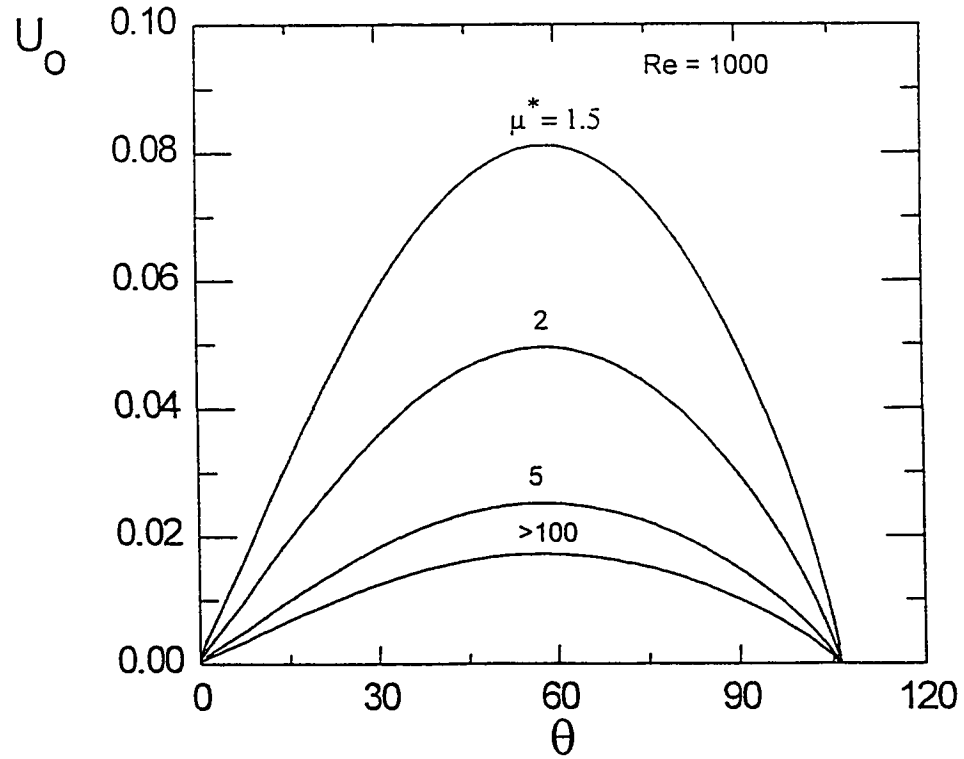

Fig. 6-6b : Effect of viscosity ratio on surface velocity versus angle for Re = 1000, μ^* = 1.5,2,5 and 100

Maximum surface velocity for different values of viscosity ratio over a wide range of Reynolds number is plotted in Fig. 6-7 where the effect of increasing the velocity at the surface of the sphere for a given μ^* due to increasing the free stream Reynolds number is clear . Meanwhile, the effect of increasing the viscosity ratio on reducing the surface velocity, for a given Re, is clear for a wide range of viscosity ratios (ranging between 1.01 and 100) .

Figure 6-8 is a cross plot of Fig. 6-7 where the effect of viscosity ratio on the surface velocity is illustrated for three values of Reynolds number (100,1000, and 10000) . For a range of viscosity ratio from 1 to 10, this figure can be used to obtain the maximum surface velocity for any given value of μ^* .

Figure 6-9 shows the effect of both viscosity ratio (μ^*) and Reynolds number (Re) on the angle of separation . For a given μ^*, increasing the Reynolds number has the effect of delaying the separation angle (retarding the flow separation) due to thinning the boundary layer . On the other hand, for a given Re, lower values of viscosity ratio lead to higher surface velocities and hence higher sphere rotation in the meridional direction and hence higher angle at which the flow separates and vice versa . In the limiting case of a very high viscosity, the separation angle approaches the corresponding value for the flow about a solid sphere .

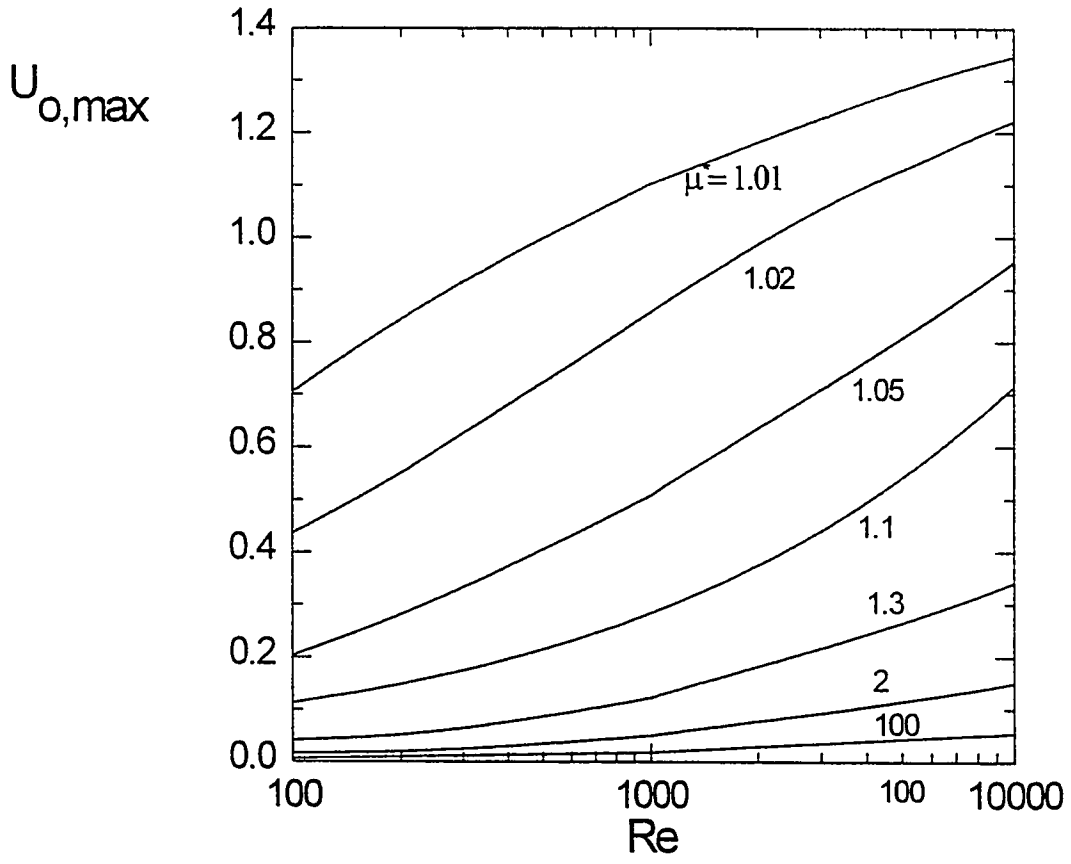

Fig. 6-7 : Maximum surface velocity versus Reynolds number for different values of viscosity ratio

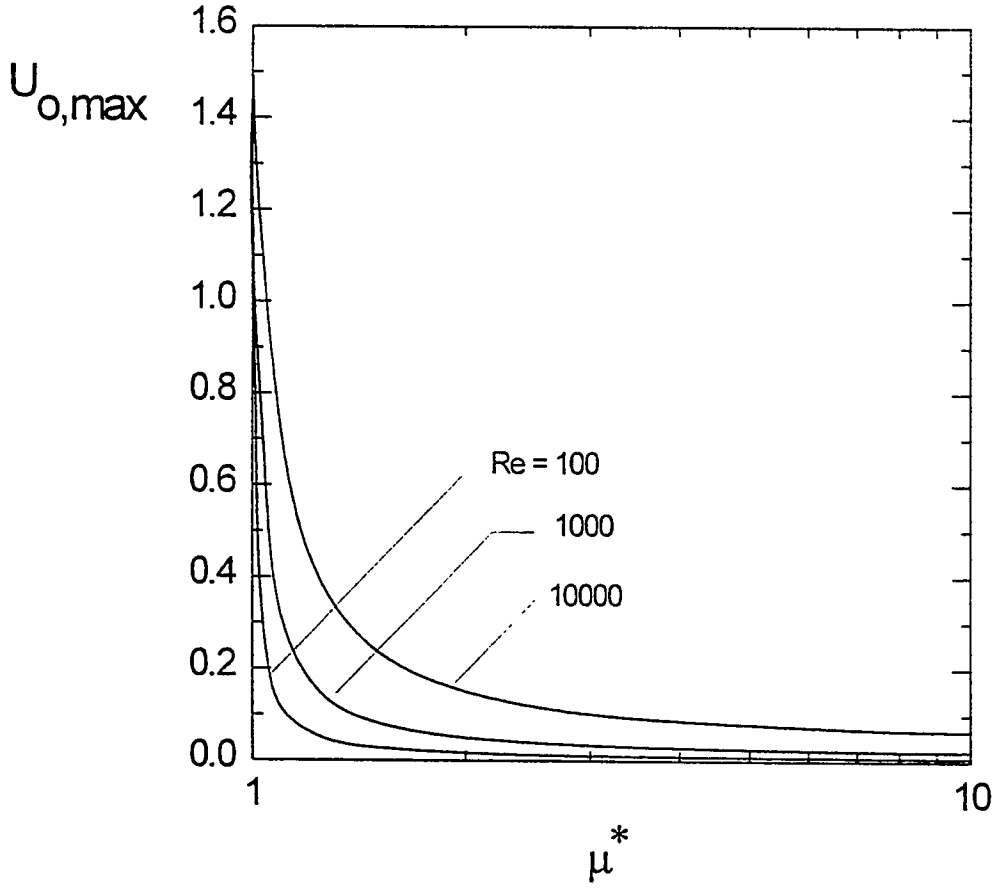

Fig. 6-8 : Variation of maximum surface velocity with viscosity ratio at different values of Reynolds number

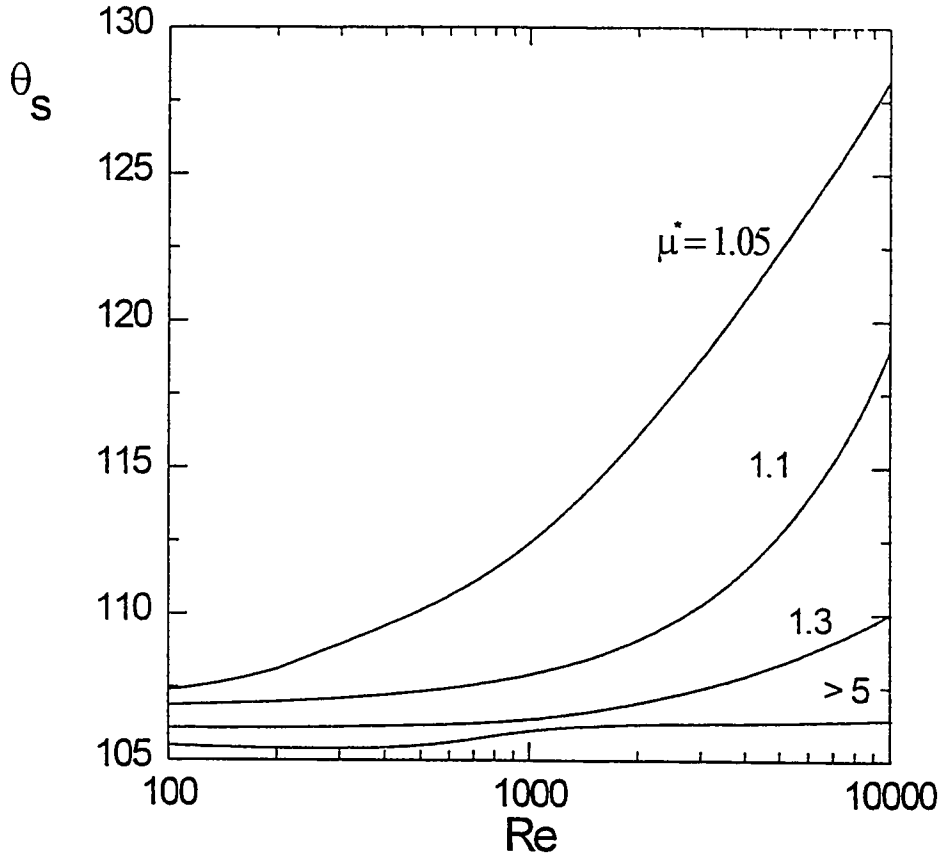

Fig. 6-9 : Effect of viscosity ratio on the variation of the angle of separation with Reynolds number

The present θ_s-results have been found to approach the corresponding solid sphere results at considerably large viscosity ratios; this finding provided a check on the adequacy of the present code . For example, for Re = 10^4, separation angle for solid sphere is 107 [10] while corresponding θ_s for μ^*=100 is 106.4°, i.e. the difference is only 0.56% .

6.2.2 Radial Velocity Profiles :

Figures 6-10, 6-11a and 6-11b present the developing radial velocity component, W, corresponding to selected values of the controlling parameters (namely Reynolds number and viscosity ratio) . In Fig. 6-10, the radial velocity profiles are plotted at the selected meridional stations (angles) θ = 30,60,90 and 105° for a given value of Reynolds number (Re = 10000) and two values of viscosity ratio (μ^* = 1.05 and 2) . It is clear that all these profiles start with a zero value at the surface of the sphere (no fluid is crossing the boundaries, i.e., no suction or blowing) . However they end at different values of the radial coordidate (Z) where the numerical solution was terminated when the solution criterion was satisfied . Profiles are negative for meridional angle < 90° while they have positive values for θ > 90° . This behaviour shows that the radial component of velocity is pushing the boundary-layer fluid towards the sphere's surface in the accelerated region of the flow . Compared with the W-profiles in the adverse region (θ> 90°) where the tendency changes to suction of the fluid, the radial component of velocity assist increasing the boundary-layer thickness till the maximum thickness is reached at the point where the flow separates . As can be seen from Fig. 6-10, increasing

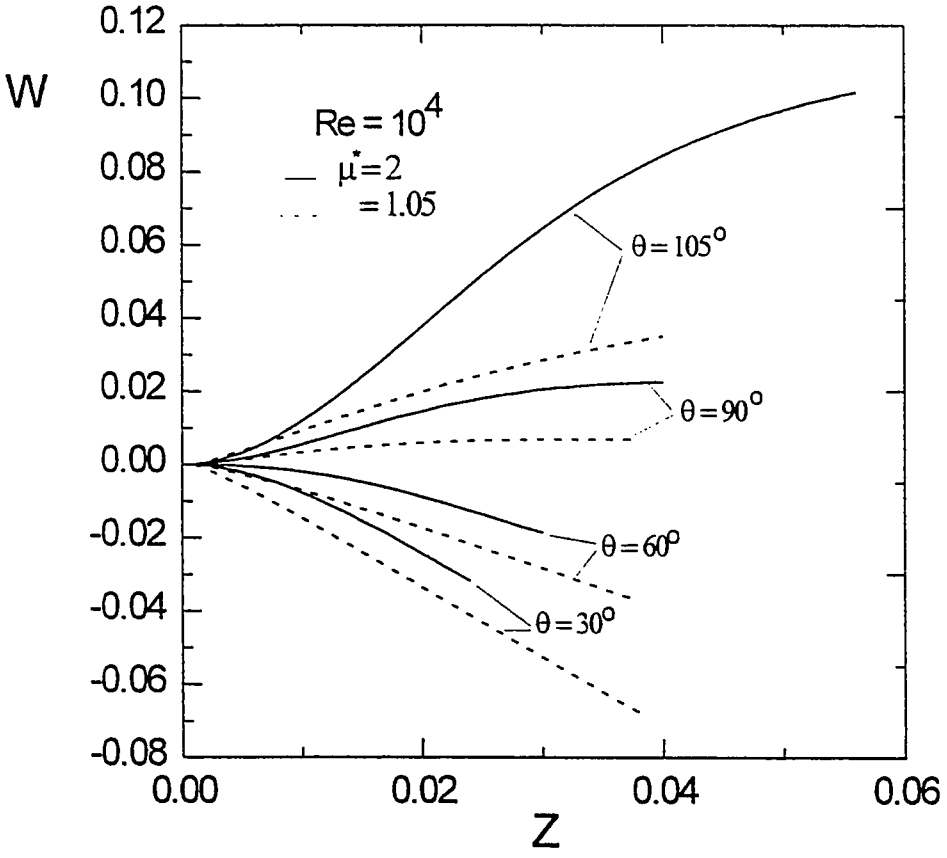

Fig. 6-10 : Radial velocity distribution at different meridional locations

the viscosity ratio (from 1.05 to 2) decreases the boundary-layer thickness in the accelerating region and increases its thickness in the adverse region (increasing the sucking effect) . This process results in an earlier point of flow separation (this is compatible with the previously reported result that the higher the value of viscosity ratio, the earlier the separation of the flow) .

For a given viscosity ratio ($\mu^* = 2$), Figs 6-11a and 6-11b illustrate the effect of Reynolds number on the radial velocity profiles at two selected angles ($\theta = 60^\circ$ in Fig. 6-11a and $\theta = 90^\circ$ in Fig. 6-11b) . Increasing the Reynolds number always has the effect of decreasing the boundary layer-thickness (as previously illustrated) in the accelerating region and hence delaying the point of flow separation while the boundary layer thickness increases the adverse region as discussed in the previous paragraph .

6.2.3 Results of Engineering Parameters :

Fig. 6.12a shows the distribution of the shear stress at the surface of the sphere for two selected values of Reynolds numbers (Re = 200 and Re = 10000) and for two values of the viscosity ratios ($\mu^* = 1.05$ and 2) . The behavior of the shear stress generally starts from a zero value at the front stagnation point arising from the meridional velocity gradient at this point and then increasing till it reaches a peak value at a meridional angle of about 60° then it drops again till it reaches zero at the corresponding

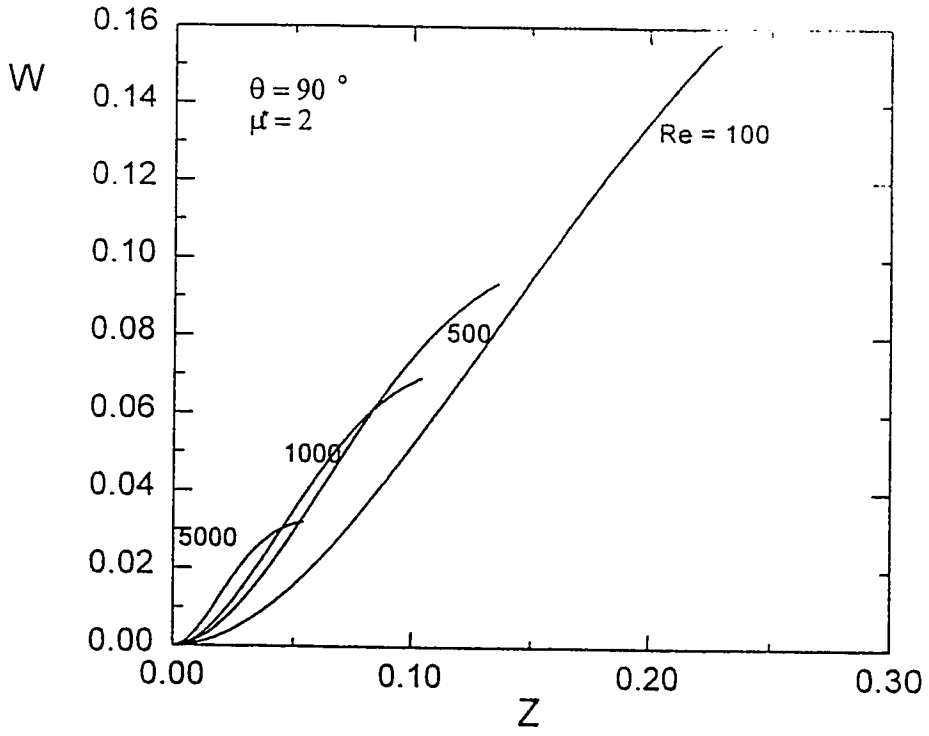

Fig. 6-11a : Effect of Reynolds number on radial velocity profiles, $\theta = 90^{o}$

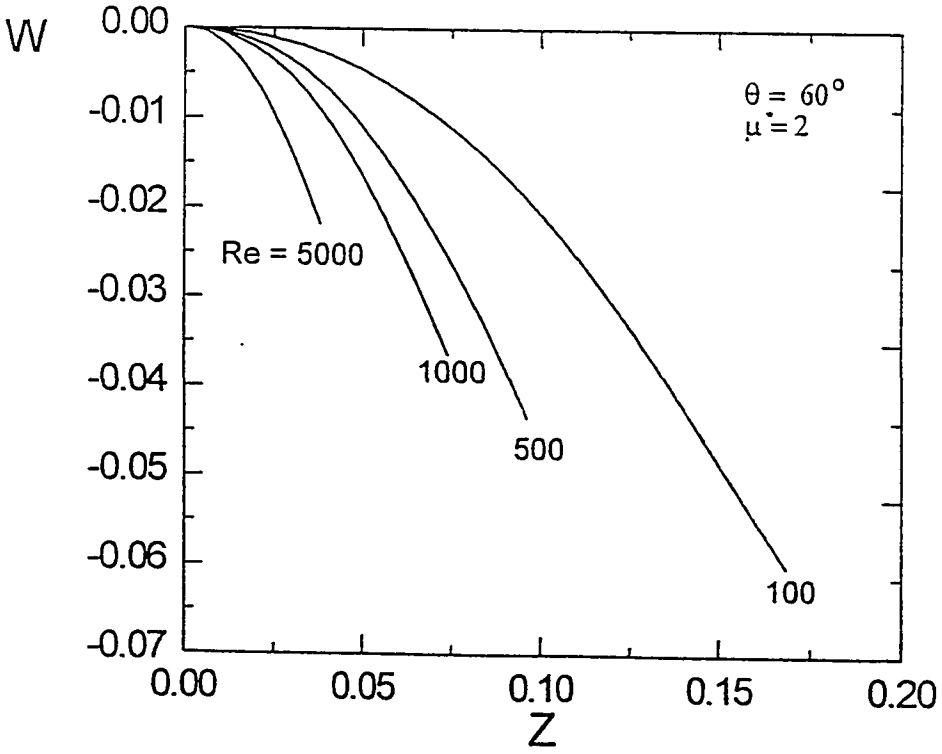

Fig. 6-11b : Effect of Reynolds number on radial velocity profiles, $\theta = 60^{o}$

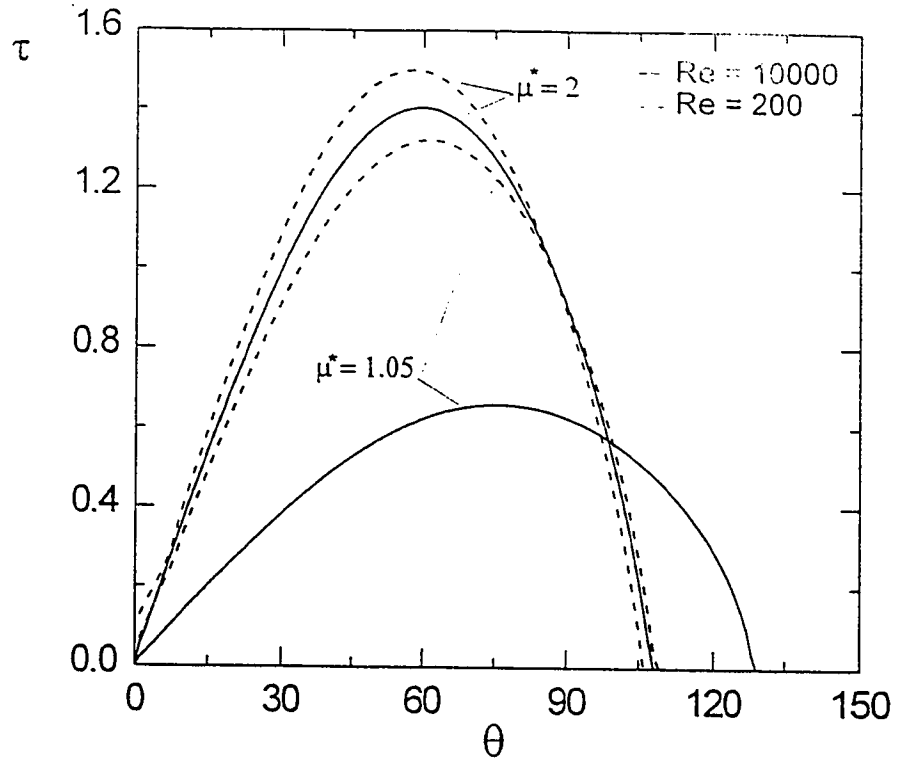

Fig. 6-12a : Effect of Reynolds number on the interface shear stress at a given value of viscosity ratio

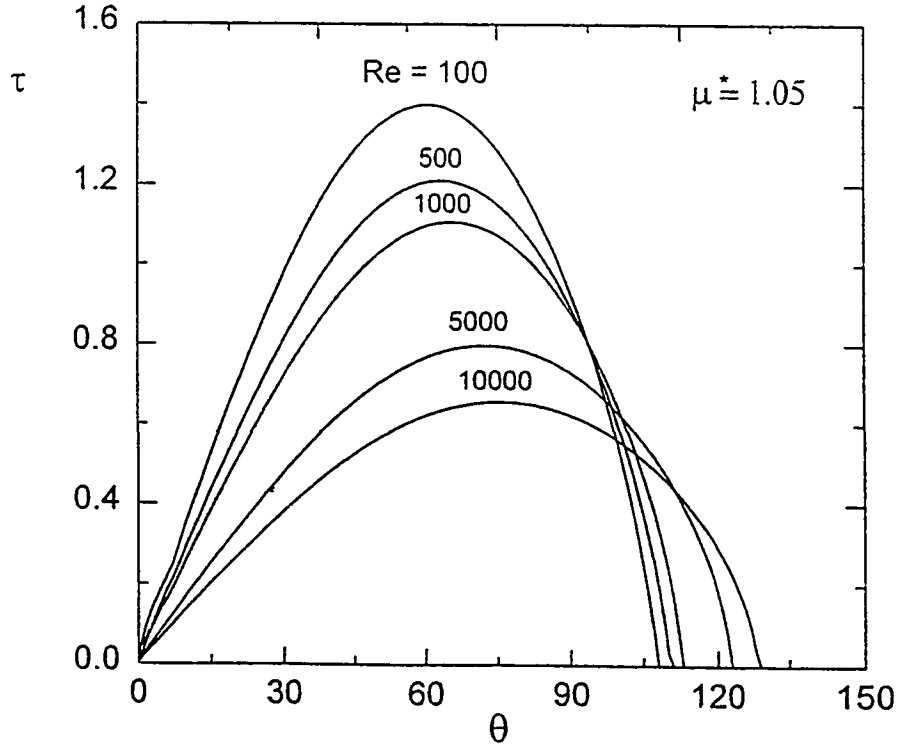

Fig. 6-12 b : Effect of Reynolds number on the interface shear stress for a given viscosity ratio

separation point . The effect of the viscosity ratio on the shear stress is illustrated in this figure where the values corresponding to higher viscosity ratio are higher than those for small values of viscosity ratio because of higher velocity gradients encountered with more viscous fluids . Figure 6-12b presents the shear stress profiles for several values of Reynolds number and clarifies the effect of increasing Re on the reduction of the shear stress values .

For a given value of Reynolds number (Re=10000), the effect of the viscosity ratio on the shear stress distribution is more clearly illustrated in Fig. 6-13 for different values of viscosity ratio (1.05, 1.1, 1.5 and 2) ; the increase in shear stress values with viscosity ratio (using more viscous liquid spheres) is obvious . The shear stress distribution for the extreme case of flow over a solid sphere (previously investigated by El-Shaarawi et. al [10]) is also presented for the sake of comparison and validation of the present results and it is clear that the shear stress values for this case are the maximum since the viscosity ratio is infinitely high .

Figure 6-14 shows the distribution of the vorticity at the surface of the sphere along the meridional direction for different values of the Reynolds number where it is clear that increasing the Reynolds number results in an increase in the surface vorticity due to increasing the rotation of the fluid particles near the sphere surface . A comparison between the surface vorticity of the current investigation at a Reynolds

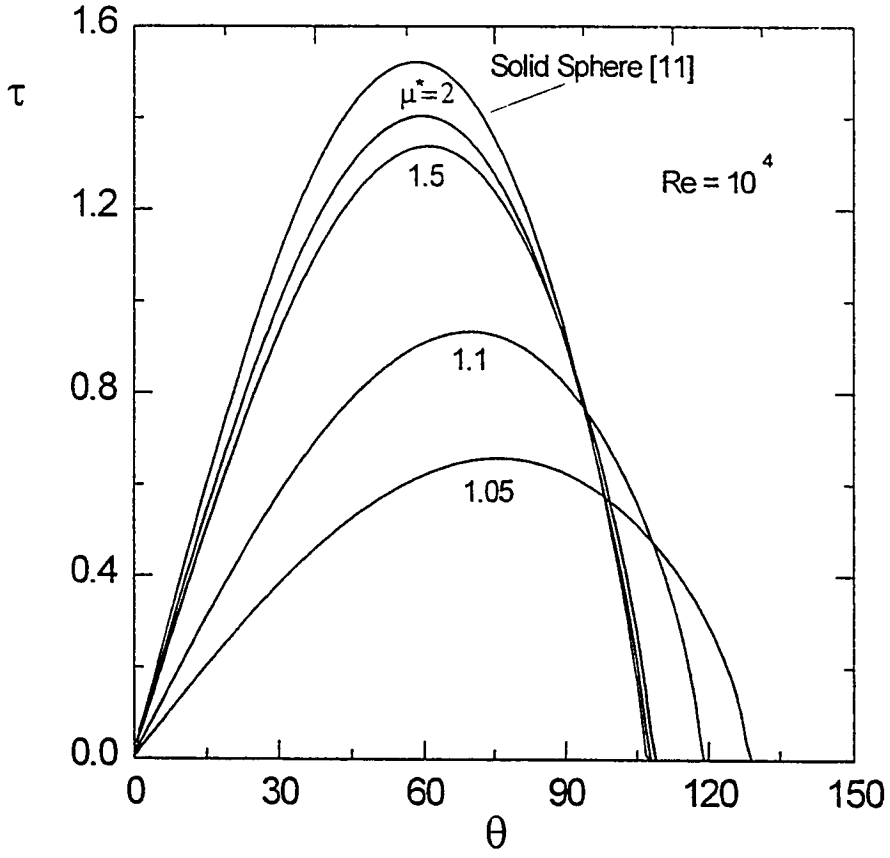

Fig. 6-13 : Effect of viscosity ratio on the wall shear stress at a fixed Reynolds number

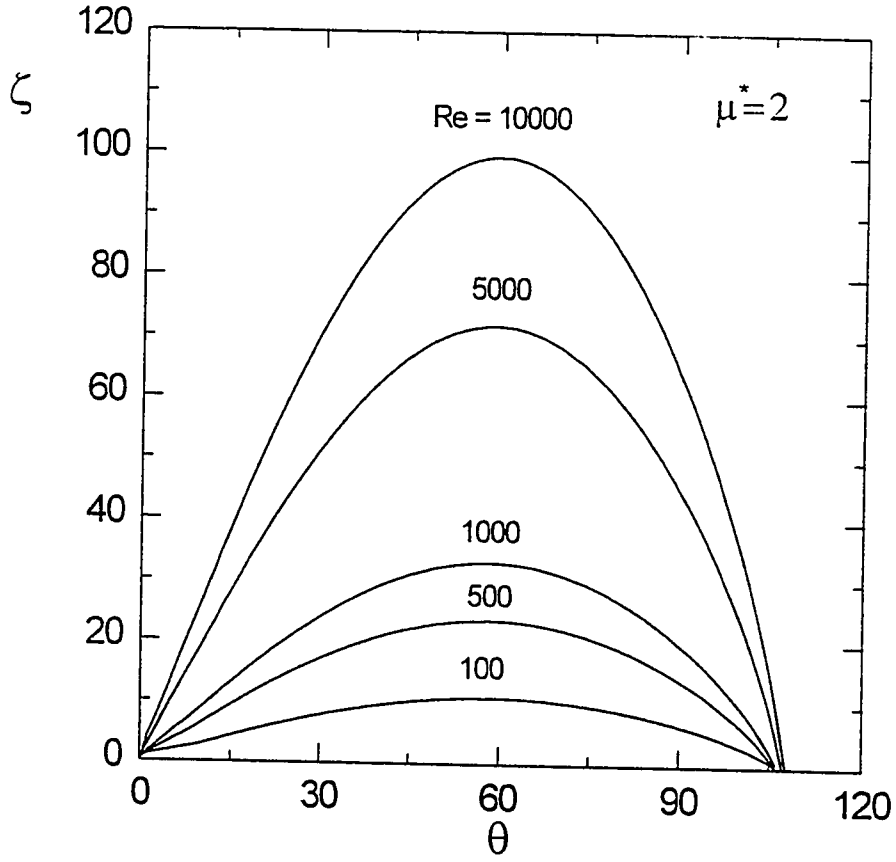

Fig. 6-14 : Surface vorticity distribution versus angle for different values of Reynolds number

number of 100 and the boundary layer analysis by Hamielec et al. [1] is shown in Fig. 6-15 where the close agreement between the two results is shown in the figure .

Knowing the shear stress at the interface, the dimensionless drag coefficient has been computed and is given as a function of the viscosity ratio μ^* and Reynolds number Re in Table 6-1 . As might be expected, the value of C_D increases with μ^* and decreases with Re . It is also worthy of note that the value of C_D at $\mu^* = 100$ and $Re = 10^4$ differs by only some 3% than that of a solid sphere ($\mu^* = \infty$) for the same value of $Re=10^4$; the latter was given by El-Shaarawi et al. [10] to be 0.06716 .

Figure 6-16 shows the effect of Reynolds number on the coefficient of friction around the sphere for a given viscosity ratio $\mu^* = 1.5$ and for five selected values of Reynolds number (Re = 100, 500, 1000, 5000 and 10000) . It is clear from the figure that higher Reynolds numbers result in higher velocities in the boundary layer and higher surface velocity and hence lower values of the coefficient of shear stress .

Figure 6-17 shows the effect of viscosity ratio on the coefficient of friction for a given value of Reynolds number Re = 1000 and for four selected values of viscosity ratio ($\mu^* = 1.01, 1.05, 1.5$ and 5) . The figure indicates that higher viscosity ratios are corresponding to higher values of C_f since the friction factor is proportional to the shear stress and hence it is proportional to the viscosity ratio for a given velocity gradient .

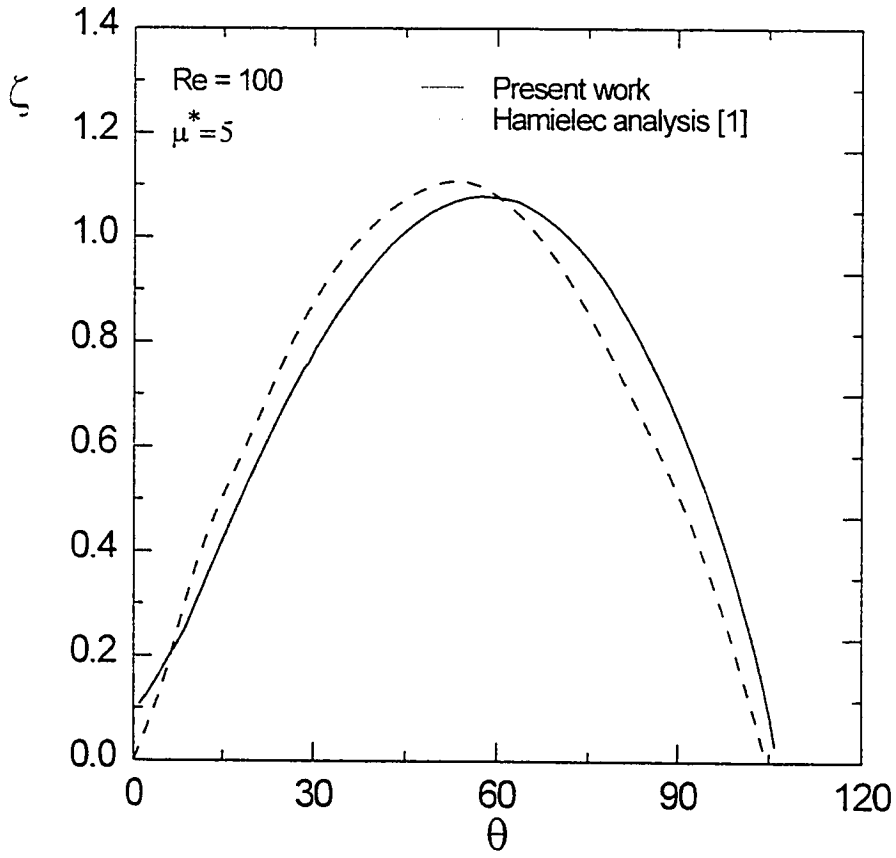

Fig. 6-15 : Surface vorticity compared with boundary layer solution of [1]

Table 6-1 : Variation of C_D with μ^* for various values of Re

μ^*	C_D			
	Re = 100	Re = 500	Re = 1000	Re = 10000
1.01	0.55586	0.17586	0.10224	0.01351
1.05	0.64023	0.26210	0.17785	0.04087
1.10	0.65415	0.27470	0.19040	0.05175
1.30	0.66414	0.28460	0.19979	0.06020
1.50	0.66589	0.28670	0.20190	0.06199
2.00	0.66811	0.28847	0.20354	0.06339
5.00	0.66825	0.28955	0.20457	0.06459
10.0	0.66870	0.28975	0.20513	0.06482
100.	0.66902	0.28990	0.20533	0.06499

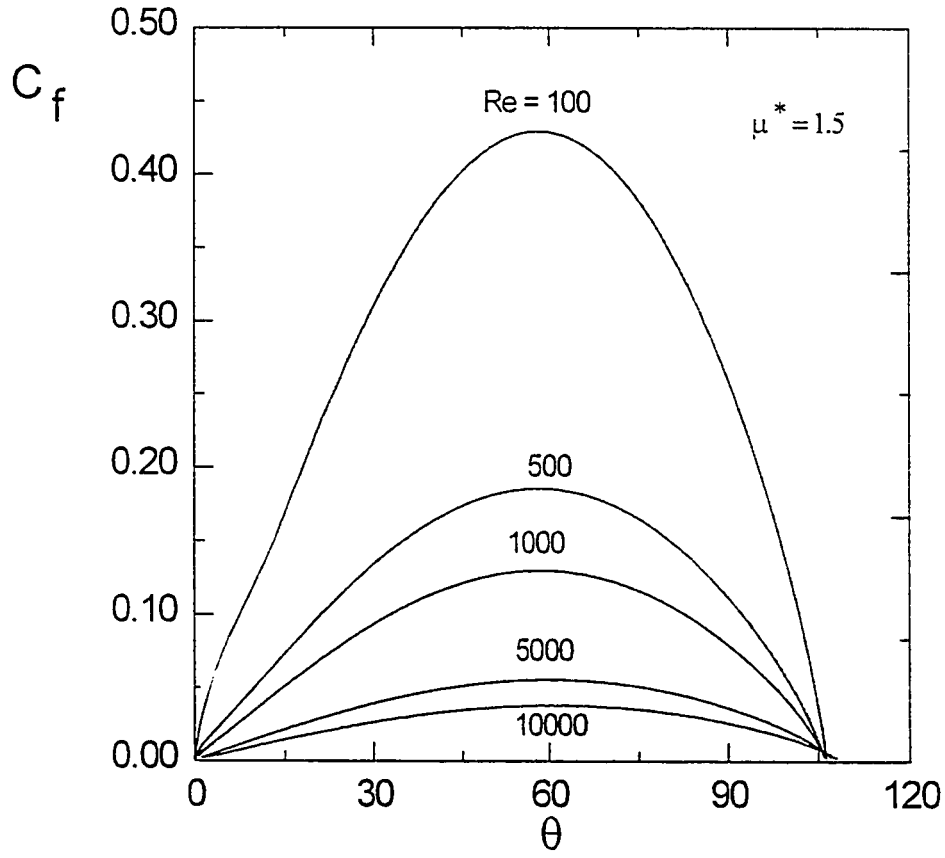

Fig. 6-16 : Effect of Reynolds number on the coefficient of friction

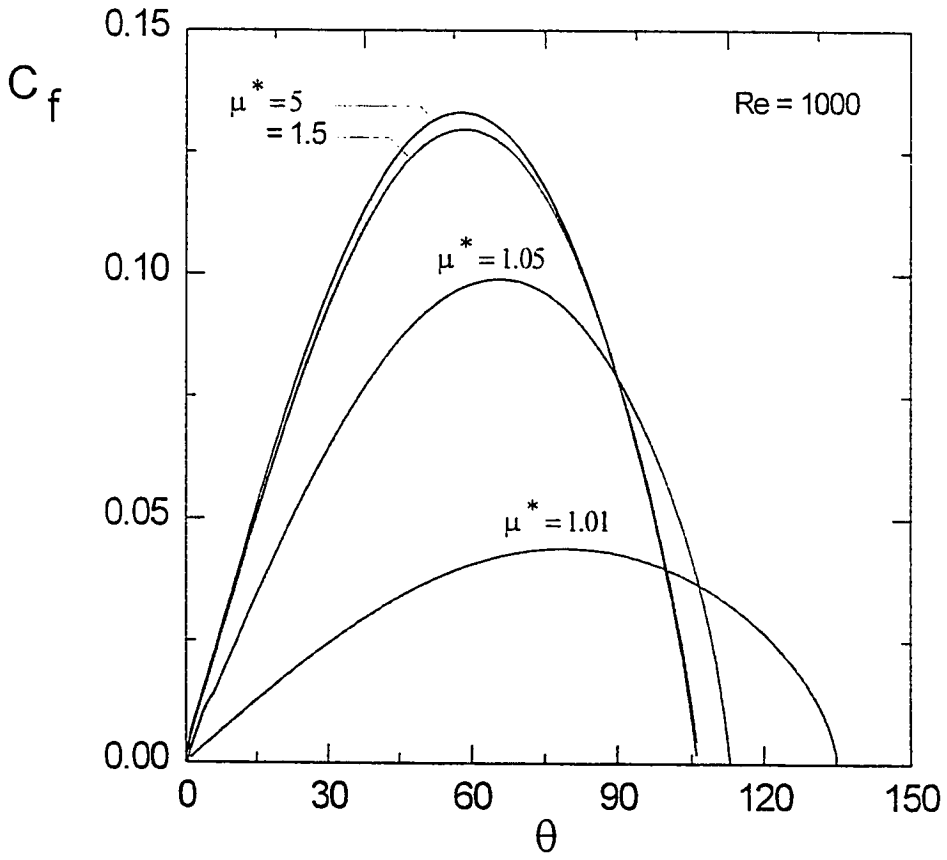

Fig. 6-17 : Effect of viscosity ratio on the coefficient of friction

6.3 Results of Velocity Profiles Inside the Sphere

6.3.1 Meridional Velocity Profiles

Results of the solution of the liquid-phase boundary-layer equations inside the sphere are presented in this section . The effect of changing the viscosity ratio on the meridional velocity profiles inside the sphere at fixed values of Reynolds number (Re = 500) , kinematic viscosity ratio ($\nu^* = 0.04$) and angle ($\theta = 60^o$) is illustrated in Fig. 6-18 for three selected values of the viscosity ratio ($\mu^* = 1.001$, 1.01 and 1.05) . The figure shows that increasing the viscosity ratio decreases the meridional velocity inside the sphere due to the lower values of the surface velocity calculated from the gas-phase solution . The liquid-phase boundary-layer thickness also increases for higher values of the viscosity ratio and this is indicated by location where the matching with Hill's vortex components starts (dotted line); this matching location indicates the thickness of the liquid-phase boundary-layer .

Figures 6-19a and 6-19b show the effect of Reynolds number on the meridional velocity at given viscosity ratios , kinematic viscosity ratios and angle ($\theta = 60^o$) . Increasing the Reynolds number increases the surface velocity of the liquid sphere, hence increases the meridional velocity in the liquid-phase boundary-layer and consequently decreases the thickness of the boundary layer in a similar manner to what was encountered for the external boundary layer . The dotted lines are representing the

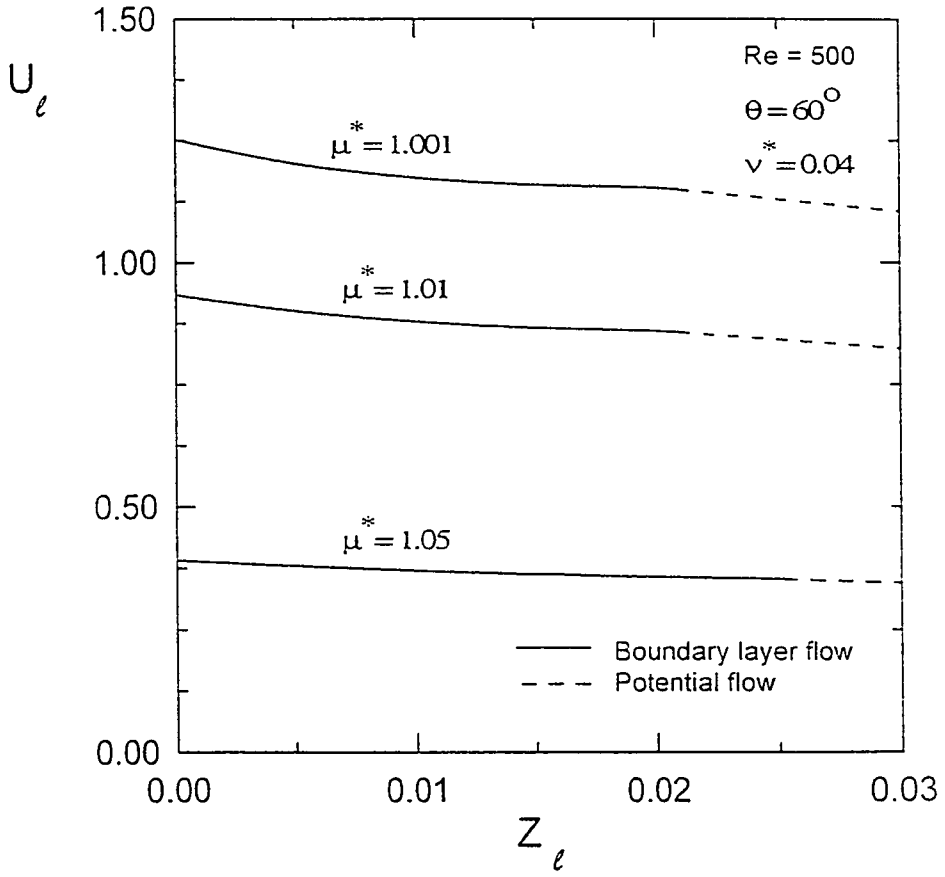

Fig. 6-18 : Effect of viscosity ratio on meridional velocity inside the sphere

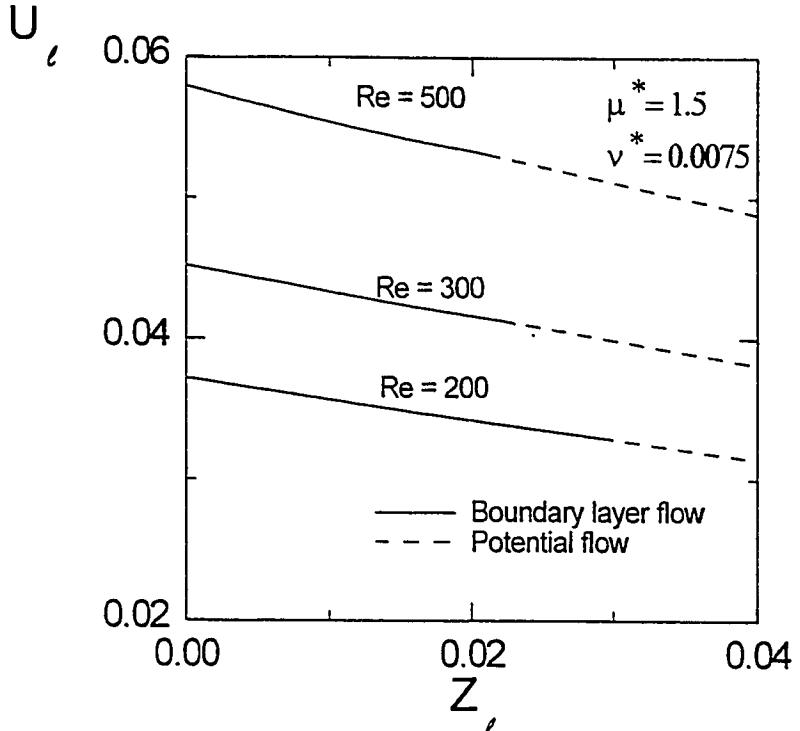

Fig. 6-19a : Effect of Reynolds number on the meridional velocity distribution inside the sphere, (Re = 200,300 and 500)

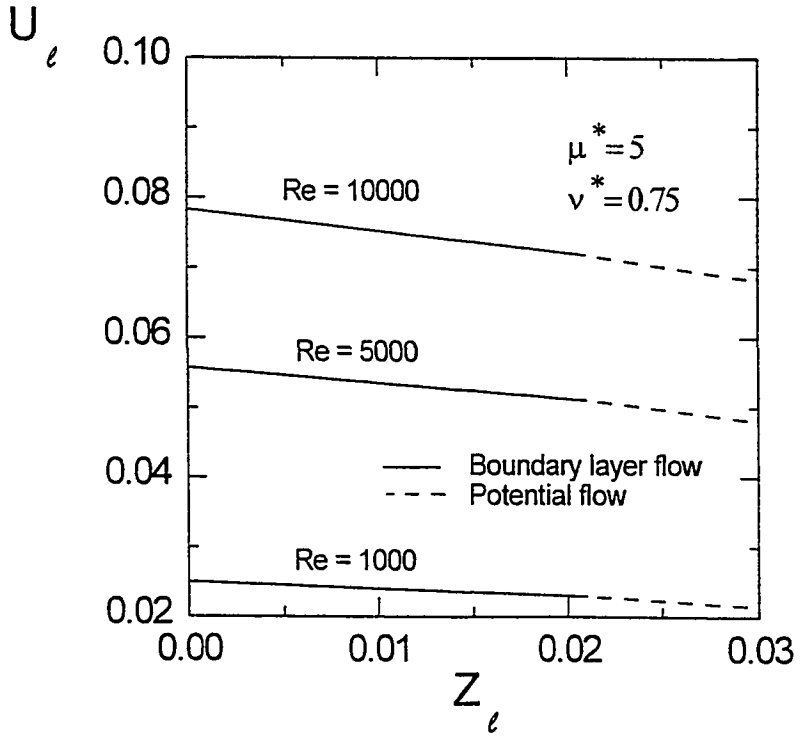

Fig. 6-19b : Effect of Reynolds number on the meridional velocity distribution inside the sphere (Re = 1000,5000 and 10000)

Hill's vortex meridional velocity component that are matching the meridional velocity at the edge of the boundary layer .

Figure 6-20 shows the meridional velocity profiles in the internal boundary-layer at fixed values of Reynolds number (Re = 300), the viscosity ratio ($\mu^* = 2$) and the meridional station (angle) $\theta = 60^o$ for three selected values of the kinematic-viscosity ratio (0.009, 0.01 and 0.075) which are corresponding to values of the liquid-to-gas density ratio of 111, 100 and 13, respectively . This figure shows that increasing the kinematic viscosity ratio (decreasing the density ratio) at a given Reynolds number decreases the boundary-layer thickness since it results in an increase in the meridional velocity component and hence thinning the boundary layer . However, although the surface velocity is not affected by changing the kinematic viscosity ratio , meridional velocity profiles inside the liquid-phase boundary layer seem to have slightly higher values at the edge of the boundary-layer with higher kinematic viscosity ratios (U_ℓ = 0.024 at the edge of the boundary layer for $\nu^* = 0.009$ while it equals 0.026 for $\nu^* = 0.075$) since the liquid in these cases would be less dense allowing slightly higher meridional velocities . Table 6-2 presents these values of U_ℓ at Re = 300 for the aforementioned three kinematic viscosity ratios . The slight change in these U_ℓ values is due to the slight curvature of the velocity profiles shown in Figs. 6-16 through 6-18 and hence the effect of ν^* on the internal velocity profiles is insignificant .

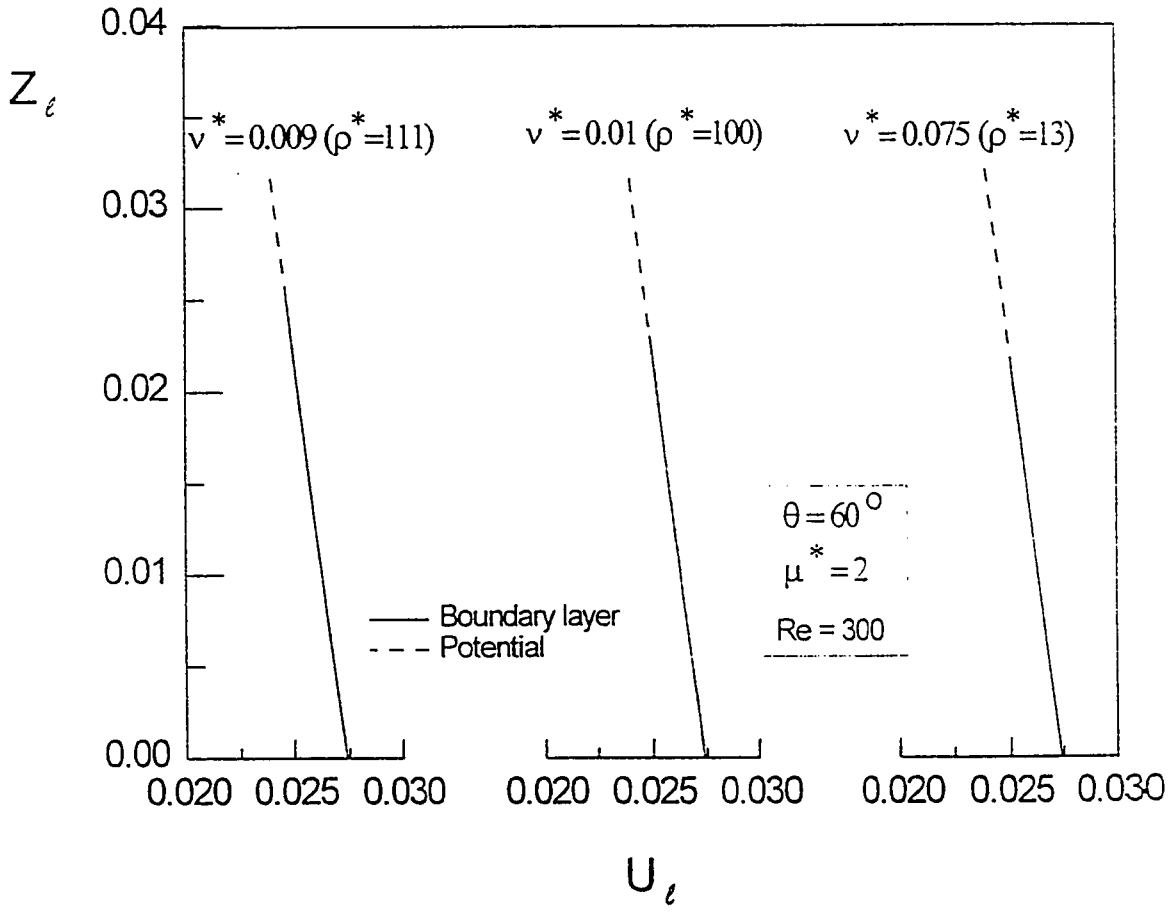

Fig. 6-20 : Effect of kinematic viscosity ratio on the meridional velocity inside the sphere

Table 6-2 Meridional velocity inside the sphere at different values of ν^*
Re = 300 & $\mu^* = 2$

Z	U_i $\nu^* = 0.009(\rho^* = 113)$	U_i $\nu^* = 0.01(\rho^* = 100)$	U_i $\nu^* = 0.075(\rho^* = 13)$
0	0.027400	0.027400	0.027400
0.005	0.026837	0.026843	0.026856
0.010	0.026281	0.026291	0.026313
0.015	0.025736	0.025749	0.025770
0.020	0.025209	0.025222	0.025230
0.021	0.025105	0.025118	0.025123
0.023	0.024801	0.024908	
0.025	0.024694		

Figure 6-21 shows the meridional velocity profiles at different angles measured from the front stagnation point . Maximum values are corresponding to higher angles (which is following the value of the velocity at the surface) with almost unremarkable change in the boundary-layer thickness at this relatively high Reynolds number (Re = 500) . However, the boundary-layer thickness increases significantly as we approach the point of flow separation as illustrated in Fig. 6-22 at a Reynolds number of (Re = 200) where the thickness of the boundary layer is shown to significantly increase at $\theta = 103^{o}$ and even with a much higher rate between $\theta = 103^{o}$ and $\theta = 105^{o}$, the latter ($\theta = 105^{o}$) is very close to the point of separation (almost at 106^{o}) . It is also noticeable that the surface velocity and hence the liquid-phase boundary-layer velocity decrease significantly at these angles .

6.3.2 Radial Velocity Profiles

Figure 6-23 shows the effect of the viscosity ratio on the radial-velocity distribution in the liquid-phase boundary-layer . As previously mentioned in the gas-phase boundary-layer results, all radial components of the velocity have a zero value at the surface of the sphere representing a non-evaporating liquid sphere . Increasing the viscosity ratio (representing the use of more viscous fluids) decreases the radial velocity. However, the increase in the viscosity ratio is also accompanied by an increase in the boundary-layer thickness as illustrated in the figure . This was also noticed because of the decrease in the surface velocity (hence the values of the velocity inside the sphere)

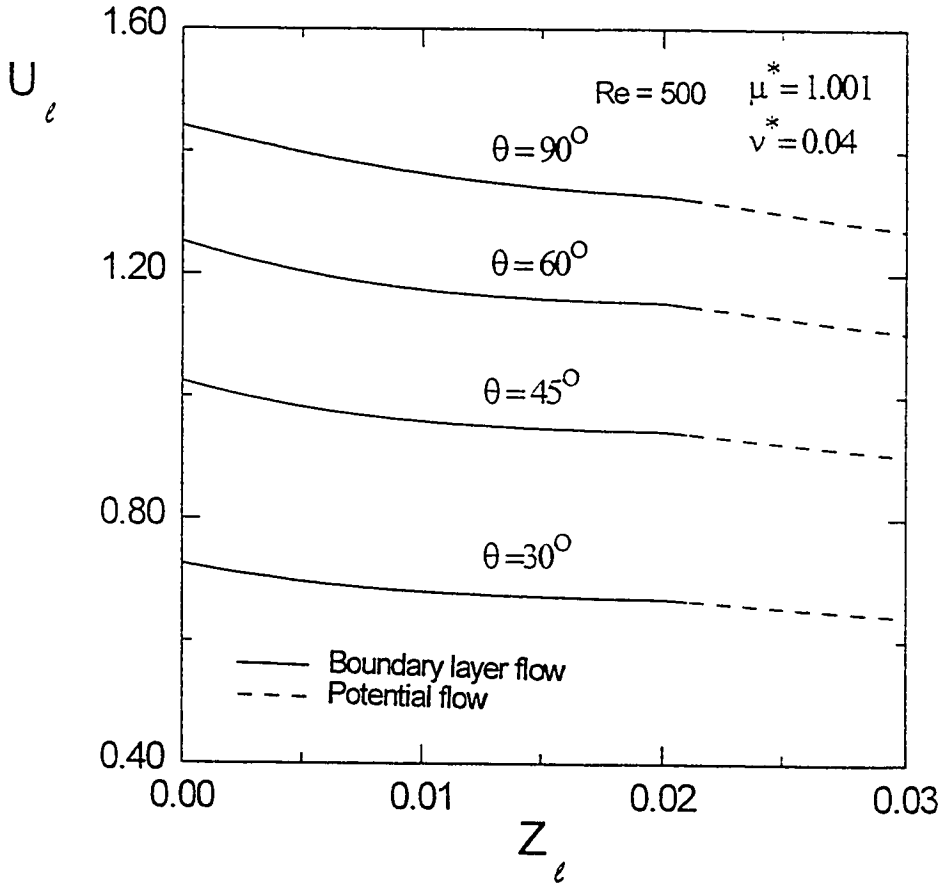

Fig. 6-21 : Meridional velocity distribution inside the sphere at different angles

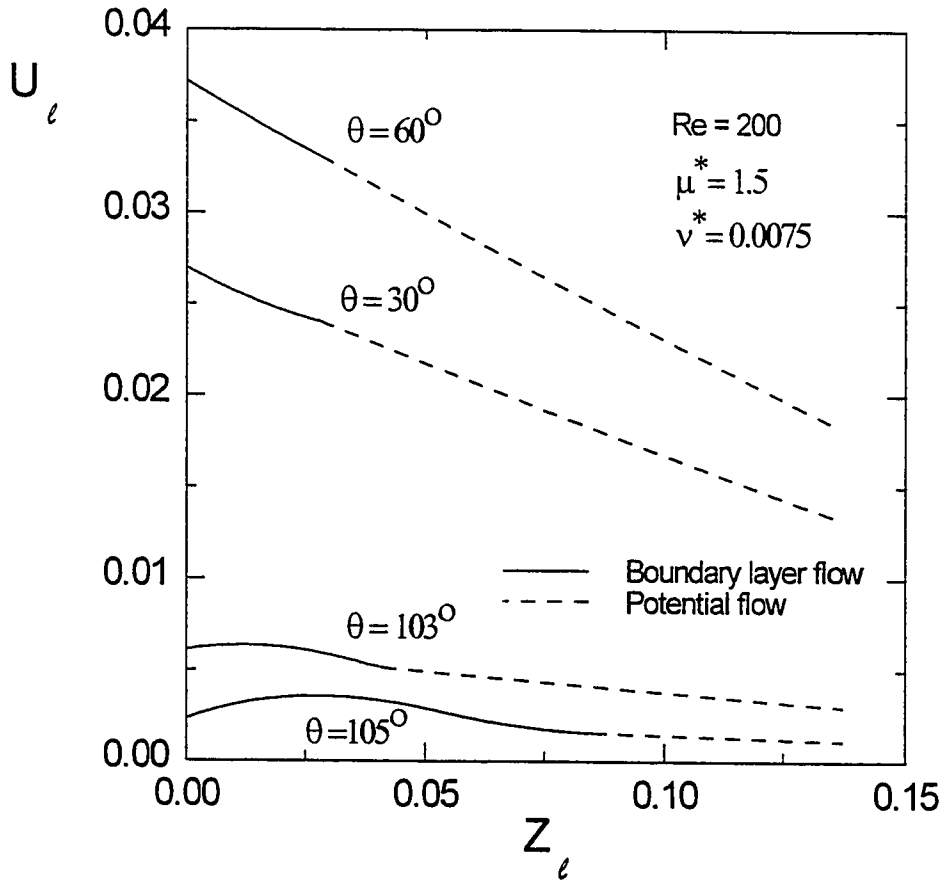

Fig. 6-22 : Meridional velocity distribution inside the sphere at different angles

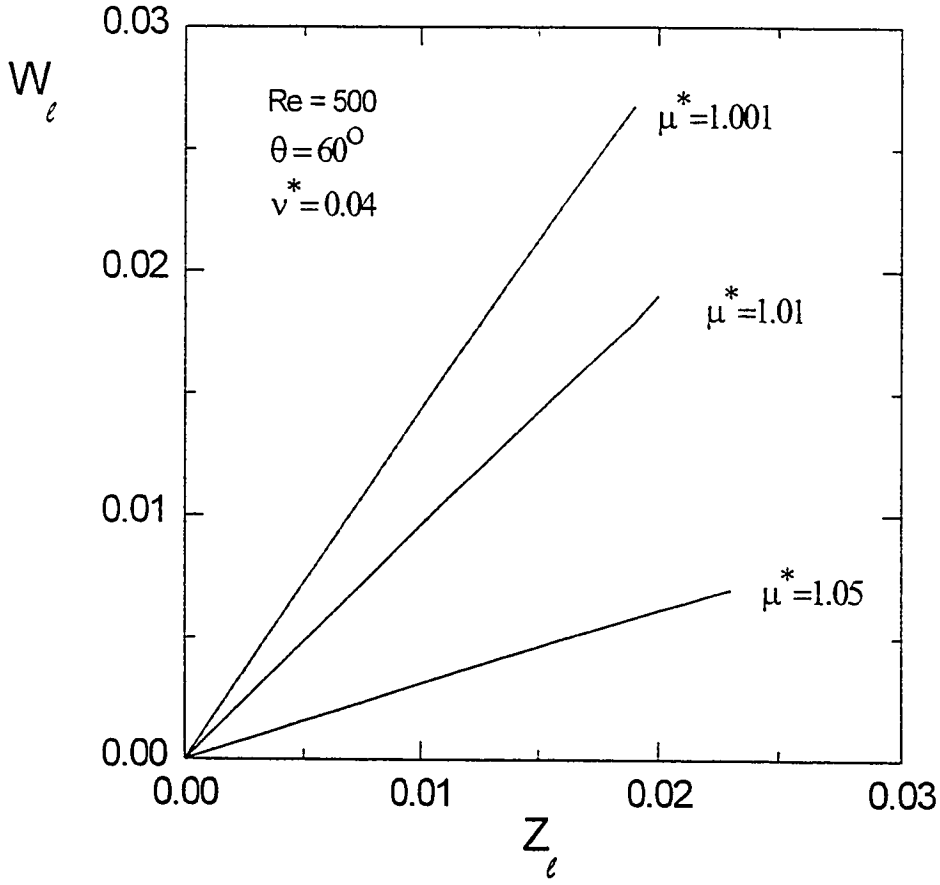

Fig. 6-23 :Effect of the viscosity ratio on the radial velocity inside the sphere

similar to the effect of decreasing Reynolds number on the increase of the boundary-layer thickness .

The effect of the kinematic viscosity ratio on the radial velocity is shown in Fig. 6-24 . This figure shows that the thickness of the boundary layer is affected by the kinematic viscosity ratio as was previously explained in Fig. 6-20 by linking the decrease in velocity (and hence increasing boundary layer thickness) to the decrease in kinematic viscosity ratio (or the increase in density ratio) at constant viscosity ratio and Reynolds number .

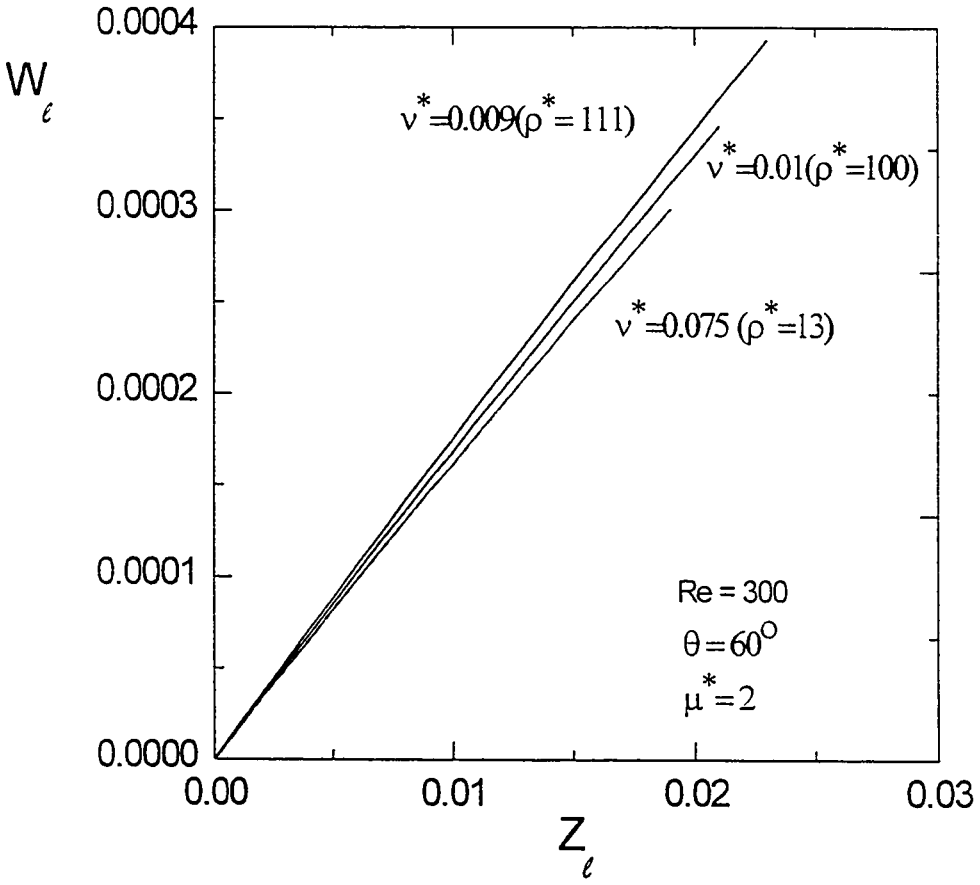

Fig. 6-24 :Effect of the kinematic viscosity ratio on the radial velocity inside the sphere

CHAPTER VII

HEAT TRANSFER RESULTS AND DISCUSSION

7.1 Introduction

In this chapter, the results of solving the energy equation around and inside the liquid sphere are presented . Two cases were studied when solving the energy equation around the sphere . In case (1), the steady energy equation was solved to obtain the temperature distribution in the external boundary layer emphasizing the effect of the flow controlling parameters such as Reynolds numbers, viscosity ratio, and Prandtl number on the temperature profiles at different meridional stations . Then, in case (2), the transient energy equation was solved to obtain the temporal temperature profiles as time elapses till the surface of the sphere approaches the free stream temperature (within a certain numerical tolerance of 0.005) . It is worth mentioning that transient solution of the energy equation was considered for three cases (a,b and c) according the initial temperature profile . In case (2-a), the initial temperature distribution throughout the external boundary layer is assumed equal to the free stream temperature, i.e., a step temperature change (from zero to one) takes place at the surface of the sphere . In case (2-b), an initial linear variation of the temperature is assumed starting from zero at the

surface and increasing linearly till unity at the edge of the boundary layer . The third case in the transient model, (case 2-c), assumes a step change in temperature occurring at the outer edge of the boundary layer . In other words, the initial temperature throughout the boundary layer is zero while it equals unity at the boundary layer edge . The transient temperature profiles around the sphere for the three former cases are presented for different values of the controlling parameters, namely, Reynolds number (Re), interior-to-exterior viscosity ratio (μ^*), and Prandtl number (Pr) . The effect of these parameters on the time required for the surface of the sphere to reach the free stream temperature is then presented for each case . Engineering parameters such as Nusselt number are also illustrated for each case . Finally the results of the transient temperature profiles inside the liquid sphere up the core of the sphere are presented and the time required to reach the steady-state condition (i.e., when the temperature at the center of the sphere approaches the free stream temperature) is presented . For a given time, the effect of Reynolds number and viscosity ratio on the temperature profiles inside the sphere is then presented and discussed .

7.2 Results of Temperature Profiles Around the Sphere

In this section, temperature profiles around the sphere are presented . First, the steady temperature distribution, (Case 1), is shown . Then, transient temperature distributions (Case 2) for each of the three cases (a,b and c) representing different initial temperature profiles are presented showing the effect of the controlling parameters for each case .

7.2.1 Case 1 : Steady State Temperature Distribution Around the Sphere

7.2.1.1 Temperature Profiles

The steady energy equation was solved with the boundary conditions specified . The dimensionless temperature is considered equal to zero at the sphere's surface and is equal to unity at the edge of the thermal boundary layer . In the meridional direction the boundary condition is taken at the front stagnation point where the boundary layer thickness is equal to zero and the value of the temperature is unity .

Figure 7-1 shows the effect of Reynolds number on the temperature distribution for given Prandtl number Pr = 0.7, viscosity ratio μ^* = 1.5 and angle $\theta = 60^\circ$. It is clear from the figure that as the Reynolds number increases, the thickness of the thermal boundary layer decreases . This implies more heat convected inward to the liquid sphere (due to higher velocities in the external boundary layer) as Re increases . Therefore, higher values of temperature at a given radial location are obtained for higher values of Reynolds number .

The effect of the interior-to-exterior viscosity ratio on the steady temperature profiles is shown in Fig. 7-2 for given Reynolds number Re = 1000, Prandtl number Pr = 0.7 and meridional angle $\theta = 60^\circ$. In this figure curves corresponding to four selected values of the viscosity ratio (μ^* = 1.01, 1.05,1.5 and 5) are shown . Lower viscosity ratios result in higher velocities in the boundary layer and hence higher rates of heat convection.

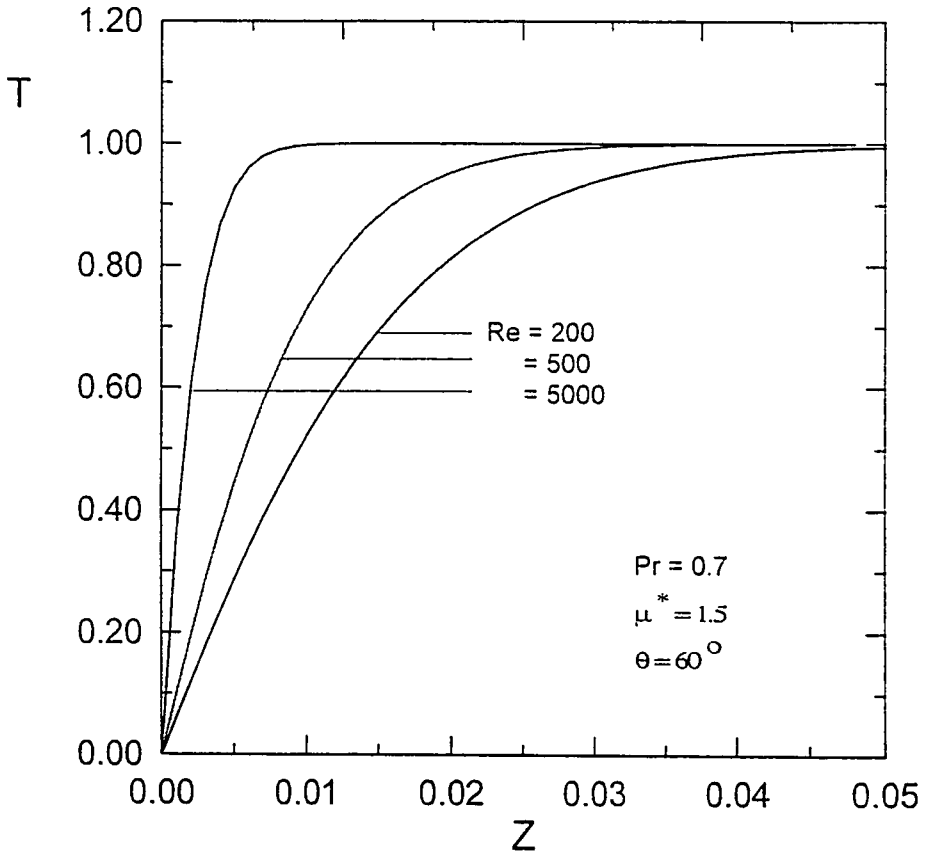

Fig. 7-1 : Effect of Reynolds number on the temperature profiles for $\theta = 60^{o}$, case (1)

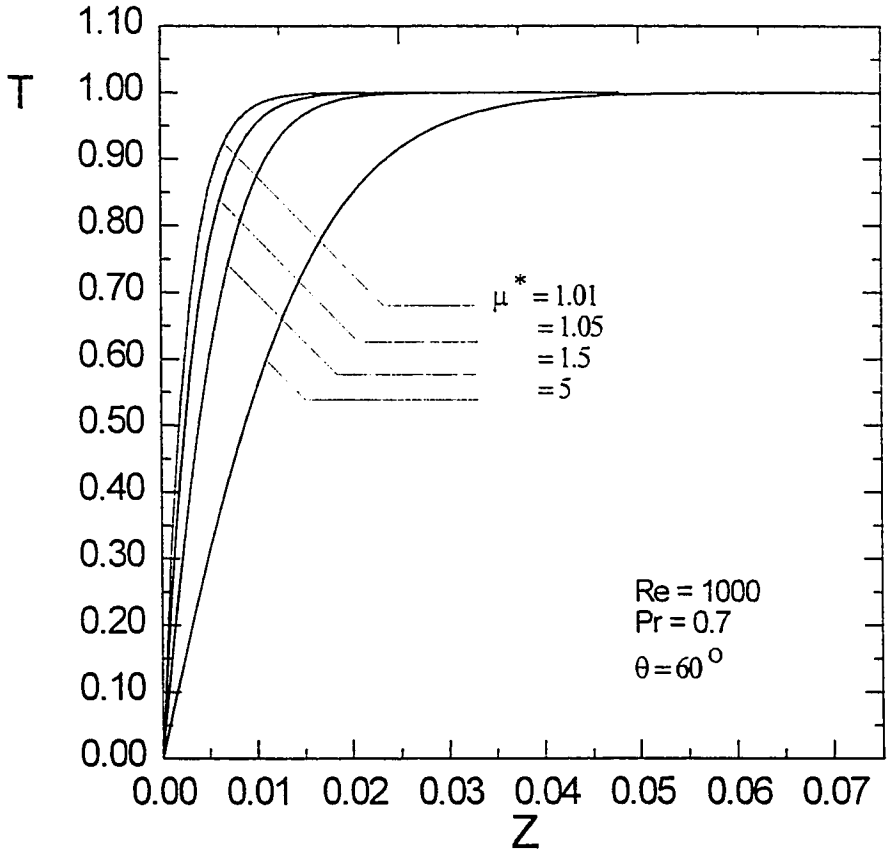

Fig. 7-2 : Effect of viscosity ratio on the temperature profile for $\theta = 60^{o}$, case (1)

Therefore, higher temperatures at the same radial location are obtained at lower viscosity ratios .

Figure 7-3 shows the temperature profiles at different meridional stations ($\theta = 30^{o}$, 60^{o}, 90^{o} and 105^{o}) for selected values of Reynolds number Re = 1000, Prandtl number Pr = 0.7 and viscosity ratio $\mu^{*} = 1.5$. Higher values of temperature are found at earlier angles since the maximum temperature is attained at the front stagnation point where the boundary layer thickness is equal to zero and T = 1 . The value of the temperature decreases as we move forward in the meridional direction till it reaches its lowest value close to the point of flow separation where higher boundary layer thickness is encountered .

The effect of Prandtl number on the temperature profiles is shown in Fig. 7-4 . Higher values of Prandtl number increase the rate of heat convection and hence result in higher temperatures at the same radial location . Therefore, less thermal boundary layer thicknesses correspond to higher values of the Prandtl number . The meridional velocity profile is also plotted in Fig. 7.4 to compare between the hydrodynamic boundary layer and the thermal boundary layer at different values of Prandtl number . It is clear from the figure that higher Prandtl numbers are corresponding to less thermal boundary layer thickness compared to the hydrodynamic boundary layer thickness .

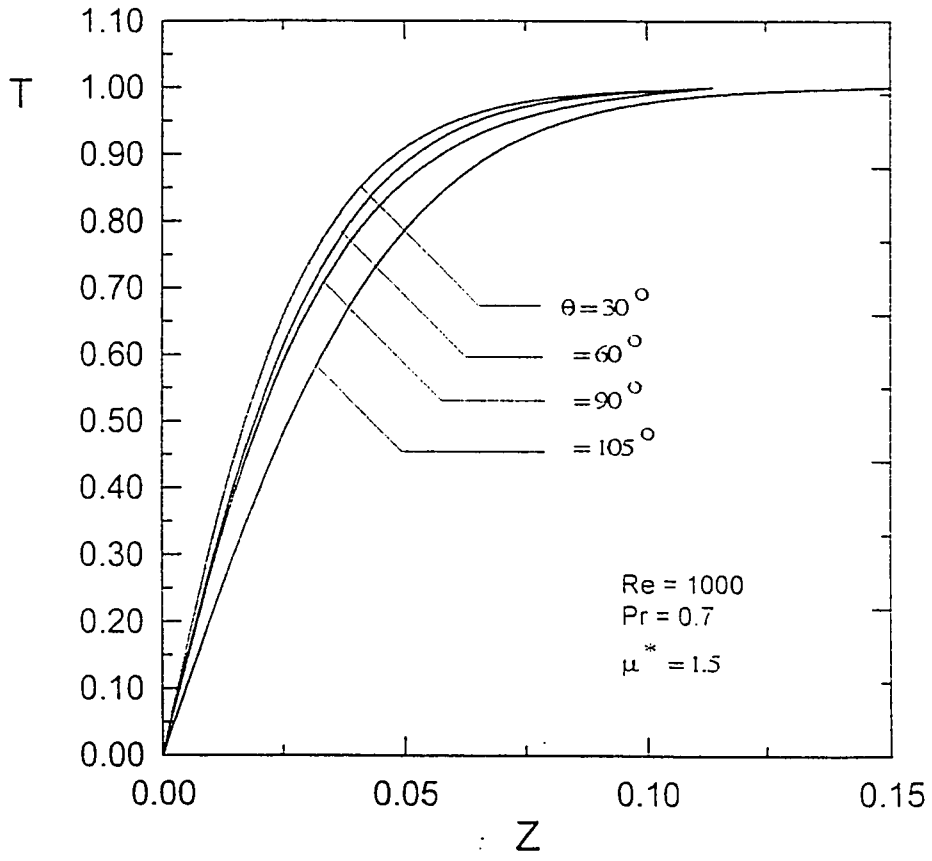

Fig. 7-3 : Temperature profiles at different angles, case (1)

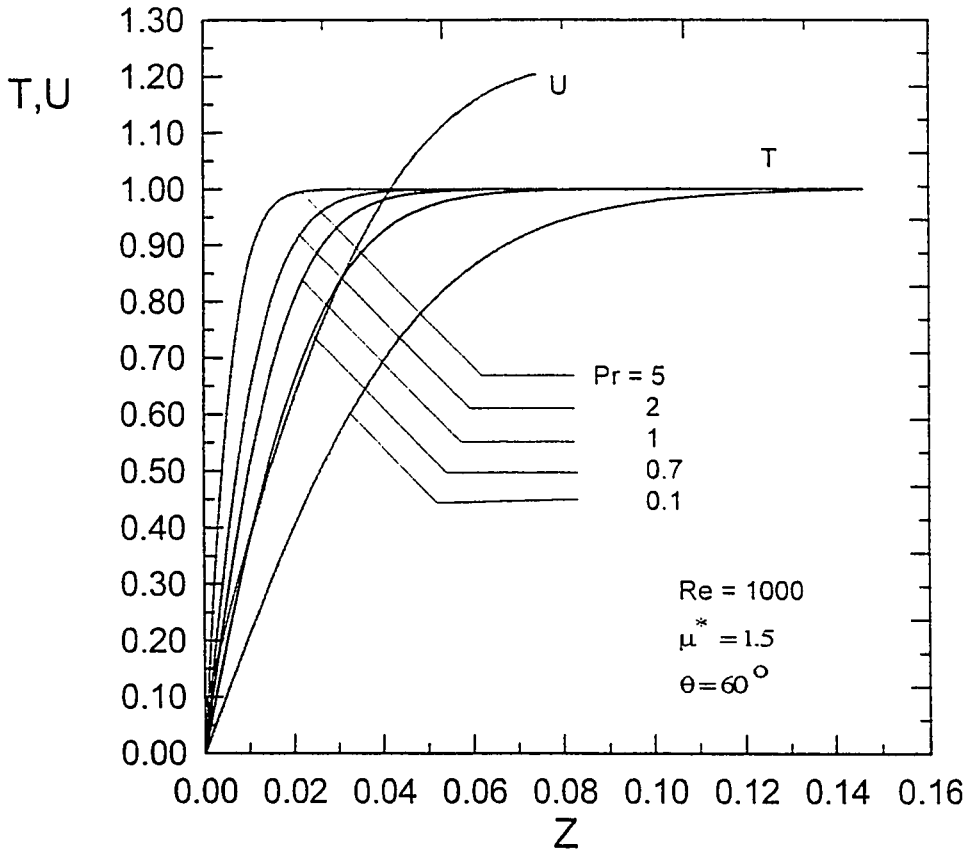

Fig. 7-4 : Temperature and meridional velocity profiles at various values of Prandtl number, case (1)

7.2.1.2 Nusselt Number

Figure 7-5 shows the effect of Reynolds number on the local Nusselt number distribution . Nusselt number profiles are plotted versus the central angle till the point of external flow separation is reached for a selected value of Prandtl number Pr = 0.7 for different values of Reynolds number (Re = 100, 500, 1000, 5000 and 10000) . It is clear from the figure that increasing Reynolds number increases the heat convected to the sphere and hence increases the temperature gradient at the surface of the sphere . Therefore, the highest values of Nusselt number correspond to the highest Reynolds number .

Figure 7-6 shows the effect of the viscosity ratio on the local Nusselt number at given Reynolds number Re = 1000 and Prandtl number Pr = 0.7 for four selected values of the viscosity ratio (μ^* = 1.05, 1.1, 1.5 and 5) . Lower viscosity ratios are resulting in higher velocities within the boundary layer and hence higher rates of heat convection . This leads to higher temperature gradient at the sphere's surface i.e., higher values of the local Nusselt number .

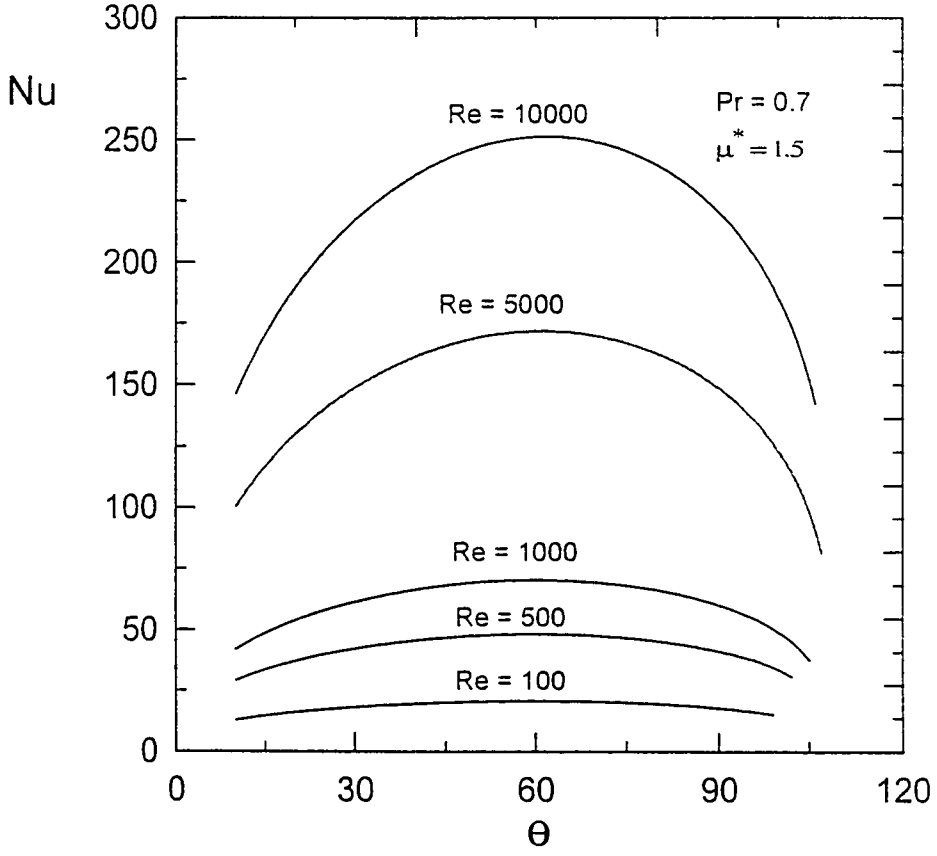

Fig. 7-5 : Effect of Reynolds number on the local Nusselt number distribution, case (1)

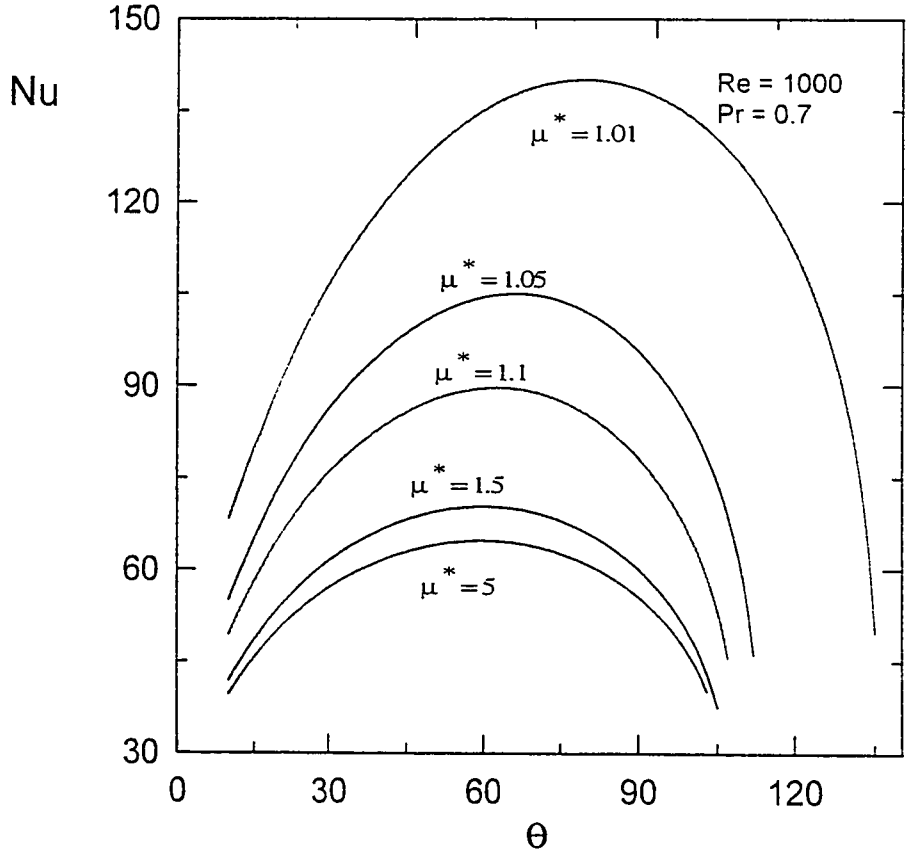

Fig. 7-6 : Effect of viscosity ratio on the local Nusselt number distribution, case (1)

7.2.2 Case 2 : Transient Temperature Distribution Around the Sphere

In this section, the transient energy equation is solved for the cases mentioned in the introduction of this chapter starting with the case where a step change in temperature is at the sphere's surface .

7.2.2.1 Case (2-a) : Step Change in Temperature at the Sphere's Surface

In this section, the results of the temperature profiles around the liquid sphere are presented for case (2-a) where the initial temperature profile around the sphere is assumed to have a step change (from zero to one) at the surface of the sphere; i.e., the temperature throughout the boundary layer is assumed to equal unity at time $t = 0$. Values of the temperature close to the surface of the sphere are expected to decrease first due to the presence of the cold surface and then increase due to the continuous transfer of heat from the free stream ($T = 1$) until the surface temperature of the sphere reaches its final uniform value that is equal to the free stream temperature (within a certain specified tolerance of 0.005) . The effect of the various controlling parameters (i.e. Reynolds number, Prandtl number and the internal-to-external viscosity ratio) on the temperature will be shown . Results of engineering quantities such as Nusselt number and the time required to reach the uniform surface temperature profile are to be deduced from these profiles .

7.2.2.1.1 Temperature Profiles

Figures 7-7a through 7-7f and 7-8a through 7-8f present the transient distribution of temperature around the sphere for case (2-a) at different radial locations (Z) for selected meridional stations (central angles) from $\theta = 30^{o}$ up to $\theta = 105^{o}$

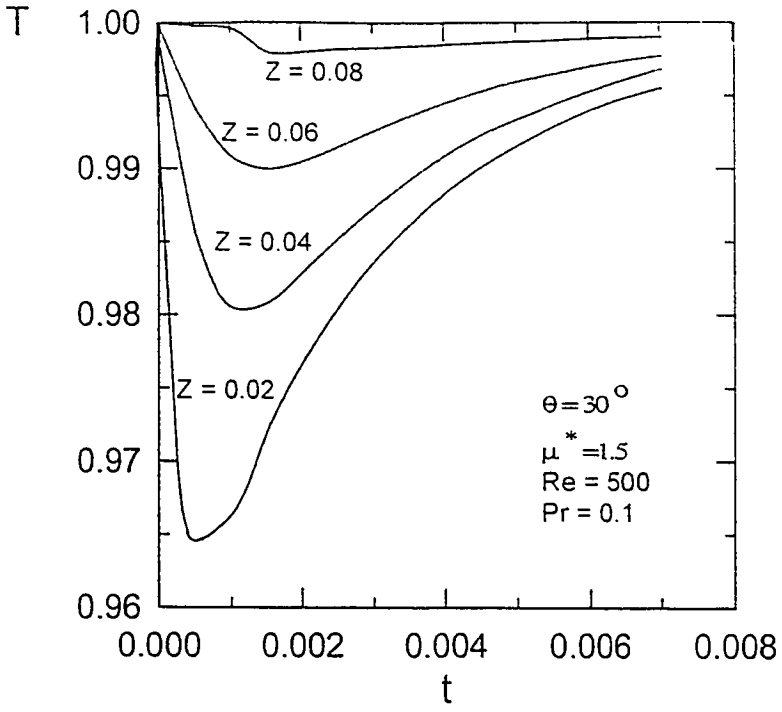

Fig. 7-7a : Transient temperature distribution at different radial distances for $\theta=30^{\circ}$ and Re = 500, case (2-a)

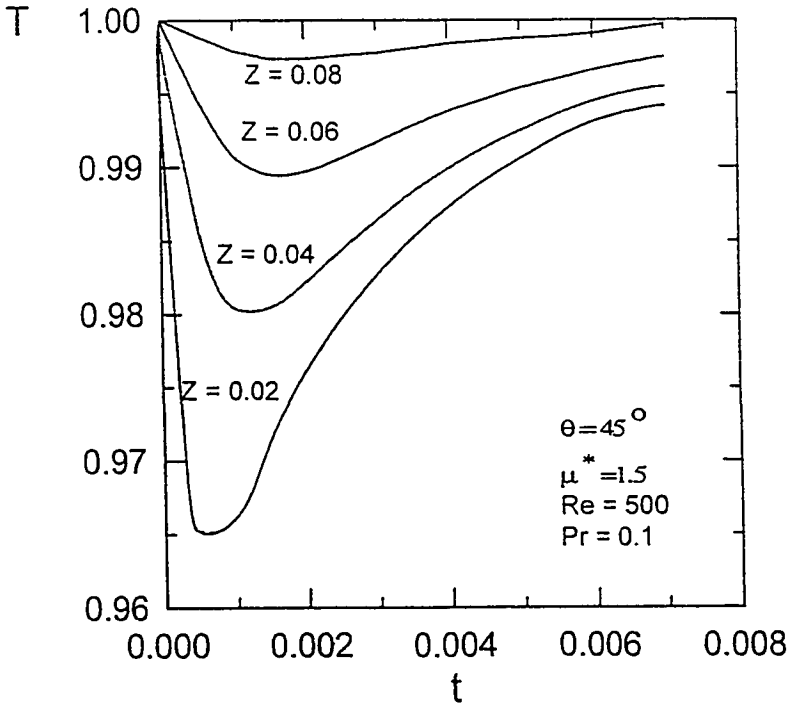

Fig. 7-7b : Transient temperature distribution at different radial distances for $\theta=45^{\circ}$ and Re = 500, case (2-a)

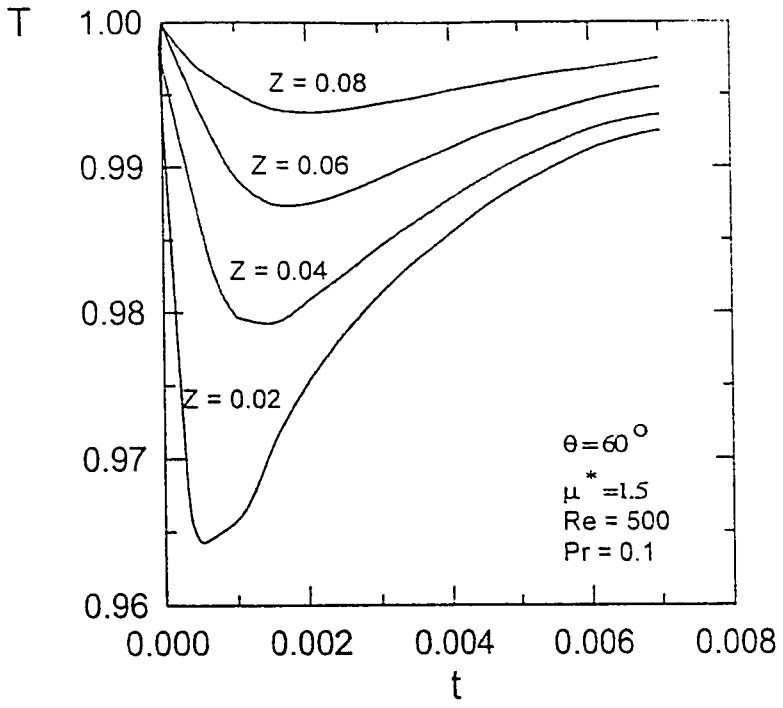

Fig. 7-7c : Transient temperature distribution at different radial distances for $\theta=60^{\circ}$ and Re = 500, case (2-a)

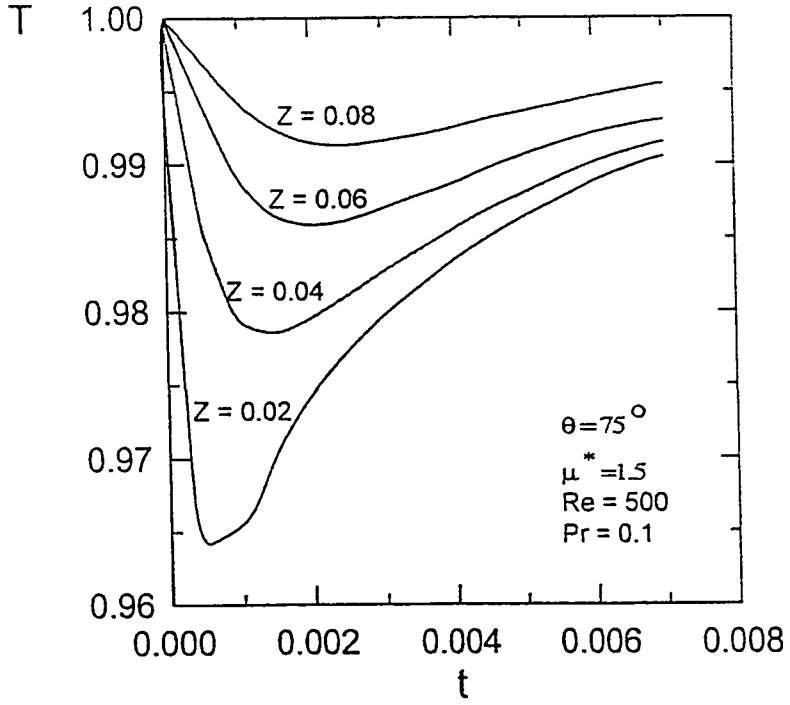

Fig. 7-7d : Transient temperature distribution at different radial distances for $\theta=75^{\circ}$ and Re = 500, case (2-a)

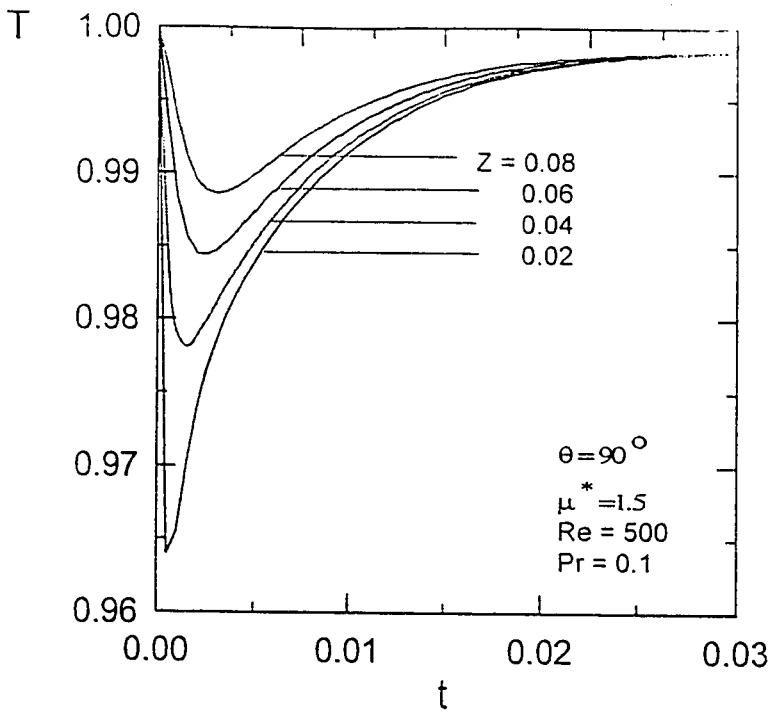

Fig. 7-7e : Transient temperature distribution at different radial distances, $\theta=90^{\circ}$,Re = 500, case (2-a)

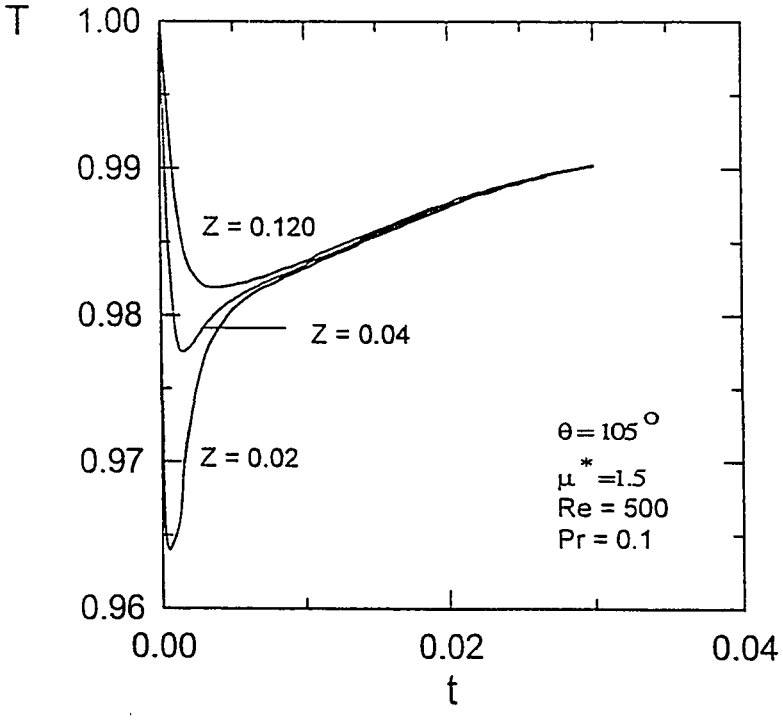

Fig. 7-7f : Transient temperature distribution at different radial distances, $\theta=105^{\circ}$,Re = 500, case (2-a)

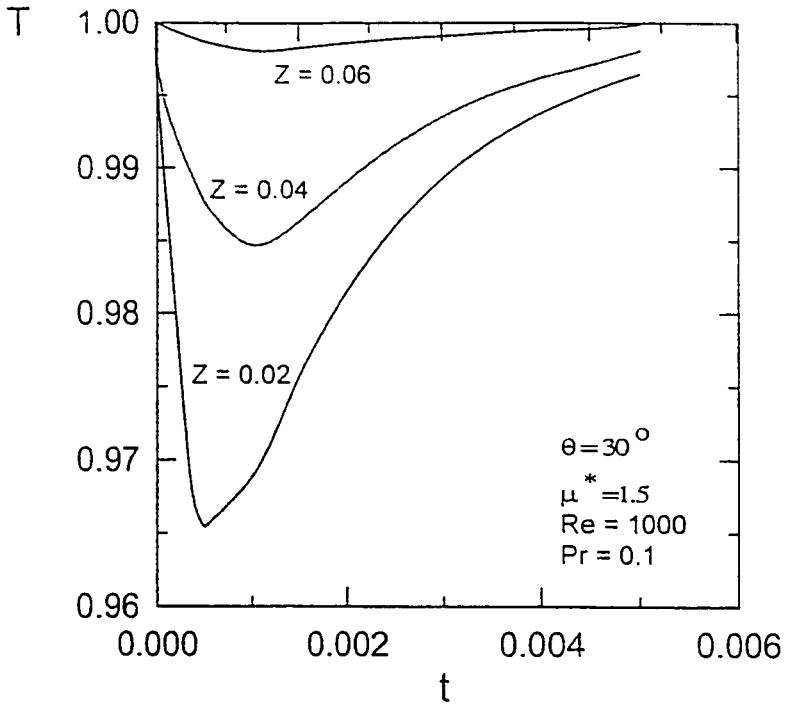

Fig. 7-8a : Transient temperature distribution at different radial distances for $\theta=30^{\circ}$ and Re = 1000, case (2-a)

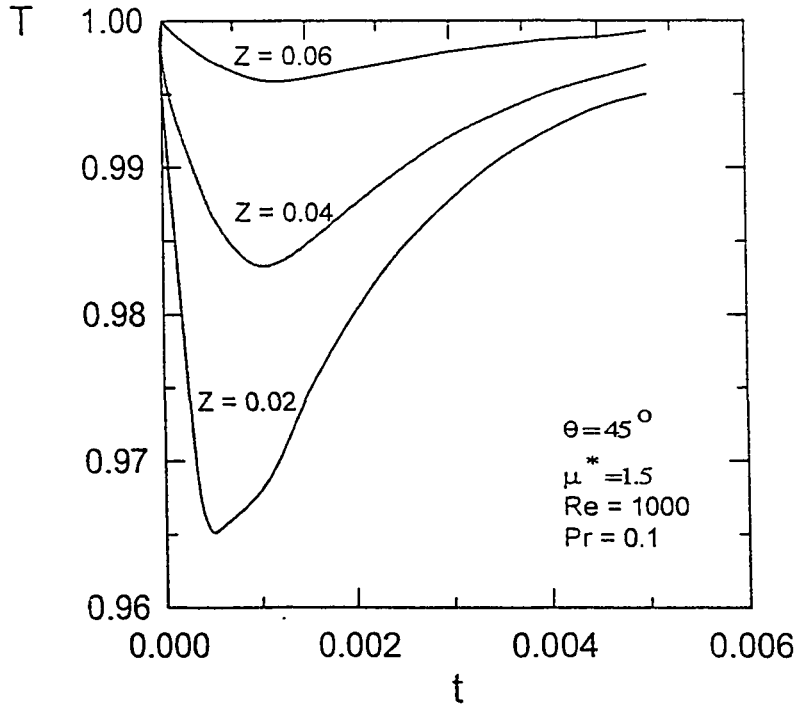

Fig. 7-8b : Transient temperature distribution at different radial distances for $\theta=45^{\circ}$ and Re = 1000, case (2-a)

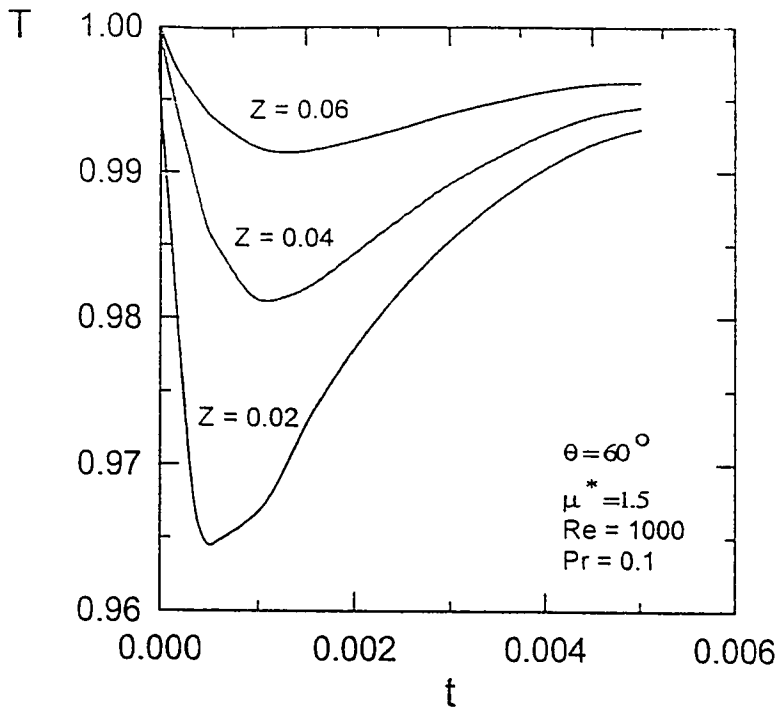

Fig. 7-8c : Transient temperature distribution at different radial distances for $\theta=60^{\circ}$ and Re = 1000, case (2-a)

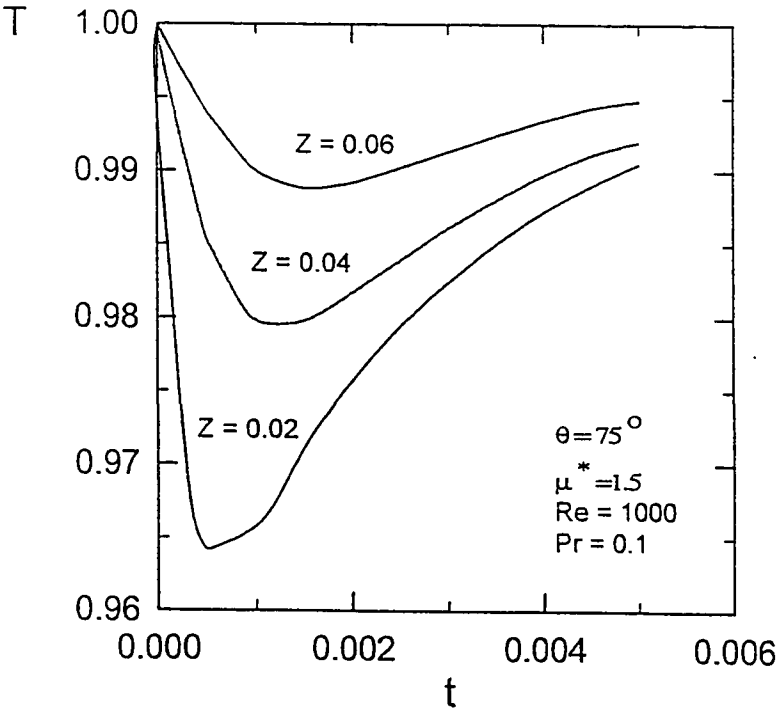

Fig. 7-8d : Transient temperature distribution at different radial distances for $\theta=75^{\circ}$ and Re = 1000, case (2-a)

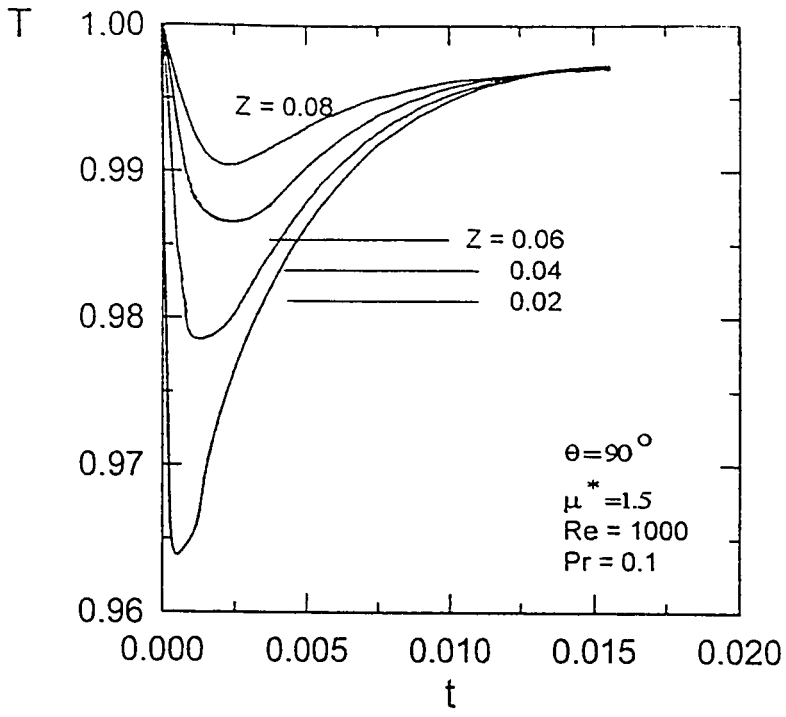

Fig. 7-8e : Transient temperature distribution at different radial distances, $\theta = 90^{\circ}$, Re = 1000, case (2-a)

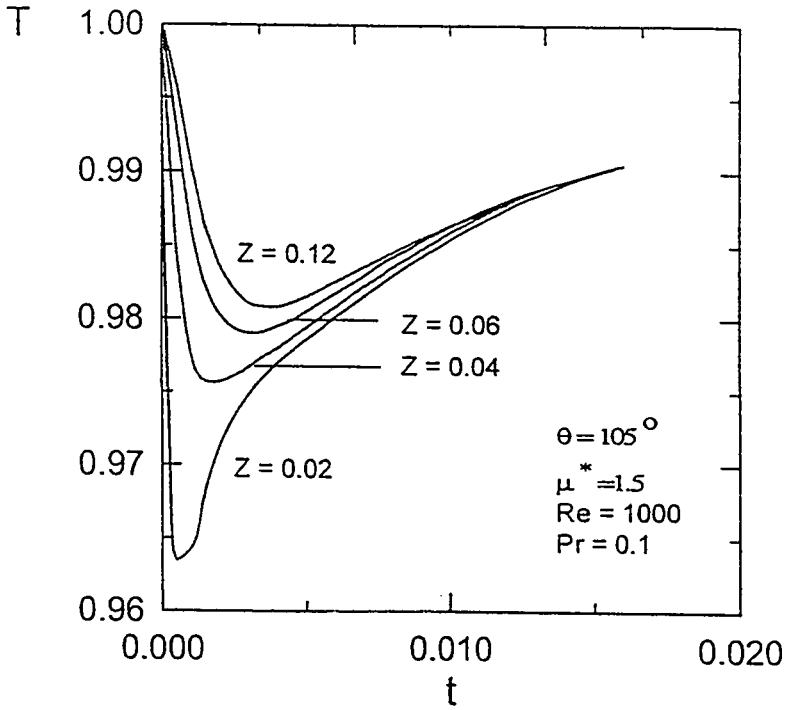

Fig. 7-8f : Transient temperature distribution at different radial distances, $\theta = 105^{\circ}$, Re = 1000, case (2-a)

which is before the point of external flow separation . Temperature distributions are presented for Prandtl number Pr = 0.7. viscosity ratio μ^* = 1.5 and two selected values of Reynolds number, namely, Re = 500 in (Figs. 7-7a through 7.7f) and Re = 1000 (in Figs. 7-8a through 7-8f). It is clear from these figures that the temperature in the boundary layer starts initially from unity, decreases for a short period of time due to the presence of the cold sphere and then increases along the surface due to the continuous transfer of energy from the free stream till it reaches a uniform value which is equal to its the free stream value . Higher values of temperature are noticed for outer radial locations that are essentially far from the sphere surface . The effect of Reynolds number on the time required to reach a uniform surface temperature (equal to the free stream temperature within a specified tolerance of 0.005) can be seen from the comparison of the figures . For high Reynolds number (Re=1000) this time is 0.07 while it equals 0.1 for Re = 500 . This is attributed to the increase in convective heat transfer for higher Reynolds numbers (higher velocities in the boundary layer) .

Figure 7.9 shows the transient development of the temperature profiles inside the boundary layer for given values of Reynolds number (Re = 500), Prandtl number (Pr = 0.7) , viscosity ratio (μ^* = 1.5) and meridional angle ($\theta = 60^o$) . Dimensionless temperature (T) starts initially from zero at the surface of the sphere and unity throughout the boundary layer . As time proceeds, the surface temperature increases and the adjacent layers' temperature first decreases and then increases until it approaches the free stream

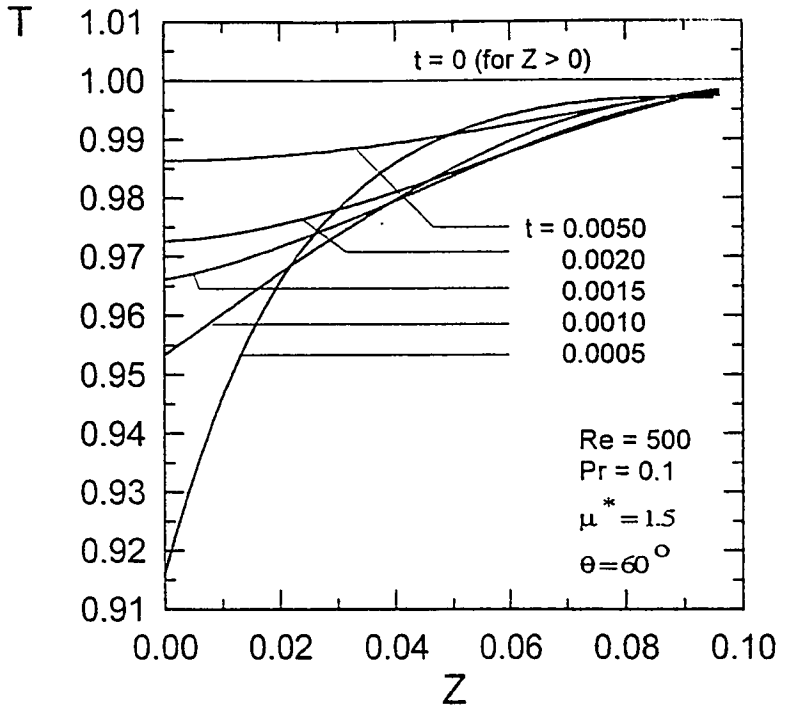

Fig. 7-9a : Transient temperature profiles at $\theta=60^{\circ}$, Re = 500, case(2-a)

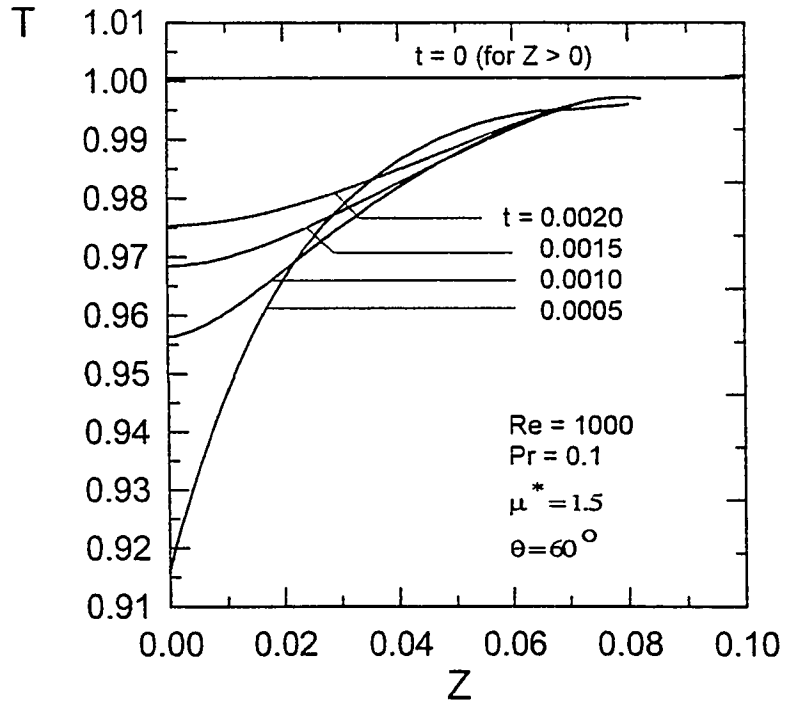

Fig. 7-9b : Transient temperature profiles at $\theta=60^{\circ}$, Re = 1000, case(2-a)

value . When such a uniform surface temperature is achieved, the external flow program is stopped .

Figure 7-10 shows the temperature profiles for some selected meridional stations under the same conditions stated above (the same values of the controlling parameters; Re, Pr and μ^*) for a given time step (t = 0.0005) . This figure shows the variation in the temperature profiles as the hydrodynamic boundary-layer thickness increases along the surface of the sphere until the maximum boundary layer thickness is encountered near the point of flow separation . It is clear also from Fig. 7-10 that the temperature decreases at the same radial distance as the meridional angle increases as a result of the increase in the boundary layer thickness with the meridional angle .

The effect of Reynolds number on the developing temperature distribution while the other controlling parameters are kept unchanged is shown in Fig. 7-11 at a fixed radial distance (Z = 0.02) . It is clear from this figure that increasing the value of Reynolds number increases the rate of heat transfer from the hot surrounding to the cold sphere . This effect is due to the thinning of the boundary layer with Re as was discussed in the previous chapter.

Figure 7-12 gives the variation of the time required to reach uniform surface temperature with Reynolds number for two selected values of the interior-to-exterior viscosity ratio, namely 1.05 and 5 . The time to reach a uniform surface temperature

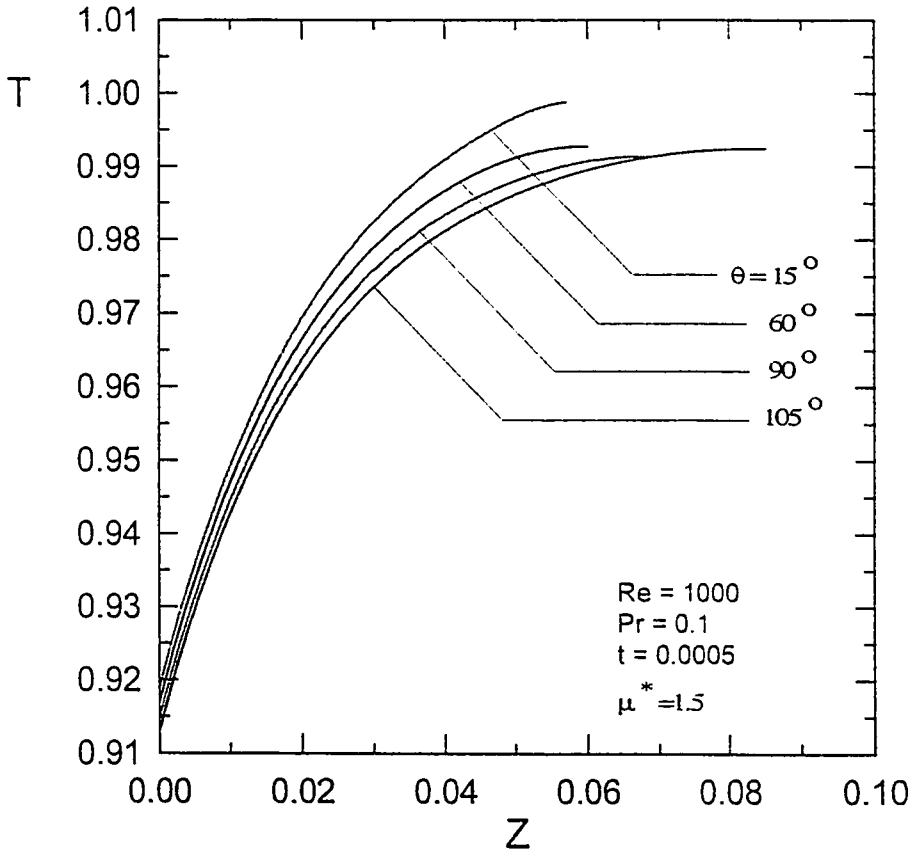

Fig. 7-10 : Temperature distribution at different angles at t = 0.0005, case (2-a)

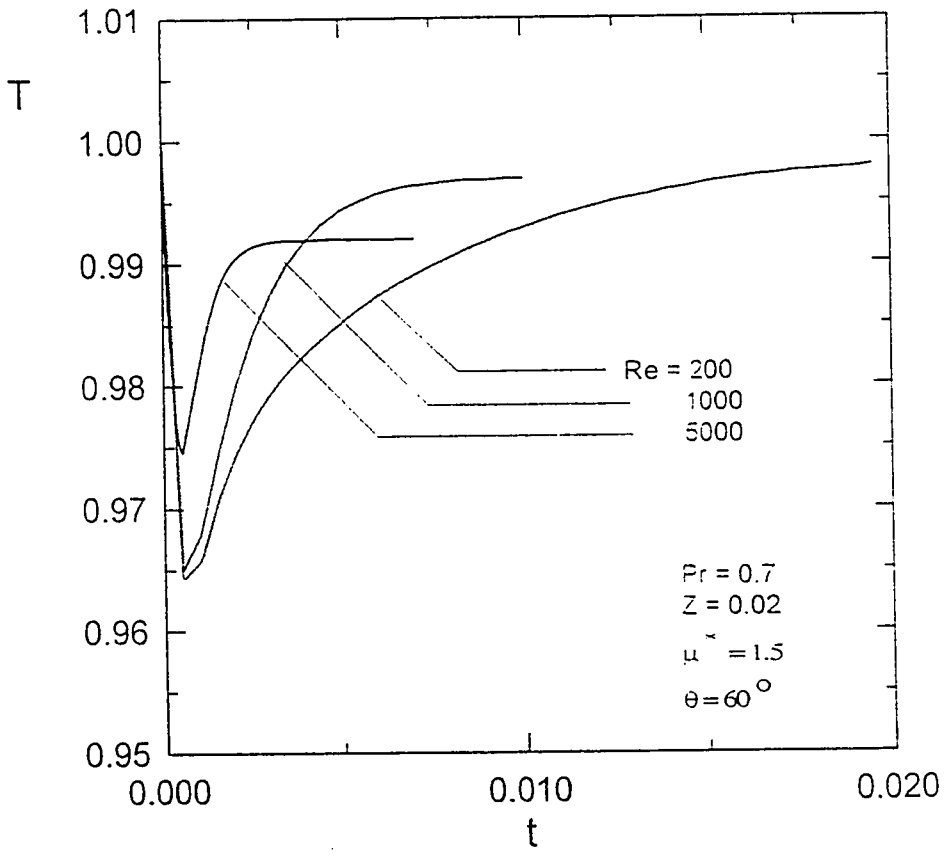

Fig. 7-11 : Effect of Reynolds number on the transient temperature profiles at a selected radial location (Z = 0.02), case (2-a)

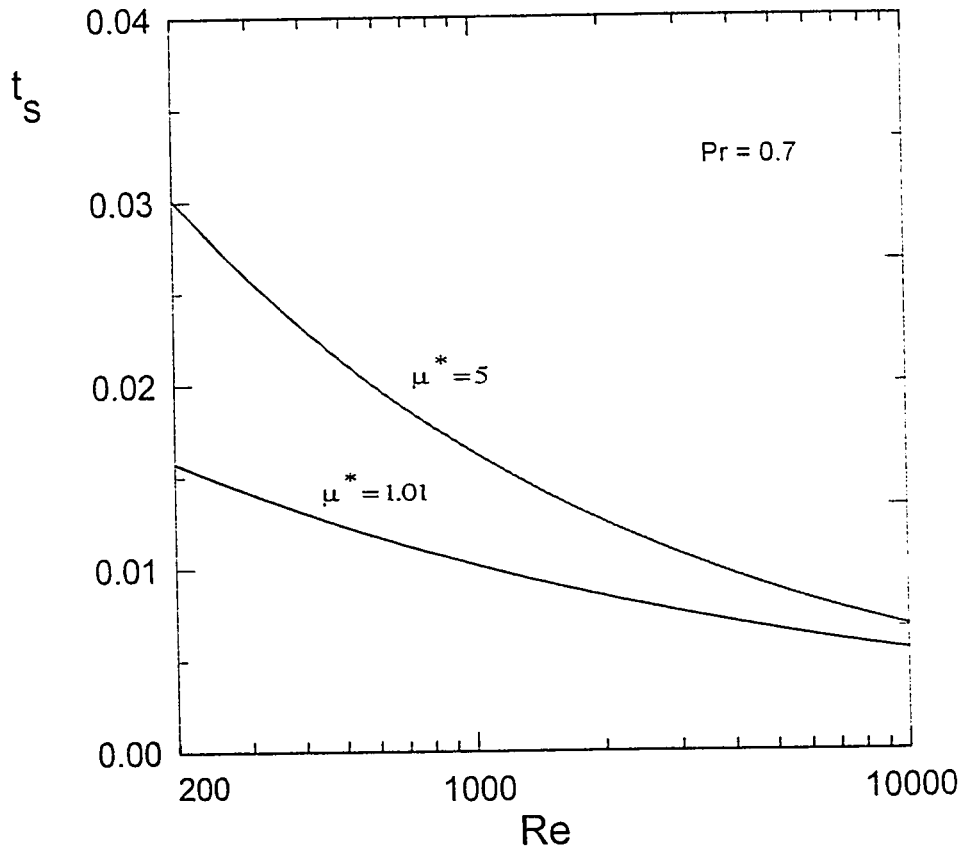

Fig. 7-12 : Effect of Reynolds number on the time required to reach uniform surface temperature, case (2-a)

(equal to its free stream value) is maximum at the lowest Reynolds number investigated (Re = 200) and its value decreases as Reynolds number increases . Moreover, for a given Re, t_s increases as μ^* increases . This is attributed to the thickening of the hydrodynamic boundary layer with μ^* as was explained in the previous chapter .

Figure 7-13 shows the effect of the viscosity ratio on the temperature profile for a selected time step (t = 0.0005) at a fixed meridional position ($\theta = 60^o$) . The figure shows that increasing the internal-to-external viscosity ratio decreases the heat transfer and hence it results in lower values of the temperature at the same radial distance . This is attributed to the decrease in the heat convected to the sphere due to lower velocities and larger boundary-layer thickness corresponding to higher viscosity ratios . The effect of changing the viscosity ratio on the transient temperature profiles at a fixed radial distance (Z = 0.02) for the same meridional angle is shown in the figure . Higher values of temperature in the boundary-layer are corresponding to the lower viscosity ratios .

Figure 7-14 illustrates the effect of viscosity ratio on the temperature distribution in the boundary layer at selected values of Reynolds number Re = 1000, Prandtl number Pr = 0.7, meridional angle $\theta = 60^o$ and for a fixed radial location Z = 0.02 . It is clear from the figure that lower viscosity ratios result in higher values of the temperature.

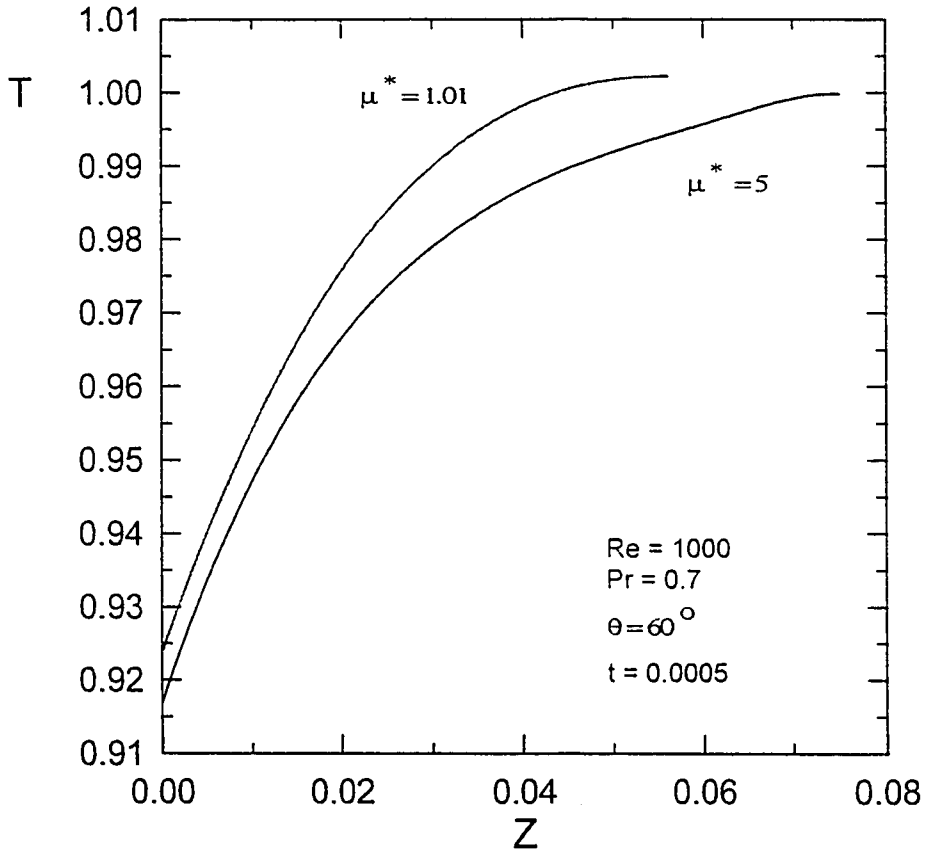

Fig. 7-13 : Effect of viscosity ratio on the temperature profiles, t = 0.0005, case (2-a)

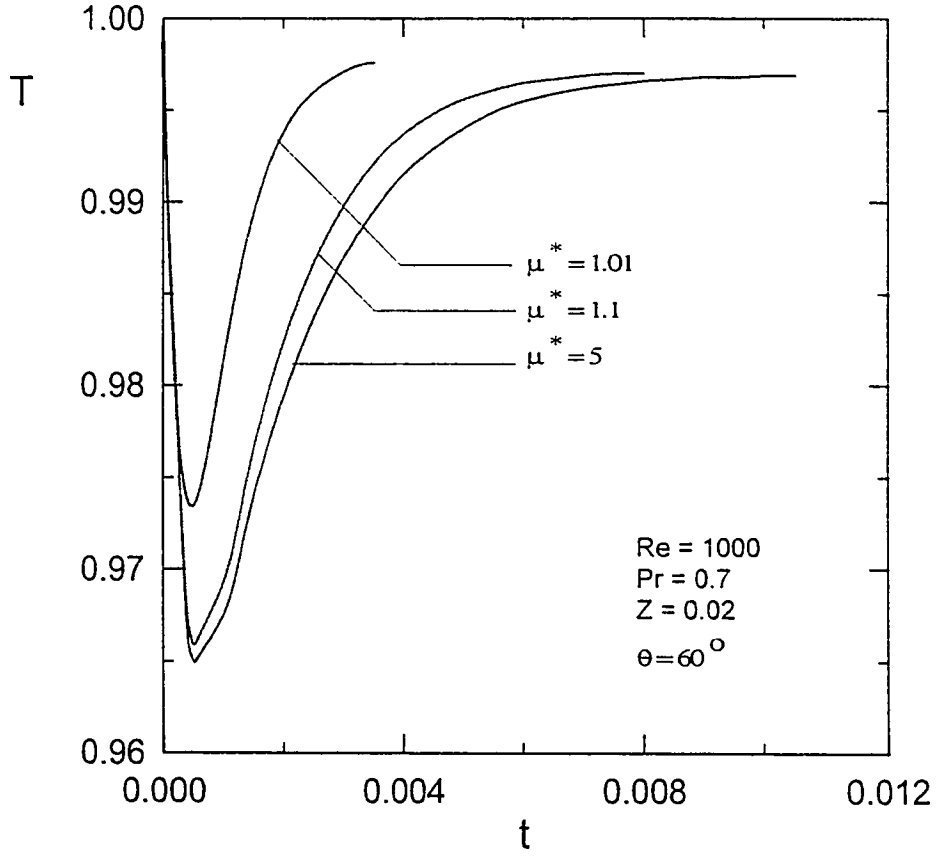

Fig. 7-14 : Effect of viscosity ratio on the temperature distribution, Z = 0.02, case (2-a)

Figures 7-15a and 7-15b show the surface temperature profiles for two selected values of Reynolds number, namely, Re = 500 in Fig. 7-15a and Re = 1000 in Fig. 7-15b . It is clear from these figures that, for a given time, the surface temperature starts with one at the front stagnation point and then decreases with θ. However, the surface temperature does not vary significantly along the surface for the initial condition used in this case where the temperature throughout the boundary layer is initially unity .

The effect of Reynolds number on the time required to reach uniform surface temperature (that can be considered a gas-phase steady state after which the external program is stopped) is presented in Fig. 7-16 for a given value of Prandtl number (Pr = 0.7) at a viscosity ratio of $\mu^* = 1.5$. It is clear from the figure that the time required to reach the uniform surface temperature increases as Reynolds number is decreased . This is attributed to the increase in heat convected to the sphere at higher Reynolds numbers.

Figure 7-17 shows the effect of viscosity ratio on the variation of surface temperature with time for a given Reynolds number Re = 1000 and at a meridional station $\theta = 60^{\circ}$. Increasing the viscosity ratio leads to less heat convected to the sphere and hence requires more time to reach the uniform surface temperature . The shortest time to reach a uniform surface temperature corresponds to the lowest viscosity ratio .

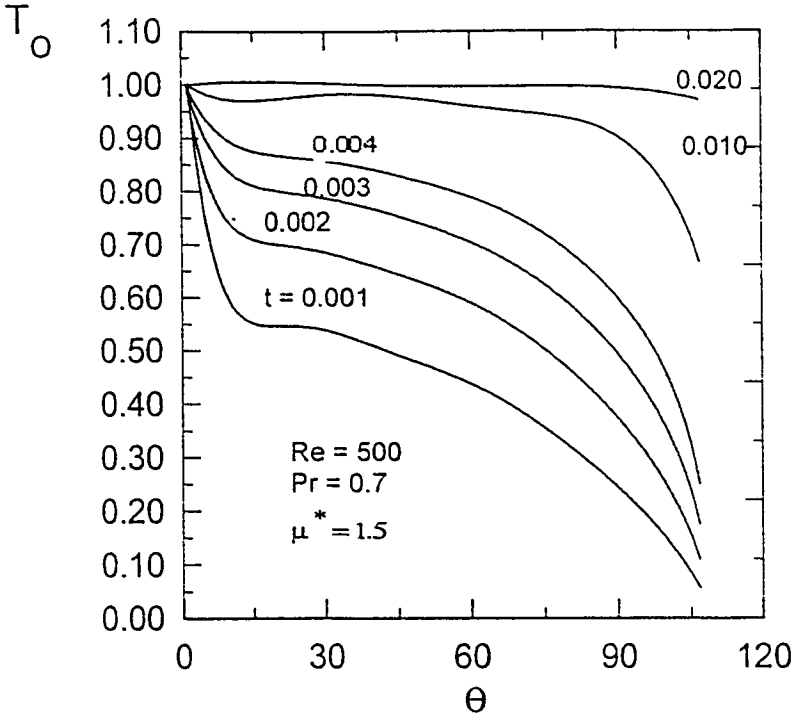

Fig. 7-15a : Transient surface temperature distribution around the sphere, Re = 500, case (2-a)

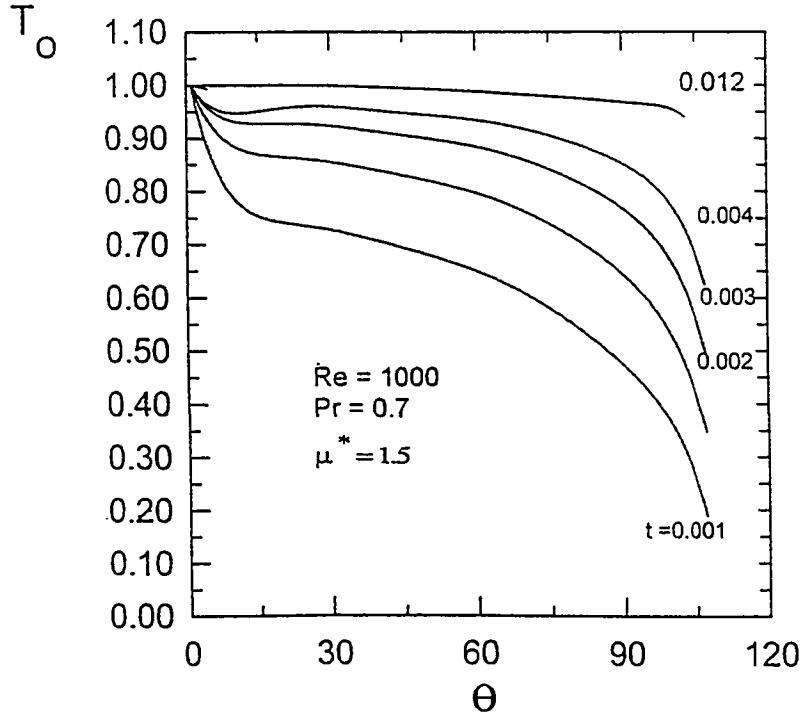

Fig. 7-15b : Transient surface temperature distribution around the sphere, Re = 1000 , case (2-a)

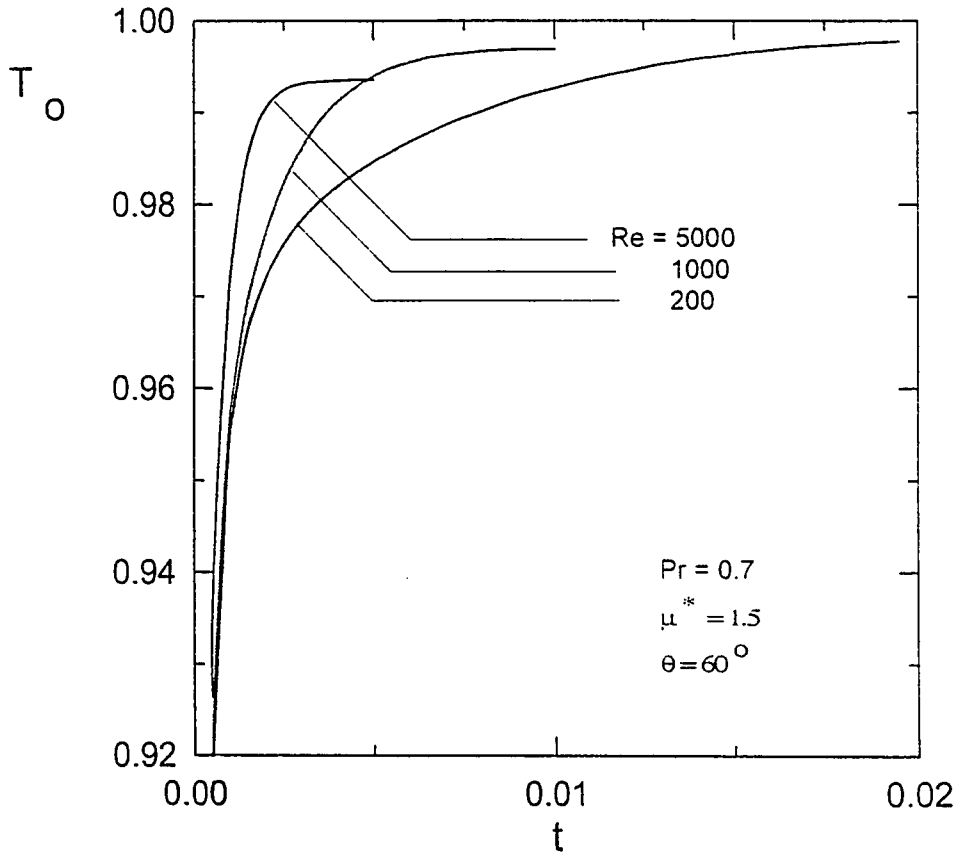

Fig. 7-16 : Effect of Reynolds number on the transient surface temperature distribution, case (2-a)

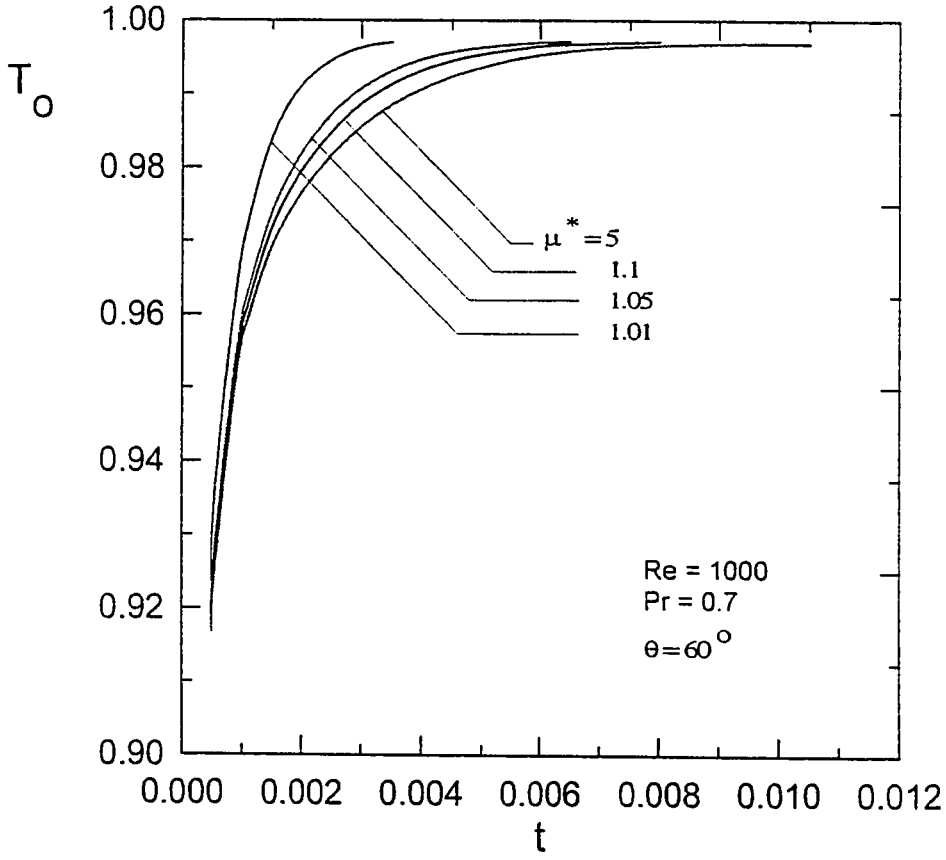

Fig. 7-17 : Effect of viscosity ratio on the transient surface temperature, case (2-a)

Increasing the value of Prandtl number increases the heat convected inward to the sphere and hence results in higher surface temperature and shorter time to attain a uniform surface temperature . This is illustrated in Fig. 7-18 where three selected values of Prandtl numbers were used (namely, Pr = 2, 0.7 and 0.01) and the shortest time to attain a uniform surface temperature and also the highest surface temperature are corresponding to Pr = 2 .

Figure 7-19 shows the transient profile of the rate of change of surface temperature with time for a given Reynolds number (Re = 1000), Prandtl number (Pr = 0.7) , viscosity ratio ($\mu^* = 1.5$) and at selected meridional angles ($\theta = 30^o, 60^o, 90^o$ and 105^o) . It is clear from the figure that the rate of change of temperature $\frac{\partial T_o}{\partial t}$ decreases with time for all angles because of the increase in the sphere's surface temperature and the thermal boundary layer till they approach unity and the rate of change of temperature diminishes . Moreover, the decrease of the rate of temperature is faster at lower angles where higher surface temperature are reported .

7.2.2.1.2 Nusselt Number

Figure 7-20 shows the transient profiles of the local Nusselt number along the surface of the sphere as we move in the meridional direction . As time elapses, the temperature of the surface of the sphere increases and hence the temperature gradient at

the surface decreases until it reaches a minute value as the surface approaches the free stream temperature . At a given time, the local Nusselt number values decrease as we move along in the meridional direction (as θ increases) . This is attributed to the increase in the boundary layer thickness that leads to decreased temperatures in the meridional direction and hence decreased temperature gradient at the surface of the sphere.

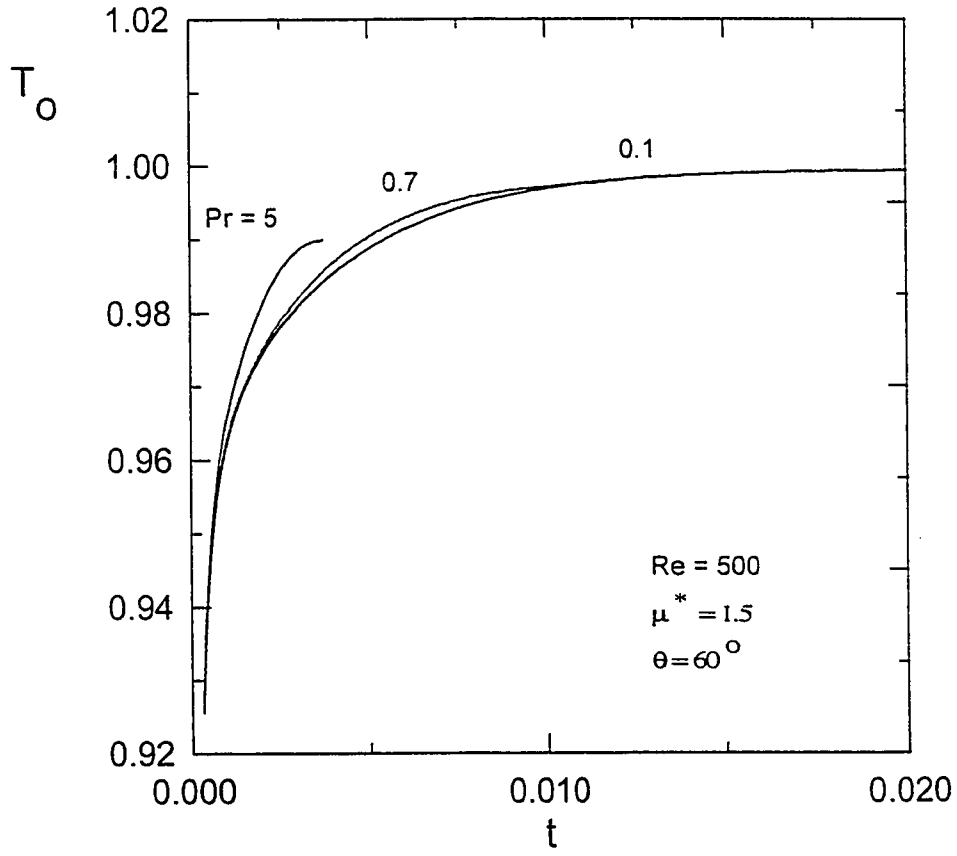

Fig. 7-18 : Effect of Prandtl number on the transient surface temperature distribution, case (2-a)

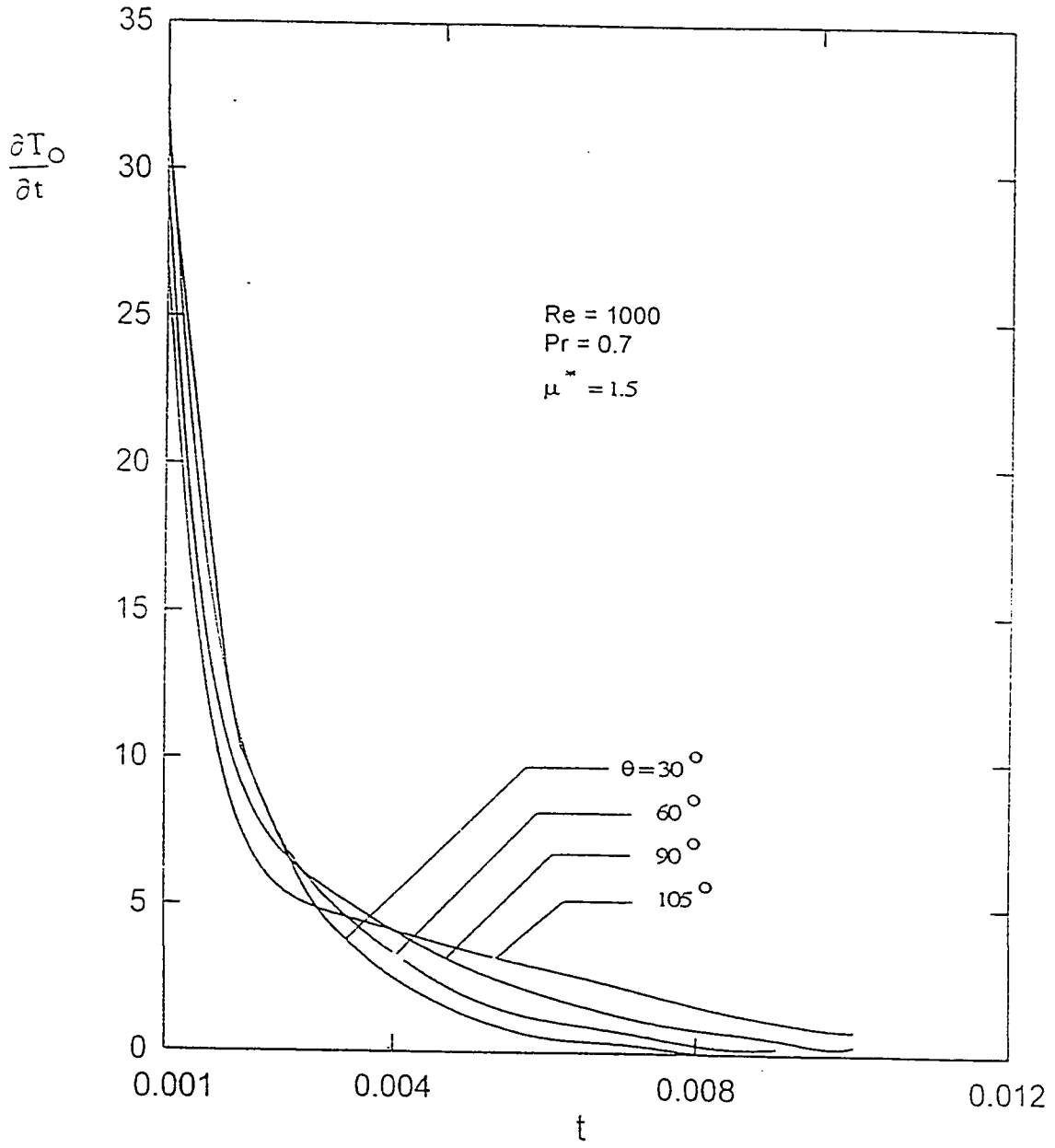

Fig. 7-19 : Rate of change of surface temperature versus time at different angles, case (2-a)

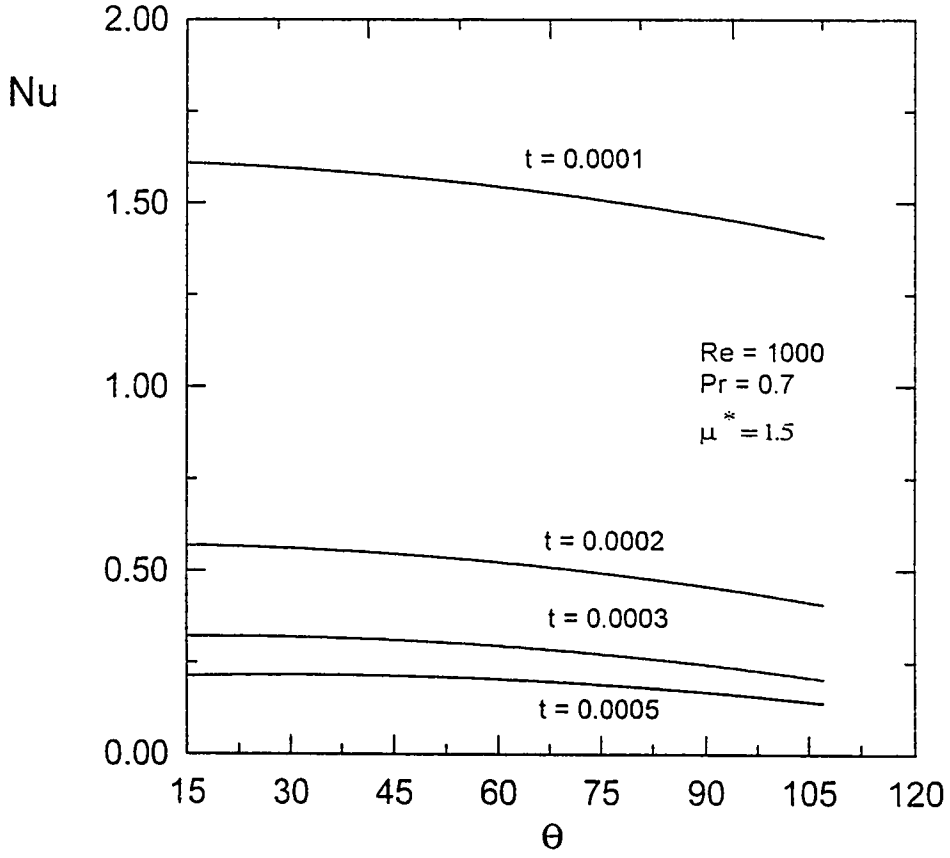

Fig. 7-20 : Transient local Nusselt number profiles along the surface of the sphere, case (2-a)

7.2.2.2 Case (2-b) : Linear Initial Temperature Profiles

In this case (2-b), the initial temperature starts from zero at the surface of the sphere and increases linearly till the edge of the thermal boundary layer where the value of the temperature is equal to unity .

7.2.2.2.1 Temperature Profiles

Figure 7-21 shows the increase in the temperature profiles around the sphere as time elapses at a given value of Reynolds slumber Re = 1000, Prandtl number Pr = 0.7, viscosity ratio $\mu^* = 1.5$ and at an angle $\theta = 60^o$. Temperature profile starts at the initial time (t = 0) then increases linearly as time elapses till it reaches the free stream value along the surface .

Figure 7-22 shows the temperature profiles at a particular time t = 0.0005, a given Reynolds number Re = 1000, Prandtl number Pr = 0.6 and viscosity ratio $\mu^* = 1.5$ for selected meridional stations . Higher temperature at the same radial location Z are corresponding to earlier angles and decreases as we move along the sphere surface in the meridional direction since the temperature has a maximum value of 1 at the front stagnation point (zero boundary-layer thickness) and then decreases as the boundary layer thickness increases in the meridional direction .

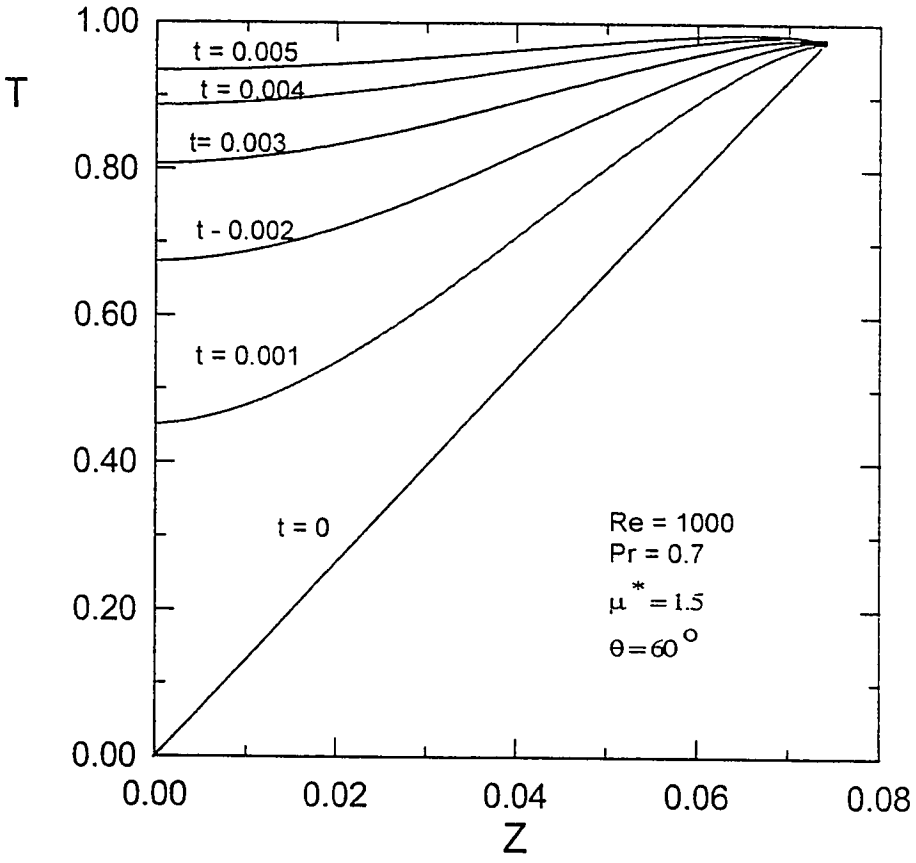

Fig. 7-21 : Transient temperature profiles around the sphere, case (2-b)

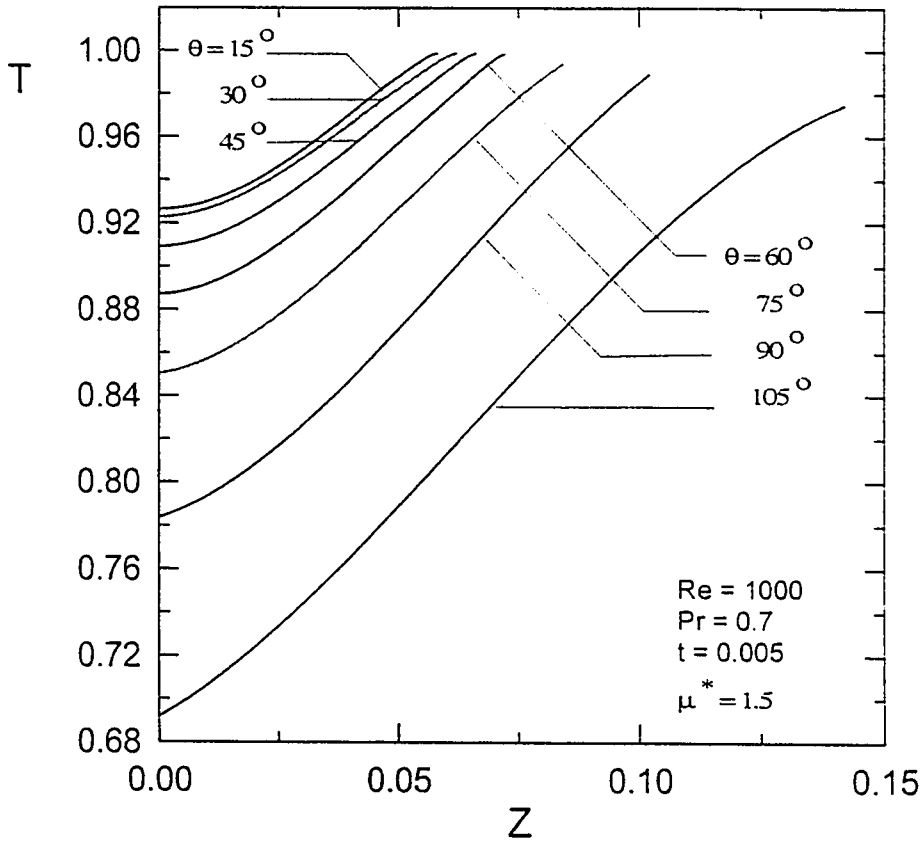

Fig. 7-22 : Temperature profiles at different angles, t = 0.005, case (2-b)

Figure 7-23 illustrates the effect of increasing Reynolds number on the temperature profiles for given values of Prandtl number Pr = 0.7, viscosity ratio $\mu^* = 1.5$, angle $\theta = 60^o$. It is clear from the figure that increasing Reynolds number leads to higher values of the temperature due to the increase in heat convected at a fixed radial distance . Hence shorter times are required to reach the uniform surface temperature at higher Reynolds numbers .

Figure 7-24 shows the effect of Reynolds number on the time required to reach the uniform surface temperature for two given values of the viscosity ratio ($\mu^* = 1.05$ and 1.5) and at a given value of Prandtl number Pr = 0.7 . Decreasing the values viscosity ratio leads to shorter times required to reach the uniform surface temperature due to the increase in convected heat transfer , similar to the effect of increasing Re .

Transient surface temperature profiles are shown in Fig. 7-25a and 7-25b for Re = 500 and Re = 1000 respectively . For all the profiles, surface temperature starts with unity at the front stagnation point ($\theta = 0$) and decreases in the meridional direction till the point of external flow separation . It is also clear from both figures that the surface temperature increases with time till it reaches a uniform value that is equal to the free stream temperature (T = 1) in time t = 0.012 for Re = 500 and t = 0.008 for the higher Reynolds number case (Re = 1000) .

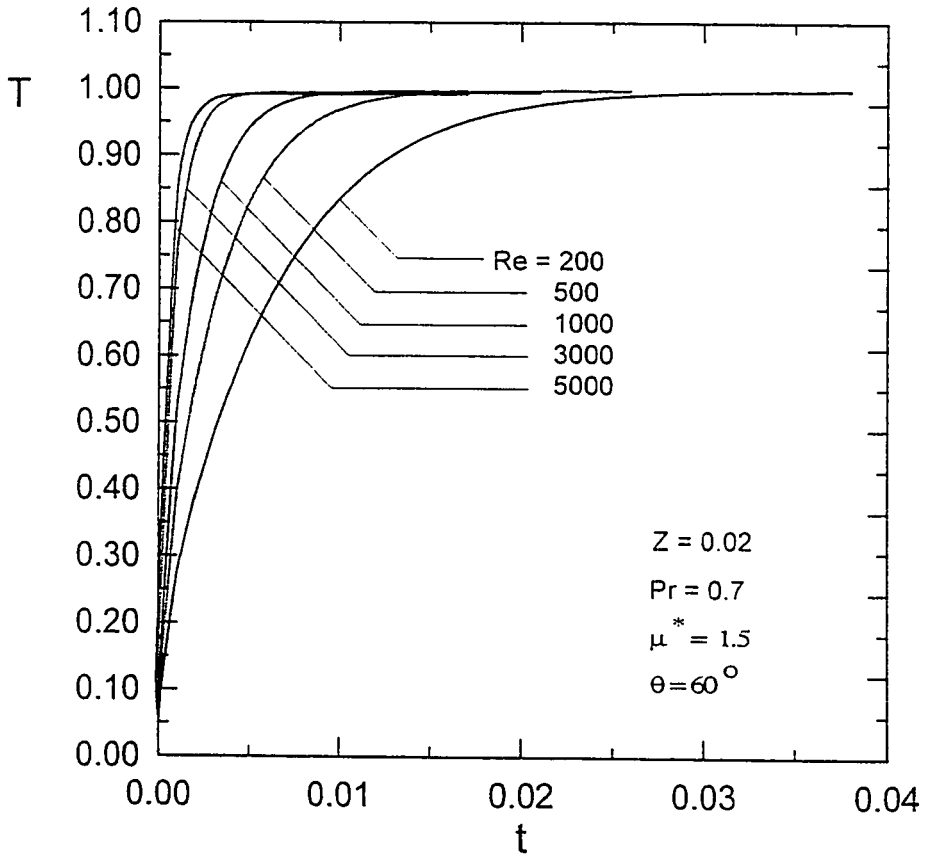

Fig. 7-23 : Effect of Reynolds number on the transient temperature profiles at a fixed radial distance (Z = 0.02), case (2-b)

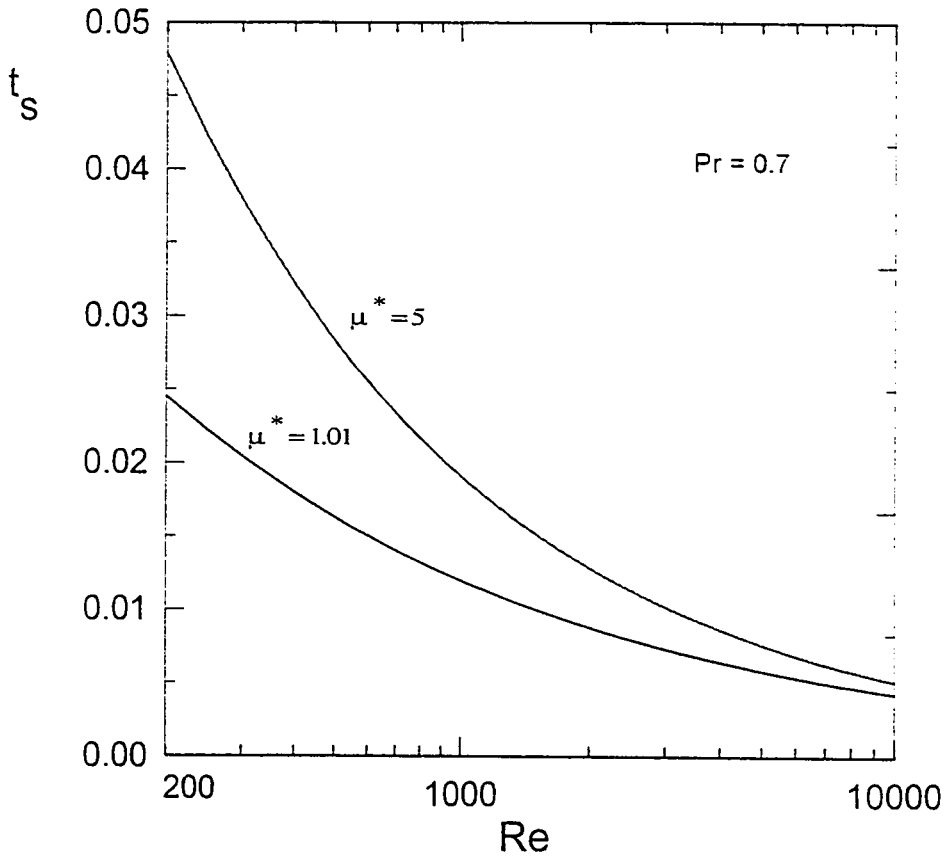

Fig. 7-24 : Effect of Reynolds number on the time required to reach uniform surface temperature, case (2-b)

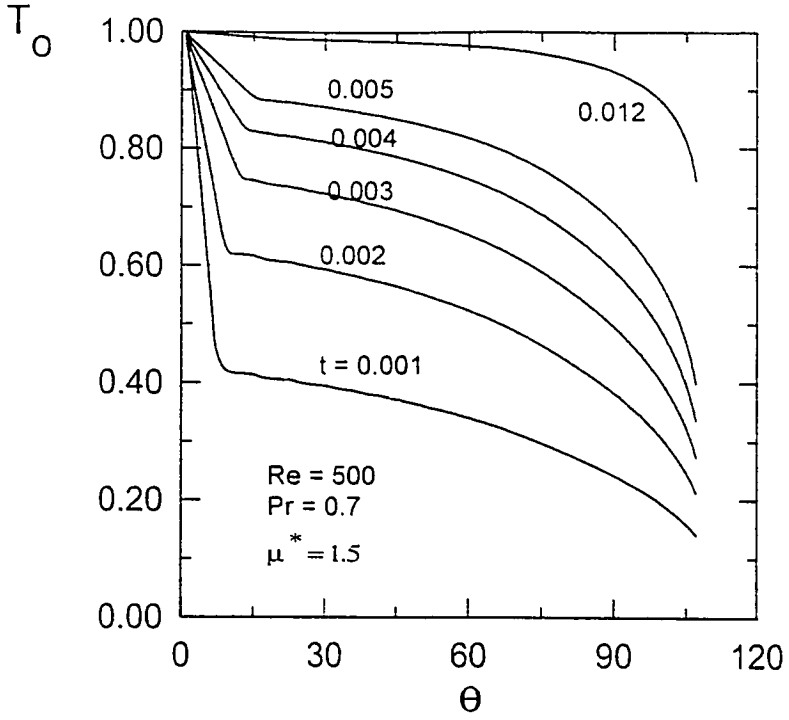

Fig. 7-25a : Transient surface temperature at different times for Re = 500, case (2-b)

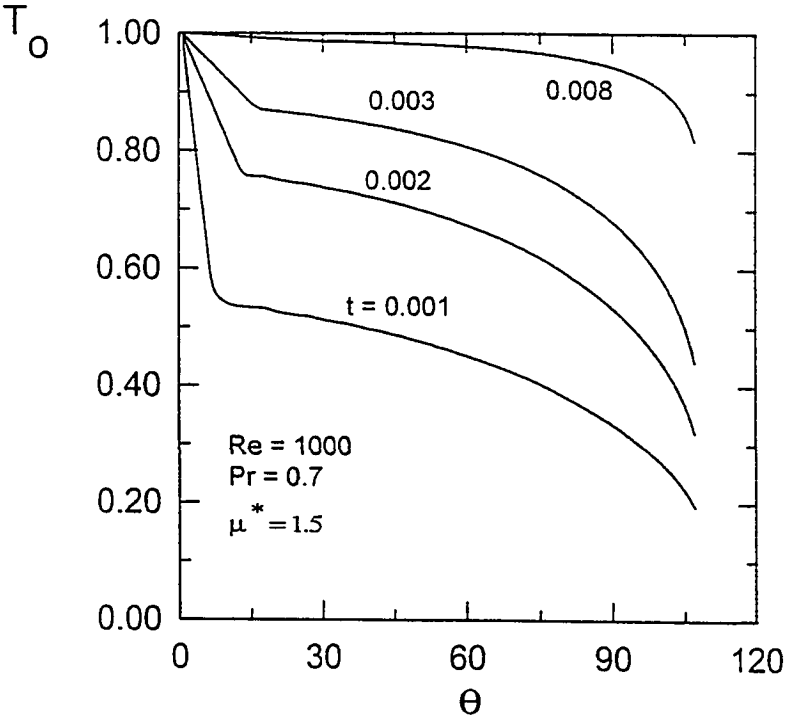

Fig. 7-25b : Transient surface temperature at different times for Re = 1000, case (2-b)

Figure 7-26 shows the effect of Reynolds number on the transient surface temperature profiles . Higher Reynolds numbers result in higher surface temperatures at a given time and hence shorter time are required to reach the free stream value for high Re.

The effect of viscosity ratio on the transient surface temperature profile is illustrated in Fig. 7-27 for a given Reynolds number Re = 1000, Prandtl number Pr = 0.7 and meridional angle ($\theta = 60^{o}$) . The figure shows that lower viscosity ratios lead to higher surface temperature and shorter time required to reach the free stream temperature, and hence higher rates of heat convected to the sphere .

The effect of Prandtl number on the surface temperature is showed in Fig. 7-28 for a given Reynolds number Re = 1000, viscosity ratio $\mu^{*} = 1.5$ and meridional angle $\theta = 60^{o}$. Higher Prandtl numbers (i.e. higher heat convection to the sphere) any given time t result in higher surface temperature .

Figure 7-29 presents the transient profile of the rate of change of surface temperature with time for a given Reynolds number (Re = 1000), Prandtl number (Pr = 0.7) , viscosity ratio ($\mu^{*} = 1.5$) and at selected meridional angles ($\theta = 30^{o}$, 60^{o}, 90^{o} and 105^{o}) . It is clear from the figure that the rate of change of temperature $\frac{\partial T_{o}}{\partial t}$ decreases with time for all presented angles because of the increase in the dimensionless surface

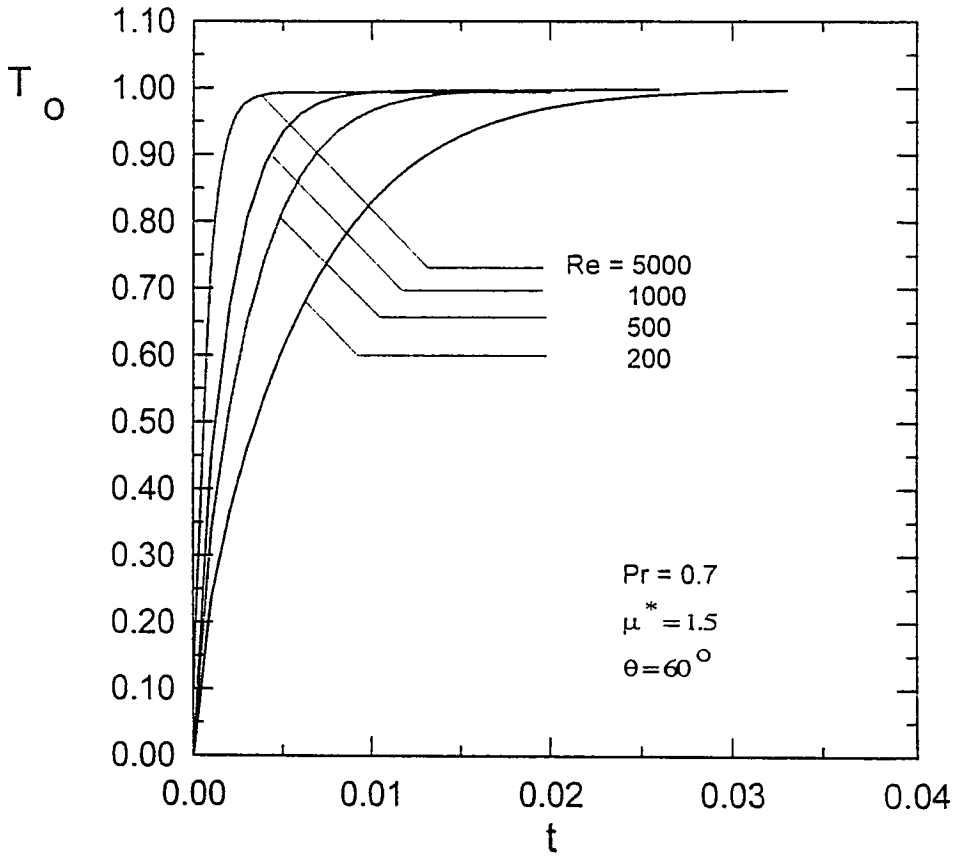

Fig. 7-26 : Effect of Reynolds number on the transient surface temperature profiles, case (2-b)

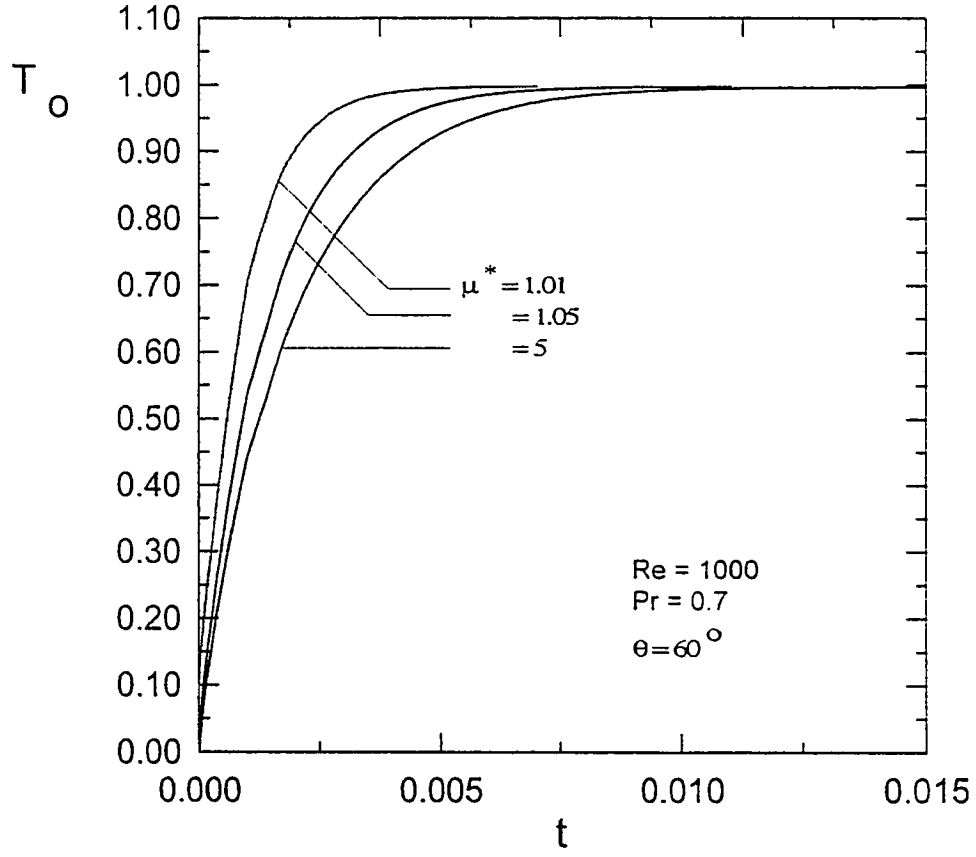

Fig. 7-27 : Effect of viscosity ratio on the transient surface temperature profiles, case (2-b)

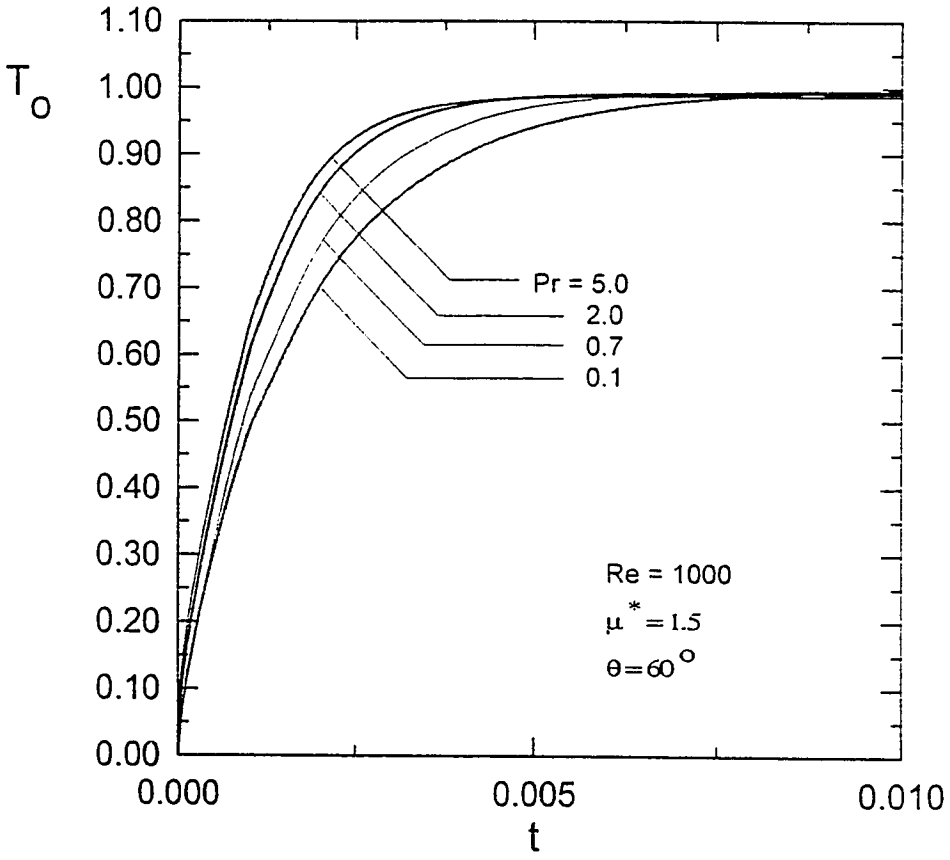

Fig. 7-28: Effect of Prandtl number on the transient surface temperature profile, case (2-b)

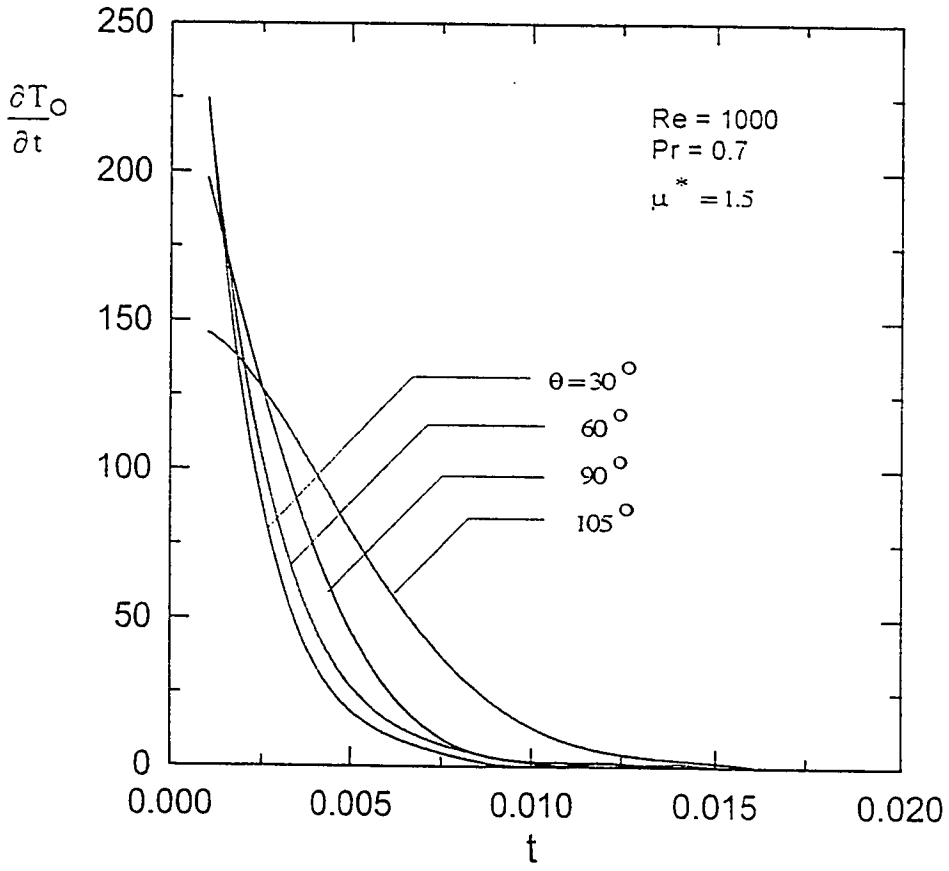

Fig. 7-29 : Rate of change of surface temperature versus time at different central angles, case (2-b)

temperature and the thermal boundary layer till they approach unity at the state of uniform surface temperature and the rate of change of temperature diminishes . Furthermore, the decrease of the rate of temperature is faster at lower angles where higher surface temperature are reported .

7.2.2.2.2 Nusselt Number

Figure 7-30 presents the transient local Nusselt number along the surface of the sphere . For any given time t, the value of the local Nusselt number decreases as one moves along the surface of the sphere in the meridional direction due to the increase in the boundary layer thickness and the decrease in the values of the temperature . Nusselt number profile also decreases with time due to the increase in the surface temperature as time elapses .

7.2.2.3 Case (2-c) : A Step Change in Temperature at the Boundary-Layer Edge

In this section the case where the initial temperature throughout the boundary layer is equal to zero while its value at the boundary layer edge is unity is presented, i.e., a step change in the value of the temperature from zero to unity occurs at the edge of the boundary layer .

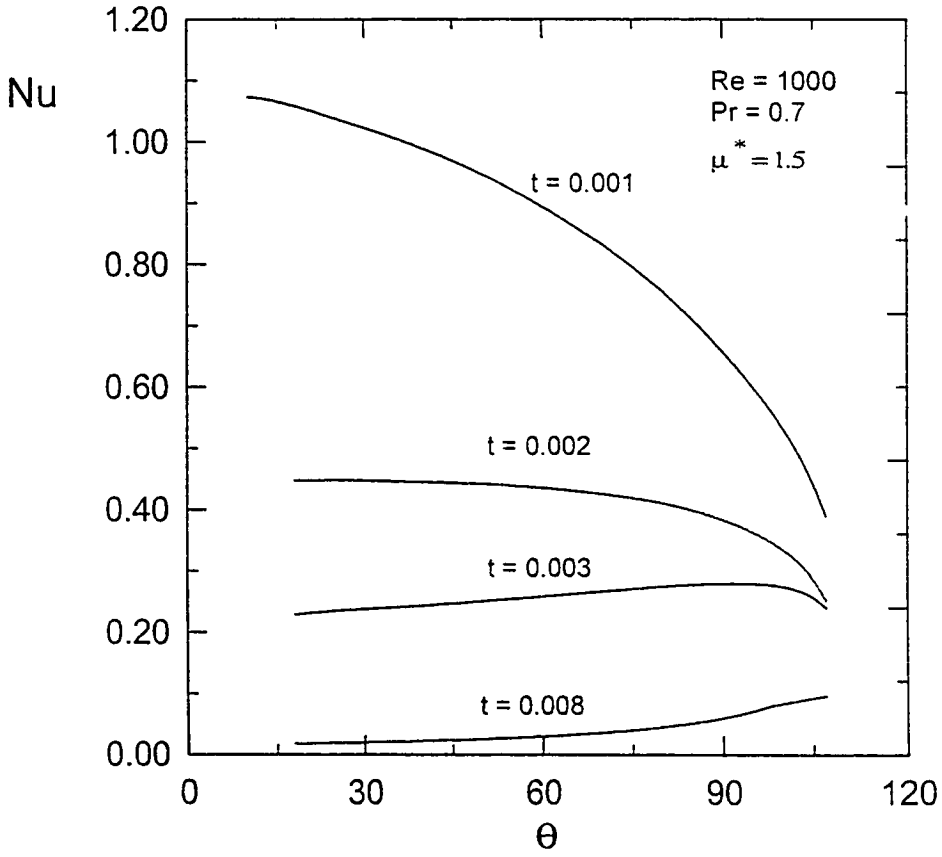

Fig. 7-30 : Transient profiles of local Nusselt number along the surface of the sphere, case (2-b)

7.2.2.3.1 Temperature Profiles

Figures 7-31a through 7-31f, 7-32a through 7-32f and 7-33a through 7-33f present the transient increase in temperature inside the thermal boundary layer as one rotates around the sphere at different radial locations (Z) from $\theta = 30^{o}$ up to $\theta = 105^{o}$ (this angle is just before the point of external flow separation) . In these figure. temperature profiles are presented for Prandtl number (Pr = 0.7), viscosity ratio ($\mu^{*} = 1.5$) and three selected values of Reynolds number, namely, Re = 200, 1000 and 10000 respectively . It is clear from these figures that the dimensionless surface temperature starts from zero and then increases both with time and along the surface till it reaches a uniform value which is equal to the free stream temperature . For a given time, higher values of temperature are noticed for earlier angles since the boundary layer thickness starts from zero at the front stagnation point ($\theta = 0$) where the surface temperature theoretically equals the free stream value and then the boundary layer thickness increases as one moves along the surface of the. The effect of Reynolds number on the time required to reach the state of uniform surface temperature (equal to the free stream temperature within a certain numerical tolerance) can be seen from these three sets of figures . For high Reynolds number (Re = 10000) this time is 0.001, for Re = 1000, time is 0.007 while it equals 0.03 for the low Reynolds number (Re = 200) . This is attributed to the increase in convective heat transfer as Reynolds number increases .

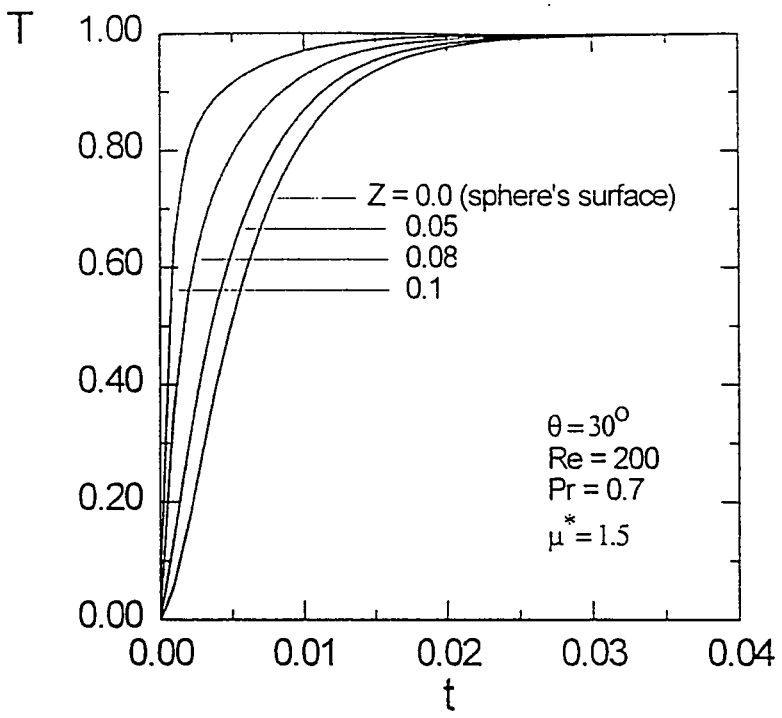

Fig. 7-31a :Transient temperature distribution at different radial distances for $\theta = 30^{o}$ and Re = 200, case (2-c)

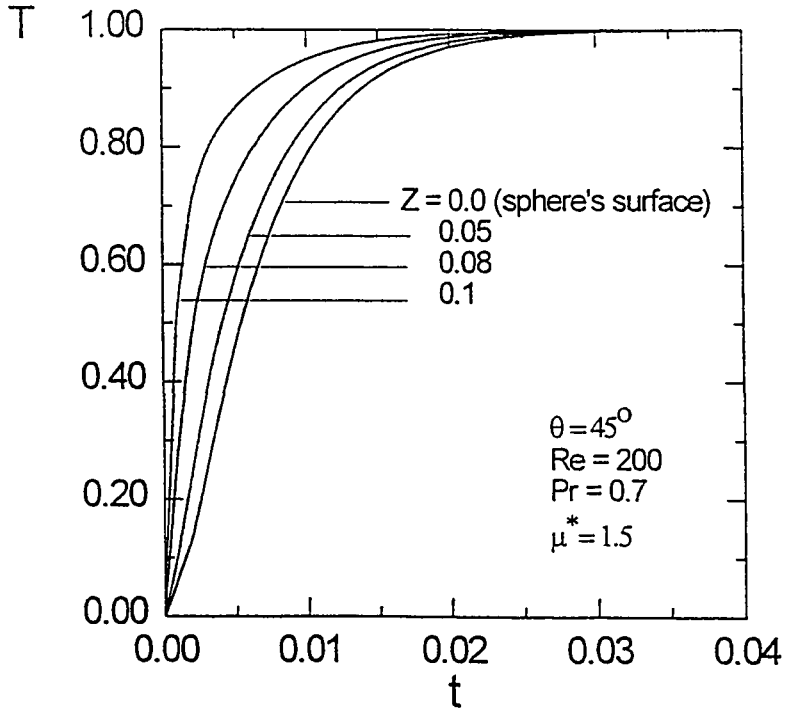

Fig. 7-31b :Transient temperature distribution at different radial distances for $\theta = 45^{o}$ and Re = 200, case (2-c)

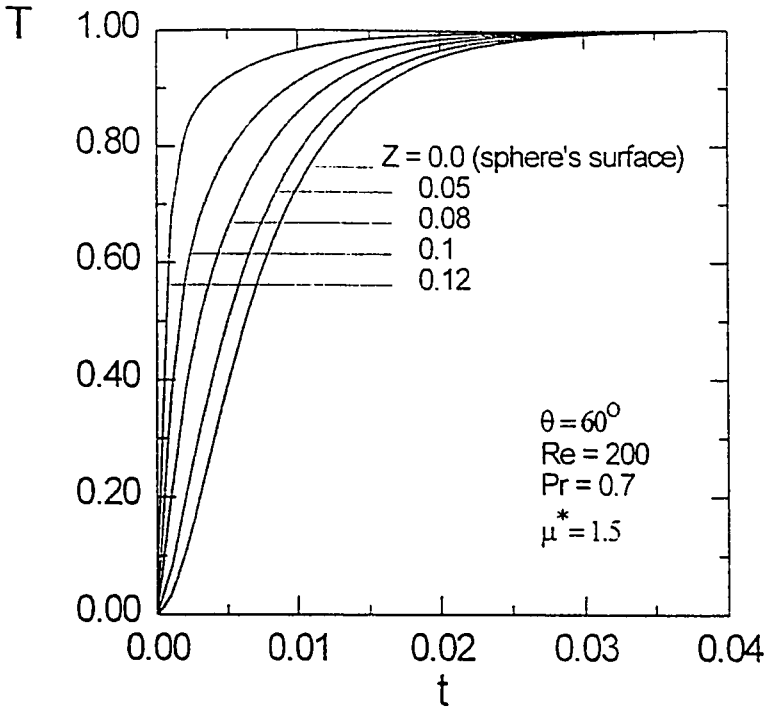

Fig. 7-31c :Transient temperature distribution at different radial distances for $\theta = 60^{o}$ and Re = 200, case (2-c)

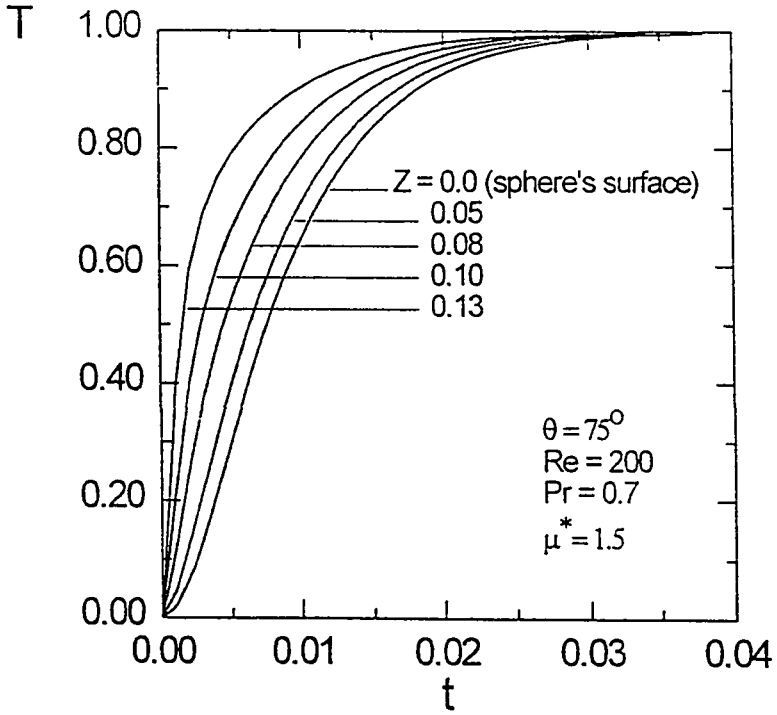

Fig. 7-31d :Transient temperature distribution at different radial distances for $\theta = 75^{o}$ and Re = 200, case (2-c)

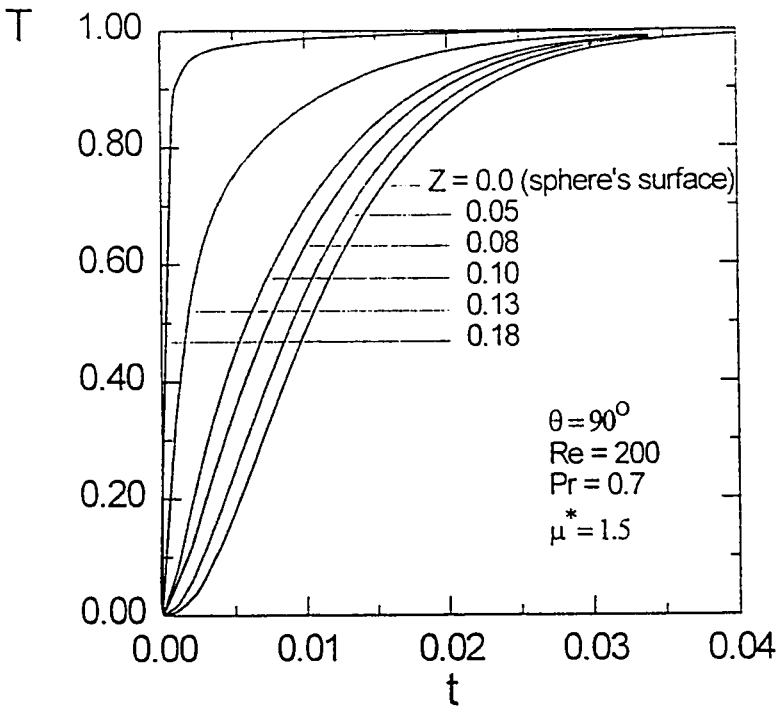

Fig. 7-31e :Transient temperature distribution at different radial distances for $\theta = 90^{o}$ and Re = 200, case (2-c)

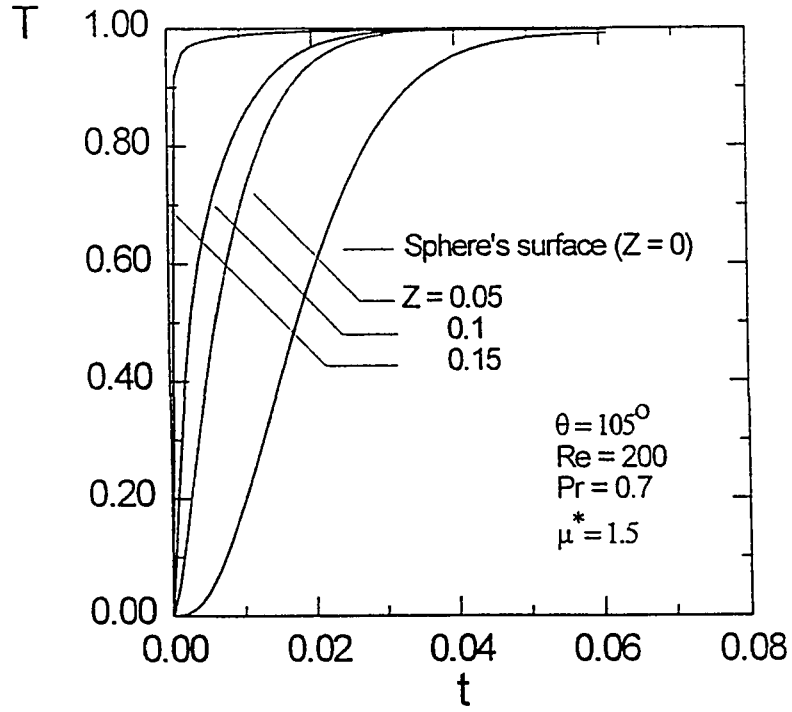

Fig. 7-31f :Transient temperature distribution at different radial distances for $\theta = 105^{o}$ and Re = 200, case (2-c)

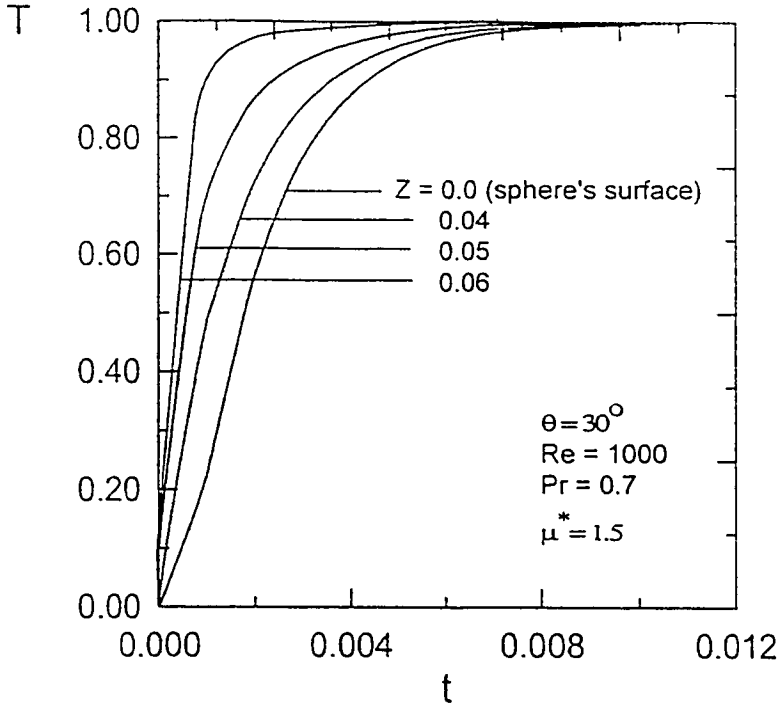

Fig. 7-32a :Transient temperature distribution at different radial distances for $\theta = 30^{o}$ and Re = 1000, case (2-c)

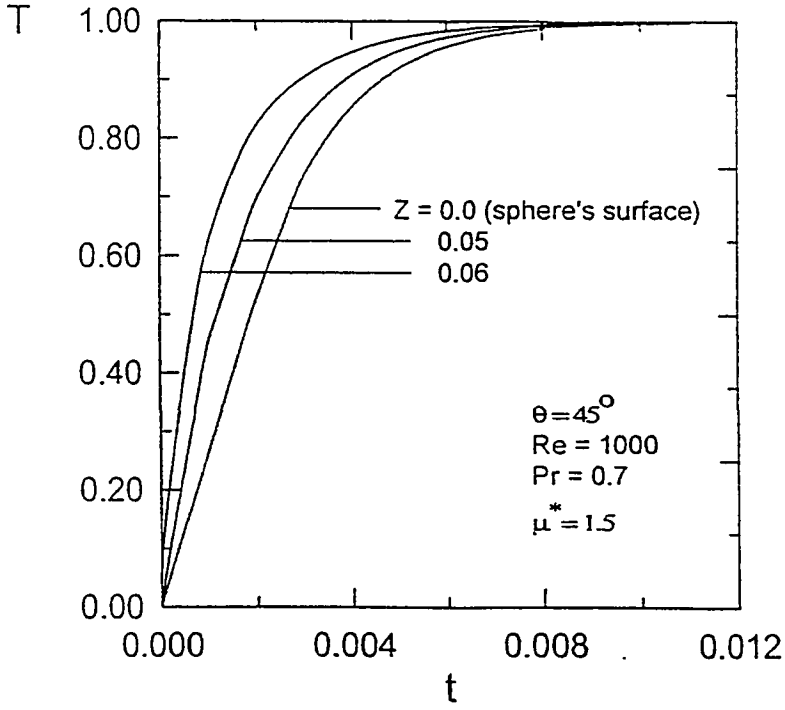

Fig. 7-32b :Transient temperature distribution at different radial distances for $\theta = 45^{o}$ and Re = 1000, case (2-c)

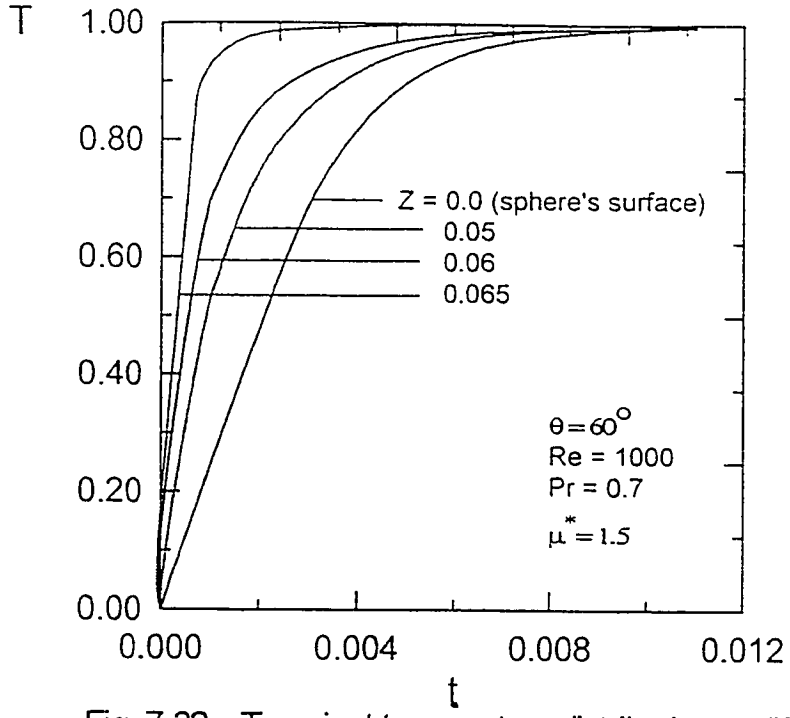

Fig. 7-32c :Transient temperature distribution at different radial distances for $\theta = 60^{o}$ and Re = 1000, case (2-c)

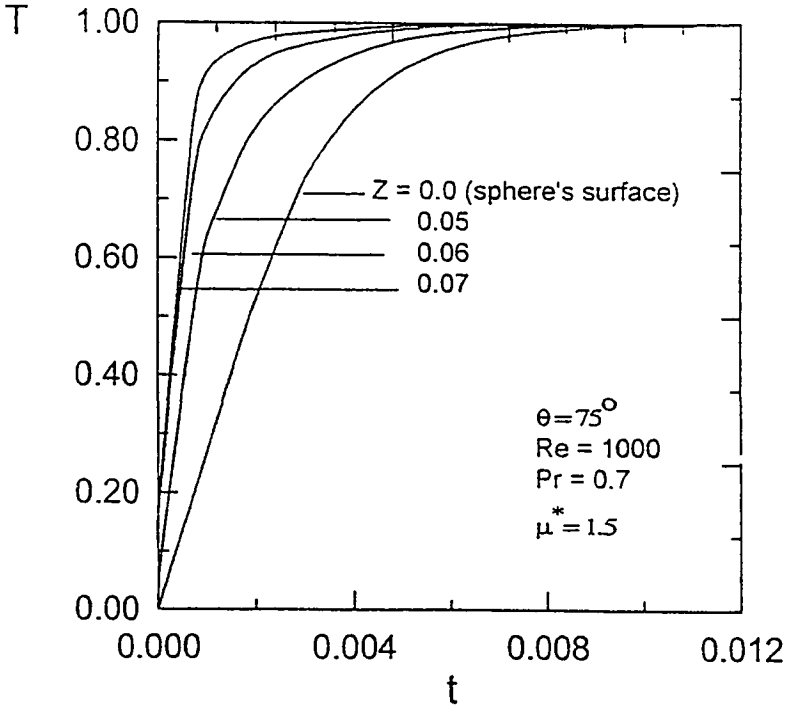

Fig. 7-32d :Transient temperature distribution at different radial distances for $\theta = 75^{o}$ and Re = 1000, case (2-c)

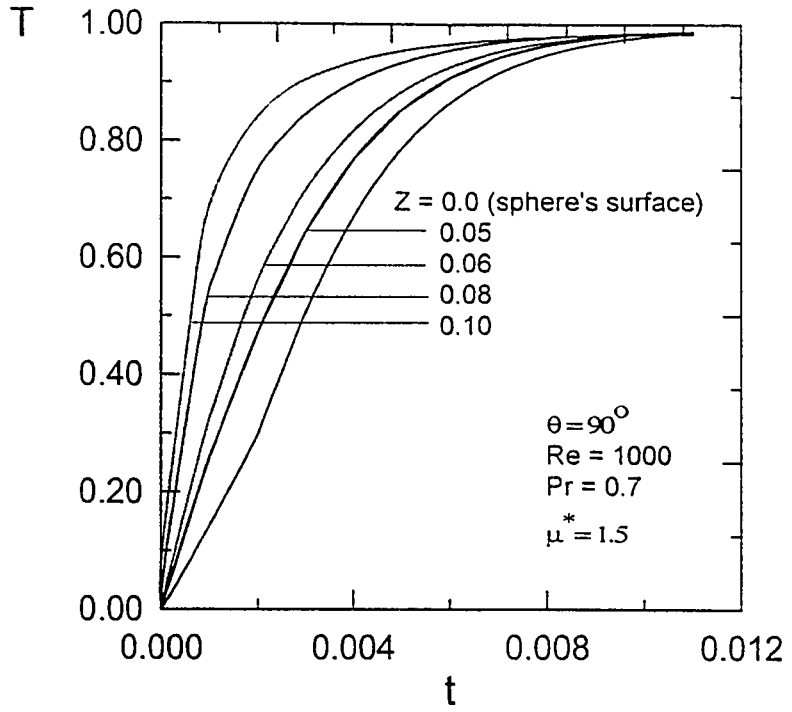

Fig. 7-32e :Transient temperature distribution at different radial distances for $\theta = 90^{O}$ and Re = 1000, case (2-c)

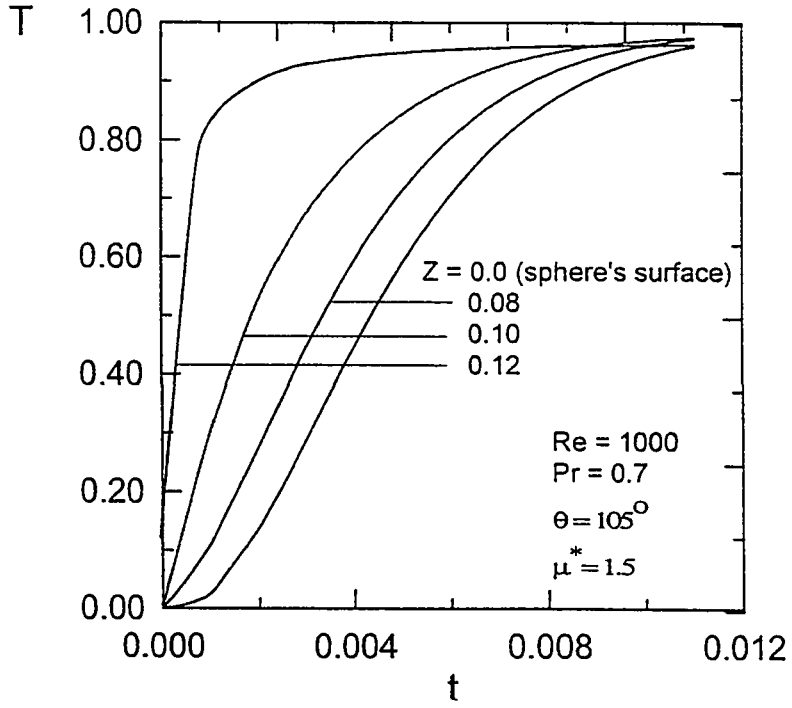

Fig. 7-32f :Transient temperature distribution at different radial distances for $\theta = 105^{O}$ and Re = 1000, case (2-c)

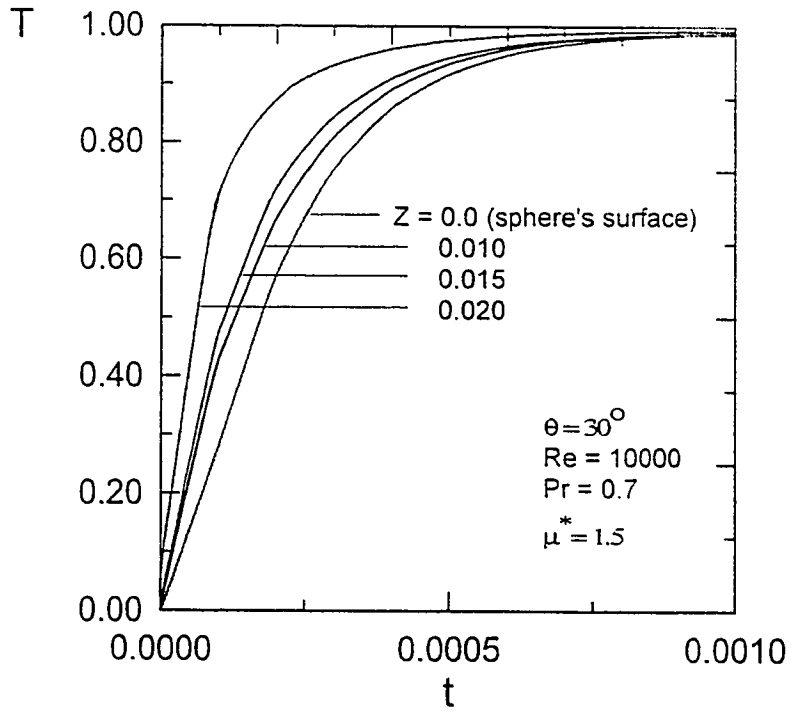

Fig. 7-33a :Transient temperature distribution at different radial distances for $\theta = 30^{O}$ and Re = 10000, case (2-c)

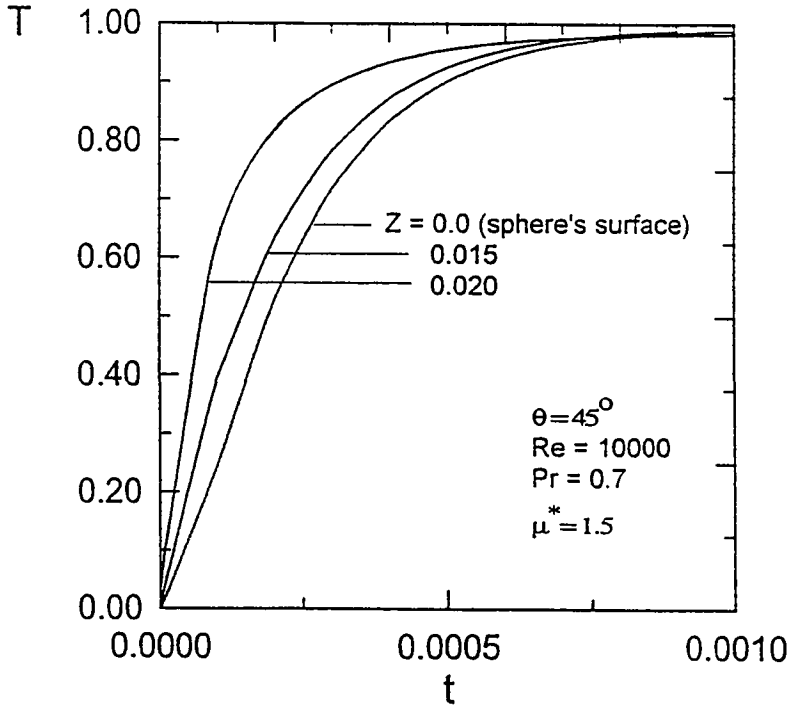

Fig. 7-33b :Transient temperature distribution at different radial distances for $\theta = 105^{O}$ and Re = 10000, case (2-c)

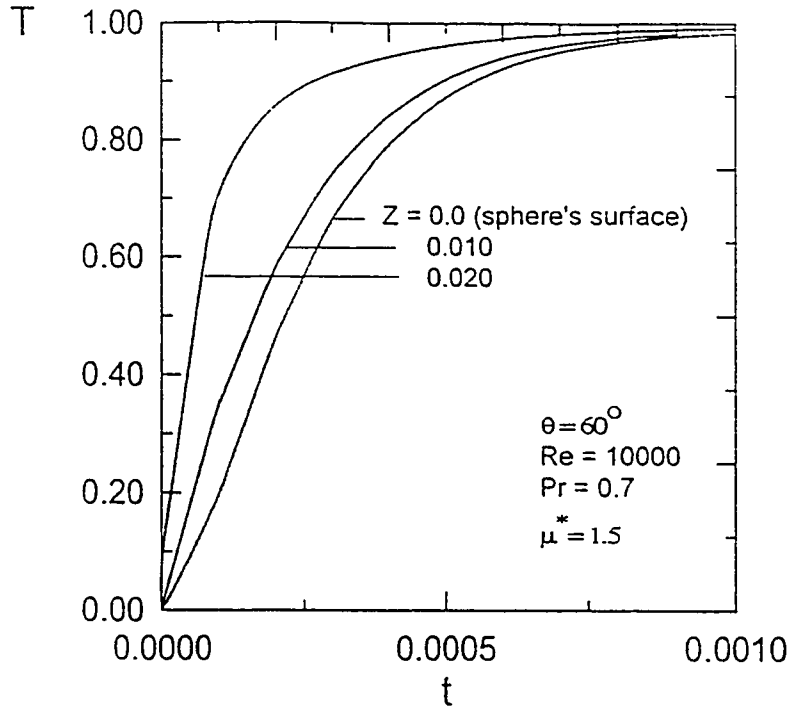

Fig. 7-33c : Transient temperature distribution at different radial distances for $\theta = 60^{o}$ and Re = 10000, case (2-c)

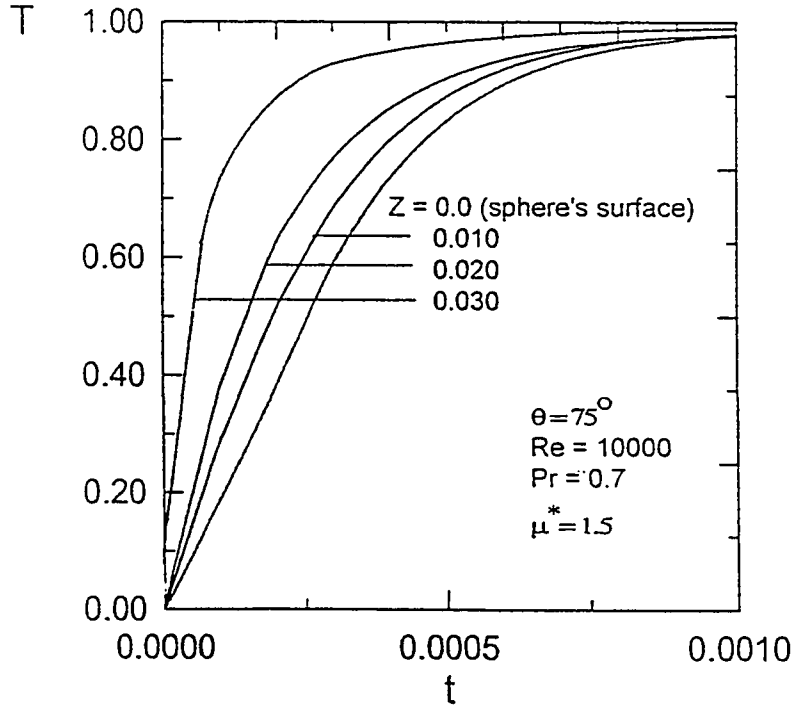

Fig. 7-33d :Transient temperature distribution at different radial distances for $\theta = 75^{o}$ and Re = 10000, case (2-c)

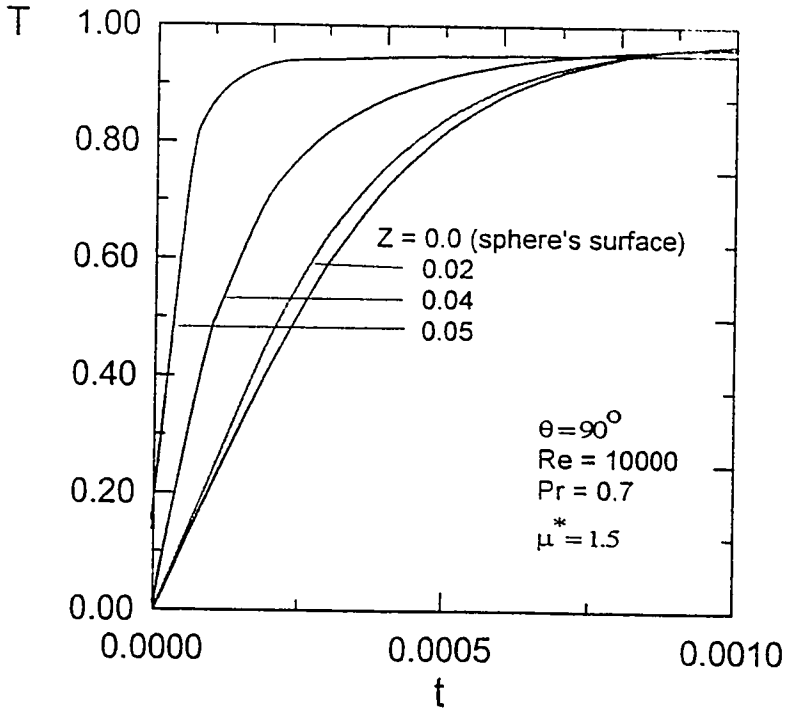

Fig. 7-33e :Transient temperature distribution at different radial distances for $\theta = 90^{O}$ and Re = 10000, case (2-c)

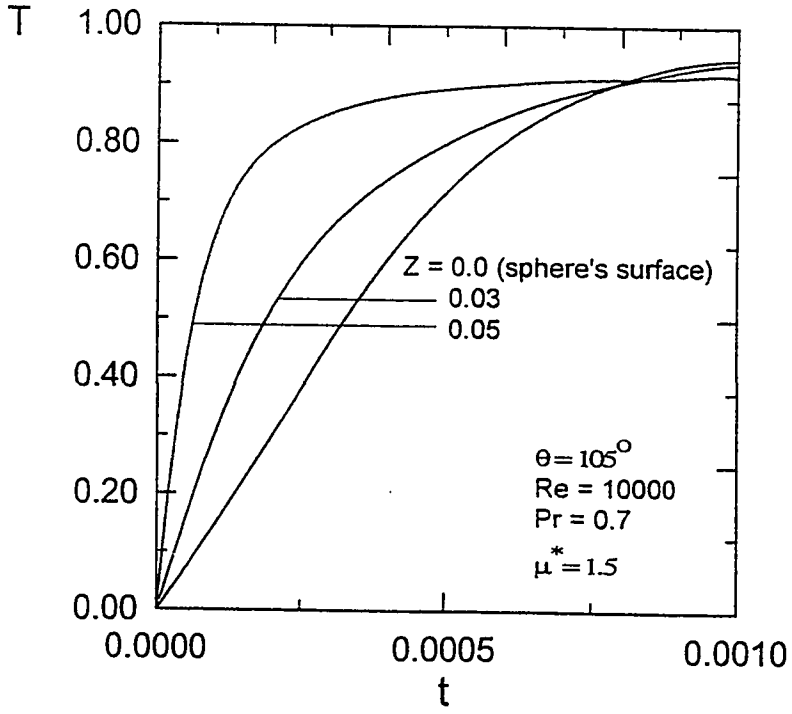

Fig. 7-33f :Transient temperature distribution at different radial distances for $\theta = 105^{O}$ and Re = 10000, case (2-c)

Figure 7-34 shows the development of the transient temperature profiles inside the boundary layer for given values of Reynolds number (Re = 1000), Prandtl number (Pr = 0.7) , viscosity ratio (μ^* = 1.5) and meridional angle ($\theta = 60^o$) . Such profiles can be obtained by cross plotting in Fig. 7-31c . Dimensionless temperature (T) starts initially from zero at the surface of the sphere while the free stream temperature has a value of T=1 . As time proceeds, the temperature increases inside the boundary layer and the temperature of the surface of the sphere increases each time increment until it approaches the free stream value . Such a uniform surface temperature is achieved in Fig. 7-33 when the time t = 0.007 then the external flow program is stopped .

Figure 7-35 shows the temperature profiles for some selected meridional stations under the same conditions stated formerly (the same values of the controlling parameters; Re, Pr and μ^*) and for t = 0.005 . This figure shows the variation in the temperature profiles as the hydrodynamic boundary-layer thickness increases along the surface of the sphere until the maximum boundary layer thickness is encountered near to the point of flow separation . It is clear from Fig. 7-35 that the temperature decreases at the same radial distance as the meridional angle increases as a result of the increase in the boundary layer thickness with θ .

The effect of Reynolds number on the developing temperature profiles while the other controlling parameters are kept unchanged is shown in Fig. 7-36 at a fixed radial distance (Z = 0.02) . It is clear from this figure that increasing the value of Reynolds

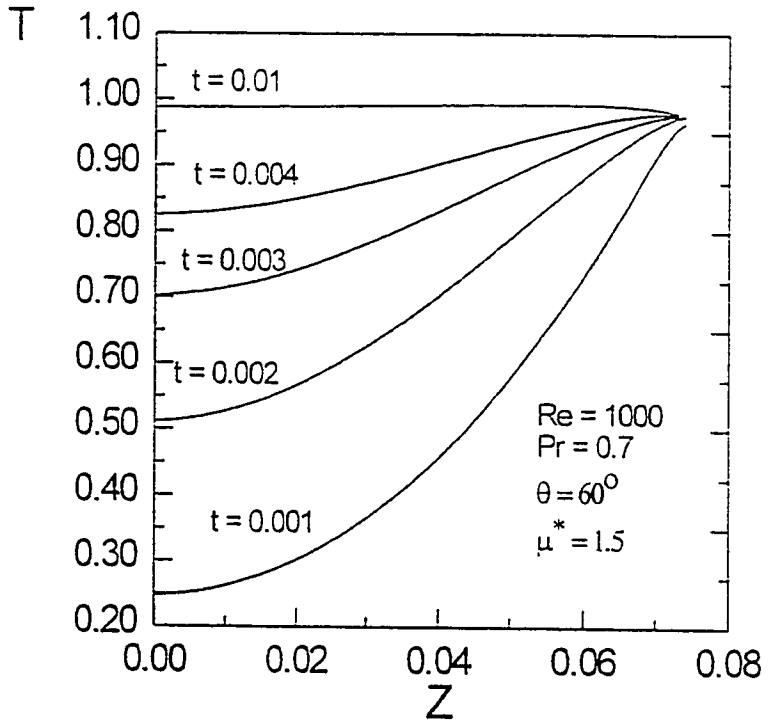

Fig. 7-34 : Transient temperature profiles for $\theta = 60^{\circ}$, case (2-c)

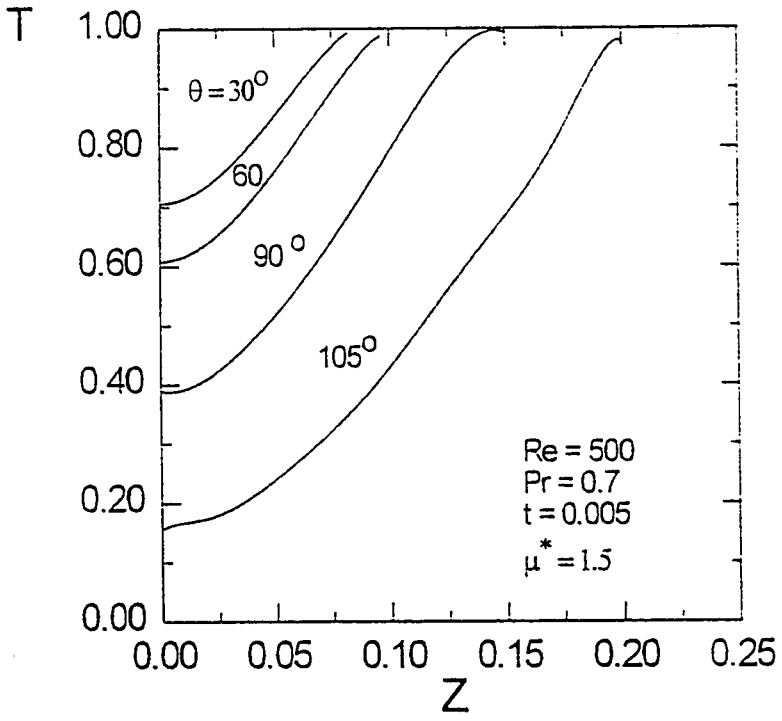

Fig. 7-35 : Temperature distribution at different angles, (t = 0.005), case (2-c)

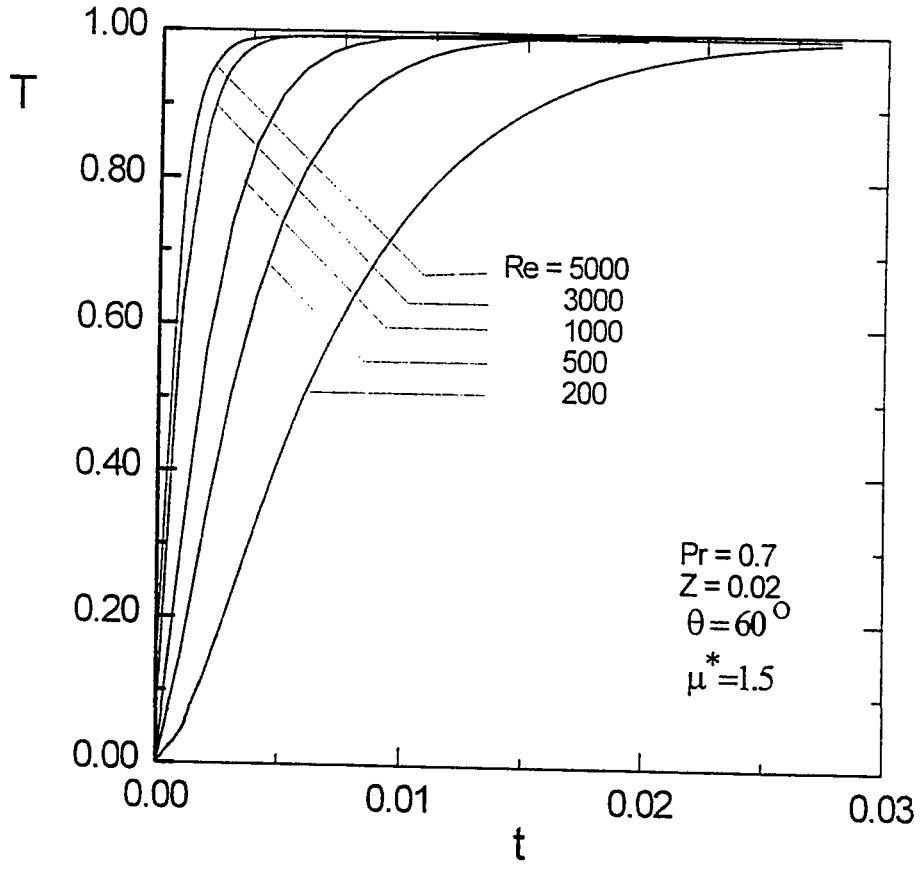

Fig. 7-36 : Effect of Reynolds number on the temperature distribution at a fixed radial distance (Z=0.02), case (2-c)

number increases the rate of heat transfer from the hot surrounding to the cold sphere and so decreases the time required to reach the state of uniform surface temperature . This effect is due to the thinning of the boundary layer which has already been discussed in chapter 6 .

Figure 7-37 summarizes this result by showing the effect of increasing Reynolds number on the time required to attain uniform surface temperature for three selected values of the interior-to-exterior viscosity ratio, namely 1.01, 1.05 and 5 . The time required to reach a uniform surface temperature (equal to its free stream value) increases as Reynolds number decreases

The effect of changing Prandtl number on the temperature profiles at a particular time (t = 0.005) for a given $\theta = 60^{\circ}$ is shown in Fig. 7-38 for three values of Prandtl number (Pr = 0.1, 0.7 and 2) . It is clear from this figure that increasing Prandtl number increases the heat convected to the sphere and hence results in higher values of the temperature at the same radial distance .

Figure 7-39 shows the effect of changing the viscosity ratio on the transient temperature profile at a selected time (t = 0.005) at meridional angle ($\theta = 60^{\circ}$) . The figure shows that increasing the internal-to-external viscosity ratio decreases the heat convected to the sphere and hence it results in lower values of the temperature at the same radial distance . This is attributed to the decrease in boundary layer velocities at higher

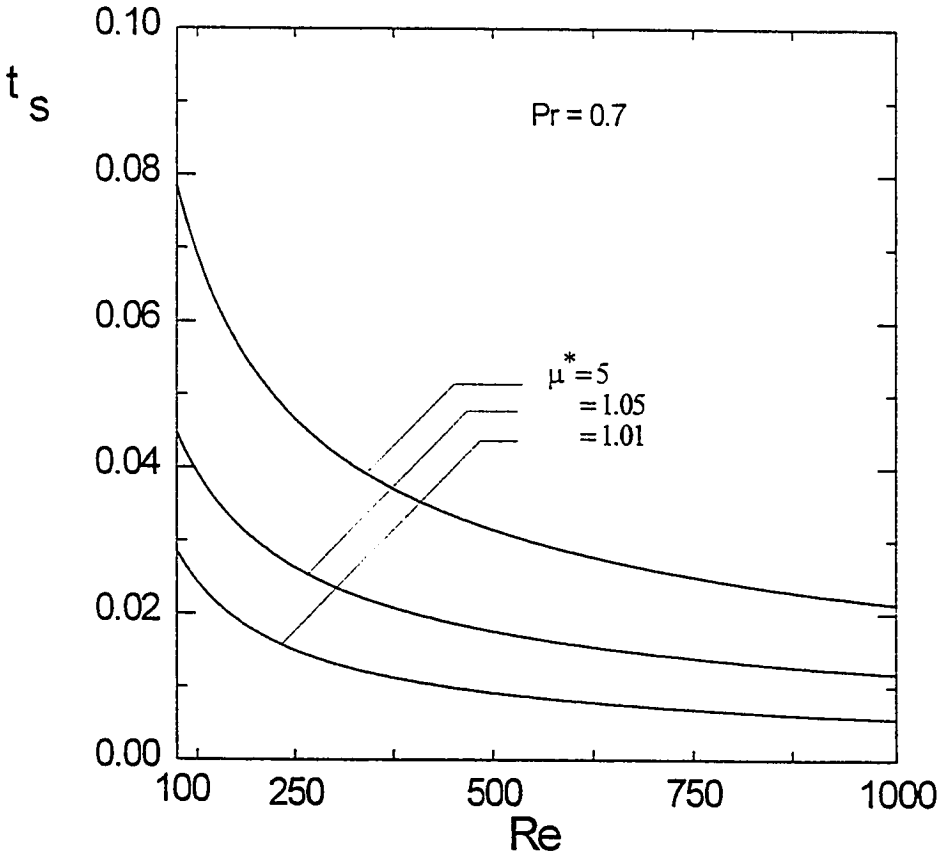

Fig. 7-37 : Effect of Reynolds number on the time required to reach uniform surface temperature, case (2-c)

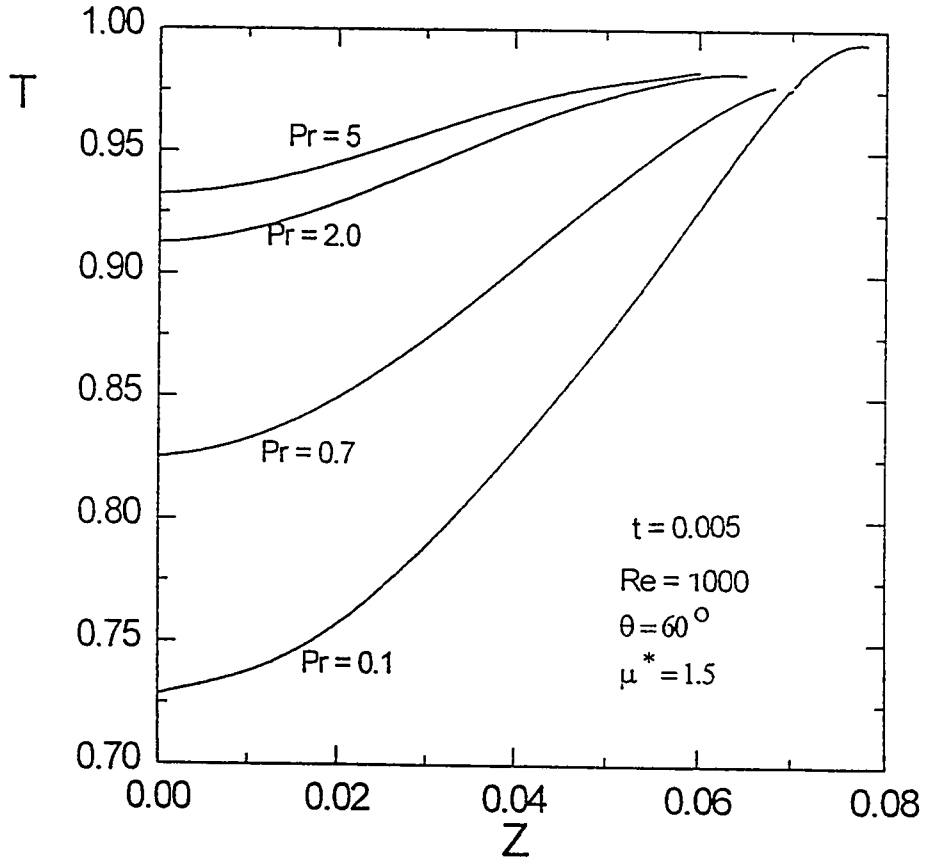

Fig. 7-38 : Effect of Prandtl number on the transient temperature profile for $\theta = 60^{\circ}$ and t = 0.005, case (2-c)

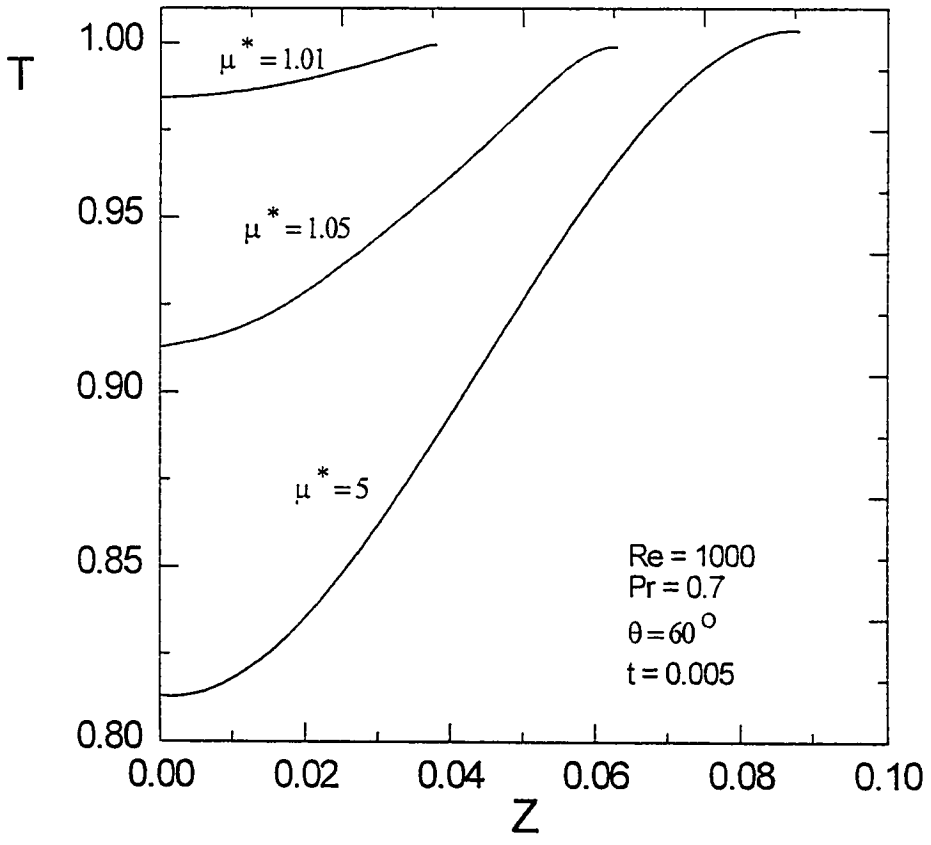

Fig. 7-39 : Effect of viscosity ratio on the transient temperature profile for $\theta = 60^{o}$ and t = 0.005, case (2-c)

viscosity ratios and larger boundary-layer thickness as was discussed in the previous chapter .

Figures 7-40 and 7-41 show the transient temperature profiles at five selected meridional angles (θ = 15°, 30°, 60°, 90° and 105°) for particular times . Each figure represents a given time and the temperature distribution is plotted versus the radial distance starting from the surface of the sphere (Z = 0) till the edge of the boundary layer where the value of the dimensionless temperature approaches unity (T = 1) . Two values of Reynolds number were selected, Fig 7-40 shows the temperature distribution for Re = 500 while Fig. 7-41 presents the temperature distribution for Re = 1000 . Increasing Re reduces the time required to attain the state of a uniform surface temperature .

For a given radial position (Z=0.02) , Fig. 4-42 shows the temporal increase in temperature at different meridional angles for a Reynolds number (Re = 1000), Prandtl number (Pr = 0.7) and a viscosity ratio (μ^* = 1.5) . It is clear from this figure that the temperature decreases as one moves along the sphere in the meridional direction since the maximum temperature (T = 1) is located at the front stagnation point where the boundary layer thickness is zero and then the thickness increases in meridional direction hence decreasing the temperature .

For a given meridional station θ = 60°, Fig. 7-43 shows the increase in temperature with time at different radial distances (Z = 0.0, 0.02, 0.05 and 0.07). It is

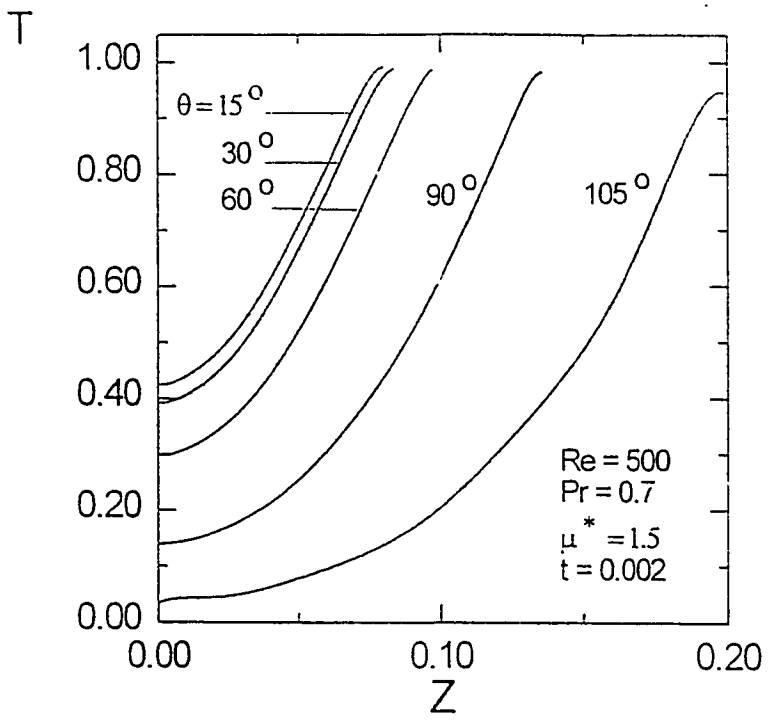

Fig. 7-40a : Temperature profiles around the sphere at different angles, Re = 500, t = 0.002, case (2-c)

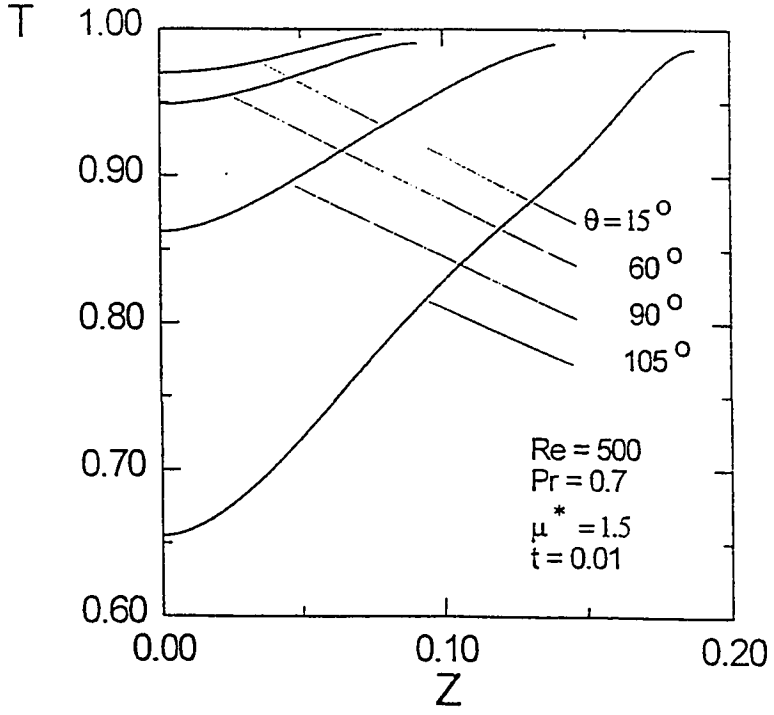

Fig. 7-40b : Temperature profiles around the sphere at different angles, Re = 500, t = 0.01, case (2-c)

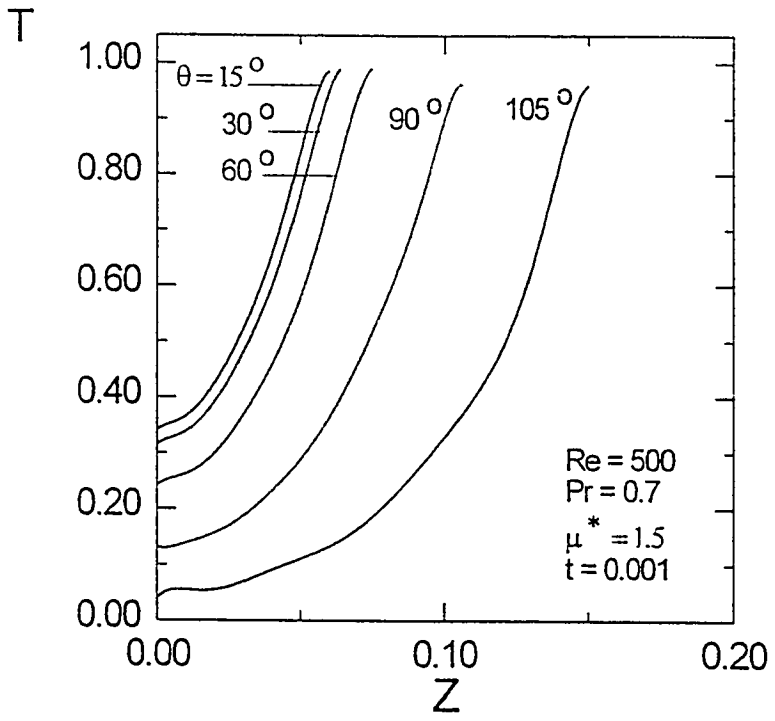

Fig. 7-41a : Temperature profiles around the sphere at different angles, Re = 500, t = 0.001, case (2-c)

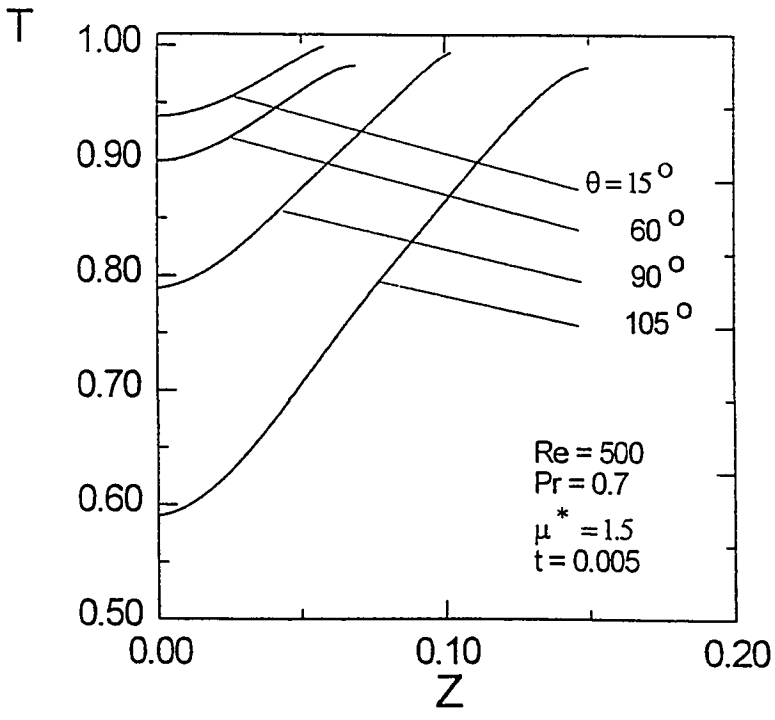

Fig. 7-41b : Temperature profiles around the sphere at different angles, Re = 500, t = 0.005, case (2-c)

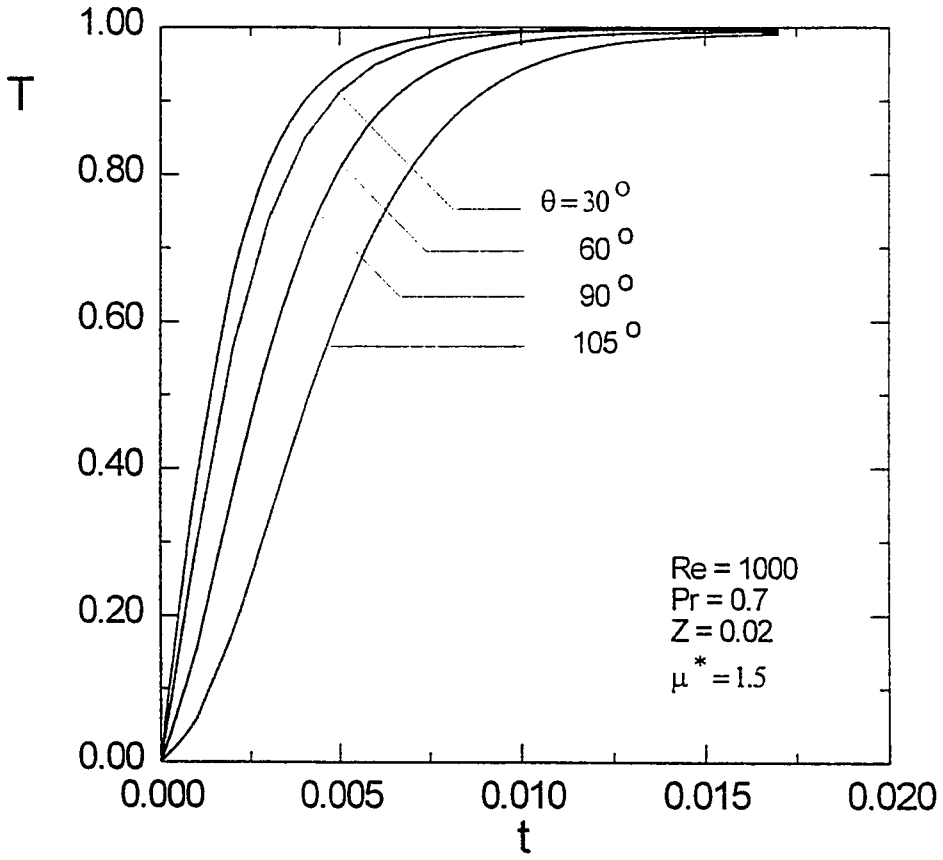

Fig. 7-42 : Temperature distribution at different angles at a fixed radial distance (Z = 0.02), case (2-c)

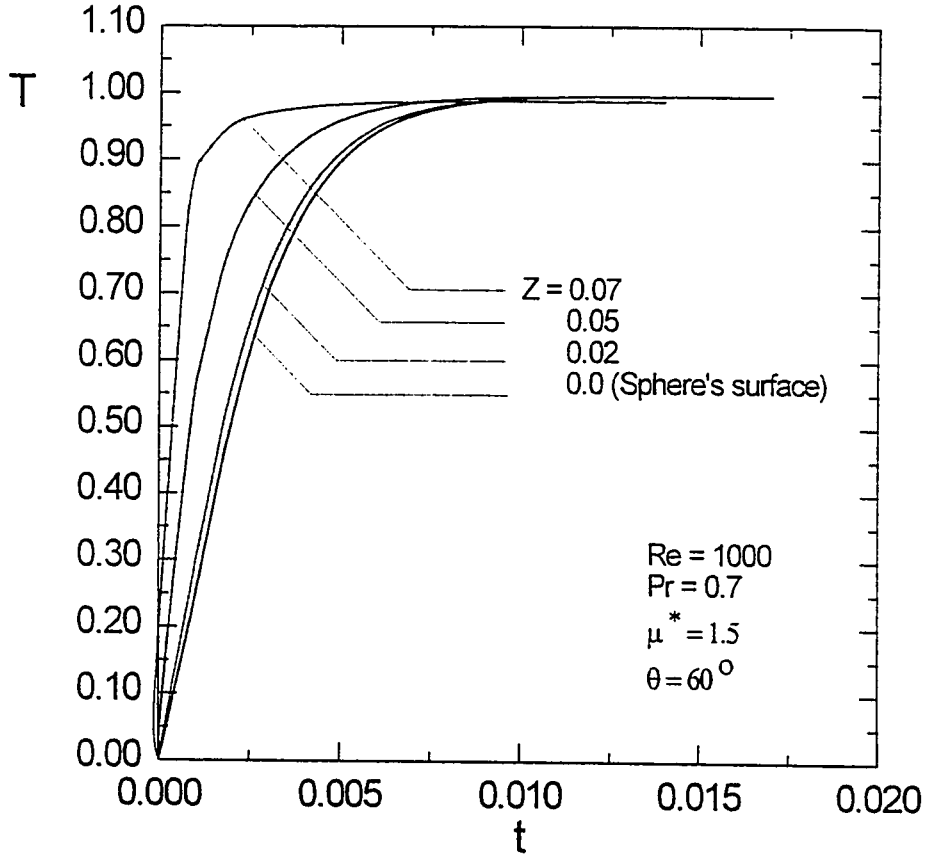

Fig. 7-43 : Transient temperature distribution at different radial distances, case (2-c)

worth stating that the curve corresponding to (Z = 0) represents the condition at the surface of the sphere . The values of the temperature at any time are higher at the outer locations of the boundary layer and heat is convected inward increasing the temperature of the locations closer to the surface of the sphere till state of the uniform surface temperature is attained .

Figure 7-44a shows the variation in the surface temperature with time versus the angle θ for a given value of Reynolds numbers Re = 500, Prandtl number Pr = 0.7, and viscosity ratio $\mu^* = 1.5$. Surface temperature starts from a value of (T = 1) at the front stagnation point and then decreases as the angle increases (and the boundary-layer grows in thickness) till it reaches a minimum values at the angle of external flow separation ($\theta_s = 106.2^\circ$) . It is worth mentioning that the program is stopped when the lowest surface temperature approaches the free stream temperature .

Figure 7-44b presents the surface temperature profiles versus the angle as time elapses for a selected value of Reynolds number Re = 1000, Prandtl number Pr = 0.7 and viscosity ratio $\mu^* = 1.5$. It is noted in the figure that the time required to approach free stream temperature is less than the case of Re = 500 discussed in Fig. 7-44a . However, the same profile of decreasing temperature from the front stagnation point along the surface is shown in the figure .

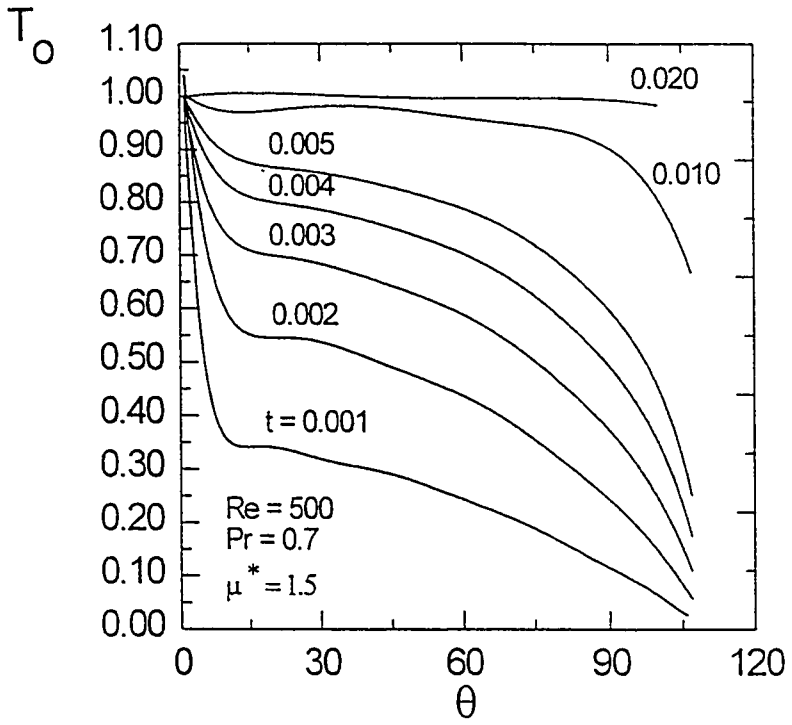

Fig. 7-44 : Surface temperature profiles around the sphere at different times, Re = 500, case (2-c)

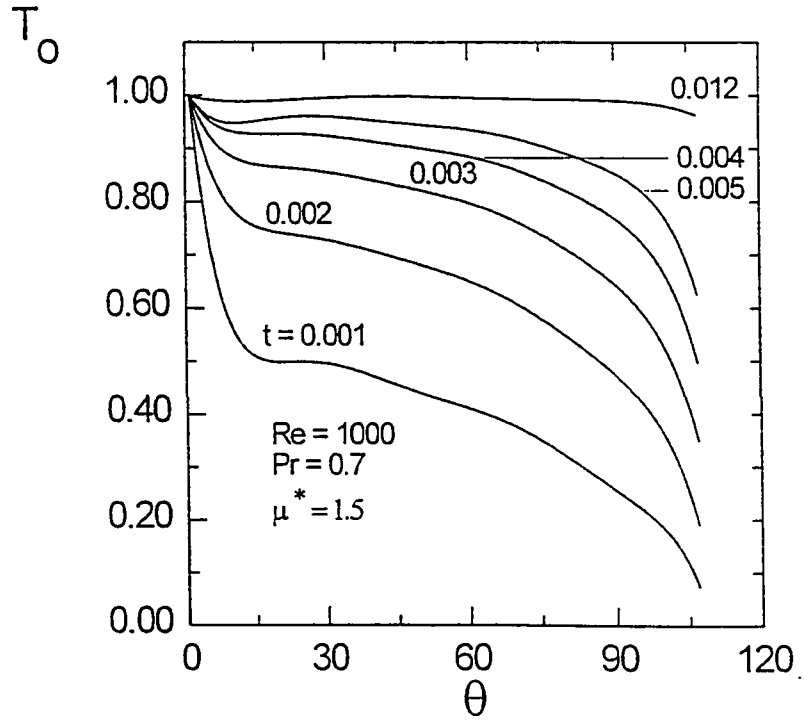

Fig. 7-45 : Surface temperature profiles around the sphere at different times, Re = 1000, case (2-c)

Transient variation of the surface temperature with time at different angles is shown in Fig. 7-45 . Initially the temperature of the surface of the sphere is zero (T = 0) and it increases till it approaches the free stream temperature (T = 1) . On the other hand, the temperature values decrease around the surface of the sphere in the meridional direction .

Figure 7-46 shows the effect of the viscosity ratio on the transient surface temperature for a given Reynolds number (Re = 1000), Prandtl number (Pr = 0.7) and meridional angle ($\theta = 30^{o}$) . Higher values of the surface temperature correspond to lower values of the viscosity ratio due to the higher convective effects (higher velocities attributed to lower viscosity ratios) .

The effect of Reynolds number on the transient surface temperature is illustrated in Fig. 7-47 . Higher Reynolds numbers yield higher surface temperatures at any given time . This is attributed to the high rate of heat convection to the sphere at higher values of Reynolds number .

Figure 7-48 shows the effect of Prandtl number on the transient surface temperature profiles for a given Reynolds number Re = 1000, viscosity ratio $\mu^{*} = 1.5$, meridional angle $\theta = 60^{o}$. Higher Prandtl numbers are corresponding to higher heat convected to the sphere and hence require less time to attain the uniform surface

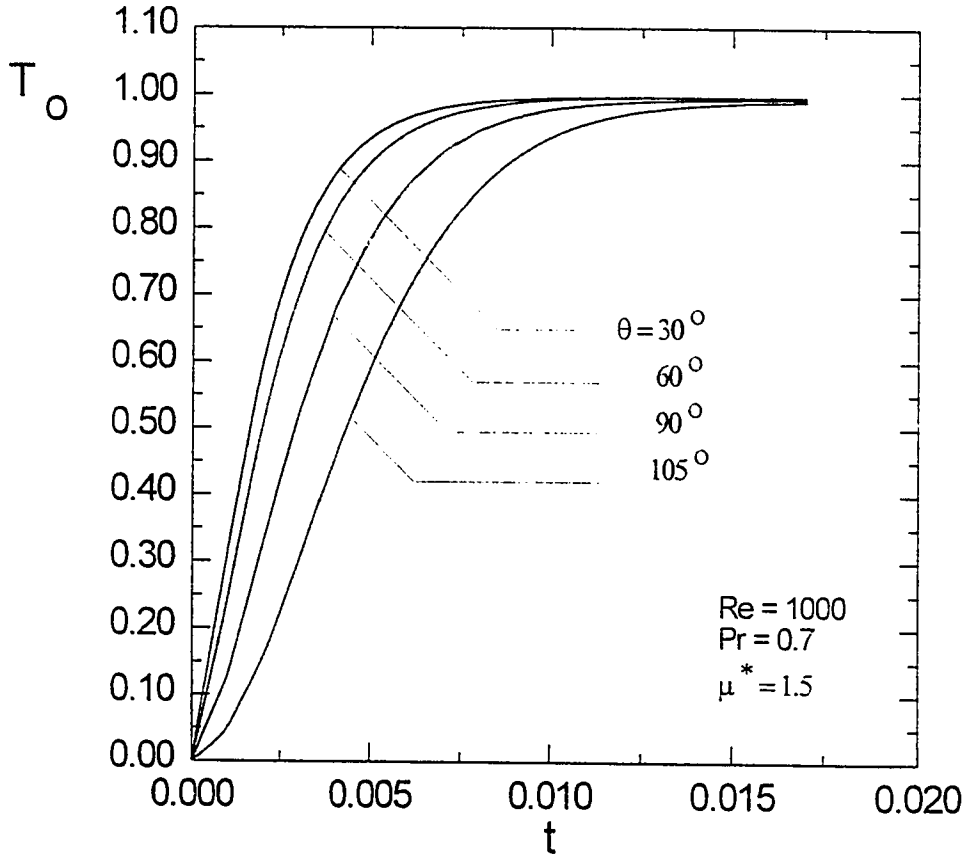

Fig. 7-45 : Surface temperature profiles at different central angles, case (2-c)

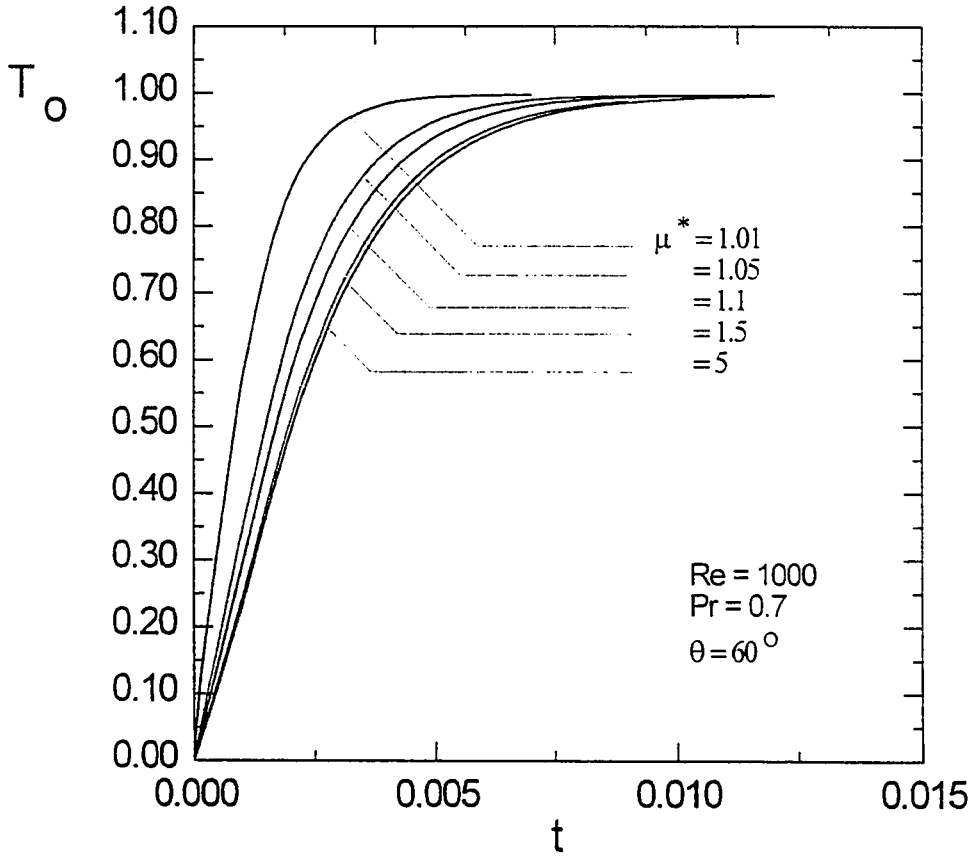

Fig. 7-46 : Effect of viscosity ratio on the surface temperature distribution, case (2-c)

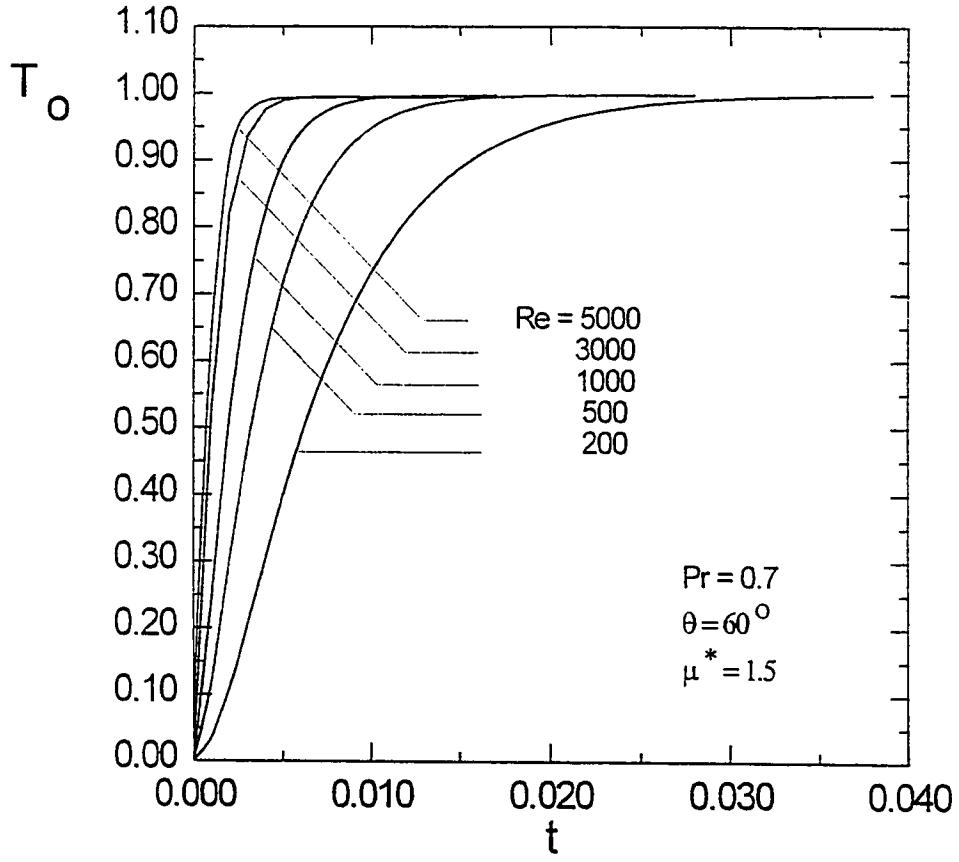

Fig. 7-47 : Effect of Reynolds number on the surface temperature distribution, case (2-c)

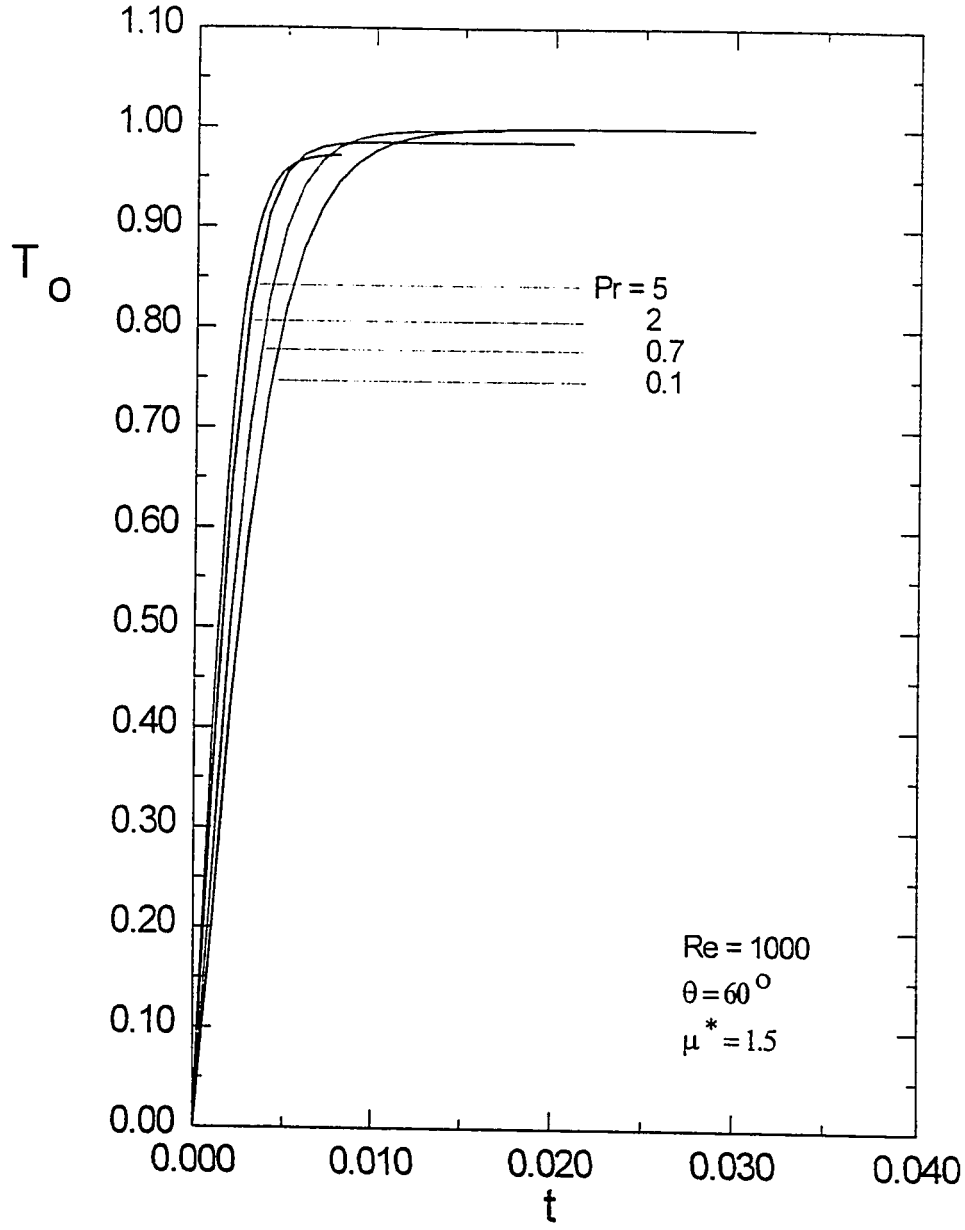

Fig. 7-48 : Effect of Prandtl number on the surface temperature distribution, case (2-c)

temperature . Meanwhile, lower values of the temperature at any time are corresponding to lower Prandtl number .

Figure 7-49 presents the transient profile of the rate of change of surface temperature with time for a given Reynolds number (Re = 1000), Prandtl number (Pr = 0.7) , viscosity ratio ($\mu^* = 1.5$) and at selected meridional angles ($\theta = 30^o$, 60^o, 90^o and 105^o) . It is clear from the figure that the rate of change of temperature $\frac{\partial T_o}{\partial t}$ decreases with time for all presented angles because of the increase in the dimensionless surface temperature and the thermal boundary layer till they approach unity at the state of uniform surface temperature and the rate of change of temperature diminishes . Furthermore, the decrease of the rate of temperature is faster at lower angles where higher surface temperature are reported . On the other hand, the rate of decrease of temperature is faster for case (2-a) where initial temperature profile throughout the boundary-layer is assumed unity and it is less for case (2-b) where a linear initial temperature profile from zero at the surface to unity at the boundary-layer edge is assumed while this rate has its lowest value for case (2-c) where the initial temperature throughout the boundary layer is assumed equal to zero .

7.2.2.3.2 Nusselt Number

The effect of increasing Reynolds number on the values of Nusselt number which is defined as the dimensionless temperature gradient at the surface is shown in Fig. 7-50

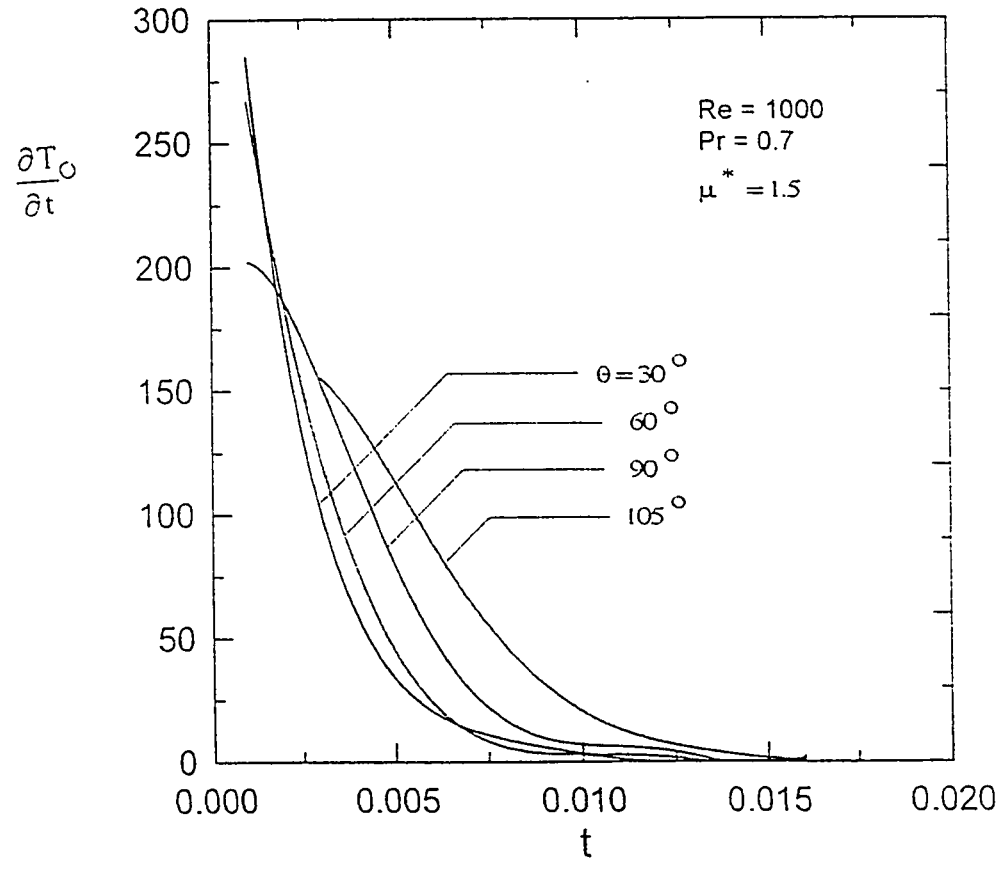

Fig. 7-49 : Rate of change of surface temperature versus time at different central angles, case (2-c)

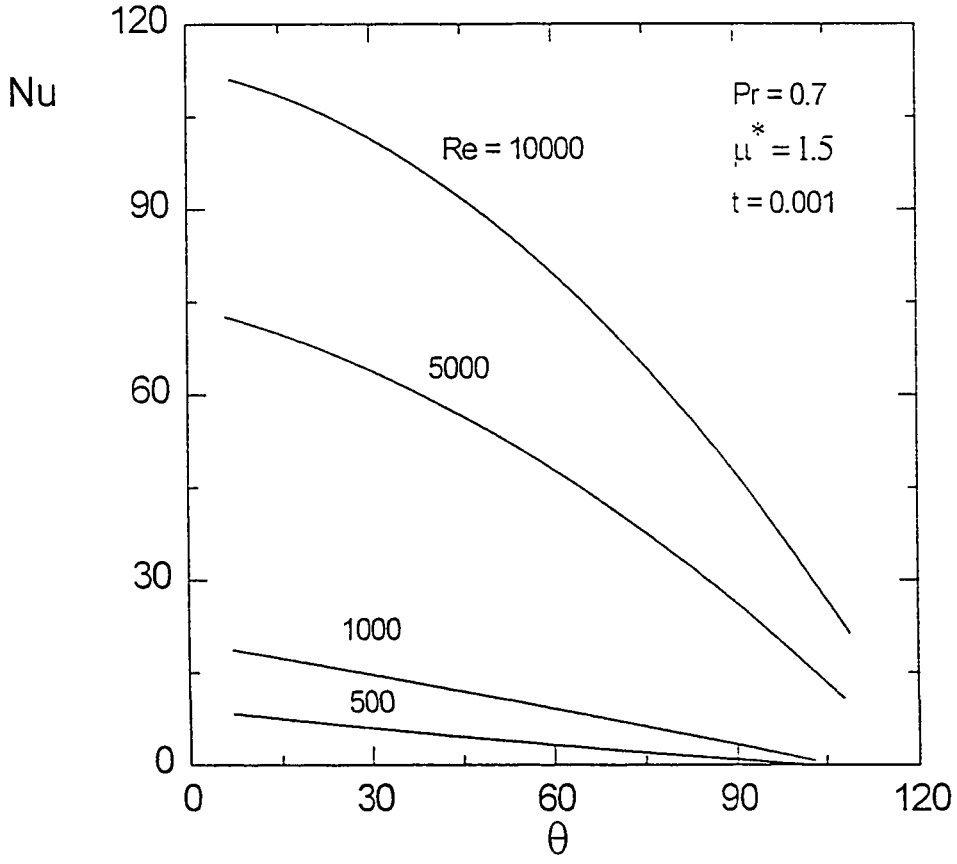

Fig. 7-50 : Effect of Reynolds number on the local Nusselt number along the surface of the sphere, case (2-c)

at given values of time (t = 0.005), Prandtl number (Pr = 0.7), and for a viscosity ratio (μ^* = 1.5) . The figure shows higher values of Nusselt number corresponding to higher Reynolds numbers . This is attributed to the increase of heat convected to the sphere at high Reynolds numbers thus increasing the temperature gradient . Furthermore, Nusselt number decreases as the meridional angle increases for all Reynolds numbers because of the lower surface temperatures as we move along the surface of the sphere and thicker boundary layer resulting in lower temperature gradients and hence lower values of the Nusselt number .

Figure 7-51 shows the effect of viscosity ratio on the values of the local Nusselt number at a particular time (t = 0.005) for Re = 1000, Prandtl = 0.7 at a particular time for Re = 1000, Prandtl = 0.7 . Higher values of Nu obtained at lower viscosity ratios that are leading to higher rates of heat convection (higher velocities in the boundary layer) and hence higher temperature gradients . It is worth to mention that increasing the viscosity ratios more than (μ^* = 10) resulted in no changes in the values of Nusselt number and this high viscosity ratio is closer to the case of flow over a solid sphere where no more changes in Nusselt number occur .

Transient temperatures of the sphere and its boundary layer increase as time elapses and the temperature gradient at the wall and hence Nusselt number decreases significantly till the uniform surface temperature when the Nusselt number reduces to zero as shown in Fig. 7-52 .

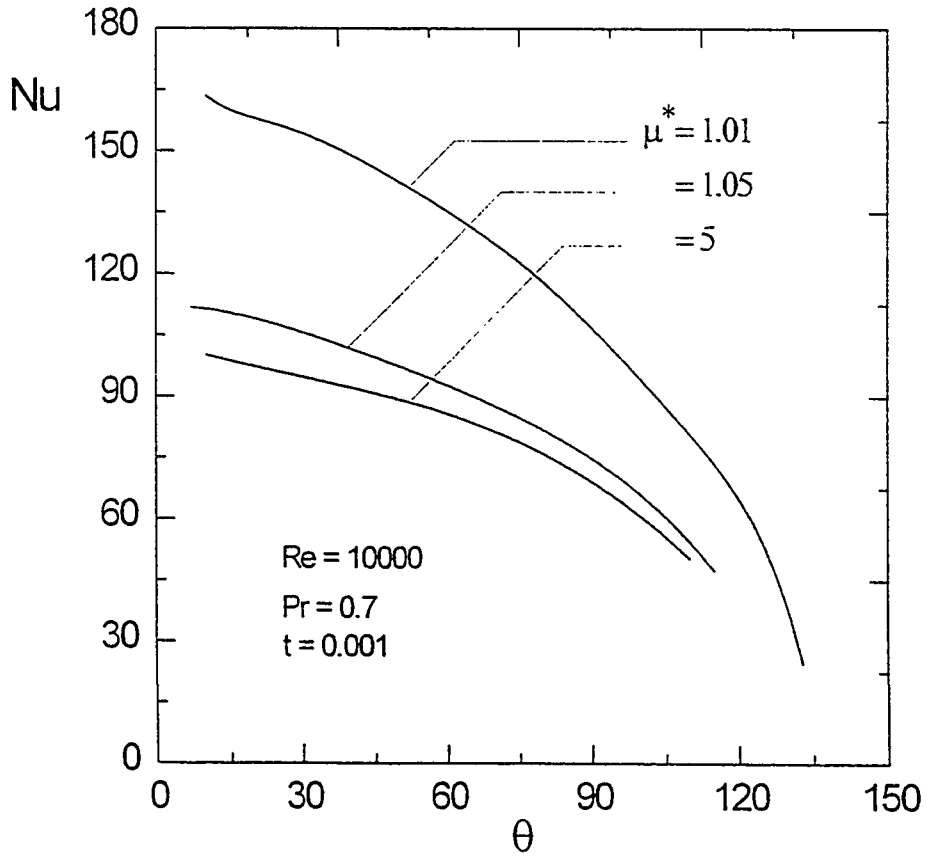

Fig. 7-51 : Effect of viscosity ratio on the local Nusselt number profile , case (2-c)

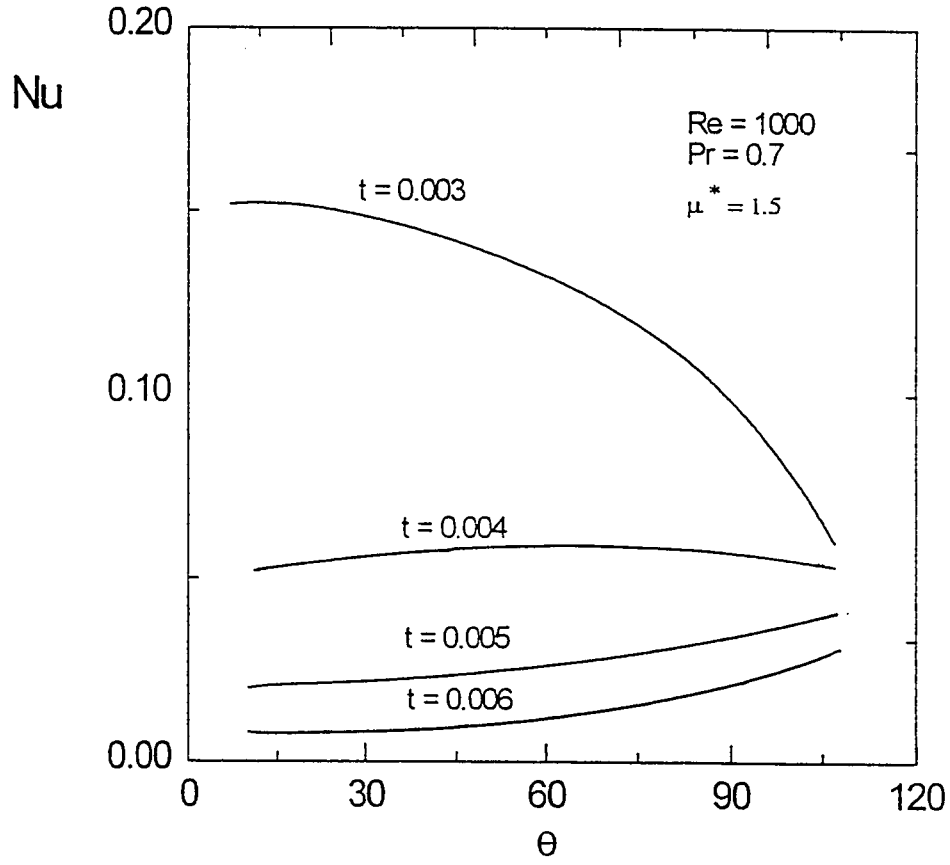

Fig. 7-52 : Nusselt number profiles at different times around the sphere, case (2-c)

Values of the local Nusselt number were calculated at the first time step (t = 0.001) at a low Reynolds number Re = 100 and Prandtl number Pr = 0869 for sake of comparison with reported data in the literature . Fig. 7.53 shows the comparison between the local Nusselt number values calculated in the present study and those reported by Renksizbulut and Yuen [48] for a Reynolds number (Re = 100) and Prandtl number (Pr = 0.869) . The match of the present analysis with those given by Renksizbulut and Yuen is excellent with a maximum difference of about 8 % . However, It should be pointed out that the analysis of Renksizbulut and Yuen is based on solving the full Navier-Stokes equations while the present analysis considers the boundary-layer approximation that leads to a simpler and much faster solution .

Figure 7-54 shows the comparison between the local Nusselt number obtained by the present analysis and that reported by Chiang et. Al. [58] for a Reynolds number (Re = 100) and a Prandtl number of (Pr = 0.7) . The two profiles match with a maximum difference of about 7 % . It is worth to say that Chiang et al. solved numerically the full Navier-Stokes equation and hence their solution is valid up to the rear stagnation point while the present analysis uses the boundary-layer approximation and hence its solution is valid up to the point of flow separation .

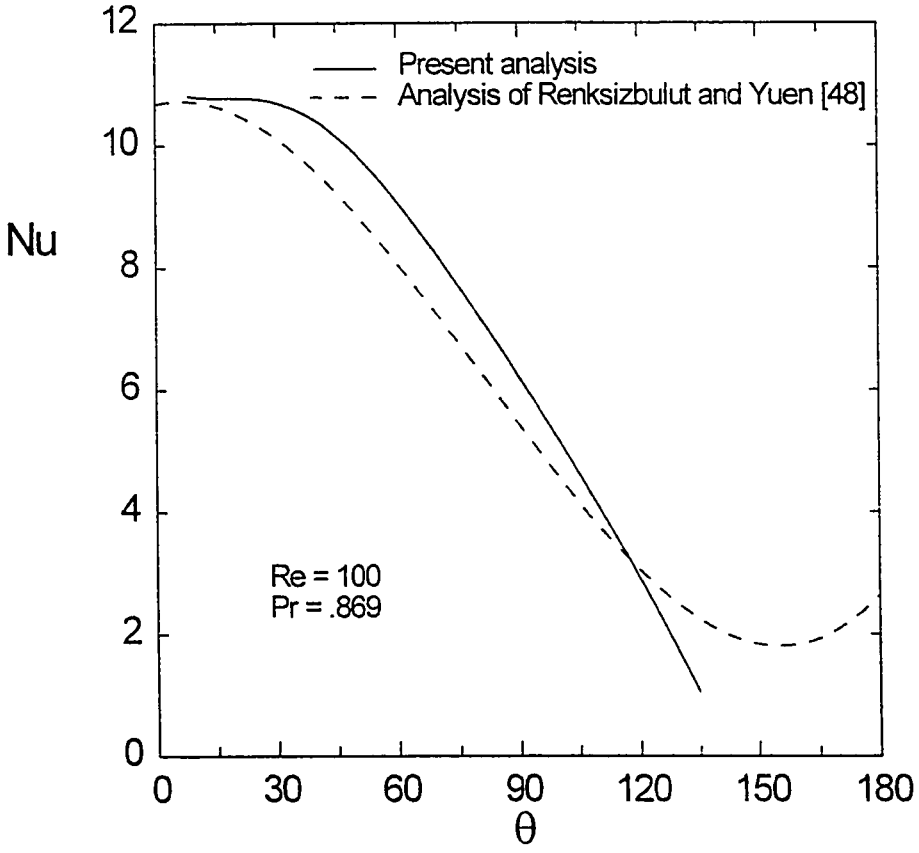

Fig. 7-53 Comparison of the local Nusselt number of case (2-c) distribution with the analysis of Renksizbulut and Yuen [48]

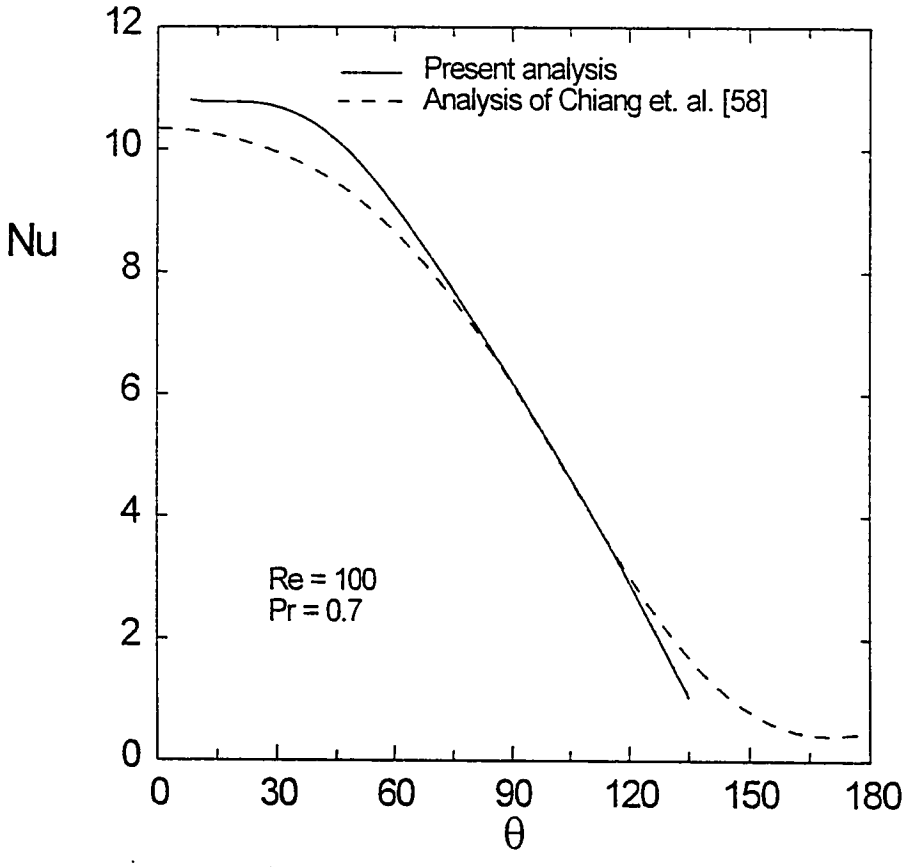

Fig. 7-54 : Comparison of the local Nusselt number distribution, case (2-c) with the analysis of Chiang et. al. [58]

It is worth of mentioning that the values of the average Nusselt number were computed from the present analysis and compared with some reported correlations in the literature . Table 7-1 Presents a comparison between the present analysis and some of the correlations reported in the literature such as the formula suggested by Raithby and Eckert [79], $Nu_d = 0.257\,Re_d^{0.588}$, the formula suggested by McAdams [80], $Nu_d = 0.37\,Re_d^{0.6}$, the formula suggested by Achenbach [81], $Nu_d = 2 + (0.25\,Re_d + 3\times10^{-4}\,Re_d^{1.6})^{0.5}$. However, it is worth stating that these formulae did not account the effect of Prandtl number or the viscosity ratio . The formula suggested by Whitaker [82] considered Prandtl number in calculating the value of the average Nusselt number around a sphere, $Nu_d = 2 + (0.4\,Re_d^{0.5} + 0.06\,Re_d^{0.67})\,Pr^{0.4}\left(\frac{\mu}{\mu_s}\right)^{0.25}$

On the other hand, this formula contains a ratio of the viscosities that does not represent the interior-to-exterior viscosity ratio but it is the ratio of the gas phase viscosities at two different values of the temperature namely the free stream temperature and the sphere's initial temperature . To the best of the author knowledge, no formula in the literature considered the viscosity ratio between liquid and gas phase .

Table 7-1 : Comparison of the average Nusselt number with reported data

	Nu_{av}				
Analysis	Re = 200	Re = 500	Re = 1000	Re = 5000	Re=10000
Present Study	4.57	10.06	17.4	49.77	72.98
Raithby and Eckert [79]	5.8	9.93	14.925	38.453	57.8
McAdmas [80]	8.9	15.4	23.34	61.32	92.94
Achenbach [81]	9.17	13.45	18.4	40.7	59.04
Whitaker [82]	8.7	13.1	18.3	42.17	61.58

The time mean value of the Nusselt number was calculated by obtaining the average Nusselt number along the sphere's surface then by computing the average value over the time required to reach the state of uniform surface temperature . The Effect of Reynolds number and the viscosity ratio on the time mean value of the average Nusselt number is presented in Fig. 7-55 . It is shoen in the figure that increasing Reynolds number or decreasing the viscosity ratio increases both the local and the average Nusselt number and hence increases the time mean value of Nusselt number .

Figure 7-56 presents a comparison between the three cases showing the effect Reynolds number on the time required to reach the state of uniform surface temperature . It is clear from the figure that case (2-a) was the first to reach uniform surface temperature because in this case it is assumed that the initial temperature throughout the boundary layer is unity and hence less time is required to raise the temperature of the sphere's surface . Case (2-b) in which an initial linear temperature profile is assumed (dimensionless temperature is zero at the sphere's surface and unity at the boundary-layer edge) required more time to reach a uniform surface temperature while the initial temperature is zero throughout the boundary-layer resulted in the highest values of the time required to attain a uniform surface temperature .

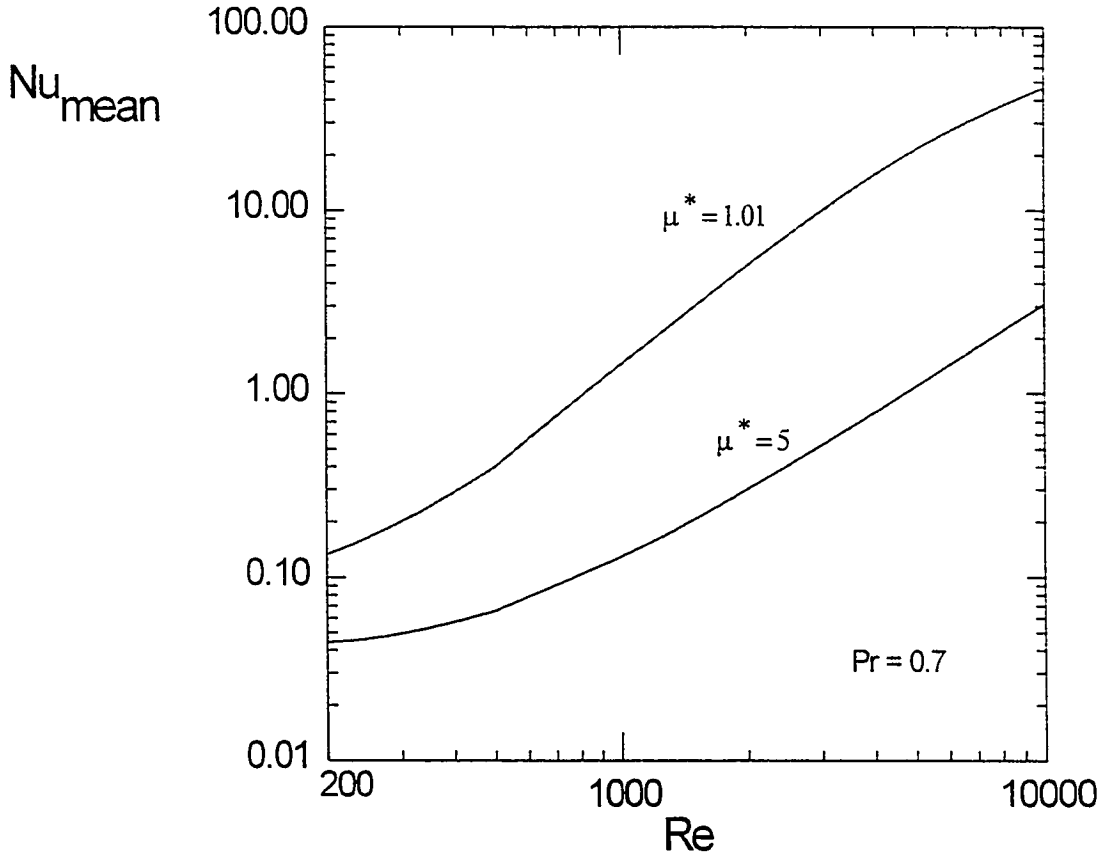

Fig. 7-55 : Effect of Reynolds number on the time average Nusselt number

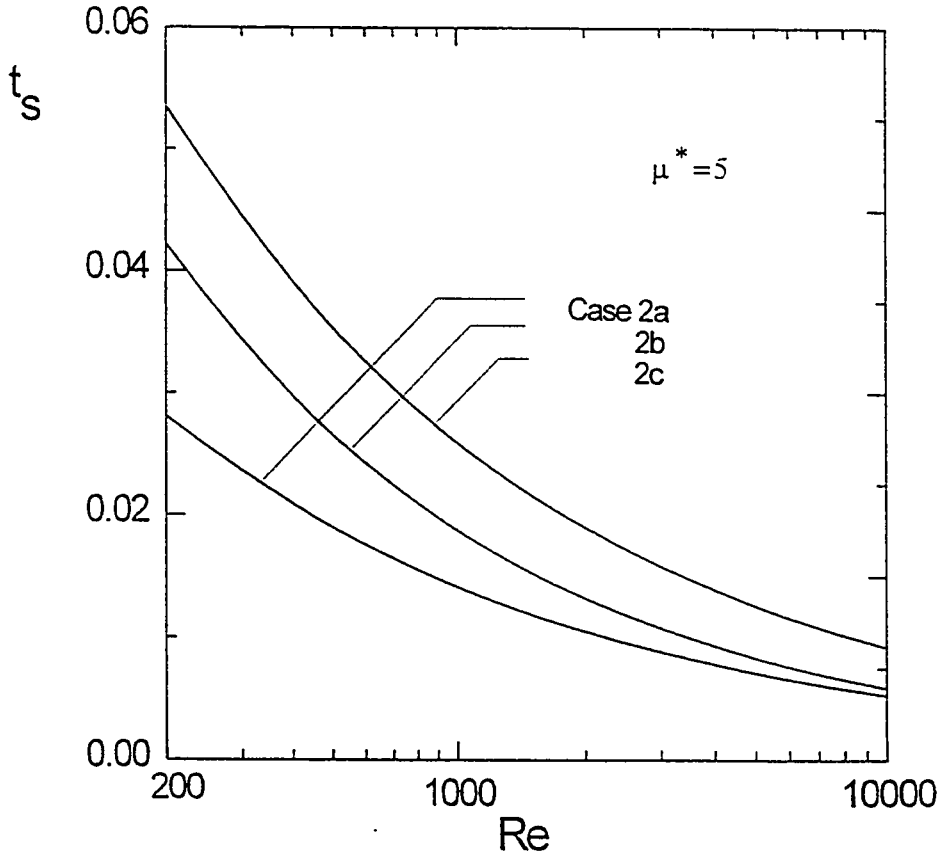

Fig. 7-56 : Effect of Reynolds number on the time required to reach uniform surface temperature for the three cases

7.4 Temperature Profiles Inside the Sphere

Results of the temperature profiles inside the liquid sphere are presented in this section . It is worth to mention that throughout the present work, the time increment inside the sphere (liquid phase) and outside the sphere (gas phase) is kept at the same value so that the values of the surface temperature obtained from the gas phase solution can be used as boundary conditions at the sphere's surface at different times in the liquid phase solution thus giving temporal temperature rise in the liquid phase . However, the gas phase solution stops when the surface temperature approaches the free stream temperature (T = 1) while the liquid phase solution continues beyond this time until the sphere center is heated up to this temperature (within a certain tolerance) as will be shown in the next paragraphs .

Figure 7-57 shows the transient development of the temperature distribution for a given value of Reynolds number (Re = 500), viscosity ratio ($\mu^* = 1.5$), Prandtl number ($Pr_\ell = 10$) and meridional angle ($\theta = 60^o$) at different time increments . The surface temperature increases till it reaches a constant value at (t = 0.012) at which the gas phase solution stops and the surface temperature is fixed at its uniform value of unity . However, liquid phase heating continues beyond this time till the steady state condition is reached, i.e., when the sphere center is heated to the free stream temperature . For this case, the dimensionless time required to reach the steady state is 0.4 .

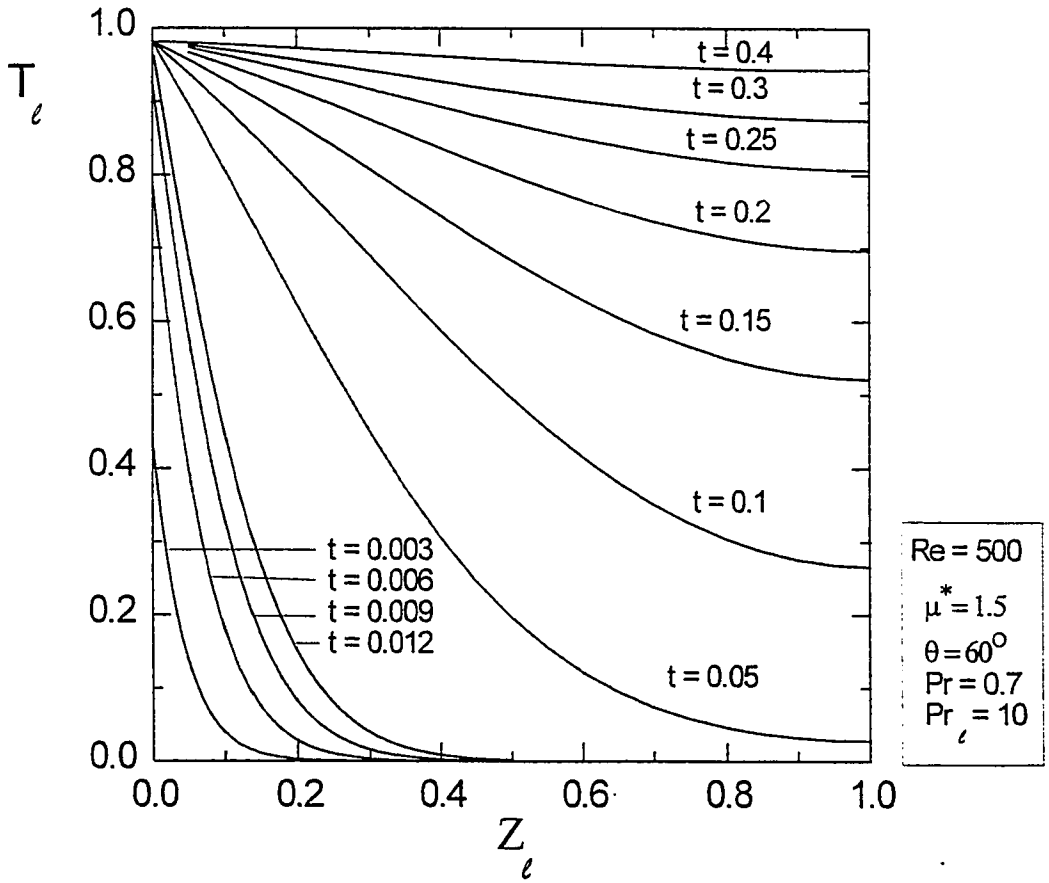

Fig. 7-57 : Transient temperature profiles inside the liquid sphere

The effect of Reynolds number on temperature distribution inside the liquid sphere is shown in Fig. 7-58 at fixed values of viscosity ratio (μ^* = 1.5), meridional station ($\theta = 60^o$), and at a selected time (t = 0.09) . The figure shows that increasing Reynolds number leads to higher values of the temperature at the same radial location due to the increase of convective effects that are attributed to higher velocities at higher Reynolds numbers .

Figure 7-59 presents the temperature distribution inside the sphere at different meridional locations (angles) for a selected value of Reynolds number Re = 500, viscosity ratio μ^* = 1.5 at a selected time t = 0.009 where it is clear that higher values of the temperature are corresponding to earlier meridional angles (measured from the front stagnation point) since the higher surface temperatures are also corresponding to earlier angles with a maximum value of (T =1) at the front stagnation point where the thickness of the external boundary layer is zero and the surface temperature is equal to the free stream temperature . The surface temperature decreases as we move along the meridional direction as shown earlier leading to lower values of the temperature inside the sphere .

Figure 7-60 shows the effect of the viscosity ratio on the temperature distribution inside the sphere for given values of Reynolds number, Re = 500, Prandtl number, Pr = 10, time, t = 0.009 and for four selected values of the viscosity ratio (μ^* = 1.01, 1.1, 1.5 and 5 respectively) . It is clear from the figure that lower viscosity ratios are corresponding to higher velocities at the surface of the sphere as shown in the previous

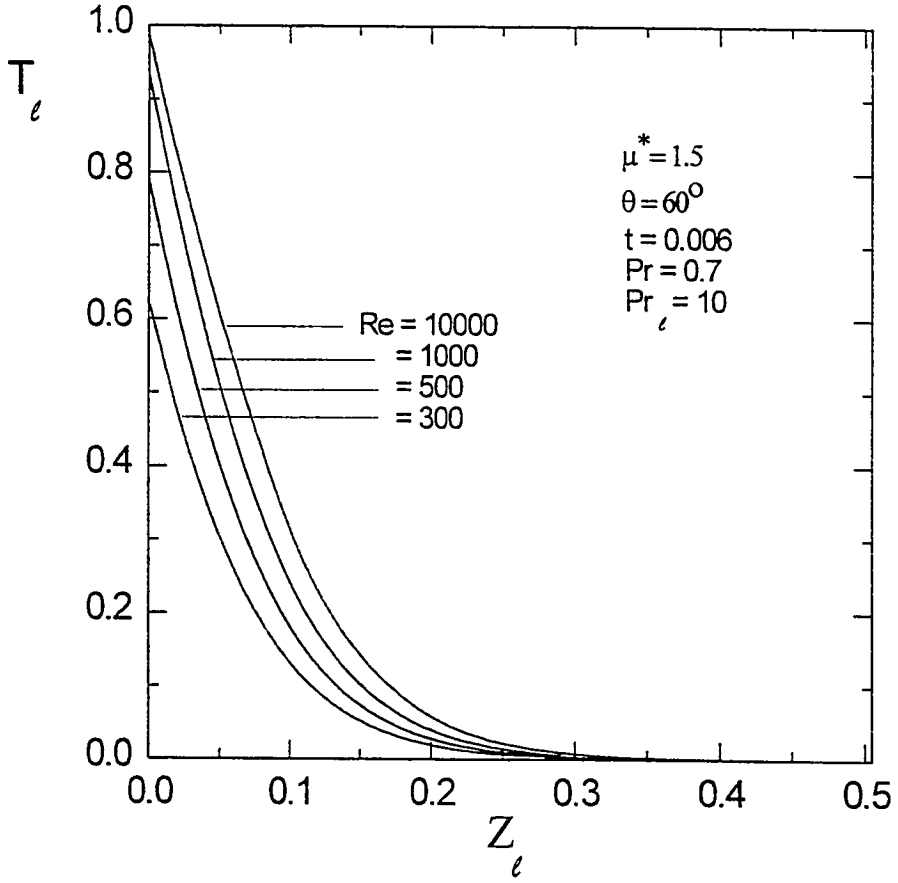

Fig. 7-58 : Effect of Reynolds number on the temperature profiles inside the liquid sphere, (t = 0.006)

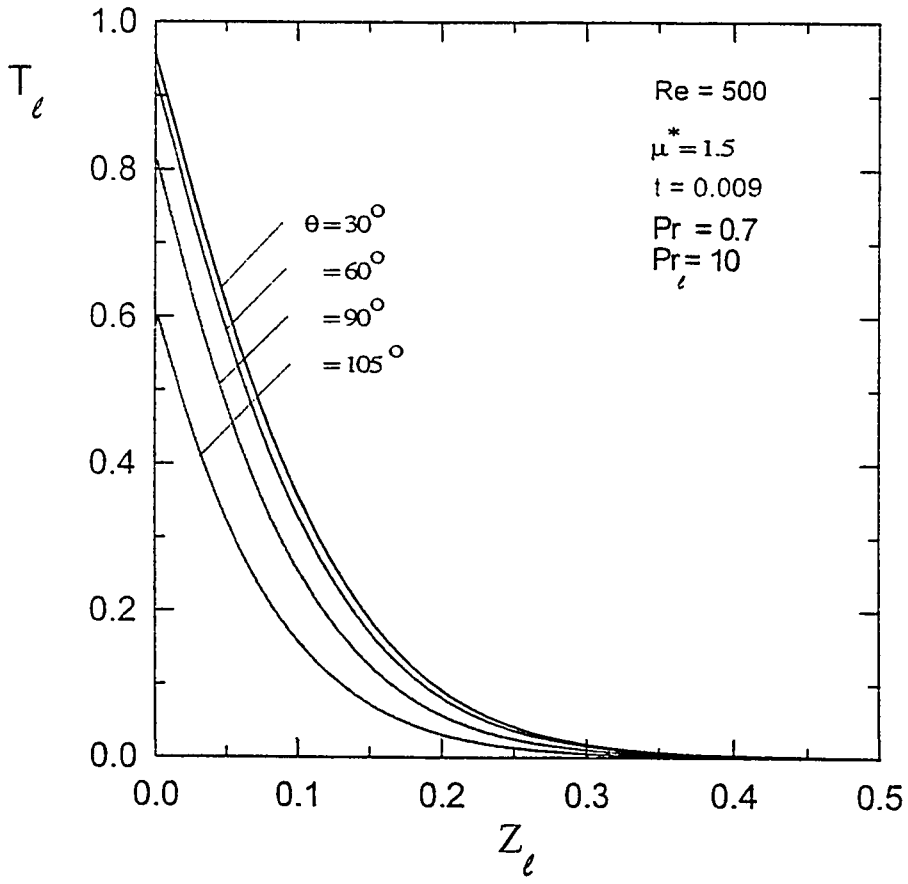

Fig. 7-59 : Temperature profiles inside the liquid sphere at different angles , (t = 0.009)

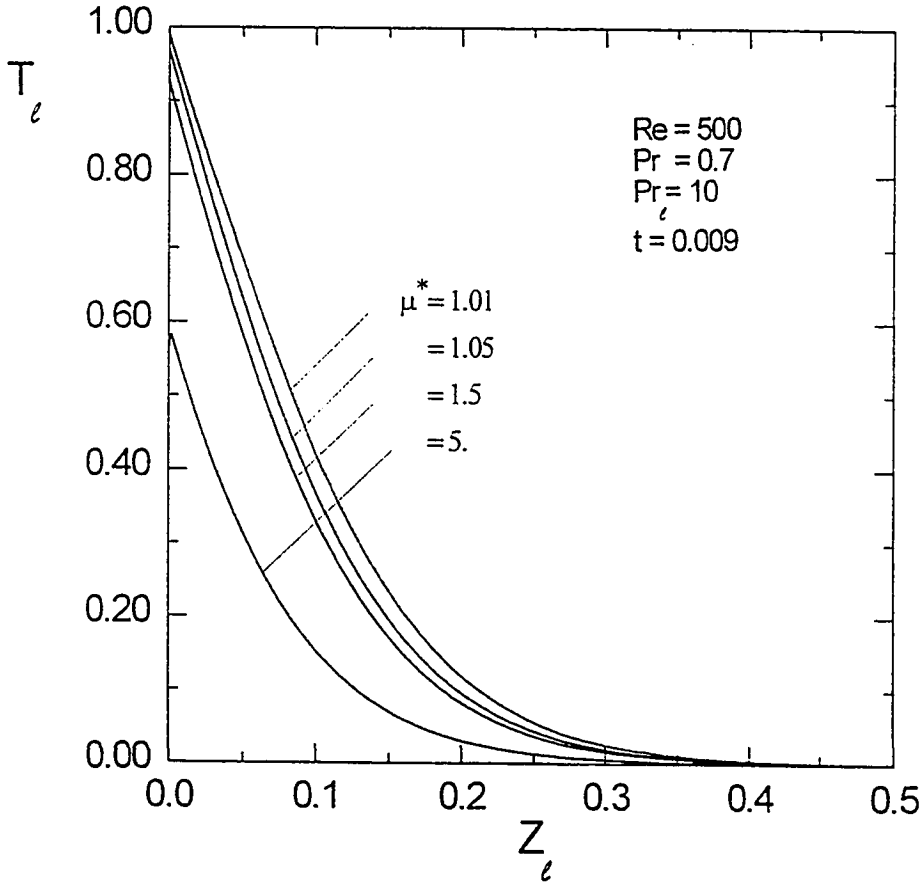

Fig. 7-60 : Effect of viscosity ratio on the temperature profiles inside the sphere , (t = 0.009)

chapter and thus higher velocities inside the sphere are also expected leading to higher convective effects increasing the temperature at all radial locations .

Figure 7-61 presents the combined temperature distributions both outside and inside the sphere as time is proceeding to show the temperature profiles as they increase with time from the edge of the external boundary layer up to the center of the sphere . higher velocities in the gas phase boundary layer leads to a rapid increase in temperature However, since the velocities in the liquid phase are much less in magnitude compared to gas phase velocities, slower rate of temperature rise are encountered in the liquid phase. It is worth mentioning that temperature distribution around the sphere takes about twelve time steps to reach its steady state value in the external boundary layer whose thickness is about (Z = 0.1) while 400 time steps are required to heat the sphere center that is at a distance of (Z = 1) from the surface of the sphere .

7-5 Computer Run Time

It is worth mentioning that one of the remarkable advantages of the present models is the short total computer run time . Run time for the gas-phase program does not exceed 20 seconds on a personal computer (Pentium 100 Mhz) while the liquid phase program has an average total run time of about 7 minutes . This may be considered a considerable improvement in the models compared to the much more excution time reported in the literature using super computers and workstations that may range between several minutes in the gas-phase programs to several hours for the liquid-phase programs.

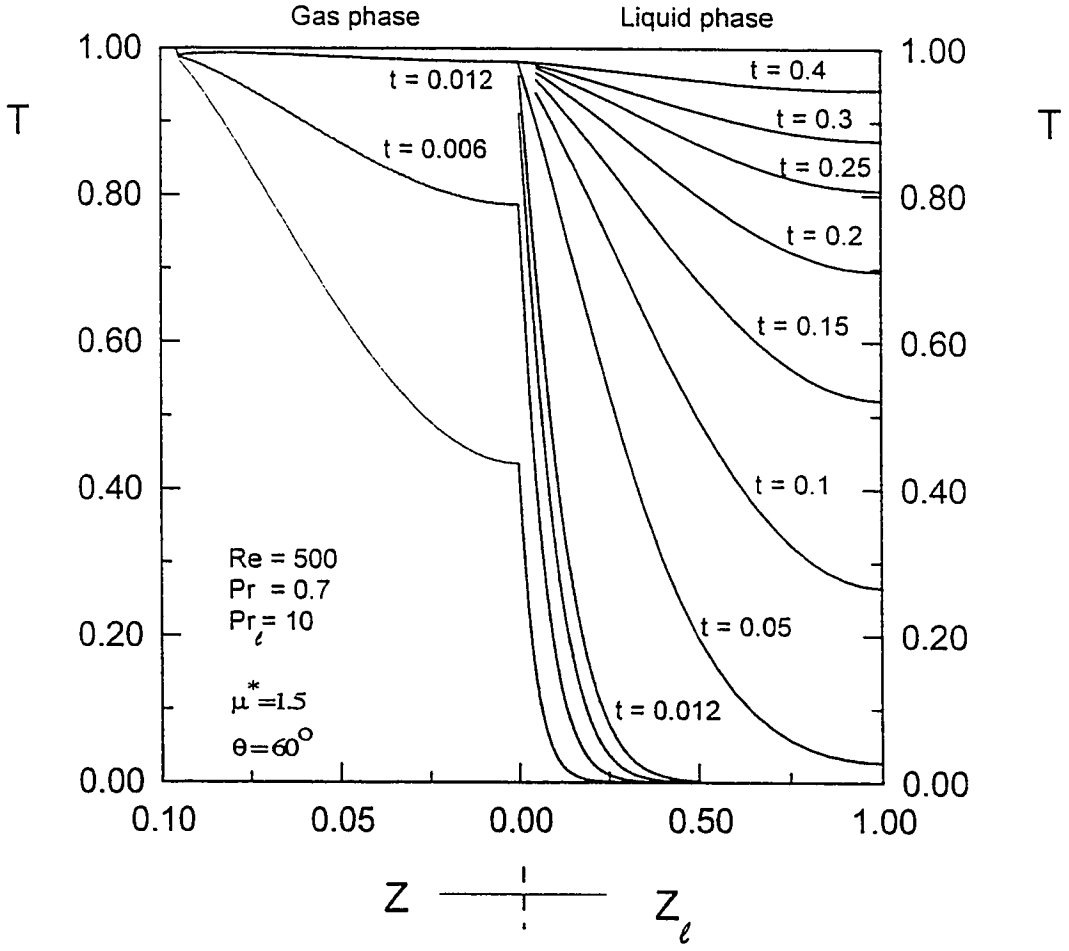

Fig. 7-61 : Transient temperature profiles outside and inside the liquid sphere

CHAPTER VIII

CONCLUSIONS AND RECOMMENDATIONS

8-1 Conclusions

A simple, linearized and non-iterative finite-difference scheme has been developed and successfully used to solve the boundary-layer equations governing the laminar flows around and inside a spherical fluid sphere moving steadily in another immiscible fluid . Two hydrodynamic similarity parameters are needed to describe the external flow around the sphere; these are the Reynolds number (Re) and the interior-to-exterior viscosity ratio (μ^*) . An additional parameter of similitude, ν^* (the kinematic viscosity ratio), is needed for the description of the flow inside the sphere . Results not available in the literature have been obtained for circulating spheres at intermediate and high viscosity ratios (i.e., with a strong coupling between the internal and external flows) and large values of the external flow Reynolds number . The obtained results clarify that each of μ^* and Re has significant effects on the flow characteristics both inside and outside the sphere while the third parameter (ν^*) has negligible effects on the flow inside the sphere . Over the ranges $1.01 \leq \mu^* \leq \infty$ (solid sphere : $\mu^* > 100$) and $100 \leq Re \leq 10000$ results are presented for the meridional velocity profiles inside and outside the spherical sphere, the interface shear stress, the external flow point of separation, the sphere's surface velocity and the drag coefficient .

The energy equation was then solved for both gas phase and liquid phase (up to the center of the liquid sphere) presenting the transient temperature distribution for both phases . Three cases for the initial temperature distribution throughout the external boundary layer were considered . First, a step change in dimensionless temperature from zero to unity is assumed at the surface of the sphere . Second, a linear temperature profile across the thermal boundary-layer was considered as an initial condition . In the third case, a step change in temperature from zero to unity was assumed at the boundary-layer edge (i.e., initial temperature throughout the boundary layer is zero) . Higher values of the temperature at a fixed time are corresponding to case 2-a and less values of temperature are corresponding to case 2-b while the lowest values are corresponding to case 2-c . The effect of the controlling parameters, namely Reynolds number and the viscosity ratio on the temperature profiles and the time required to reach the steady state condition was presented and discussed for each case in addition to the Effect of changing Prandtl number on the temperature distribution . Increasing Reynolds number or decreasing the viscosity ratio result in higher temperature at the same radial location and thinner thermal boundary-layer for all cases . Case 2-a required less time to reach the state of uniform surface temperature while case 2-b required more time and the maximum time to reach uniform surface temperature was corresponding to case 2-c . The effect of the hydrodynamic similarity parameters on Nusselt number was also analyzed where increasing Reynolds number or decreasing viscosity ratio result in higher values of Nusselt number . A comparison between the computed values of Nusselt number with some data found in the literature was carried out in the reported

range of Reynolds number and viscosity ratio obtaining a good agreement between the present analysis and these values .

8-2 Recommendations for Future Work

It is recommended to extend the present work to account for :

1. variable properties (e.g. ρ, α, C_p, ... etc) . New values of these quantities that change with temperature may be computed at each time step applying the 1/3 rule discussed in Chapter 2 .
2. dynamics of the sphere motion (deceleration of the sphere and hence the Reynolds number will decrease with time) which is the typical condition in combustors .
3. mass transfer at the surface of the sphere (radial velocity, W, at the interface would not equal to zero) and the latent heat for vaporization may be utilized in the matching boundary condition at the interface for solving the energy equation .
4. evaporation effect (surface regression of the sphere) .
5. high temperature and pressure environment .

References

1. Hamielec, A. E. , Hoffman, T. W. and Ross, L.L., "Numerical Solution of The Navier-Stokes Equation for Flow Past Spheres: Part I. Viscous Flow Around Spheres with and Without Radial Mass Efflux", *A.I.Ch.E. Journal*, Vol. 13, No. 2, pp. 212-219, 1967 .
2. Pruppacher, H.R. , Le Clair, B.P. and Hamielec, A.E., "Some Relations Between Drag and Flow Pattern of Viscous Flow Past a Sphere and Cylinder at Low and Intermediate Reynolds Numbers", *Journal of Fluid Mechanics*, Vol . 44, part 4, pp.781-790 , 1970 .
3. Rimon, Y. and Cheng, S.I., "Numerical Solution of a Uniform Flow Over a Sphere at Intermediate Reynolds Numbers", *The Physics of Fluids*, Vol. 12, No. 5, pp. 949-959, May , 1989 .
4. Achenbach, E., "Experiments on The Flow Past Spheres at Very High Reynolds Numbers", *Journal of Fluid Mechanics*, Vol. 54, part 3, pp. 565-575 , 1972 .
5. Seeley, L.E. , Hummel, R.L. and Smith, J.W., "Experimental Velocity Profiles in Laminar Flow Around Spheres at Intermediate Reynolds Numbers", *Journal of FLuid Mechanics*, Vol. 68, part 3, pp. 591-608 , 1975 .
6. Esmail, M.N. , Hummel, R.L. and Smith, J.W., "Notes on Experimental Velocity Profiles in Laminar Flow Around Spheres at Intermediate Reynolds Numbers", *Journal of Fluid Mechanics*, Vol. 90, pp. 755-759 , 1979 .

7. El-Shaarawi, M. A. I. , Kemry, M. M. and El-Bedeawi, S. A., "Experiments on Laminar Flow About a Rotating Sphere in an Air Stream", *Proc. Instn. Mech. Engrs.*, London, Vol. 201, No. 6 , 1987 .

8. Karyagin, V.P. , Lopatkin, A.I., Shvets, A.I. and Shilin, N.M., "Experimental Investigation of the Separation of Flow Around a Sphere", *Fluid Dynamics*, Vol. 26, No. 1, pp. 126-129, 1991 .

9. El-Bedeawi, S. A., "The Boundary Layer Flow on a Rotating Body", *Ph.D. Thesis Mechanical Engineering Department, Al-Azhar University* , Cairo , *Egypt*, 1985 .

10. El-Shaarawi, M. A. I. , El-Refaie, M. F. and El-Bedeawi, S. A., "Numerical Solution of Laminar Boundary Layer Flow About a Rotating Sphere in an Axial Stream", *Journal of Fluids Engineering*, Vol. 107, pp. 97-104 , 1985 .

11. Baird, M.H.I. and Hamialec, A.E., "Forced Convection Transfer Around Spheres at Intermediate Reynolds Numbers", *The Canadian Journal of Chemical Engineering*, pp. 119-121 , 1962 .

12. LePalec, G. L. and Daguenet, M., "Laminar Three-Dimensional Mixed Convection About a Rotating Sphere in a Stream", *Int. J. Heat and Mass Transfer*, Vol. 30, No. 7, pp. 1511-1523 , 1987 .

13. Wang, T. and Kleimstreuer, C., "Mixed Convection over Rotating Bodies with Blowing and Suction", *Int. J. Heat and Mass Transfer*, Vol. 32, No. 7. pp. 1309-1319 , 1989 .

14. LePalec, G. and Daguuenet, M., "Mixed Convection about a Sphere Rotating in a Forced Axial Flow", *International Chemical Engineering*, Vol. 30, No. 4, pp. 683-690 , 1990 .

15. Shoup. T.E., " Applied Numerical Methods for the Microcomputer" Printice-Hall, 1984.

16. Dennis. S. C. R. , Singh, S. N. and Ingham, D. B., "The Steady Flow Due to a Rotating Sphere at Low and Moderate Reynolds Numbers", *Journal of Fluid Mechanics*, Vol. 101, part 2, pp. 257-279 , 1980 .

17. Yefimova, V.G. and Yakushin, V.I., "Fluid Motion in the Vicinity of a Rotating Sphere", *Heat Transfer, Soviet Research*, Vol. 23, No. 8 , pp. 1139-1147, 1991 .

18. Iosilevskii, G., Mendoza-Blanco, A.E. and Brenner, H., "The Slow Axisymmetric Rotation of a Sphere in a Trnasversely Isotropic Fluid", *Quarterly Journal of Mechanics and Applied Mathematics*, Vol. 46, part 1, pp. 153-161, February , 1993 .

19. Raman, V. M. , "Numerical Prediction of a Laminar Boundary Layer Flow on a Rotating Sphere", *Computer Methods in Applied Mechanics and Engineering* , Vol. 43, pp. 37-44 (North Holland) , 1984 .

20. El-Shaarawi, M.A.I. , El-Refaie, M.E., Kemry, M.M. and El-Bedeawi, S.A., "Induced Laminar Flow Due to a Rotating Sphere", *JSME International Journal*, Series B, Vol. 36, No. 4, pp. 553-559 , 1993 .

21. Moore, D.W., "The Rise of a Gas Bubble in a Viscous Liquid", *Journal of Fluid Mechanics*, Vol. 6, pp. 113-130 , 1959 .

22. Chao, B.T., "Motion of Spherical Gas Bubbles in a Viscous Liquid at Large Reynolds Number", *The Physics of Fluids*, Vol. 5, No. 1 , pp. 69-79, 1962 .

23. Hadamard, M., "Mouvement Permenant Lent D'une Sphere Liquide et Risqueuse Dans un Liquide Risqueux", *Comptes rendus, Academie des Sciences*, Vol. 152,pp. 1735-1739 , 1911.

24. Batchelor, G.K., "An Introduction to Fluid Dynamics" Cambridge University Press, 1967 .

25. Spells, K.E., "A Study of Circulation Patterns within Liquid Drops Moving Through a Liquid", *Proc., Phys., Soc.*, Sect. B, Vol. 65, pp. 541-546 , 1952 .

26. Hamielec, A.E. and Johnson, A.I., "Viscous Flow Around Fluid Spheres at Intermediate Reynolds Numbers", *Canadian Journal of Chemical Engineering*, pp. 41-45, April , 1962.

27. Hamielec, A.E. , Hoffman, T.W. and Ross, L.L., "Numerical Solution of the Navier Stokes Equation for Flow Past Spheres: Part II. Viscous Flow Around Circulating Spheres of Low Viscosity .", *A.I.Ch.E. Journal*, Vol. 13, No. 2, pp. 220-224. March , 1967 .

28. Rivikind, V.Y. and Ryskin, G.M., "Flow Structure in Motion of a Spherical drop in a Fluid Medium at Intermediate Reynolds Numbers", *Translated from Russian Fluid Dynamics*, Vol. 11, No. 1, pp. 5-12 , 1976 .

29. Oliver, D.L.R. and Chung, J.N., " Steady Flows Inside and Around a Fluid Sphere at Low Reynolds Numbers " *Journal of Fluid Mechanics*, Vol. 154, pp. 215- , 1985 .

30. Oliver, D.L.R. and Chung, J.N., "Flow About a Fluid Sphere at Low to Moderate Reynolds Numbers", *Journal of Fluid Mechanics*, Vol. 177, pp. 1-18 , 1987 .

31. Mechailidis, E.E., "On the Drag Coefficient and the Correct Integration of the Equation of Motion of Particles in Gases", *Journal of Fluids Engineering*, Vol. 110, pp. 339-341, 1988.

32. Harper, J. F. and Moore, D.W., "The Motion of a Spherical Liquid Drop at High Reynolds Number", *Journal of Fluid Mechanics*, Vol. 32, part 2, pp. 367-391 , 1968.

33. Tomoeda, M., "Flow of Rarefied Gas Past a Liquid Sphere", *AIAA Journal*, Vol. 30, No. 12, pp. 2977-2980 , 1992 .

34. Godsave, G.A.E., "Burning of Fuel Droplets", *Fourth Symposium (International) on Combustion*, Williams and Wilkins, Baltimore, pp. 818-830 , 1953 .

35. Spalding, D.B., "The combustion of liquid fuels", *Fourth Symposium (International) on Combustion*, Williams and Wilkins, Baltimore, pp. 847-864, 1953 .

36. Kotake, S. and Okazaki, T., "Evaporation and Combustion of a Liquid Fuel Droplet", *Int. Journal of Heat and Mass Transfer*, Vol. 12, p. 595-609, 1969 .

37. Hubbard, G.L. , Denny, V.E. and Mills, A.F., "Droplet evaporation : Effects of Transient and Variable Properties", *Int. Journal of Heat and Mass Transfer*, Vol. 18, pp. 1003-1008 , 1975 .

38. Faeth, G.M., "Current Status of Droplet and Liquid Combustion", *Prog. Energy Combustion Sci.*, Vol. 3,pp. 191-224 , 1977 .

39. Yuen, M.C. and Chen, L.W., " On Drag of Evaporating Liquid Droplets", *Combustion Science and Technology*, Vol. 14, pp. 147-154, 1976 .

40. Kadota, T. and Hiroyasu, H., "Evaporation of a Single Droplet at Elevated Pressures and Temperatures (2nd Report, Theoretical Study)", *Bulletin of the JSME*, Vol. 19, No. 138, pp. 1515-1521 , 1976 .

41. Law, C.K., "Unsteady Droplet Combustion With Droplet Heating", *Combustion and Flame*, Vol. 26, pp. 17-22 , 1976 .

42. Law, C.K.and Sirignano, W.A., "Unsteady Droplet Combustion With Droplet Heating - II Conduction Limit", *Combustion and Flame*, Vol. 28, pp. 175-186, 1977.

43. Law, C.K. and Law, H.K., "Theory of Quasi-steady One-Dimensional Diffusional Combustion With Variable Properties Including Distinct Binary Diffusion Coefficients", *Combustion and Flame*, Vol. 29, pp. 269-275 , 1977 .

44. Sayegh, N.N. and Gauvin, W.H., "Numerical Analysis of Variable Property Heat Transfer to a Single Sphere in High Temperature Surroundings", *AIChE Journal*, Vol. 25, No. 3, pp. 522-534, May , 1979 .

45. Law, C.K. , "Recent Advances in Droplet Vaporization and Combustion", *Prog. Energy Combustion Sci.*, Vol. 8, pp. 171-201 , 1982 .

46. Dwyers, H. A. , Kee, R.J., Barr, P.K. and Sanders, B.R., "Transient Droplet Heating at High Peclet Number", *Journal of Fluids Engineering*, Vol. 105, pp. 83-87 , 1983 .

47. Sirignano, W.A., "Fuel Droplet Vaporization and Spray Combustion Theory", *Prog. Energy Combustion Sci.*, Vol. 9, pp. 291-322 , 1983 .

48. Renksizbulut, M. and Yuen, M.C., " Numerical Study of Droplet Evaporation in a High Temperature Stream", *Journal of Heat Transfer, Transactions of the ASME*, Vol. 105, pp. 389-397, May 1983 .

49. Renksizbulut, M. and Yuen, M.C., "Experimental Study of Droplet Evaporation in a High Temperature Air Stream", *Journal of Heat Transfer, Transactions of the ASME*, Vol. 105, pp. 384-388 , 1983 .

50. Aggarwal S.K., Tong, A. Y. and Sirignano, W.A., "A Comparison of Vaporization Models in Spray Calculations", *AIAA Journal*, Vol. 22, No. 10, pp. 1448-1457 , 1984 .

51. Aggarwal, S., "Effects of Internal Heat Transfer Models on the Ignition of a Fuel Droplet", *Combustion Science and Technology*, Vol. 42, pp. 325-334 , 1985 .

52. Aggarwal, S. K. and Sirignano, W.A. "Unsteady Spray Flame Propagation in a Closed Volume", *Combustion and Flame*, Vol. 62 , pp. 69-84 , 1985 .

53. Patnaik, G. , Sirignano, W.A.,Dwyer, W.A. and Sanders, B.R., "A Numerical Technique for the Solution of a Vaporizing Fuel Droplet. Dynamics of Reactive Systems", *Progress in Astronautics and Aeronautics*, Vol. 105, pp. 253-266 , 1986 .

54. Renksizbulut, M. and Haywood, R. J., "Transient Droplet Evaporation With Variable Properties and Internal Circulation At Intermediate Reynolds Numbers", *Int. J. Multiphase Flow* , Vol. 14, No. 2, pp. 189-202 , 1988 .

55. Abramzon, B. and Sirignano, W.A., "Droplet Vaporization Model For Spray Combustion Calculations", *Int. J. Heat and Mass Transfer*, Vol. 32, No. 9, pp. 1605-1618 , 1989 .

56. Abramzon, B. and Sirignano, W. A., "Approximate Theory of a Single Droplet Vaporizing in a Convective Field: Effects of Variable Properties, Stefan Flow and ransient Liquid Heating", *Proceedings of second ASME-JSME Thermal Engineering Joint Conference, Honolulu, HI*, 1989 .

57. Haywood, R. J. , Nafziger, R. and Renksizbulut, M., "A Detailed Examination of Gas and Liquid Phase Transient Processes in Convective Droplet Evaporation", *Journal of Heat Transfer*, Vol. 111, pp. 495-502, May , 1989 .

58. Chiang, C.H., Raju, M.S. and Sirignano, W.A., "Numerical Analysis of Convective, Vaporizing Fuel Droplet with Variable Properties", *Int. J. Heat and Mass Transfer*, Vol. 35, No. 5, pp.1307-1324 , 1992 .

59. Chiang, H. and Kleinstreuer, C., "Numerical Analysis of Variable Fluid Property Effect on the Convective Heat and Mass Transfer of Fuel Droplets", *Combustion and Flame*, Vol. 92, pp. 459-464 , 1993 .

60. Chen, W. , Jiang, T.L. and Chiui, H., "Computational Investigation of Single Droplet Evaporation in a Convective Flow", *J. CSME,* Vol. 14, No. 1 , pp. 100-105, 1993 .

61. Megaridis, C.M. , "Comparison Between Experimental Measurements and Numerical Predictions of Internal Temperature Distributions of a Droplet Vaporizing Under High-Temperature Convective Conditions", *Combustion and Flame*, Vol. 93, pp. 287-302 , 1993 .

62. Takei, M. , Tsukamoto, T. and Niioki, T., "Ignition of Blended-Fuel Droplet in High-Temperature Atmosphere", *Combustion and Flame*, Vol. 93, pp. 149-156 , 1993 .

63. Prakash, S. and Sirignano, W.A. "Liquid Fuel Droplet Heating With Internal Circulation", *Int. Journal of Heat and Mass Transfer*, Vol. 21, pp. 885-895 , 1978 .

64. Prakash, S. and Sirignano, W.A., "Theory of Convective Droplet Vaporization with Unsteady Heat Transfer in The Circulating Liquid Phase", *Int. Journal of Heat ans Mass Transfer*, Vol. 23, pp. 253-268 , 1980 .

65. Tong, A.Y. and Sirignano, W.A., " Analytical Solution for Diffusion in the Core of a Droplet With Internal Circulation", *AIChE Symposium Series, Vol. 77, pp. 400-407*, 1981 .

66. Tong, A.Y. and Sirignano, W.A., "Analytical Solution for Diffusion and Circulation in a Vaporizing Droplet", *Proceedings of Nineteenth Symposium (International) on Combustion, Combustion Institute, Pittsburg*, pp.1007-1020 , 1982 .

67. Tong, A.Y. and Sirignano, W.A., "Transient Thermal Boundary Layer in Heating of Droplet with Internal Circulation : Evaluation of Assumptions", *Combustion Science and Technology*, Vol. 29, pp. 87-94 , 1982 .

68. Fernandez-Pello, A. C. , "An Analysis of the Forced Convective Burning of a Combustible Particle", *Combustion Science and Technology*, Vol. 28, pp. 305-313 , 1982 .

69. Fernandez-Pello, A. C. and Law, C. K., "A Theory for The Free Convective Burning of a Condensed Fuel Particle", *Combustion and Flame*, Vol. 44, pp. 97-112 , 1982 .

70. Wu, X. , Law, C.K. and Fernandez-Pello, A.C., "A Unified Criterion for The Convective Extinction of Fuel Particles", *Combustion and Flame*, Vol. 44, pp. 125-135 , 1982 .

71. Fernandez-Pello, A.C., "Theory of Mixed Convective Combustion of a Spherical Fuel Particle", *Combustion and Flame*, Vol. 53, pp. 23-32 , 1983 .

72. Rangel, R.H. , and Fernandez-Pello, A.C., "Mixed Convective Droplet Combustion With Internal Circulation", *Combustion Science and Technology*, Vol. 42, pp. 47-65, 1984 .

73. Williams, A. , "Combustion of Droplets of Liquid Fuels : A Review", *Combustion And Flame*, Vol. 21, pp. 1-31 , 1973 .

74. Haywood, R. and Renksizbulut, M. " On Variable Property Blowing, and Transient Effects in Convective Droplet Evaporation with Internal Circulation", *In Proc. of the 8th Int. heat Transfer Conf., San Francisco, Calif.*, Vol. 4, pp. 1861-1866, 1986 .

75. Milne-Thomson, L.M., "Theoretical Hydrodynamics ", fifth ed., Macmillan and Co., London, 1968 .

76. Schlichting , H., "Boundary Layer Theory ", Seventh edition, McGraw-Hill, 1979.

77. White, F., "Viscous Fluid Flow ", Second edition, McGraw-Hill, 1991 .

78. El-Shaarawi, M.A.I., "Derivation of Boundary for Cases With Curved Boundaries", *Int. J. Engineering Fluid Mechanics*, Vol. 3, No.2, pp 113-128, 1990 .

79. Raithby, G. D., and Eckert, E. R. G., " The Effect of Turbulence Parameters and Support Position on the Heat Transfer From Spheres", *Int. Journal of Heat and Mass Transfer*, Vol. 11, pp. 1233-1252, 1968 .

80. McAdams, W. H., "Heat Transmission", Third Edition, McGraw-Hill, 1953 .

81. Achenbach, E., "Heat Transfer From Spheres up to Re = 6 x 10^6", *Proc. 6th Int. Heat Transfer Conf.*, Vol. 5, Hemisphere, Washington, D.C., 1978 .

82. Whitaker, S., "Forced Convection Heat Transfer Correlations for Flow in Pipes, Past Flat Plates, Single Cylinders, Single Spheres, and for Flow in Packed Beds and Tube Bundles", *AIChE J.*, Vol. 18, pp. 361-371, 1972 .

Appendix A

GAS PHASE GOVERNING EQUATIONS

A.1 Introduction

In this appendix , the governing equations for the case of flow around a liquid sphere are derived . Navier Stokes equations for spherical coordinates as well as the continuity equation are presented first and then the equations are simplified using the assumptions stated in Chapter III . Equations are then transformed to orthogonal curvilinear coordinates whose relation to spherical polar coordinates were given originally by El-Bedeawi [9] . Nondimensional parameters are then introduced and the equations were transformed using these parameters to a final dimensionless form . An order of magnitude analysis then is carried out and the final boundary layer equations were reached .

Then the same procedure is done for the energy equation reaching to a final dimensionless form of the energy equation in the curvilinear orthogonal coordinate system defined early in this appendix .

A.2. Continuity and Momentum Equations :

Starting from the Navier Stokes equations in the spherical polar coordinates for axisymmetric flow (in r and θ directions only) . It is to be noted that changes with respect

to φ are absent as well as its velocity component v_φ (refer to the assumptions and simplifications in Chapter III) . Therefore, equations can be written as follows ;

A.2.1 Equations in the Spherical Polar Coordinates

Continuity equation :

$$\frac{\partial w}{\partial r}+\frac{1}{r}\frac{\partial u}{\partial \theta}+\frac{2w}{r}+\frac{u\cot\theta}{r}=0 \qquad \textbf{(A. 1)}$$

where u : meridional velocity component (v_θ)

w : radial velocity component (v_r)

Meridional Momentum equation

$$w\frac{\partial u}{\partial r}+\frac{u}{r}\frac{\partial u}{\partial \theta}+\frac{uw}{r}=\frac{-1}{\rho r}\frac{dP}{d\theta}+\nu\left[\begin{array}{l}\frac{1}{r}\frac{\partial^2(ru)}{\partial r^2}+\frac{1}{r^2}\frac{\partial^2 u}{\partial \theta^2}+\frac{\cot\theta}{r^2}\frac{\partial u}{\partial \theta}+\\ +\frac{2}{r^2}\frac{\partial w}{\partial \theta}-\frac{u}{r^2\sin^2\theta}\end{array}\right] \qquad \textbf{(A. 2)}$$

Radial momentum equation

$$w\frac{\partial w}{\partial r}+\frac{u}{r}\frac{\partial w}{\partial \theta}-\frac{u^2}{r}=\frac{-1}{\rho}\frac{dP}{dr}+\nu\left[\begin{array}{l}\frac{1}{r}\frac{\partial^2(rw)}{\partial r^2}+\frac{1}{r^2}\frac{\partial^2 w}{\partial \theta^2}+\frac{\cot\theta}{r^2}\frac{\partial w}{\partial \theta}+\\ -\frac{2}{r^2}\frac{\partial u}{\partial \theta}-\frac{2w}{r^2}-\frac{2\cot\theta\, u}{r^2}\end{array}\right] \qquad \textbf{(A. 3)}$$

A.2.2 Orthogonal Curvilinear Axisymmetric Coordinate System

Now transforming the equations to the curvilinear coordinate system shown in Figure 3.1 in Chapter III , we'd define ;

$$\frac{\partial}{\partial\theta}=r\frac{\partial}{\partial x} \quad since \quad x=r\theta$$

$$\frac{\partial x}{\partial\theta}=r \qquad \frac{\partial}{\partial\theta}=\frac{\partial}{\partial x}\frac{\partial x}{\partial\theta}=r\frac{\partial}{\partial x}$$

$$r=a+z \qquad \frac{\partial r}{\partial z}=1 \tag{A.4}$$

$$\frac{\partial}{\partial r}=\frac{\partial}{\partial z}\frac{\partial z}{\partial r}=-\frac{\partial}{\partial z}$$

$$\frac{\partial^2}{\partial r^2}=\frac{\partial}{\partial r}\left(\frac{\partial}{\partial r}\right)=\frac{\partial}{\partial z}\left(\frac{\partial}{\partial r}\right)\frac{\partial z}{\partial r}=\frac{\partial}{\partial z}\left(\frac{\partial}{\partial z}\right)=\frac{\partial^2}{\partial z^2}$$

Hence , continuity equation becomes

$$\frac{\partial w}{\partial z}+\frac{\partial u}{\partial x}+\frac{2w}{a+z}+\frac{u\cot\theta}{a+z}=0 \tag{A.5}$$

meridional momentum equation becomes

$$w\frac{\partial u}{\partial z}+u\frac{\partial u}{\partial x}+\frac{uw}{a+z}=\frac{-1}{\rho}\frac{dP}{dx}+\nu\left[\begin{array}{l}\dfrac{1}{z+a}\dfrac{\partial^2((z+a)u)}{\partial z^2}+\dfrac{\partial^2 u}{\partial x^2}+\dfrac{\cot\theta}{a+z}\dfrac{\partial u}{\partial x}+\\ \dfrac{2}{a+z}\dfrac{\partial w}{\partial x}-\dfrac{u}{(a+z)^2\sin^2\theta}\end{array}\right] \tag{A. 6}$$

and the radial momentum equation becomes

$$w\frac{\partial w}{\partial z}+u\frac{\partial w}{\partial x}-\frac{u^2}{a+z}=\frac{-1}{\rho}\frac{dP}{dz}+\nu\left[\begin{array}{l}\dfrac{1}{z+a}\dfrac{\partial^2((z+a)w)}{\partial z^2}+\dfrac{\partial^2 w}{\partial x^2}+\dfrac{\cot\theta}{a+z}\dfrac{\partial w}{\partial x}-\\ \dfrac{2}{a+z}\dfrac{\partial u}{\partial x}-\dfrac{2w}{(a+z)^2}-\dfrac{2\cot\theta\, u}{(a+z)^2}\end{array}\right] \tag{A. 7}$$

A.2.3 Dimensionless Form of the Equations

Non-dimensionalizing parameters

$$U=\frac{u}{U_\infty}\ ,\ W=\frac{w}{U_\infty}\ ,\ Z=\frac{z}{a}\ ,\ X=\frac{2x}{a\,\mathrm{Re}}\ ,\ \mathrm{Re}=\frac{2U_\infty a}{\nu_g}$$
$$U^*=\frac{u^*}{U_\infty}\ ,\ R=\frac{2r_0}{a\,\mathrm{Re}}\ ,\ P=\frac{p}{\rho_g U^2_\infty} \qquad \textbf{(A. 8)}$$

Now, by nondimensionalizing the continuity equation we get,

$$\frac{U_\infty}{a}\frac{\partial W}{\partial Z}+\frac{2U_\infty}{a\,\mathrm{Re}}\frac{\partial U}{\partial X}+\frac{2U_\infty W}{a(1+Z)}+\frac{U_\infty U\cot\theta}{a(1+Z)}=0 \qquad \textbf{(A. 9)}$$

$$\frac{\partial W}{\partial Z}+\frac{2}{\mathrm{Re}}\frac{\partial U}{\partial X}+\frac{2W}{(1+Z)}+\frac{U\cot\theta}{(1+Z)}=0 \qquad \textbf{(A. 10)}$$

Meridional momentum becomes ;

$$W\frac{U^2_\infty}{a}\frac{\partial U}{\partial Z}+U\frac{2U^2_\infty}{a\,\mathrm{Re}}\frac{\partial U}{\partial X}+\frac{U^2_\infty}{a}\frac{UW}{1+Z}=\frac{-2}{2\rho}\frac{dP}{dx}\frac{2\rho U^2_\infty}{a\,\mathrm{Re}}+$$
$$+\nu\left[\frac{U_\infty}{a^3(1+Z)}\frac{\partial^2 a(1+Z)U}{\partial Z^2}+\frac{4U_\infty}{a^2\,\mathrm{Re}^2}\frac{\partial^2 U}{\partial X^2}+\right.$$
$$\left.+\frac{2\cot\theta\,U_\infty}{a^2(1-Z)\,\mathrm{Re}}\frac{\partial U}{\partial X}+\frac{4U_\infty}{a^2(1+Z)\,\mathrm{Re}}\frac{\partial W}{\partial X}-\frac{UU_\infty}{a^2(1+Z)^2\sin^2\theta}\right] \qquad \textbf{(A.11)}$$

$$W\frac{\partial U}{\partial Z}+U\frac{2}{\mathrm{Re}}\frac{\partial U}{\partial X}+\frac{UW}{1+Z}=-\frac{dP}{dX}\frac{1}{\mathrm{Re}}+$$
$$+\left[\frac{2}{\mathrm{Re}(1+Z)}\frac{\partial^2(1+Z)U}{\partial Z^2}+\frac{8}{\mathrm{Re}^3}\frac{\partial^2 U}{\partial X^2}\right.$$
$$\left.+\frac{4\cot\theta}{(1+Z)\,\mathrm{Re}^2}\frac{\partial U}{\partial X}+\frac{8}{(1-Z)\,\mathrm{Re}^2}\frac{\partial W}{\partial X}-\frac{2U}{(1+Z)\,\mathrm{Re}\sin^2\theta}\right] \qquad \textbf{(A. 12)}$$

while the radial momentum equation becomes ;

$$W\frac{U_\infty^2}{a}\frac{\partial W}{\partial Z}+U\frac{2U_\infty^2}{a\,\mathrm{Re}}\frac{\partial W}{\partial X}+\frac{U_\infty^2}{a}\frac{U^2}{1+Z}=\frac{-1}{2\rho}\frac{dP}{dZ}\frac{2\rho U_\infty^2}{a}+$$
$$+\left[\begin{array}{l}\dfrac{\nu U_\infty}{a^3(1+Z)}\dfrac{\partial^2 a(1+Z)W}{\partial Z^2}+\dfrac{4U_\infty}{a^2\,\mathrm{Re}^2}\dfrac{\partial^2 W}{\partial X^2}++\dfrac{\cot\theta\,U_\infty}{a^2(1+Z)}\dfrac{\partial W}{\partial Z}\\ -\dfrac{4U_\infty}{a^2(1+Z)\,\mathrm{Re}}\dfrac{\partial U}{\partial X}-\dfrac{2WU_\infty}{a^2(1+Z)^2}-\dfrac{2\cot\theta\,UU_\infty}{a^2(1+Z)^2}\end{array}\right] \qquad \textbf{(A. 13)}$$

$$W\frac{\partial W}{\partial Z}+U\frac{2}{\mathrm{Re}}\frac{\partial W}{\partial X}-\frac{U^2}{1+Z}=\frac{-1}{2}\frac{dP}{dZ}+$$
$$+\left[\begin{array}{l}\dfrac{2}{\mathrm{Re}(1+Z)}\dfrac{\partial^2(1+Z)W}{\partial Z^2}+\dfrac{8}{\mathrm{Re}^3}\dfrac{\partial^2 W}{\partial X^2}\\ +\dfrac{4\cot\theta}{(1+Z)\,\mathrm{Re}^2}\dfrac{\partial U}{\partial X}-\dfrac{8}{(1+Z)\,\mathrm{Re}^2}\dfrac{\partial U}{\partial X}-\dfrac{4W}{(1+Z)^2\,\mathrm{Re}^2}-\dfrac{4UCot\theta}{\mathrm{Re}(1+Z)^2}\end{array}\right] \qquad \textbf{(A.14)}$$

A.2 Order of Magnitude Analysis for the Governing Equations

$$\mathrm{Re}\gg 1 \quad , \quad \delta \ll 1$$
$$U=\frac{u}{U_\infty}\approx O(1) \quad , \quad W=\frac{w}{U_\infty}\approx O(\delta)$$
$$Z=\frac{z}{a}\approx O(\delta) \quad , \quad X=\frac{2x}{a\,\mathrm{Re}}\approx O\left(\frac{1}{\mathrm{Re}}\right) \qquad \textbf{(A.15)}$$
$$\frac{\partial}{\partial X}\approx O(\mathrm{Re}) \quad , \quad \frac{\partial^2}{\partial X^2}\approx O(\mathrm{Re}^2)$$
$$\frac{\partial}{\partial Z}\approx O(1/\delta) \quad , \quad \frac{\partial^2}{\partial Z^2}\approx O(1/\delta^2)$$

A.3.1 Order of Magnitude Analysis for the Continuity Equation :

$$\frac{\partial W}{\partial Z}+\frac{2}{\mathrm{Re}}\frac{\partial U}{\partial X}+\frac{2W}{(1+Z)}+\frac{U\cot\theta}{(1+Z)}=0 \qquad \textbf{(A. 16)}$$

δ/δ $\quad$ $1/\mathrm{Re}$ $\quad$ (Re) $\quad$ δ $\quad$ 1

1 $\quad$ 1 $\quad$ δ $\quad$ 1

The third term in this equation has a lower magnitude (δ) compared to the other three terms O(1) and it can be safely be dropped . However, this term will be retained in the equation since it would lead to a simpler solution algorithm for the continuity equation as described in Chapter 3 .

A.3.2 Order of Magnitude Analysis for the Meridional Momentum Equation

$$W\frac{\partial U}{\partial Z}+U\frac{2}{\mathrm{Re}}\frac{\partial U}{\partial X}+\frac{UW}{1+Z}=\frac{-1}{\mathrm{Re}}\frac{dP}{dX}+$$

$$\delta\ \frac{1}{\delta}\qquad 1\ \frac{1}{\mathrm{Re}}\frac{1}{\frac{1}{\mathrm{Re}}}\qquad \frac{\delta}{1}-\qquad \frac{1}{\mathrm{Re}}\frac{P}{\frac{1}{1/\mathrm{Re}}}$$

$$+\left[\begin{array}{l}\dfrac{2}{\mathrm{Re}(1+Z)}\dfrac{\partial^2(1+Z)U}{\partial Z^2}+\dfrac{8}{\mathrm{Re}^3}\dfrac{\partial^2 U}{\partial X^2}\\ \dfrac{1}{\mathrm{Re}}\dfrac{1}{\delta^2}\qquad\qquad\qquad \dfrac{1}{\mathrm{Re}^3}\dfrac{1}{1/\mathrm{Re}^2}\\ +\dfrac{4\cot\theta}{(1+Z)\mathrm{Re}^2}\dfrac{\partial U}{\partial X}+\dfrac{8}{(1+Z)\mathrm{Re}^2}\dfrac{\partial W}{\partial X}-\dfrac{2U}{\mathrm{Re}(1+Z)^2\sin^2\theta}\\ \dfrac{1}{\mathrm{Re}^2}\dfrac{1}{1/\mathrm{Re}}\qquad\qquad \dfrac{1}{\mathrm{Re}^2}\dfrac{\delta}{1/\mathrm{Re}}\qquad 1/\mathrm{Re}\end{array}\right] \qquad \textbf{(A. 17)}$$

Therefore, it is obvious that : $O(\mathrm{Re}\,\delta^2)\sim 1$ or $\mathrm{Re}\sim O(1/\delta^2)$

$O(P)\sim O(1)$

Terms of order δ and more can be safely dropped and hence the meridional momentum equation becomes :

$$W\frac{\partial U}{\partial Z}+U\frac{2}{\mathrm{Re}}\frac{\partial U}{\partial X}=\frac{-2}{\mathrm{Re}}\frac{dP}{dX}+\frac{2}{\mathrm{Re}}\frac{\partial^2 U}{\partial Z^2} \qquad \textbf{(A. 18)}$$

or

$$\frac{\mathrm{Re}}{2}W\frac{\partial U}{\partial Z}+U\frac{\partial U}{\partial X}=-\frac{dP}{dX}+\frac{\partial^2 U}{\partial Z^2} \qquad \textbf{(A. 19)}$$

At the edge of the boundary layer, meridional velocity component is U^* which is the meridional component of the potential flow around a sphere and it is a function of x only and hence its first and second derivatives with respect to Z are essentially zero . Substituting in the momentum equation leads to

At the edge of the internal boundary layer ($Z = \delta$) we have

$$\frac{\mathrm{Re}}{2}W^*\cdot\frac{\partial U^*}{\partial Z}+U^*\cdot\frac{\partial U^*}{\partial X}=-\frac{dP}{dX}+\frac{\partial^2 U^*}{\partial Z^2} \qquad \textbf{(A. 20)}$$

Then ,

$$U^*\cdot\frac{\partial U^*}{\partial X}=-\frac{dP}{dX} \qquad \textbf{(A. 21)}$$

Finally, the meridional momentum equation becomes;

$$U\frac{\partial U}{\partial X}+\frac{\mathrm{Re}}{2}W\frac{\partial U}{\partial Z}=U^*\cdot\frac{\partial U^*}{\partial X}+\frac{\partial^2 U}{\partial Z^2} \qquad \textbf{(A. 22)}$$

A.3.3 Order of Magnitude Analysis for the Radial Momentum Equation

$$W\frac{\partial W}{\partial Z}+U\frac{2}{\mathrm{Re}}\frac{\partial W}{\partial X}+\frac{U^2}{1+Z}=\frac{-1}{2}\frac{dP}{dZ}+$$

$$\begin{array}{cccccc}\delta & \frac{\delta}{\delta} & 1 & \frac{1}{\mathrm{Re}}\frac{\delta}{\frac{1}{\mathrm{Re}}} & \frac{1}{1} & \frac{P}{\delta}\end{array}$$

$$+\left[\begin{array}{cccc}\frac{2}{\mathrm{Re}(1+Z)}\frac{\partial^2(1+Z)W}{\partial Z^2}+\frac{8}{\mathrm{Re}^3}\frac{\partial^2 W}{\partial X^2} & & & \\ \frac{1}{\mathrm{Re}}\frac{\delta}{\delta^2} & & \frac{1}{\mathrm{Re}^3}\frac{\delta}{1/\mathrm{Re}^2} & \\ +\frac{4\cot\theta}{(1+Z)\mathrm{Re}^2}\frac{\partial W}{\partial Z}-\frac{8}{(1+Z)\mathrm{Re}^2}\frac{\partial U}{\partial X}-\frac{4W}{(1+Z)^2\mathrm{Re}^2}-\frac{4U\,Cot\theta}{\mathrm{Re}(1+Z)^2} & & & \\ \frac{1}{\mathrm{Re}^2}\frac{\delta}{1/\mathrm{Re}} & & \frac{1}{\mathrm{Re}^2}\frac{1}{1/\mathrm{Re}} & \frac{\delta}{\mathrm{Re}^2}\qquad 1/\mathrm{Re}\end{array}\right] \qquad \textbf{(A. 23)}$$

from which we get $1 = P/\delta$ that indicates that the variation of pressure P in the boundary layer is proportional to δ and it can be neglected . Therefore, dropping the terms of order δ and higher order leads to safely dropping the whole equation .

A.4 Formulation of the Energy Equation Around the Liquid Sphere :

Energy equation in spherical polar coordinates can be written for incompressible constant properties neglecting viscous dissipation term [77]

$$\rho C_p \frac{DT^*}{Dt} = k\nabla^2 T^* + q''' \qquad \textbf{(A. 24)}$$

Where;

$$\frac{DT^*}{Dt^*} = \frac{\partial T^*}{\partial t^*} + v_r \frac{\partial T^*}{\partial r} + \frac{v_\theta}{r}\frac{\partial T^*}{\partial \theta} + \frac{v_\phi}{r\sin\theta}\frac{\partial T^*}{\partial \phi}$$

$$\nabla^2 T^* = \frac{1}{r^2}\frac{\partial}{\partial r}\left(r^2 \frac{\partial T^*}{\partial r}\right) + \frac{1}{r^2 \sin\theta}\frac{\partial}{\partial \theta}\left(\sin\theta \frac{\partial T^*}{\partial \theta}\right) + \frac{1}{r^2 \sin^2\theta}\frac{\partial^2 T^*}{\partial \phi^2} \qquad \textbf{(A. 25)}$$

$q''' = Heat\ Genarated\ (source\ term)$

Assumptions :

$$\text{Axisymmetric flow} \qquad v_\phi = \frac{\partial}{\partial \phi} = 0 \qquad \textbf{(A. 26)}$$

Therefore, equation A.24 reduces to;

$$\rho C_p \left(\frac{\partial T^*}{\partial t} + v_r \frac{\partial T^*}{\partial r} + \frac{v_\theta}{r}\frac{\partial T^*}{\partial \theta}\right) = k\left[\begin{array}{l} \frac{1}{r^2}\frac{\partial}{\partial r}\left(r^2 \frac{\partial T^*}{\partial r}\right) + \\ \frac{1}{r^2 \sin\theta}\frac{\partial}{\partial \theta}\left(\sin\theta \frac{\partial T^*}{\partial \theta}\right) \end{array}\right] + q'' \qquad \textbf{(A. 27)}$$

$$\left(\frac{\partial T^*}{\partial t}+v_r\frac{\partial T^*}{\partial r}+\frac{v_\theta}{r}\frac{\partial T^*}{\partial \theta}\right)=\alpha\left[\begin{array}{l}\frac{1}{r^2}\frac{\partial}{\partial r}\left(r^2\frac{\partial T^*}{\partial r}\right)+\\ \frac{1}{r^2\sin\theta}\frac{\partial}{\partial \theta}\left(\sin\theta\frac{\partial T^*}{\partial \theta}\right)\end{array}\right]+\frac{q'''}{\rho C_p}$$

Now using the definitions in equation (A.4) and the nondimensionalizing parameters in equation (A.15) we get ;

$$\left(\frac{\partial T^*}{\partial t}+WU_\infty\frac{\partial T^*}{\partial z}+\frac{UU_\infty}{r}r\frac{\partial T^*}{\partial x}\right)=\alpha\left[\begin{array}{l}\frac{1}{r^2}\frac{\partial}{\partial z}\left(r^2\frac{\partial T^*}{\partial z}\right)+\\ \frac{1}{r^2\sin\theta}r\frac{\partial}{\partial x}\left(\sin\theta\, r\frac{\partial T^*}{\partial x}\right)\end{array}\right]+\frac{q'''}{\rho C_p} \qquad \textbf{(A. 28)}$$

$$\left(\frac{1}{U_\infty}\frac{\partial T^*}{\partial t}+W\frac{\partial T^*}{\partial z}+U\frac{\partial T^*}{\partial x}\right)=\frac{\alpha}{U_\infty}\left[\begin{array}{l}\frac{1}{(a+z)^2}\frac{\partial}{\partial z}\left((a+z)^2\frac{\partial T^*}{\partial z}\right)+\\ \frac{1}{r\sin\theta}\frac{\partial}{\partial x}\left(\sin\theta\, r\frac{\partial T^*}{\partial x}\right)\end{array}\right]+\frac{q'''}{U_\infty\rho C_p} \qquad \textbf{(A. 29)}$$

Introducing the nondimensionalizing quantities :

$$T=\frac{T^*-T^*_o}{T^*_\infty-T^*_o}\quad,\quad Z=\frac{z}{a}\quad,\quad X=\frac{2x}{a\,\mathrm{Re}}\quad,\quad t=\frac{\alpha t^*}{a^2} \qquad \textbf{(A. 30)}$$

Using the same nondimensionalizing parameters as done for momentum and continuity equations, the energy equation becomes;

$$\left(\frac{\alpha}{a^2 U_\infty}\frac{\partial T}{\partial t}+W\frac{\partial T}{a\partial Z}+\frac{2U}{a\,\mathrm{Re}}\frac{\partial T}{\partial X}\right)=$$

$$\frac{\alpha}{U_\infty}\left[\begin{array}{l}\dfrac{1}{a^2(1+Z)^2}\dfrac{\partial}{a\partial Z}\left(a^2(1+Z)^2\dfrac{\partial T}{a\partial Z}\right)+\\ \dfrac{2^2}{a^2(1+Z)\sin\theta\,\mathrm{Re}^2}\dfrac{\partial}{\partial X}\left(\sin\theta\, a(1+Z)\dfrac{\partial T}{\partial X}\right)\end{array}\right]+\frac{q'''}{U_\infty \rho C_p(T^*_\infty - T^*_o)} \qquad \textbf{(A. 31)}$$

Note that Reynolds (Re) is defined as : ($2\ U_\infty\ a\ /\ \nu$) and Prandtl number (Pr) is defined as :(ν/α)

$$\frac{1}{\mathrm{Re\,Pr}}\frac{\partial T}{\partial t}+\frac{U}{\mathrm{Re}}\frac{\partial T}{\partial X}+\frac{\alpha}{2}W\frac{\partial T}{a\partial Z}=\frac{1}{\mathrm{Re\,Pr}}\left[\begin{array}{l}\dfrac{1}{(1+Z)^2}\dfrac{\partial}{\partial Z}\left((1+Z)^2\dfrac{\partial T}{\partial Z}\right)+\\ \dfrac{4}{(1+Z)\sin\theta}\dfrac{1}{\mathrm{Re}^2}\dfrac{\partial}{\partial X}\left((1+Z)\sin\theta\dfrac{\partial T}{\partial X}\right)\end{array}\right] \qquad \textbf{(A. 32)}$$

$$+\frac{aq'''}{2U_\infty \rho C_p(T^*_\infty - T^*_o)}$$

$$\frac{1}{\mathrm{Pr}}\frac{\partial T}{\partial t}+U\frac{\partial T}{\partial X}+\frac{\mathrm{Re}}{2}W\frac{\partial T}{\partial Z}=\frac{1}{\mathrm{Pr}}\left[\begin{array}{l}\dfrac{1}{(1+Z)^2}\dfrac{\partial}{\partial Z}\left((1+Z)^2\dfrac{\partial T}{\partial Z}\right)+\\ \dfrac{4}{(1+Z)\sin\theta}\dfrac{1}{\mathrm{Re}^2}\dfrac{\partial}{\partial X}\left((1+Z)\sin\theta\dfrac{\partial T}{\partial X}\right)\end{array}\right]+S \qquad \textbf{(A. 33)}$$

where S (dimensionless heat generation term " source term") = $\dfrac{aq'''\mathrm{Re}}{2U_\infty \rho C_p(T^*_\infty - T^*_o)}$

With regard to the order of magnitude analysis, the second term in the previous equation has the quantity $(1/\mathrm{Re}^2)$ and since Reynolds number is in the order of $(1/\delta^2)$

hence, $1/\mathrm{Re}^2 \approx O(\delta^4)$. Then, this term can be dropped . This is supported by the fact that for boundary layer analysis, the longitudinal changes (with respect to X) are much smaller than the lateral changes (with respect to Z) and hence can be neglected .

Then, energy equation reduces to :

$$\frac{1}{\mathrm{Pr}}\frac{\partial T}{\partial t}+U\frac{\partial T}{\partial X}+\frac{\mathrm{Re}}{2}W\frac{\partial T}{\partial Z}=\frac{1}{\mathrm{Pr}}\left[\frac{1}{(1+Z)^2}\frac{\partial}{\partial Z}\left((1+Z)^2\frac{\partial T}{\partial Z}\right)\right]+S \qquad \textbf{(A. 34)}$$

Note;
$$\frac{\partial}{\partial Z}\left((1+Z)^2\frac{\partial T}{\partial Z}\right)=2(1+Z)\frac{\partial T}{\partial Z}+(1+Z)^2\frac{\partial^2 T}{\partial Z^2} \qquad \textbf{(A. 35)}$$

$$o(1)\ o(1/\delta) \ll o(1/\delta^2)$$

Finally, the energy equation becomes;

$$\frac{1}{\mathrm{Pr}}\frac{\partial \mathrm{T}}{\partial \mathrm{t}}+\mathrm{U}\frac{\partial \mathrm{T}}{\partial \mathrm{X}}+\frac{\mathrm{Re}}{2}\mathrm{W}\frac{\partial \mathrm{T}}{\partial \mathrm{Z}}=\frac{1}{\mathrm{Pr}}\frac{\partial^2 \mathrm{T}}{\partial \mathrm{Z}^2}+\mathrm{S} \qquad \textbf{(A. 36)}$$

Appendix B

LIQUID PHASE GOVERNING EQUATIONS

B.1. Equations in Spherical Coordinates :

Starting from the Navier stokes equations in the spherical coordinates .

Continuity equation :

$$\frac{\partial w}{\partial r}+\frac{1}{r}\frac{\partial u}{\partial \theta}+\frac{2w}{r}+\frac{u\cot\theta}{r}=0 \qquad \textbf{(B. 1)}$$

Meridional Momentum equation

$$w\frac{\partial u}{\partial r}+\frac{u}{r}\frac{\partial u}{\partial \theta}+\frac{uw}{r}=\frac{-1}{\rho r}\frac{dP}{d\theta}+\nu_l\left[\begin{array}{l}\frac{1}{r}\frac{\partial^2(ru)}{\partial r^2}+\frac{1}{r^2}\frac{\partial^2 u}{\partial \theta^2}+\frac{\cot\theta}{r^2}\frac{\partial u}{\partial \theta}+\\ +\frac{2}{r^2}\frac{\partial w}{\partial \theta}-\frac{u}{r^2\sin^2\theta}\end{array}\right] \qquad \textbf{(B. 2)}$$

Now define ;

$$\begin{aligned}&\frac{\partial}{\partial \theta}=r\frac{\partial}{\partial x} \quad \text{since} \quad x=r\theta\\ &\frac{\partial x}{\partial \theta}=r \qquad\qquad \frac{\partial}{\partial \theta}=\frac{\partial}{\partial x}\frac{\partial x}{\partial \theta}=r\frac{\partial}{\partial x}\\ &r=a-z \qquad\qquad \frac{\partial r}{\partial z}=-1\\ &\frac{\partial}{\partial r}=\frac{\partial}{\partial z}\frac{\partial z}{\partial r}=-\frac{\partial}{\partial z}\\ &\frac{\partial^2}{\partial r^2}=\frac{\partial}{\partial r}\left(\frac{\partial}{\partial r}\right)=\frac{\partial}{\partial z}\left(\frac{\partial}{\partial r}\right)\frac{\partial z}{\partial r}=\frac{\partial}{\partial z}\left(-\frac{\partial}{\partial z}\right)(-1)=\frac{\partial^2}{\partial z^2}\end{aligned} \qquad \textbf{(B. 3)}$$

Hence , continuity equation becomes

$$-\frac{\partial w}{\partial z}+\frac{\partial u}{\partial x}+\frac{2w}{a-z}+\frac{u\cot\theta}{a-z}=0 \qquad \textbf{(B. 4)}$$

and the meridional momentum equation becomes

$$-w\frac{\partial u}{\partial z}+u\frac{\partial u}{\partial x}+\frac{uw}{a-z}=\frac{-1}{\rho_l}\frac{dP}{dx}+\nu_l\left[\begin{array}{l}-\dfrac{\partial^2 u}{\partial z^2}-\dfrac{2}{a-z}\dfrac{\partial u}{\partial z}+\dfrac{\partial^2 u}{\partial x^2}+\dfrac{\cot\theta}{a-z}\dfrac{\partial u}{\partial x}+\\ \dfrac{2}{a-z}\dfrac{\partial w}{\partial x}-\dfrac{u}{(a-z)^2\sin^2\theta}\end{array}\right] \qquad \textbf{(B. 5)}$$

It is worth mentioning that from now on, the velocity components and the temperature of the liquid phase will have the subscript "ℓ" in order to be distinguished from the gas phase parameters . Introducing the non-dimensionalizing parameters;

$$\begin{array}{llll} U_l=\dfrac{u_l}{U_\infty}, & W_l=\dfrac{w_l}{U_\infty}, & Z_l=\dfrac{z}{a}, & X=\dfrac{2x}{a\,Re}, \quad Re=\dfrac{2U_\infty a}{\nu_g} \\ U_H=\dfrac{u_H^*}{U_\infty}, & R=\dfrac{2r_0}{a\,Re}, & P=\dfrac{p}{\rho_g U^2_\infty} & \end{array} \qquad \textbf{(B. 6)}$$

$$-W_l\frac{U_\infty^2}{a}\frac{\partial U_l}{\partial Z_l}+U_l\frac{2U_\infty^2}{a\,Re}\frac{\partial U_l}{\partial X_l}+\frac{U_\infty^2}{a}\frac{U_lW_l}{1-Z_l}=\frac{-1}{\rho_l}\frac{dP}{dX_l}\frac{2\rho_gU_\infty^2}{a\,Re}+$$
$$+\nu_l\left[\begin{array}{l}-\dfrac{U_\infty}{a^2}\dfrac{\partial^2 U_l}{\partial Z_l^2}-\dfrac{U_\infty}{a^2}\dfrac{2}{1-Z_l}\dfrac{\partial U_l}{\partial Z_l}+\dfrac{4U_\infty}{a^2Re^2}\dfrac{\partial^2 U_l}{\partial X_l^2}\\ +\dfrac{2\cot\theta\,U_\infty}{a^2(1-Z_l)Re}\dfrac{\partial U_l}{\partial X_l}+\dfrac{4U_\infty}{a^2(1-Z_l)Re}\dfrac{\partial W_l}{\partial X_l}-\dfrac{U_lU_\infty}{a^2(1-Z_l)^2\sin^2\theta}\end{array}\right] \qquad \textbf{(B. 7)}$$

$$-W_l\frac{\partial U_l}{\partial Z_l}+U\frac{2}{Re}\frac{\partial U_l}{\partial X_l}+\frac{U_lW_l}{1-Z_l}=\frac{-1}{\rho_l}\frac{dP}{dX_l}\frac{2\rho_g}{Re}+$$
$$+\frac{\nu_l}{\nu_g}\left[\begin{array}{l}-\dfrac{\nu_g}{U_\infty a}\dfrac{\partial^2 U_l}{\partial Z_l^2}-\dfrac{\nu_g}{U_\infty a}\dfrac{2}{1-Z_l}\dfrac{\partial U_l}{\partial Z_l}+\dfrac{4\nu_g}{U_\infty aRe^2}\dfrac{\partial^2 U_l}{\partial X_l^2}\\ +\dfrac{2\cot\theta\,\nu_g}{aU_\infty(1-Z_l)Re}\dfrac{\partial U_l}{\partial X_l}+\dfrac{4\nu_g}{aU_\infty(1-Z_l)Re}\dfrac{\partial W_l}{\partial X_l}-\dfrac{U_l\nu_g}{aU_\infty(1-Z_l)^2\sin^2\theta}\end{array}\right] \qquad \textbf{(B. 8)}$$

$$-W_i\frac{\partial U_i}{\partial Z_i}+U\frac{2}{Re}\frac{\partial U_i}{\partial X_i}+\frac{U_iW_i}{1-Z_i}=\frac{-2}{Re}\frac{dP}{dX_i}\frac{2\rho_g}{\rho_i}+$$
$$+\nu\left[-\frac{2}{Re}\frac{\partial^2 U_i}{\partial Z_i^2}-\frac{4}{Re(1-Z_i)}\frac{\partial U_i}{\partial Z_i}+\frac{8}{Re^3}\frac{\partial^2 U_i}{\partial X_i^2}\right.$$
$$\left.+\frac{4\cot\theta\,\nu_g}{(1-Z_i)Re^2}\frac{\partial U_i}{\partial X_i}+\frac{8}{(1-Z_i)Re^2}\frac{\partial W_i}{\partial X_i}-\frac{2U}{Re(1-Z_i)^2\sin^2\theta}\right] \quad \textbf{(B. 9)}$$

While, by nondimensionalizing the continuity equation we get,

$$-\frac{U_\infty}{a}\frac{\partial W_i}{\partial X_i}+\frac{2U_\infty}{aRe}\frac{\partial U_i}{\partial X_i}+\frac{2U_\infty W_i}{a(1-Z_i)}+\frac{U_\infty U_i\cot\theta}{a(1-Z_i)}=0 \quad \textbf{(B. 10)}$$

$$-\frac{\partial W_i}{\partial Z_i}+\frac{2}{Re}\frac{\partial U_i}{\partial X_i}+\frac{2W_i}{(1-Z_i)}+\frac{U_i\cot\theta}{(1-Z_i)}=0 \quad \textbf{(B. 11)}$$

B.2 Order of Magnitude Analysis for the Governing Equations

$$U=\frac{u}{U_\infty}\approx O(1) \quad , \quad W=\frac{w}{U_\infty}\approx O(\delta)$$
$$Z=\frac{z}{a}\approx O(\delta) \quad , \quad X=\frac{2x}{aRe}\approx O(\frac{1}{Re}) \quad \textbf{(B. 12)}$$

B.2.1 Order of Magnitude Analysis for the Continuity Equation :

$$-\frac{\partial W_i}{\partial Z_i}+\frac{2}{Re}\frac{\partial U_i}{\partial X_i}+\frac{2W_i}{(1-Z_i)}+\frac{U_i\cot\theta}{(1-Z_i)}=0 \quad \textbf{(B. 13)}$$

$\delta/\delta \quad 1/Re\,(Re) \quad \delta \quad 1$

$1 \quad 1 \quad \delta \quad 1$

The third term in this equation has a lower magnitude (δ) compared to the other three terms O(1) and it can be safely be dropped . However, this term will be retained in the

equation since it would lead to a simpler solution algorithm for the continuity equation as described in Chapter III .

B.2.2 Order of Magnitude Analysis for the Meridional Momentum Equation

$$-W_t \frac{\partial U_t}{\partial Z_t} + U_t \frac{2}{Re} \frac{\partial U_t}{\partial X_t} + \frac{U_t W_t}{1 - Z_t} = \frac{-2}{Re} \frac{dP}{dX_t} \frac{2\rho_g}{\rho_t} +$$

$$\delta \frac{1}{\delta} \quad 1 \frac{1}{Re} \frac{1}{\frac{1}{Re}} \quad \frac{\delta}{1} - \quad \frac{1}{Re} \frac{P}{\frac{1}{1/Re}}$$

$$+ \nu \cdot \left[\begin{array}{l} -\frac{2}{Re} \frac{\partial^2 U_t}{\partial Z_t^2} - \frac{4}{Re(1 - Z_t)} \frac{\partial U_t}{\partial Z_t} + \frac{8}{Re^3} \frac{\partial^2 U_t}{\partial X_t^2} \\ \frac{1}{Re} \frac{1}{\delta^2} \quad \frac{1}{Re} \frac{1}{\delta} \quad \frac{1}{Re^3} \frac{1}{1/Re^2} \\ + \frac{4 \cot\theta \, v_g}{(1 - Z_t) Re^2} \frac{\partial U_t}{\partial X_t} + \frac{8}{(1 - Z_t) Re^2} \frac{\partial W_t}{\partial X_t} - \frac{2U_t}{Re(1 - Z_t)^2 \sin^2\theta} \\ \frac{1}{Re^2} \frac{1}{1/Re} \quad \frac{1}{Re^2} \frac{\delta}{1/Re} \quad 1/Re \end{array} \right] \qquad \textbf{(B. 14)}$$

Therefore, it is obvious that : $O(Re\,\delta^2) \sim 1$ or $Re \sim O(1/\delta^2)$

$$O(P) \sim O(1)$$

Terms of order δ and more can be safely dropped and hence the meridional momentum equation becomes :

$$-W_t \frac{\partial U_t}{\partial Z_t} + U_t \frac{2}{Re} \frac{\partial U_t}{\partial X_t} = \frac{-2}{Re} \frac{dP}{dX_t} \frac{\rho_g}{\rho_t} + \nu \cdot \left[\frac{2}{Re} \frac{\partial^2 U_t}{\partial Z_t^2} \right] \qquad \textbf{(B. 15)}$$

$$-\frac{Re}{2} W_t \frac{\partial U_t}{\partial Z_t} + U_t \frac{\partial U_t}{\partial X_t} = -\frac{dP}{dX_t} \frac{2\rho_g}{\rho_t} + \nu \cdot \left[\frac{\partial^2 U_t}{\partial Z_t^2} \right] \qquad \textbf{(B. 16)}$$

At the edge of the boundary layer, meridional velocity component is U_H which is a function of x only and hence its first and second derivatives with respect to z are

essentially zero . Therefore. applying the momentum equation at the edge of the internal boundary layer ($Z_l = \delta$) is expressed as;

$$-\frac{Re}{2} W_H \frac{\partial U_H}{\partial Z_l} + U_H \frac{\partial U_H}{\partial X_l} = -\frac{dP}{dX_l}\frac{2\rho_g}{\rho_l} + \nu^* \left[\frac{\partial^2 U_H}{\partial Z_l^2}\right] \qquad \textbf{(B. 17)}$$

Then ,

$$U_H \frac{\partial U_H}{\partial X_l} = -\frac{dP}{dX_l}\frac{2\rho_g}{\rho} \qquad \textbf{(B. 18)}$$

Finally, the momentum equation becomes;

$$U_l \frac{\partial U_l}{\partial X_l} - \frac{Re}{2} W_l \frac{\partial U}{\partial Z} = U_H \frac{\partial U_H}{\partial X_l} + \nu^* \left[\frac{\partial^2 U_l}{\partial Z_l^2}\right] \qquad \textbf{(B. 19)}$$

B.3 Formulation of the Energy Equation Inside the Liquid Sphere

Energy equation in spherical coordinates is written as follows :

$$\frac{\partial T_l^*}{\partial t^*} + w\frac{\partial T_l^*}{\partial r} + \frac{u}{r}\frac{\partial T_l^*}{\partial \theta} = \alpha\left[\frac{1}{r^2}\frac{\partial}{\partial r}\left(r^2\frac{\partial T_l^*}{\partial r}\right) + \frac{1}{r^2\sin\theta}\frac{\partial}{\partial \theta}\left(\sin\theta\frac{\partial T_l^*}{\partial \theta}\right)\right] + \frac{q'''}{\rho_l C_p} \qquad \textbf{(B. 20)}$$

Following the definitions in equation (B.3) we get ;

$$\frac{\partial T_l^*}{\partial t^*} - w_l\frac{\partial T_l^*}{\partial z_l} + u_l\frac{\partial T_l^*}{\partial x_l} = \alpha_l\left[\frac{1}{(a-z_l)^2}\frac{\partial}{\partial z_l}\left((a-z_l)^2\frac{\partial T_l^*}{\partial z_l}\right) + \frac{1}{(a-z_l)^2\sin\theta}\frac{\partial}{\partial x_l}\left(\sin\theta\, r\frac{\partial T_l^*}{\partial x_l}\right)\right] + \frac{q'''}{\rho_l C_p} \qquad \textbf{(B. 21)}$$

In addition to the non-dimensionalizing parameters in equation (B.6) ,we further define

$$T=\frac{T^{*}-T^{*}_{o}}{T^{*}_{\infty}-T^{*}_{o}} \quad , \quad t=\frac{\alpha_{f}\, t^{*}}{a^{2}} \tag{B. 22}$$

Then equation (B.21) becomes ;

$$\frac{T^{*}_{\infty}-T^{*}_{o}}{a^{2}}\alpha_{f}\frac{\partial T_{f}}{\partial t^{*}}-W_{f}U_{\infty}\frac{T^{*}_{\infty}-T^{*}_{o}}{a}\frac{\partial T_{f}}{\partial Z_{f}}+\frac{T^{*}_{\infty}-T^{*}_{o}}{a\ \mathrm{Re}}2U_{f}U_{\infty}\frac{\partial T_{f}}{\partial X_{f}}=$$
$$\alpha_{f}\left[\begin{array}{l}\dfrac{1}{a^{3}(1-Z_{f})^{2}}\dfrac{\partial}{\partial Z_{f}}\left(a^{2}(1-Z_{f})^{2}\dfrac{\partial T_{f}}{a\partial Z_{f}}(T^{*}_{\infty}-T^{*}_{o})\right)+\\ \dfrac{2(T^{*}_{\infty}-T^{*}_{o})}{\mathrm{Re}\,a^{2}(1-Z_{f})^{2}\sin\theta}\dfrac{\partial}{\partial X_{f}}\left(a\sin\theta\,(1-Z_{f})\dfrac{2}{a\,\mathrm{Re}}\dfrac{\partial T_{f}}{\partial X_{f}}\right)\end{array}\right]+\frac{q'''}{\rho_{f}C_{p}} \tag{B. 23}$$

$$\frac{\alpha_{f}}{U_{\infty}a}\frac{\partial T_{f}}{\partial t}-W\frac{\partial T_{f}}{\partial Z_{f}}+\frac{2U}{\mathrm{Re}}\frac{\partial T_{f}}{\partial X_{f}}=\frac{\alpha_{f}}{U_{\infty}a}\times$$
$$\left[\begin{array}{l}\dfrac{1}{(1-Z_{f})^{2}}\dfrac{\partial}{\partial Z_{f}}\left((1-Z_{f})^{2}\dfrac{\partial T_{f}}{\partial Z_{f}}\right)+\\ \dfrac{4}{\mathrm{Re}^{2}(1-Z_{f})\sin\theta}\dfrac{\partial}{\partial X_{f}}\left(\sin\theta\dfrac{\partial T_{f}}{\partial X_{f}}\right)\end{array}\right]+\frac{q'''}{\rho_{f}C_{p}(T^{*}_{\infty}-T^{*}_{o})U_{\infty}} \tag{B. 24}$$

However, it should be noted that

$$\mathrm{Re}=\frac{2\,\mathrm{U}_{\infty}\,\mathrm{a}}{\nu} \quad \text{and hence,} \quad \frac{\mathrm{Re}\,\alpha_{f}}{2\,\mathrm{U}_{\infty}\,\mathrm{a}}=\frac{1}{\mathrm{Pr}_{f}}$$

Therefore, the energy equation (B.24) becomes ,

$$\frac{\nu^{*}}{\mathrm{Pr}_{f}}\frac{\partial T_{f}}{\partial t}-W_{f}\frac{\mathrm{Re}}{2}\frac{\partial T_{f}}{\partial Z_{f}}+U\frac{\partial T_{f}}{\partial X_{f}}=\frac{\nu^{*}}{\mathrm{Pr}_{f}}\times$$
$$\left[\begin{array}{l}\dfrac{1}{(1-Z_{f})^{2}}\dfrac{\partial}{\partial Z_{f}}\left((1-Z_{f})^{2}\dfrac{\partial T_{f}}{\partial Z_{f}}\right)+\\ \dfrac{4}{\mathrm{Re}^{2}(1-Z)\sin\theta}\dfrac{\partial}{\partial X_{f}}\left(\sin\theta\dfrac{\partial T_{f}}{\partial T_{f}}\right)\end{array}\right]+\frac{\mathrm{Re}\,q'''}{2\rho_{f}C_{p}(T^{*}_{\infty}-T^{*}_{o})U_{\infty}} \tag{B. 25}$$

The last term in the right hand side of the previous equation represents the dimensionless source term and it will be set to zero for the case of non-combusting, non-evaporating droplet . Besides, it was proved by other investigators [47, 50, 51, 55, 56, 58, 63-65] that due to the internal motion inside the sphere, the changes of temperature in the meridional directions are neglected compared with the changes in the radial directions . It was also considered that the isotherms coincide with the streamlines . However, further investigations of the previous equations for the range of intermediate to high Reynolds number show that the value of the second term in the right hand side will be very small since it is divided by (Re^2) and hence it can be safely dropped and equation (B.25) becomes :

$$\frac{\nu^*}{Pr_l}\frac{\partial T_l}{\partial t} - W_l\frac{Re}{2}\frac{\partial T_l}{\partial Z_l} + U_l\frac{\partial T_l}{\partial X_l} = \frac{\nu^*}{Pr_l}\left[\frac{\partial}{\partial Z}\left((1-Z_l)^2\frac{\partial T_l}{\partial Z_l}\right)\right] \qquad \textbf{(B. 26)}$$

Now, considering the right hand side of this equation and noting that :

$$\left[\frac{\partial}{\partial Z}\left((1-Z_l)^2\frac{\partial T_l}{\partial Z_l}\right)\right] = (1-Z_l)^2\frac{\partial^2 T_l}{\partial Z_l^2} + \frac{\partial T_l}{\partial Z_l}\frac{\partial}{\partial Z_l}(1-Z_l)^2$$

$$= (1-Z_l)^2\frac{\partial^2 T_l}{\partial Z_l^2} - 2\frac{\partial T_l}{\partial Z_l}(1-Z_l)$$

we obtain :

$$\left[\frac{1}{(1-Z_l)^2}\frac{\partial}{\partial Z_l}\left((1-Z_l)^2\frac{\partial T_l}{\partial Z_l}\right)\right] = \frac{\partial^2 T_l}{\partial Z_l^2} - \frac{2}{(1-Z_l)}\frac{\partial T_l}{\partial Z_l} \qquad \textbf{(B. 27)}$$

Finally, the energy equation becomes :

$$\frac{\nu^*}{\mathrm{Pr}_l}\frac{\partial T_l}{\partial t} - W_l\frac{\mathrm{Re}}{2}\frac{\partial T_l}{\partial Z_l} + U_l\frac{\partial T_l}{\partial X_l} = \frac{\nu^*}{\mathrm{Pr}_l}\left[\frac{\partial^2 T_l}{\partial Z_l^2} - \frac{2}{(1-Z_l)}\frac{\partial T_l}{\partial Z_l}\right] \qquad \textbf{(B. 28)}$$

Or :

$$\frac{\nu^*}{\mathrm{Pr}_l}\frac{\partial T_l}{\partial t} - \left(W_l\frac{\mathrm{Re}}{2} - \frac{2}{\mathrm{Pr}_l(1-Z_l)}\right)\frac{\partial T_l}{\partial Z} + U_l\frac{\partial T_l}{\partial X_l} = \frac{\nu^*}{\mathrm{Pr}_l}\frac{\partial^2 T_l}{\partial Z_l^2} \qquad \textbf{(B. 29)}$$

Appendix C

FLOW CHARTS OF THE PROGRAMS

C.1 Flow Chart of the Gas Phase Program

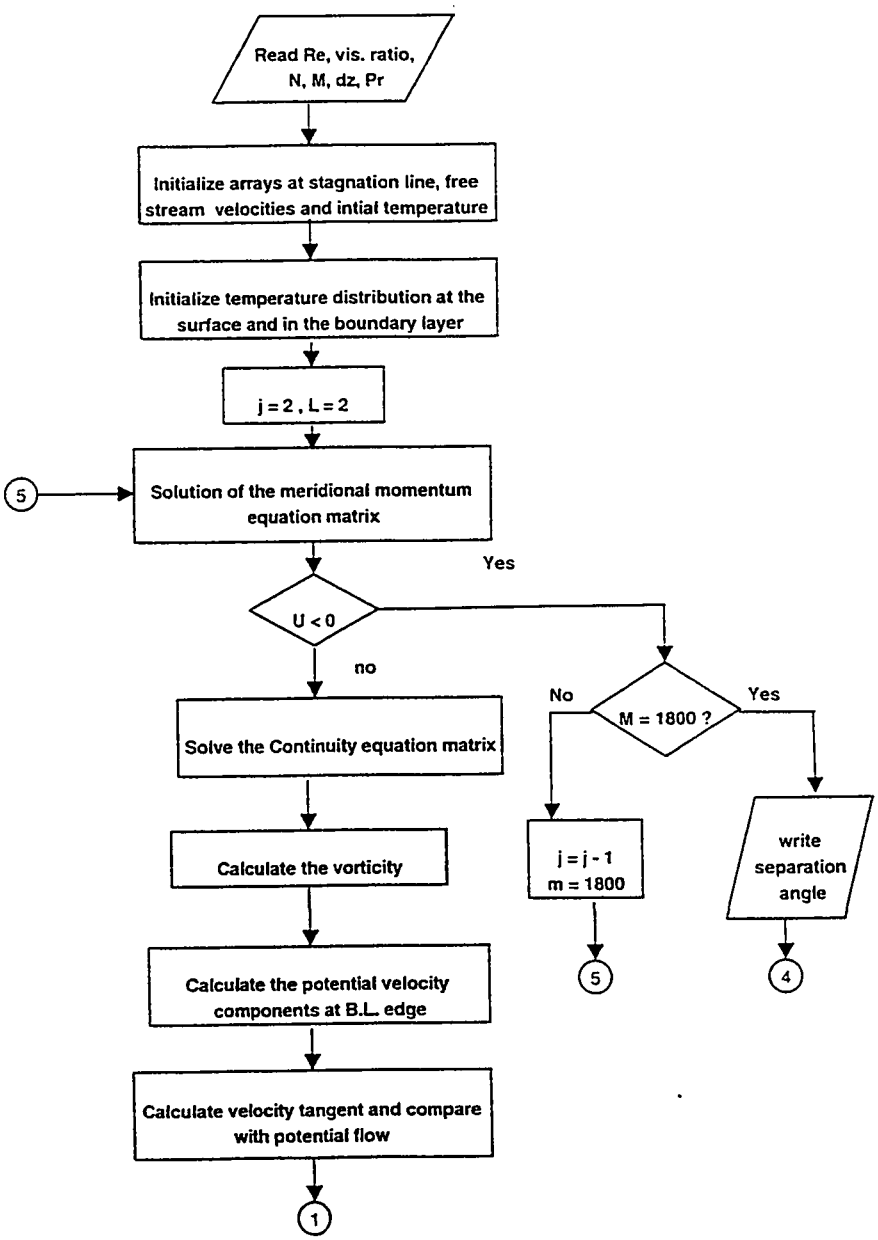

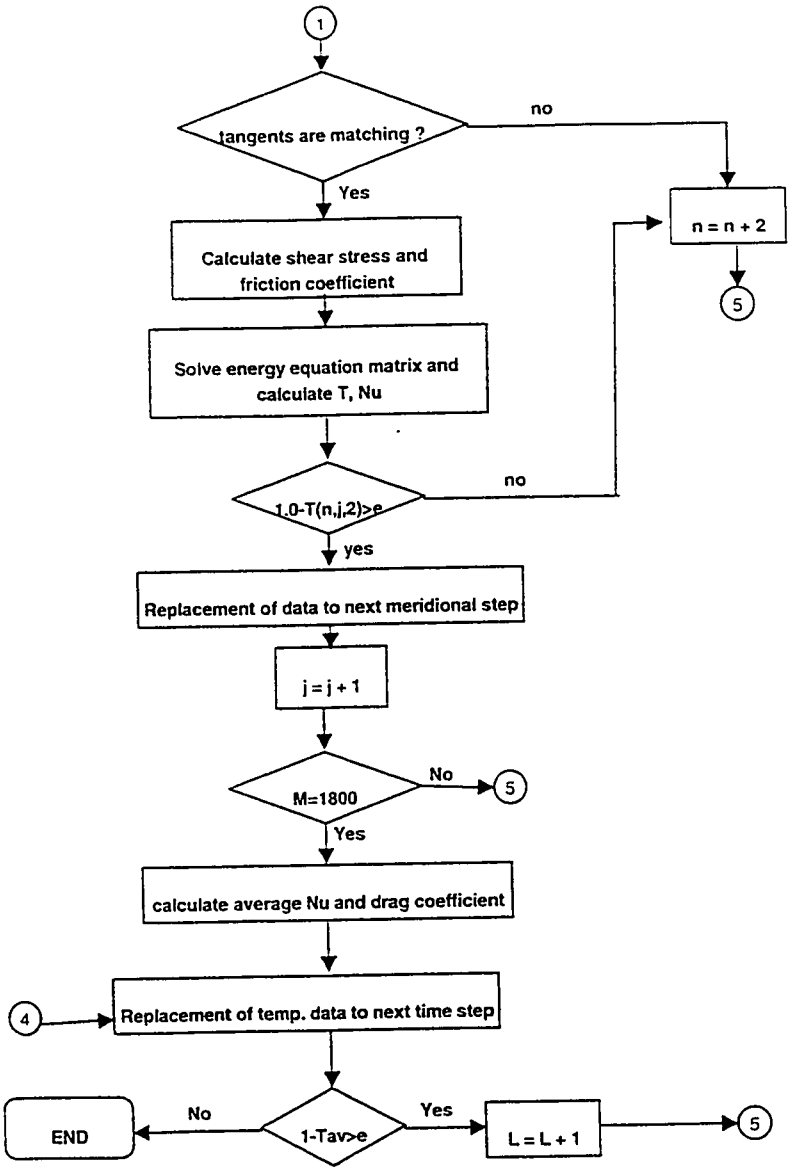
1
tangents are matching ?
no
Yes
n = n + 2
5
Calculate shear stress and friction coefficient
Solve energy equation matrix and calculate T, Nu
1.0-T(n,j,2)>e
no
yes
Replacement of data to next meridional step
j = j + 1
M=1800
No
5
Yes
calculate average Nu and drag coefficient
4
Replacement of temp. data to next time step
END
No
1-Tav>e
Yes
L = L + 1
5

C.2 Flow Chart of the Liquid-Phase Program

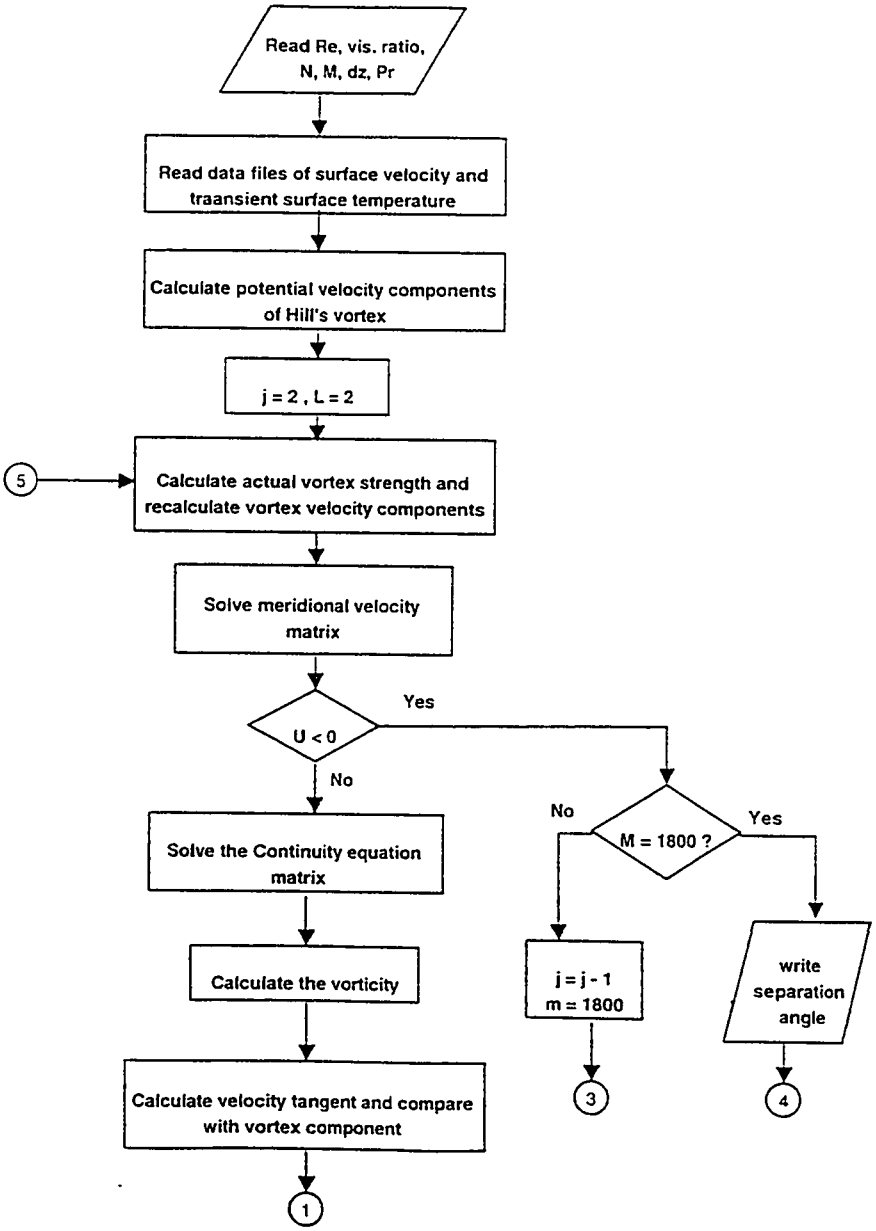

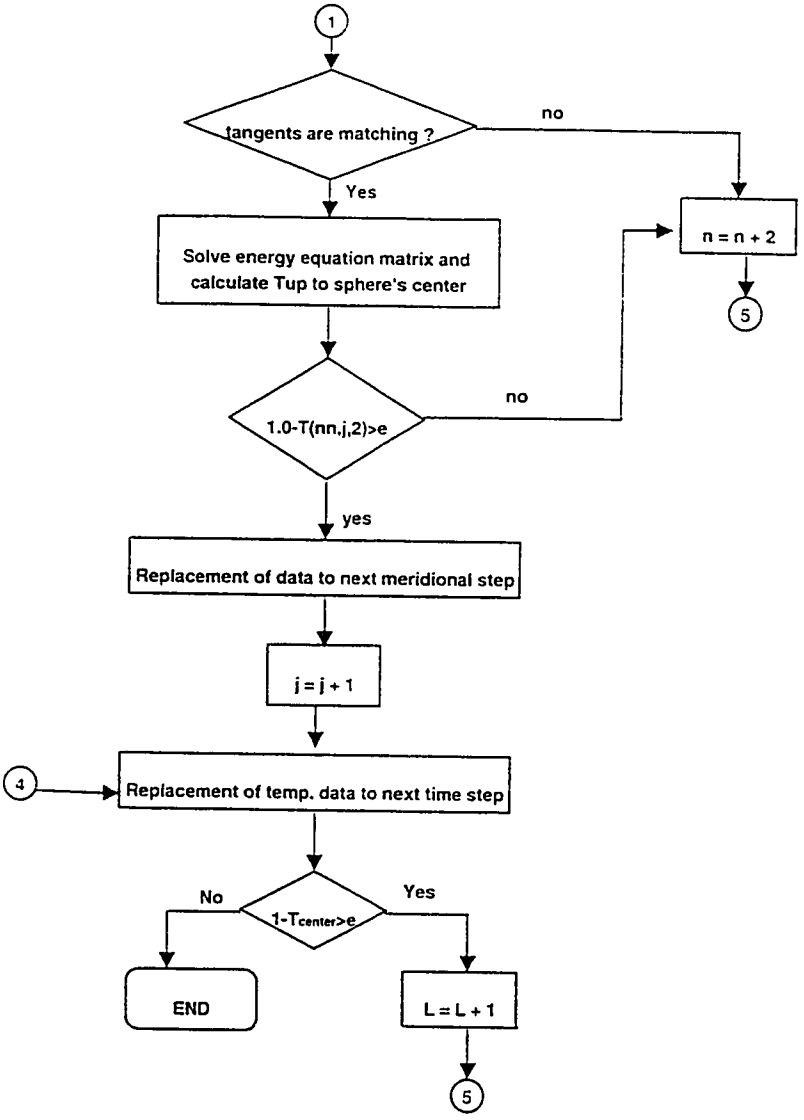
1
tangents are matching ?
no
Yes
n = n + 2
5
Solve energy equation matrix and calculate Tup to sphere's center
1.0-T(nn,j,2)>e
no
yes
Replacement of data to next meridional step
j = j + 1
4
Replacement of temp. data to next time step
No
1-Tcenter>e
Yes
END
L = L + 1
5

C.3 List of the Gas-Phase Program

```
      DIMENSION U(501,2),W(501,2),A(501),B(501),C(501)
     1 ,WP(501,2),UP(501,2),TX(150),TEM(501,180,2),FX(150)
     1 ,D(501),E(501),F(501),DRDX(2),R(2),DX(501)
      character*8 time@
      print *,'program starting execution at : ', time@()
      open(15,file='Input',status='OLD')
      open(2,file='srf.dat',status='UNKNOWN')
      open(4,file='u.dat',status='UNKNOWN')
      open(5,file='tau.dat',status='UNKNOWN')
      open(16,file='cd.dat',status='UNKNOWN')
      open(7,file='vort.dat',status='UNKNOWN')
      open(8,file='w.dat',status='UNKNOWN')
      open(9,file='t.dat',status='UNKNOWN')
      open(10,file='TSURF.dat',status='UNKNOWN')
      open(11,file='TT.DAT',STATUS='UNKNOWN')
      open(12,file='nusselt.dat',status='unknown')
      read(15,*)DZ,dzl,RE,N,M,VISR,FACT,IN,DT,PR,ISTEP,akk,K
      R(1) = 0.0
      L=1
      DO 88 J=1,180
88    TEM(1,J,1)=0.
79    DO 80 I = 1,N
      W(I,1) = 1./((1.+(I-1)*DZ)**3)-1.
      U(I,1) = 0.0
      TEM(I,1,1) = 1.0
80    CONTINUE
      J = 1
      TEM(1,J,2) = 1.0
      G = 0.0
      J = 1
      JJ = J
      IF(K.EQ.1) THEN
      DO 902 I = 1,N
      DO 902 J = 2,130
902   TEM(I,J,1) = 1.0
      ELSEIF(K.EQ.2) THEN
      DO 903 I = 1,N
      DO 903 J = 1,130
903   TEM(I,J,1) = (I-1)/(N-1)
```

```
      ENDIF
81    J = 1
      DTHETA = 3.1415926536/M
      DX(1) = 2.*DTHETA/RE
84    W(1,2)  = 0.0
      DRDX(2) = COS(G+DTHETA)
      R(2)    = 2. * SIN(G+DTHETA)/RE
      J       = J + 1
      IF(JJ.LT.J) JJ=J
      TEM(1,2,1)=0.
      IF(L.EQ.1) TEM(1,2,2)=0.
83    W(N+1,2) = -(1.-1./(1.+N*DZ)**3)*COS(G+DTHETA)
      U(N+1,2) = (1.+1./(2.*(1+N*DZ)**3))*SIN(G+DTHETA)
      U(N+2,2) = (1.+1./(2.*(1.+(N+1)*DZ)**3))*SIN(G+DTHETA)
      DO 90 I = 2,N+1
90    DX(I)=(1.+DZ*(I-1))*DX(1)
      DO 105 I = 1,N+1
105   C(I)    =-(W(I,1)*RE/(4.*DZ)+1./(DZ**2))
      DO 106 I=1,N+1
106   A(I)    = U(I,1)/DX(I)+2./(DZ**2)
      DO 107 I=1,N+1
107   B(I)    = W(I,1)*RE/(4.*DZ)-1./(DZ**2)
      DO 110 I=1,N
110   D(I) = (U(I,1)**2)/DX(I)+(9./16.) * RE * sin (2*(G+DTHETA))
      A(1) = A(1) - C(1) *(VISR-1.)/VISR
      B(1) = B(1) + C(1) / VISR
      D(N) = D(N) - B(N)*U(N+1,2)
      E(1) = A(1)
      F(1) = D(1)/E(1)
      DO 115 I=2,N
      E(I) = A(I)-C(I)*B(I-1)/E(I-1)
115   F(I) = (D(I)-C(I)*F(I-1))/E(I)
      U(N,2) = F(N)
      DO 120 II = 1,N-1
      I = N-II
      U(I,2)=F(I)-B(I)*U(I+1,2)/E(I)
      IF(U(I,2).LT.0.0)GO TO 270
120   CONTINUE
      IF(L.EQ.1) THEN
      WRITE(2,50) J-1,U(1,2)
50    FORMAT (5X,I4,5X,F12.4)
      IF(J.EQ.IN) WRITE(4,55) (DZ*(I-1),U(I,2),I=1,N+1)
55    FORMAT(2(10X,F10.4))
      ENDIF
      DO 125 I=1,N
```

```
      A(I) = RE/(2.*DZ)
125   B(I) = -RE/(2.*DZ)
      CCOT = COS(G+DTHETA)/SIN(G+DTHETA)
      DO 130 I=1,N
130   D(I) = (U(I+1,2)+U(I,2)-U(I+1,1)-U(I,1))/(DX(I)+DX(I+1))
     1 +U(I+1,2)+U(I,2)*RE*CCOT*0.25
      W(2,2) = D(1)/B(1)
      DO 135 I=3,N
135   W(I,2) = (D(I-1)-A(I-1)*W(I-1,2))/B(I-1)
      IF(L.EQ.1) THEN
      IF(J.EQ.IN) WRITE(8,55) (I*DZ,W(I,2),I=1,N)
      ENDIF
      DUDZ = (-U(3,2)+4.*U(2,2)-3.*U(1,2)) / (2.*DZ)
      VORT = (U(1,2)+DUDZ -(2./RE)*(W(2,2)-W(2,1))/DX(1))
      VORT1 = VORT / (RE**0.5)
      IF(L.EQ.1) THEN
      WRITE(7,901) J-1,VORT,VORT1
901   FORMAT(5X,I4,5X,F12.7,5X,F12.7)
      ENDIF
      WP(N-1,2)=-(1.-1./((1.+(N-2)*DZ)**3))*COS(G+DTHETA)
      WP(N,2)  =-(1.-1./((1.+(N-1)*DZ)**3))*COS(G+DTHETA)
      UP(N-1,2)=(1.+1./(2.*((1.+(N-2)*DZ)**3)))*SIN(G+DTHETA)
      UP(N,2)  =(1.+1./(2.*((1.+(N-1)*DZ)**3)))*SIN(G+DTHETA)
      SO  = 0.0
      TEM(1,1,1) = 1.0
      IF(L.EQ.1) TEM(1,J,1) = 0.0
      TEM(1,1,2) = 1.0
      TEM(N+1,J,1) = 1.0
      TEM(N+1,J,2) = 1.0
      IF(L.EQ.1) THEN
      II = 2
      ELSE
      II = 1
      ENDIF
      DO 303 I = II,N
303   A(I) = (1./DT)+(2.0/DZ**2)+U(I,2)*PR/DX(I)
      DO 304 I=II,N
304   B(I)=(RE*PR*W(I,2)/(4.0*DZ)) - 1./(DZ**2)
      DO 305 I = II,N
305   C(I) = (-RE*PR*W(I,2)/(4.0*DZ)) - 1./(DZ**2)
      DO 306 I=II,N
306   D(I) = TEM(I,J,1)/DT+U(I,2)*PR*TEM(I,J-1,2)/DX(I)+SO*PR
      IF(L.GT.1) THEN
      A(1) = A(1)-C(1)*(1-AKK)/AKK
      B(1) = C(1)/AKK + B(1)
```

```
      ENDIF
      D(N) = D(N) - B(N)
      E(II) = A(II)
      F(II) = D(II)/E(II)
      DO 715 I=II+1,N
      E(I) = A(I)-C(I)*B(I-1)/E(I-1)
715   F(I) = (D(I)-C(I)*F(I-1))/E(I)
      TEM(N,J,2) = F(N)
      DO 720 II = 1,N-II
      I = N-II
      TEM(I,J,2)=F(I)-B(I)*TEM(I+1,J,2)/E(I)
720   CONTINUE
      ANU = (1./DZ)*(TEM(2,J,2)-TEM(1,J,2))
      TEST = ABS(1.-TEM(N,J,2))
56    FORMAT(5X,I4,5X,F12.5)
      IF(J.EQ.IN) THEN
      write(9,*) 'L = ',l
      WRITE(9,55) (DZ*(I-1),TEM(I,J,2),I=1,N+1)
      WRITE(11,55) (L-1)*DT,TEM(ISTEP,J,2)
      ENDIF
      WRITE(12,56) J,ANU
      DUB  = 2.* U(N,2)-(U(N+1,2)- U(N-1,2))/2.
      DUP  = 2.*UP(N,2)-(U(N+1,2)-UP(N-1,2))/2.
      PERU = ABS(DUB-DUP)/ABS(DUB)
      DWB  = 2.* W(N,2) - (W(N+1,2)- W(N-1,2))/2.
      DWP  = 2.*WP(N,2) - (W(N+1,2)-WP(N-1,2))/2.
      PERW = ABS(DWB-DWP)/ABS(DWB)
      G = G + DTHETA
      IF(J.LT.6) GO TO 160
      IF(PERU.GT.0.005)  GO TO 180
160   TX0   = (-U(3,2)+4.*U(2,2)-3.*U(1,2)) / (2.*DZ)
      TX(J) = 4.*R(2)*(tx0)*(SIN(G))
      FX(J) = TEM(1,J,2)*SIN(G+DTHETA)/(1.-COS(108*(22./7.)/180.))
      T     = (TX0)*((2./RE)**0.5)
      TTX   =  T * (2.**0.5)
      IF(L.EQ.1) WRITE (5,6) J-1, T,TTX
 6    FORMAT(10X,I4,2(10X,F12.5))
      DO 200 I = 1, N+1
      U(I,1) = U(I,2)
200   W(I,1) = W(I,2)
      R(1)   = R(2)
      GO TO 84
180   N = N+2
      G = G - DTHETA
      DO 141 I = N,N+1
```

```
      U(I,1)=(1.+1./(2.*(1.+(I-1)*DZ)**3))*SIN(G)
141   W(I,1) = -(1.-1./(1.+(I-1)*DZ)**3)*COS(G)
      GO TO 83
270   IF(M.EQ.360) GO TO 281
      IF(M.EQ.1800)GO TO 295
      AW = TX(J-1)
      DO 221 I = 2,J-2
      IW = (I+1)/2
221   AW = AW +(2.+2.*(I+1-IW*2))*TX(I)
      CW = AW*DTHETA/3.
      TW = FX(J-1)
      DO 777 I=2,J-2
      IW = (I+1)/2
777   TW = TW + (2.+2.*(I+1-IW*2))*FX(I)
      TAVE = TW*DTHETA/3.
281   M  = 1800
      GO TO 81
295   G1 = (G)*180./3.1415926536
      GG = G
      AW=TX(J-1)
      DO 220 I=2,J-2
      IW=(I+1)/2
220   AW=AW+(2.+2.*(I+1-IW*2))*TX(I)
      CW=CW+AW*DTHETA/3.
      IF(L.EQ.1) WRITE(16,508) CW
508   FORMAT(18X,'CD = ',F16.10)
      TW = FX(J-1)
      DO 555 I=2,J-2
      IW = (I+1)/2
555   TW = TW + (2.+2.*(I+1-IW*2))*FX(I)
      TAVE = TAVE+TW*DTHETA/3.
      DO 511 J = 1,JJ
      DO 511 I = 1, N+1
511   TEM(I,J,1) = TEM(I,J,2)
      WRITE(10,56) (J,TEM(1,J,2),J=1,JJ)
      IF(TEM(1,60,2).GE.0.99) THEN
      write(6,290) G1
290   FORMAT(2X,'THE APPROXIMATE SEPARATION POINT AT',3X,F6.2)
      WRITE(6,*) 'STEADY STATE CONDITION REACHED. . . . . .'
      GOTO 300
      ELSE
      L=L+1
      N=20
      M=180
      GO TO 79
```

```
      ENDIF
300   WRITE(6,509)
      write(6,*) 'program ending execution at ', time@()
509   FORMAT(10X,'//////// END OF RESULTS //////')
      STOP
      END
```

C.4 List of the Liquid-Phase Program

```
      DIMENSION U(1001,2),W(1001,2),A(1001),B(1001),C(1001),D(1001)
     1  ,UP(999,2),US(1,200),CR(150),TEM(1001,140,2)
     1  ,E(1001),F(1001),DX(1001)
       OPEN(2,FILE='SURF.DAT',STATUS='OLD')
      OPEN(4,FILE='UIN.DAT',STATUS='unknown')
      OPEN(5,FILE='WIN.DAT',STATUS='unknown')
      OPEN(7,file='IPT',status='old')
      OPEN(8,FILE='UHILL.DAT',STATUS='UNKNOWN')
      OPEN(9,FILE='CR.DAT',STATUS='UNKNOWN')
      OPEN(10,FILE='TIN.DAT',STATUS='UNKNOWN')
      OPEN(11,FILE='UH1.DAT',STATUS='UNKNOWN')
      OPEN(14,FILE='TSURF.DAT',STATUS='OLD')
      OPEN(15,FILE='JJ',STATUS='OLD')
      READ(7,*)DZ,DZL,RE,N,M,VISR,FACT,IN,DT,PR,ISTEP
      write(10,*)DZ,DZL,RE,N,M,VISR,IN,DT,PR,ISTEP
      fact = 5000.
      DO 20 I=1,200
      READ(2,*) K,US(1,I)
      IF(K.EQ.0) GO TO 30
20    CONTINUE
30    kk=i-1
      CONTINUE
      WRITE (6,*)'NUMBER OF MERIDIONAL STATIONS = ',KK
      READ (15,*)JJ,LL
 56   FORMAT(5X,I4,5X,F12.5)
      L = 1
      do 500 j=1,jj
      do 500 i=1,999
      tem(i,j,1) = 0
500   tem(i,j,2) = 0
89    IF(L.GT.ll) GO TO 87
      DO 111 I=1,JJ
111   READ(14,56)  J,TEM(1,J,2)
87    DO 80 I = 1,N
      W(I,1) = 0.0
```

```
      U(I,1) = 0.0
80    CONTINUE
      G = 0.0
      M = 180
      N = 20
81    J = 1
      DTHETA = 3.1415926536/M
      DX(1) = 2.*DTHETA/RE
84    W(1,2)  = 0.0
      J      = J + 1
      IF(J.GT.KK) GO TO 300
      U(1,2) = US(1,J)
83    UHS = 1.5 * SIN(G+DTHETA)
      CR(J) = U(1,2)/UHS
      DO 88 I=20,999
      W(I,2) =  1.5*CR(J)*((1.-(I-1)*DZL)**2)     *COS(G+DTHETA)
88    U(I,2) = -1.5*CR(J)*(1.-2.*(1-(I-1)*DZL)**2)*SIN(G+DTHETA)
      U(N+1,2) =-1.5*CR(J)*(1.-2.*(1-N    *DZL)**2)*SIN(G+DTHETA)
      U(N+2,2) =-1.5*CR(J)*(1.-2.*(1-(N+1)*DZL)**2)*SIN(G+DTHETA)
      W(N+1,2) = 1.5*CR(J)*((1.-N*DZL)**2)*COS(G+DTHETA)
      DO 90 I = 2,1000
90    DX(I)=(1.-DZL*(I-1))*DX(1)
      DO 105 I = 2,N
105   C(I)   =(W(I,1)*RE/(4.*DZL)-FACT/(DZL**2))
      DO 106 I=2,N
106   A(I)   = U(I,1)/DX(I)+2.*FACT/(DZL**2)
      DO 107 I=2,N
107   B(I)   = (-W(I,1)*RE/(4.*DZL)-FACT/(DZL**2))
      DO 110 I=2,N
      Q = (9./4.)*CR(J)*(1.-2.*(1-N*DZL)**2)**2
      P1 = (SIN(G+DTHETA))**2*(CR(J)-CR(J-1))/DX(I)
      P2 = RE * CR(J) * SIN(2*(G+DTHETA))/(4.*(1-N*DZ))
      P  = P1 + P2
110   D(I)= Q * P + (U(I,1)**2)/DX(I)
      D(2) = D(2) - C(2) * U(1,2)
      D(N) = D(N) - B(N) * U(N+1,2)
      E(2) = A(2)
      F(2) = D(2)/E(2)
      DO 115 I=3,N
      E(I) = A(I)-C(I)*B(I-1)/E(I-1)
115   F(I) = (D(I)-C(I)*F(I-1))/E(I)
      U(N,2) = F(N)
      DO 120 II = 1,N-2
      I = N-II
      U(I,2)=F(I)-B(I)*U(I+1,2)/E(I)
```

```
120   CONTINUE
      IF(L.EQ.1) THEN
      IF(J.EQ.IN) WRITE(4,55) (DZL*(I-1),U(I,2),I=1,N+2)
      ENDIF
 55   FORMAT(2(10x,f14.6))
      DO 125 I=1,N
      A(I) = RE/(2.*DZL)
125   B(I) = -RE/(2.*DZL)
      CCOT = COS(G+DTHETA)/SIN(G+DTHETA)
      DO 130 I=1,N
130   D(I) =-(U(I+1,2)+U(I,2)-U(I+1,1)-U(I,1))/(DX(I)+DX(I+1))
     1  -(U(I+1,2)+U(I,2))*RE*CCOT*0.25
      W(2,2) = D(1)/B(1)
      DO 135 I=3,N
135   W(I,2) = (D(I-1)-A(I-1)*W(I-1,2))/B(I-1)
      IF (L.EQ.1) THEN
      IF(J.EQ.IN) WRITE(5,55) (DZL*(I-1),W(I,2),I=1,N)
      ENDIF
      UP(N-1,2) =-1.5*CR(J)*(1.-2.*(1.-(N-2)*DZL)**2)*SIN(G+DTHETA)
      UP(N,2)  =-1.5*CR(J)*(1.-2.*(1.-(N-1)*DZL)**2)*SIN(G+DTHETA)
      DUB  = 2.* U(N,2)-(U(N+1,2)- U(N-1,2))/2.
      DUP  = 2.*UP(N,2)-(U(N+1,2)-UP(N-1,2))/2.
      PERU = ABS(ABS(DUB)-ABS(DUP))/ABS(DUB)
      IF(J.LT.7) GO TO 119
      IF(PERU.GT.0.009)  GO TO 180
119   CONTINUE
      G = G + DTHETA
      tem(1,1,1) = 1.
      tem(1,1,2) = 1.
      DO 195 I = 2,999
195   C(I)=(-2./(1.-(I-1)*DZL)+RE*PR*W(I,2)/(2.*s))/(2.*DZL)-1./(DZL**2)
      DO 196 I=2,999
196   A(I)= (1./DT)+(U(I,2))*PR/(DX(I)*s)+2./(DZL**2)
      DO 197 I=2,999
197   B(I)=(2./(1.-(I-1)*DZL)-RE*PR*W(I,2)/(2.*s))/(2.*DZL)-1./(DZL**2)
      DO 198 I=2,999
198   D(I)=(U(I,2)*PR*TEM(I,J-1,2))/(DX(I)*s)+TEM(I,J,1)/DT
      D(2)=D(2)-C(2)*TEM(1,J-1,2)
      A(999)=A(999)+B(999)
      E(2) = A(2)
      F(2) = D(2)/E(2)
      DO 515 I=3,999
      E(I) = A(I)-C(I)*B(I-1)/E(I-1)
515   F(I) = (D(I)-C(I)*F(I-1))/E(I)
      TEM(999,J,2) = F(999)
```

```
      DO 520 II = 1,999-2
      I = 999-II
      TEM(I,J,2)=F(I)-B(I)*TEM(I+1,J,2)/E(I)
520   CONTINUE
      TEM(1000,J,2)=TEM(999,J,2)
      IF(J.EQ.IN) THEN
      if(l.eq.6) WRITE(10,55) (DZL*(I-1),TEM(I,J,2),I=1,1000,50)
      if(l.gt.ll) then
      IF(mod(l,50).eq.0)  THEN
      WRITE(10,*) 'L = ',L
      WRITE(10,55) (DZL*(I-1),TEM(I,J,2),I=1,1000,50)
      WRITE(10,55) DZL*(1000),TEM(999,J,2)
      ENDIF
      else
      if(mod(l,3).eq.0) then
      WRITE(10,*) 'L = ',L
      WRITE(10,55) (DZL*(I-1),TEM(I,J,2),I=1,500,2)
      endif
      endif
      endif
      DO 200 I = 1, N+1
      U(I,1) = U(I,2)
200   W(I,1) = W(I,2)
      GO TO 84
180   N = N+2
      G = G - DTHETA
      DO 141 I = N,N+1
      U(I,2) =-1.5*CR(J)*(1.-2.*(1.-(I-1)*DZL)**2)*SIN(G+DTHETA)
141   W(I,2) = 1.5*CR(J)*((1.-(I-1)*DZL)**2)*COS(G+DTHETA)
      GO TO 83
270   IF(M.EQ.360) GO TO 281
      IF(M.EQ.1800)GO TO 295
281   M  = 1800
      GO TO 81
295   G1 = (G)*180./3.1415926536
300   L      = L + 1
      IF(L.GT.LL) THEN
      DO 117 I = 1,JJ
117   TEM(1,I,1) = TEM(1,I,2)
      ENDIF
      IF(TEM(900,60,1).GT.0.9) THEN
      GO TO 301
      ELSE
      DO 201  J=1,JJ
      DO 201  I=2,1001
```

```
201   TEM(I,J,1) = TEM(I,J,2)
      GO TO 89
      ENDIF
301   write(10,*) 'L = ',l
      write(10,55) (DZL*(I-1),TEM(I,in,2),I=1,1000,50)
      WRITE(6,509)
509   FORMAT(10X,'//////// END OF RESULTS, STEADY STATE REACHED //////')
      STOP
      END
```

VITAE

Name : Mohamed Abdelkarim Mohamed Antar

Date of birth : 18th August, 1963

Marital status : Married (+ one child)

Education : B.Sc. in Mechanical Engineering, Alexandria University, Egypt, with degree of honor, June, 1985 .

Worked as a teaching assistant in Mechanical Engineering Department, Tanta University, Egypt .

M.Sc. in Mechanical Engineering, Alexandria University, Egypt, September, 1989 .

Joined KFUPM as a Ph.D. student, end April 1991 .

Ph.D. in Mechanical Engineering, KFUPM, January, 1996 .